

## ABSTRACT

Title of Dissertation: Magneto-optical response of  
WSe<sub>2</sub> excitons in sub-Kelvin regime

Jonathan R. Vannucci  
Doctor of Philosophy, 2022

Dissertation Directed by: Professor Mohammad Hafezi  
Department of Physics

Interest in correlated electron states in strongly correlated materials, such as transition metal dichalcogenides (TMDs), has been growing in recent years thanks to significant technological advancements in cryogenic quantum optics measurement techniques that allow for their experimental realization. Milli-kelvin temperatures are required to eliminate thermalization effects that otherwise mask the interesting correlated physics in these materials. In an effort to contribute to the understanding of these states, we developed an ultra-low temperature dilution refrigerator measurement system with free-space optical access that is able to achieve a base temperature of <30 milli-kelvin and apply a  $\pm 12$  T perpendicular magnetic field. We utilize a 100x cryogenic objective with 0.82 NA to make highly localized optical measurements on our samples. Our custom stage system allows for quick sample exchange and rapid characterization of our devices.

TMDs have been shown to be suitable materials for probing new and interesting exciton physics. In monolayer form, their direct band gap in the visible range and high binding energies open the possibility to optically explore higher energy Rydberg states. As the understanding of the neutral exciton's Rydberg series has grown in recent

years, interest has started to shift toward the less understood charged excitons. Using photoluminescence excitation (PLE), we sweep a laser's energy across the spectral range of the  $n > 1$  Rydberg exciton states and monitor the emission intensities of the  $1s$  excitons. Through this technique, we were able to measure the precise spectral profile and carrier density dependence of the  $3s$  neutral ( $X_0^{3s}$ ),  $2s$  neutral ( $X_0^{2s}$ ), and  $2s$  negatively charged ( $X_-^{2s}$ ) excitons in monolayer  $\text{WSe}_2$ . By applying a perpendicular magnetic field to the sample, we were also able to measure the valley dependent Zeeman splitting of both  $X_0^{2s}$  and  $X_-^{2s}$  and extracted their corresponding g-factors.



Magneto-optical response of  
WSe<sub>2</sub> excitons in sub-Kelvin regime

by

Jonathan R. Vannucci

Dissertation submitted to the Faculty of the Graduate School of the  
University of Maryland, College Park in partial fulfillment  
of the requirements for the degree of  
Doctor of Philosophy  
2022

Advisory Committee:

Professor Mohammad Hafezi, Advisor/Chair  
Professor Glenn Solomon  
Professor Sunil Mittal  
Professor You Zhou  
Professor Oded Rabin

## Acknowledgments

First and foremost, I would like to thank Mohammad Hafezi for welcoming me into his lab and giving me this opportunity. Mohammad's passion for science is contagious such that even on days that I discovered something was not working or not possible, after discussing it with him, I always found myself motivated to pursue the next project. I was lucky to have him to guide me through this experience.

I express my sincerest thanks and gratitude to Sunil Mittal who taught me so much over the past years that allowed me to become the experimentalist I am today. I am very lucky to have had his guidance and wisdom as we built the lab together from an empty storage room to a fully functional low temperature spectroscopy laboratory. I wish him all the best in his new faculty position at Northeastern University.

I would like to thank Glenn Solomon and his post-docs Tobias Huber and Markus Mueller. I was lucky to have their expertise and help as we began the construction of our current lab. I wish Glenn, Tobi, and Markus all the best in their future endeavors.

Thank you Berry Jonker and his group at NRL including Hsun-Jen Chuang, Kathy McCreary, and Matthew Rosenberger. We have enjoyed our collaboration over the years and the sample provided by their group was utilized in all of the data collected in this dissertation.

I was lucky enough to have a number of undergraduate students work with me on

a number of projects in our lab. Bruce Wang, Daniel Stone, and Kevin Li were three exceptional undergraduate students and it was a pleasure to have had them work with me. I wish them all the best in their future endeavors.

Special thanks to Julia Sell, co-author of the paper most of the work in this dissertation is based upon. Julia helped heavily in the theoretical understanding of our reported results and the analysis of our magnetic field PLE data. We started in this lab together and saw it rise from nothing to fully functional. I wish Julia all of the best in her future pursuits.

I would like to thank Bin Cao and Chris Flower for the many interesting and helpful discussions we have had over the years. As well as Deric Session, who I was lucky enough to have worked with and could always rely on. Both are excellent physicists and I wish them all the best in their research.

I was lucky to also work with Daniel Gustavo Suárez Forero who helped a lot in the new lab design and is taking over operations of the lab. I look forward to all of the great results that will come from his hard work and passion for science.

Special thanks to both Deric and Daniel for posing in all of the candid photos used in the BlueFors procedures found in the appendix.

Two new students, Supratik Sarkar and Beini Gao, joined toward the end of my graduate career in Mohammad's lab, but I enjoyed working with them and wish them all the best in their future pursuits.

I've made a number of friends through my graduate school experience, and I would like to thank Alexander Craddock, Jimmy Juno, Natalia Pankratova, and Rodney Snyder who helped keep me entertained and laughing as we pursued our degrees in this program.

I wish them all the best.

My parents, Richard and Helen Vannucci, made this opportunity possible and I would not have been able to do it without their support over the years. My sister, Jessica Vannucci, was also an incredibly important pillar of support in my pursuit of graduate school. And thank you to all of my aunts, uncles, and cousins who encouraged me and supported me through this experience. Special thanks to Maria Zielinski for reading through this dissertation for grammar and spelling error as well as always supporting me through this journey. I was lucky to have such a supportive immediate and extended family through this chapter of my life.

And, of course, I express my sincerest thanks to my wife, Hilma Monteiro-Vannucci, for dealing with me through graduate school. I was lucky to have you there with me through the end of this experience, and look forward to everything that comes next.

Finally, I would like to thank Smash Mouth. In 1999, they wrote "You'll never shine if you don't glow," and that is not only a catchy and inspirational lyric that helped me push through the difficulties of graduate school, but also a wonderful description of the off- and on-resonant nature of our PLE measurements.

# Table of Contents

|  |           |
|--|-----------|
| <b>Abstract</b>  | <b>1</b>  |
| <b>Acknowledgements</b>  | <b>ii</b> |
| <b>Table of Contents</b>   | <b>v</b>  |
| <b>List of Tables</b>  | <b>ix</b> |
| <b>List of Figures</b>   | <b>ix</b> |
| <b>Chapter 1: Introduction</b>   | <b>1</b>  |
| <b>Chapter 2: Introduction to 2D Materials</b>                           | <b>4</b>  |
| 2.1 Overview . . . . .   | 4         |
| 2.2 Other 2D Materials . . . . .   | 5         |
| 2.3 2D Material Possibilities . . . . .                                  | 8         |
| <b>Chapter 3: Physical Properties of Transition Metal Dichalgeniodes</b> | <b>9</b>  |
| 3.1 Overview . . . . .   | 9         |
| 3.2 In-direct vs Direct Bandgap . . . . .                                | 9         |
| 3.3 Circular Dichroism in TMDs . . . . .                                 | 11        |
| 3.4 Spin-Orbit Coupling . . . . .  | 17        |
| <b>Chapter 4: WSe<sub>2</sub> Device Details</b>                         | <b>20</b> |
| 4.1 WSe <sub>2</sub> Stacking Procedure . . . . .                        | 20        |
| <b>Chapter 5: Photoluminescence Measurements</b>                         | <b>25</b> |
| 5.1 Introduction . . . . .   | 25        |
| 5.2 Exciton formation through Photoluminescence (PL) . . . . .           | 25        |
| 5.3 Experimental Realization . . . . .                                   | 30        |
| 5.4 Rydberg Series . . . . .   | 32        |
| 5.5 Other Exciton Species . . . . .                                      | 37        |
| 5.6 Extraction of Carrier Concentration . . . . .                        | 41        |
| 5.7 2s Negatively Charged Excitons . . . . .                             | 43        |
| <b>Chapter 6: Photoluminescence Excitation Measurements</b>              | <b>48</b> |
| 6.1 Overview . . . . .   | 48        |

|                    |  |            |
|--------------------|--|------------|
| 6.2                | Photoluminescence Excitation                       | 50         |
| 6.3                | PLE Gate Voltage Dependence                        | 54         |
| 6.4                | Phonon Modes                                       | 59         |
| <b>Chapter 7:</b>  | <b>Magnetic Field Dependence of Exciton States</b> | <b>62</b>  |
| 7.1                | Introduction                                       | 62         |
| 7.2                | Valley Zeeman Splitting                            | 62         |
| 7.3                | PLE Magnetic Field Dependence                      | 67         |
| 7.4                | Magneto-photoresponse of the 2s Exciton Species    | 72         |
| <b>Chapter 8:</b>  | <b>Conclusion</b>                                  | <b>78</b>  |
| <b>Chapter A:</b>  | <b>BlueFors Procedures</b>                         | <b>80</b>  |
| A.1                | Introduction to BlueFors                           | 80         |
| A.2                | Gas Handling System Configurations and Schematics  | 83         |
| A.3                | Probe Procedures:                                  | 93         |
| A.3.1              | Unloading the Probe                                | 94         |
| A.3.2              | Loading the Probe                                  | 101        |
| A.4                | Condensing   | 116        |
| A.4.1              | Condensing Procedure:                              | 118        |
| A.4.2              | Stop Condensing Procedure:                         | 121        |
| A.5                | Opening/Closing the System                         | 124        |
| A.5.1              | Warm-up Procedure:                                 | 126        |
| A.5.2              | Opening Procedure:                                 | 128        |
| A.5.3              | Closing Procedure:                                 | 139        |
| A.5.4              | Cool-down Procedure:                               | 150        |
| A.6                | BlueFors Traps                                     | 151        |
| A.6.1              | LN2 Trap Cleaning Procedure:                       | 153        |
| A.7                | Procedure Check Sheets                             | 158        |
| <b>Appendix B:</b> | <b>BlueFors Probe</b>                              | <b>167</b> |
| B.1                | Summary  | 167        |
| B.2                | Wiring on the Probe                                | 169        |
| B.2.1              | Type of Wire Used for the Probe                    | 169        |
| B.2.2              | On Probe Wiring Configuration                      | 170        |
| B.2.3              | Sapphire Boards                                    | 175        |
| B.2.4              | Break-out DC wiring outside the BlueFors           | 177        |
| B.3                | Sample Positioning                                 | 179        |
| B.3.1              | Cage Assembly                                      | 179        |
| B.3.2              | Attocube Positioners                               | 182        |
| B.3.3              | Additional Attocube Stages                         | 186        |
| B.3.4              | Blank Stage Mount                                  | 187        |
| B.4                | Probe Optics                                       | 188        |
| B.4.1              | Objective Mount Assembly                           | 188        |
| B.4.2              | Attocube Objective                                 | 190        |

|  |   |            |
|--|---|------------|
| B.4.3  | Lens Mount Assembly . . . . .   | 191        |
| B.5  | Probe Testing Station . . . . .                                       | 192        |
| B.6  | Thermometer and Heater . . . . .                                      | 195        |
| <b>Appendix C: Sample Stage Design</b>         |   | <b>197</b> |
| C.1  | Outline of Chip Carrier and Carriage System . . . . .                 | 197        |
| C.2  | Chip Carriers and Sample Carriages . . . . .                          | 200        |
| C.2.1  | Manufacturing of the PCB Boards . . . . .                             | 200        |
| C.2.2  | Two types of Carriage Boards . . . . .                                | 203        |
| C.2.3  | Sample Mounting . . . . .   | 205        |
| C.2.4  | Chip Carrier and Sample Carriage Storage . . . . .                    | 207        |
| <b>Appendix D: BlueFors Measurement Optics</b> |   | <b>209</b> |
| D.1  | Internal BlueFors Optics . . . . .                                    | 209        |
| D.1.1  | BlueFors Windows . . . . .  | 210        |
| D.1.2  | BlueFors 45 Deg Cold Mirror Mount . . . . .                           | 212        |
| D.2  | External BlueFors Optics . . . . .                                    | 216        |
| D.2.1  | Aluminum Breadboard Optical Assembly . . . . .                        | 216        |
| D.2.2  | LED and CCD Imaging System . . . . .                                  | 219        |
| D.2.3  | Spectroscopy Optics . . . . .   | 223        |
| D.2.4  | Andor Camera Readout . . . . .  | 228        |
| D.3  | Magnetic Field Dependent Motion of the Sample and/or Optics . . . . . | 231        |
| D.3.1  | BlueFors low drift and vibrations without magnetic field . . . . .    | 232        |
| D.3.2  | BlueFors Optical Table and Breadboard Designs . . . . .               | 234        |
| D.3.3  | Additional Magnetic Dependent Spot Motion (X-K Zeeman Data) . . . . . | 235        |
| <b>Appendix E: BlueFors Magnet</b>             |   | <b>241</b> |
| E.1  | Summary . . . . .   | 241        |
| E.2  | Computer Control . . . . .  | 243        |
| E.3  | Quench Event . . . . .  | 246        |
| <b>Appendix F: Sirah Matisse DR Dye Laser</b>  |   | <b>249</b> |
| F.1  | Introduction . . . . .  | 249        |
| F.2  | Mixing of DCM Dye . . . . .   | 252        |
| F.3  | Dye Mixture Circulator . . . . .                                      | 254        |
| F.4  | Changing Dye . . . . .  | 260        |
| F.5  | Dye Jet Problems . . . . .  | 263        |
| F.6  | Replacing Mirrors . . . . .   | 266        |
| F.7  | Alignment . . . . .   | 268        |
| F.8  | Sirah Matisse Commander Software, Homing, and Calibration . . . . .   | 276        |
| F.9  | Output Optics . . . . .   | 282        |
| F.10   | Filtering Side Bands . . . . .  | 284        |
| F.11   | Power Stabilization . . . . .   | 288        |
| <b>Appendix G: Additional Lab Equipment</b>    |   | <b>292</b> |

|                     |   |            |
|---------------------|---|------------|
| G.1                 | Montana Cryostat . . . . .              | 292        |
| G.1.1               | Table Top Cryostat Details . . . . .    | 294        |
| G.1.2               | Montana Pumps . . . . .                 | 296        |
| G.1.3               | Optical Excitation . . . . .            | 297        |
| G.1.4               | DC Wiring . . . . .                     | 299        |
| G.2                 | Continuous Wave Laser Systems . . . . . | 301        |
| G.2.1               | Summary . . . . .                       | 301        |
| G.2.2               | M-Squared Laser . . . . .               | 302        |
| G.2.3               | HeNe and 532 nm Diode Lasers . . . . .  | 306        |
| G.3                 | 3D Printed SM1 Tube Holders . . . . .   | 308        |
| G.4                 | Encapsulation System . . . . .          | 309        |
| <b>Bibliography</b> |   | <b>314</b> |



## List of Figures

|      |   |    |
|------|---|----|
| 2.1  | Graphene Sticky Tape Revolution . . . . .   | 5  |
| 2.2  | Other 2D Materials and their properties . . . . .   | 6  |
| 2.3  | TMD lattice structure . . . . .   | 7  |
| 3.1  | DFT of MoS <sub>2</sub> showing transition the bulk indirect band gap to a direct band gap in the monolayer limit . . . . . | 10 |
| 3.2  | Circular Dichroism in TMDs . . . . .  | 12 |
| 3.3  | WSe <sub>2</sub> Spin-Orbit Coupling Illustration . . . . .   | 17 |
| 4.1  | WSe <sub>2</sub> Sample Summary . . . . .   | 21 |
| 4.2  | WSe <sub>2</sub> Full Stacking Procedure . . . . .  | 24 |
| 5.1  | Schematic of the formation of an Exciton in photoluminescence . . . . .   | 26 |
| 5.2  | Thermalization of an exciton bound state . . . . .  | 28 |
| 5.3  | Schematic of the steady state excitation of excitons . . . . .  | 30 |
| 5.4  | Schematic of a PL Measurement . . . . .   | 31 |
| 5.5  | Schematic of a PL Measurement of Rydberg Series . . . . .   | 33 |
| 5.6  | Non-radiative relaxation time scales of Rydberg excitons . . . . .  | 35 |
| 5.7  | PL vs Gate . . . . .  | 37 |
| 5.8  | Spin configuration of exciton species . . . . .   | 40 |
| 5.9  | Extraction of Carrier Density . . . . .   | 42 |
| 5.10 | N-doped PL emission including 2s Rydberg Series Excitons . . . . .  | 44 |
| 5.11 | PL vs Gate showing the emergence of X <sub>-</sub> <sup>2s</sup> and X <sub>0</sub> <sup>2s</sup> . . . . .                 | 45 |
| 5.12 | Analysis of PL vs Gate showing the emergence of X <sub>-</sub> <sup>2s</sup> and X <sub>0</sub> <sup>2s</sup> . . . . .     | 47 |
| 6.1  | PL vs PLE . . . . .   | 49 |
| 6.2  | Off-resonant vs On-resonant PLE . . . . .   | 51 |
| 6.3  | PLE analysis summary . . . . .  | 53 |
| 6.4  | PLE schematic and data for charge neutrality and n-doped regimes . . . . .  | 55 |
| 6.5  | PLE analysis n-doping while monitoring X <sub>0</sub> and X <sub>-</sub> <sup>t</sup> emission . . . . .                    | 58 |
| 6.6  | Phonon modes in X <sub>0</sub> Emission Energy PLE . . . . .  | 60 |
| 7.1  | Magnetic Moment Contributions to the valley Zeeman splitting in WSe <sub>2</sub> . . . . .                                  | 63 |
| 7.2  | Summary of Valley Zeeman Splitting in WSe <sub>2</sub> . . . . .  | 66 |
| 7.3  | Illustration of Valley Zeeman Splitting in PLE data . . . . .   | 68 |
| 7.4  | Illustration of the Comparison of PLE Valley Zeeman Splitting for ±B Fields . . . . .                                       | 70 |

|      |  |     |
|------|--|-----|
| 7.5  | PLE data of the Valley Zeeman Splitting while monitoring the $X_0$ emission energy . . . . .               | 71  |
| 7.6  | PLE data of the Valley Zeeman Splitting while monitoring the $X_-^t$ emission energy . . . . .             | 72  |
| 7.7  | PLE Valley Zeeman Splitting from PLE monitoring $X_-^t$ . . . . .  | 73  |
| 7.8  | Extracted Zeeman Splitting and g-factor Fit of $2s$ Excitons from PLE monitoring $X_-^t$ . . . . .         | 73  |
| 7.9  | Extracted Zeeman Splitting and g-factor Fit of $2s$ Excitons from PLE monitoring $X_-^s$ . . . . .         | 75  |
| 7.10 | $1s$ $X_0$ and $X_-^{t,s}$ g-factor calculated from magnetic field dependent PL at $V_g = 0.6$ V . . . . . | 76  |
|      |  |     |
| A.1  | BlueFors cryostat Images Closed and Open . . . . .   | 81  |
| A.2  | Tools Mounted on the Wall for use While Working on the BlueFors . . . .                                    | 82  |
| A.3  | BlueFors GHS: All Valves Off . . . . .   | 84  |
| A.4  | BlueFors GHS: Start Condensing . . . . .   | 85  |
| A.5  | BlueFors GHS: Normal Circulation . . . . .   | 86  |
| A.6  | BlueFors GHS: Stop Condensing . . . . .  | 87  |
| A.7  | BlueFors GHS: Pump Probe Bellows . . . . .   | 88  |
| A.8  | BlueFors GHS: Vent Probe Bellows . . . . .   | 89  |
| A.9  | BlueFors GHS: Pump Vacuum Can . . . . .  | 90  |
| A.10 | BlueFors GHS: Vent Vacuum Can . . . . .  | 91  |
| A.11 | BlueFors GHS: Pump LN2 Traps . . . . .   | 92  |
| A.12 | Phase Transition and Schematic of Dilution Refrigerator . . . . .  | 116 |
| A.13 | Details of the outer radiation shield of the BlueFors Dilution refrigerator .                              | 124 |
| A.14 | The two traps in the BlueFors Gas Handling System . . . . .  | 151 |
|      |  |     |
| B.1  | BlueFors Probe Full CAD drawing . . . . .  | 168 |
| B.2  | Probe Head CAD description . . . . .   | 170 |
| B.3  | Probe Bottom Connectors Breakout . . . . .   | 171 |
| B.4  | Images of BlueFors Probe Wiring . . . . .  | 172 |
| B.5  | Difference in SIP Connectors used on Probe . . . . .   | 173 |
| B.6  | DC Wiring Sapphire Boards . . . . .  | 175 |
| B.7  | BlueFors DC Wiring Breakout Box . . . . .  | 177 |
| B.8  | Micro D-sub connector to Fischer Connector Pin Configuration . . . . .                                     | 178 |
| B.9  | BlueFors Probe design for Attocubes and Objective . . . . .  | 179 |
| B.10 | BlueFors Probe Cage Bottom CAD . . . . .   | 181 |
| B.11 | Attocube Positioners in the BlueFors Probe . . . . .   | 182 |
| B.12 | Attocube Positioners Controller Box and Wiring . . . . .   | 183 |
| B.13 | Attocube Positioners Controller Daisy Software . . . . .   | 185 |
| B.14 | Blank Stage mount for the BlueFors Probe . . . . .   | 187 |
| B.15 | Removal of BlueFors Objective . . . . .  | 189 |
| B.16 | Attocube Objective for the BlueFors Probe . . . . .  | 190 |
| B.17 | Lens mount for BlueFors Probe . . . . .  | 191 |
| B.18 | Probe Testing Station . . . . .  | 192 |

|   |     |
|---|-----|
| B.19 Probe Testing Station Wiring . . . . .   | 193 |
| B.20 BlueFors Probe Thermometer and Heater . . . . .  | 195 |
| C.1 Design and 3D CAD of Chip Carrier and Sample Carriage . . . . .   | 198 |
| C.2 Images of the Chip Carrier and Sample Carriage . . . . .  | 201 |
| C.3 Two Different Kinds of Sample Carriages . . . . .   | 203 |
| C.4 Installation of Sample: Chip Carrier, Sample Carriage, and Wire Bonding . . . . .   | 205 |
| C.5 Storage of Chip Carriers and Sample Carriages . . . . .   | 207 |
| D.1 Spectrosil 2000 UV Fused Silica Windows Specs . . . . .   | 210 |
| D.2 BlueFors Optical Windows . . . . .  | 211 |
| D.3 BlueFors Cold Mirror Images . . . . .   | 212 |
| D.4 BlueFors Cold Mirror Design . . . . .   | 213 |
| D.5 Image of BlueFors Optical Breadboard . . . . .  | 216 |
| D.6 BlueFors Optics Schematic . . . . .   | 217 |
| D.7 BlueFors CCD Imaging . . . . .  | 219 |
| D.8 BlueFors CCD Imaging Optics . . . . .   | 220 |
| D.9 BlueFors CCD Imaging 3D Printed Pellicle BS Mount . . . . .   | 221 |
| D.10 Spectrometer Light Analysis Schematic . . . . .  | 223 |
| D.11 Images of the inside of the Princeton Spectrometer . . . . .   | 224 |
| D.12 Fiber Coupled Input Optics and Andor Camera on Princeton Spectrometer . . . . .  | 226 |
| D.13 Custom machined parts for the Princeton Spectrometer . . . . .   | 227 |
| D.14 CCD Camera Read-Out Methods . . . . .  | 228 |
| D.15 PL vs Strain on WSe <sub>2</sub> sample . . . . .  | 233 |
| D.16 BlueFors Optical Tables . . . . .  | 234 |
| D.17 Spot dependent X-K Valley Zeeman Splitting PL . . . . .  | 236 |
| D.18 Flipping of the K-shaped magnetic field dependent energy shift of X <sub>0</sub><br>when the sample is rotated 180 deg . . . . . | 239 |
| D.19 Magnetic Dependent Spot Shifts: Good Alignment vs. Bad Alignment . . . . .   | 240 |
| E.1 Details of American Magnetics ±12 Superconducting Magnet in BlueFors . . . . .  | 242 |
| E.2 RS-232 Cross-Over Connector for the Magnet Controller . . . . .   | 243 |
| E.3 Magnet controller Network Software . . . . .  | 245 |
| E.4 Magnet Quench Event Temperatures . . . . .  | 246 |
| E.5 Magnet controller and power supply before and after a quench event . . . . .  | 248 |
| F.1 Sirah Matisse Dyes . . . . .  | 250 |
| F.2 DCM Dye Mixing . . . . .  | 253 |
| F.3 Dye circulator and cooling lines . . . . .  | 254 |
| F.4 Dye circulator tubing . . . . .   | 255 |
| F.5 Dye Jet Splatter Shield . . . . .   | 256 |
| F.6 Circulator Pump Fins . . . . .  | 258 |
| F.7 Change the Dye in the circulator . . . . .  | 260 |
| F.8 Dye Jet clogged with dirt . . . . .   | 263 |
| F.9 Dye Laser Broken Sapphire Jet . . . . .   | 264 |
| F.10 Dye Laser Mirror Replacement . . . . .   | 267 |

|      |   |     |
|------|---|-----|
| F.11 | Dye Laser Schematic and Mirror Labeling . . . . .                       | 268 |
| F.12 | Dye Laser TM alignment . . . . .  | 270 |
| F.13 | Dye Laser Lasing . . . . .  | 273 |
| F.14 | Wavelength Selection via BRF and Etalons . . . . .                      | 275 |
| F.15 | Dye Laser Electronic Controller Box . . . . .                           | 277 |
| F.16 | Homing Dye Laser Motors . . . . .                                       | 278 |
| F.17 | Calibrating the BRF for Dye Laser . . . . .                             | 279 |
| F.18 | Dye Laser Output Optics . . . . .                                       | 282 |
| F.19 | PLE of hBN Showing Dye Laser Side Bands . . . . .                       | 285 |
| F.20 | Short-Pass Filter Block Dye Laser Side Bands . . . . .                  | 286 |
| F.21 | Dye Laser Power Fluctuation with Wavelength . . . . .                   | 289 |
| F.22 | Dye Laser Power Stabilization Hardware . . . . .                        | 291 |
|      |   |     |
| G.1  | Montana Cryostat Outline . . . . .                                      | 293 |
| G.2  | Assembly of the Montana Cryostat in preparation for cool down . . . . . | 294 |
| G.3  | Installation of Sample Carriage in the Montana Cryostat . . . . .       | 295 |
| G.4  | Montana Cryostat Pumps . . . . .  | 296 |
| G.5  | Montana Cryostat Optics . . . . .                                       | 297 |
| G.6  | Montana Cryostat Wiring . . . . .                                       | 300 |
| G.7  | M-Squared Laser System . . . . .  | 302 |
| G.8  | M-Squared Pump Alignment . . . . .                                      | 304 |
| G.9  | M-Squared Insides and Fiber Pick-Off . . . . .                          | 305 |
| G.10 | M-Squared Output Optics and Wavemeter . . . . .                         | 305 |
| G.11 | HeNe and 532 nm Diode Lasers . . . . .                                  | 307 |
| G.12 | 3D Printed SM1 Tube Holders . . . . .                                   | 308 |
| G.13 | First Encapsulation System with clamping mechanism . . . . .            | 309 |
| G.14 | CAD of Encapsulation System with clamping mechanism . . . . .           | 312 |
| G.15 | Newest Encapsulation System with Vacuum Mount . . . . .                 | 313 |

## Chapter 1: Introduction

The experimental realization of graphene devices opened a new branch of condensed matter physics that has been exploring other Van der Waals (vdW) materials such as Transition Metal Dichalcogenides (TMDs) that, unlike Graphene, exhibit a direct bandgap [1]. These true two-dimensional systems exhibit strong Coulomb interactions resulting in highly bound exciton states [2, 3]. Their single atomic layer structure also means TMDs are heavily influenced by their environments. While this can be useful in manipulating the electronic structure of these materials [1], environmental disorder from fabrication had previously resulted in very low quality samples and hindered the ability to study exotic exciton physics. Recent advancements in the fabrication of ultra-high quality encapsulated monolayer TMDs using hexagonal boron nitride (hBN) has allowed for devices with very low disorder to be made and for the experimental realization of new exciton related phenomenon. Furthermore, their spectra in the visible range enable the use of well-known techniques, such as photoluminescence (PL), to identify and monitor the formation and recombination of exciton bound states.

With the aim of increasing the understanding of these excitonic states, extensive optical studies have been conducted on the Rydberg series of the neutral excitons in TMDs with principal quantum numbers up to 11 having been observed [4–7]. Other

reports measure the non-zero angular momentum p-states using second harmonic optical excitation [2,8] . More recently, attention has been turned to probing for a Rydberg series of the more exotic charged exciton states. In the simplest description of a charged exciton, it is modeled similarly to a charged Hydrogen ion,  $H^-$ . Although this particular model has been shown to have only one bound state [9], in the past decade it was theoretically proposed that the charged exciton may have a Rydberg series of states, similarly to the neutral exciton [10]. Only recently has their existence been experimentally confirmed [11–14].

One of the major difficulties in optically resolving the PL signature of high principle quantum number  $n$  Rydberg exciton states is rapid non-radiative relaxation mechanisms for  $n > 1$  excitons that dominate over radiative recombination [15, 16]. This means that the PL signature from an excited exciton is expected to be very small and the only appreciable emission lines are from the  $n = 1$  exciton states. Although PL from  $n > 1$  Rydberg excitons can be measured in high-quality samples at low temperatures [5, 17], their emissions remain far dimmer than the  $n = 1$  excitons. Photoluminescence emission (PLE) allows us to reliably measure the spectral profile of excitons with  $n > 1$  by scanning a laser across their energy range and using the non-radiative relaxation mechanisms to our advantage by monitoring changes in the populations of the  $n = 1$  excitons. By measuring an increase in intensity of the  $n = 1$  excitons, we know the laser is in resonance with the energy of an  $n > 1$  exciton state.

These measurements of the magnetic field dependence of the  $2s$  exciton states in  $WSe_2$  with PLE outline the experimental expertise we have been developing in our lab since its inception. All measurements were conducted in a customized BlueFors dilution

refrigerator with a side optical axis, bottom loading probe, and a  $\pm 12$  T superconducting magnet. The complexities involved in the design of this measurement system from the design of each component on our custom probe to the procedures necessary to properly run the system are outlined in the appendices. In addition to the BlueFors, a dye laser was necessary to conduct the PLE measurements. The energy range required in our PLE measurements is quite difficult to access with solid-state CW lasers and the only solution was to rebuild a dye laser. The details involved in operating the dye laser are also outlined in the appendices for future PLE measurements of exotic Rydberg exciton states.

The intention of this dissertation is to outline the experimental measurements of the  $X_-^{2s}$  using PLE for the first time. We are able to extract the spectral dependence of the  $X_-^{2s}$  and the  $X_0^{2s}$  under changes in carrier density and perpendicular magnet field. We are able to present, the first to our knowledge, the valley Zeeman splitting and extracted g-factor of the  $2s$  negatively charged exciton in TMDs.

**Disclaimer:** Much of the discussion and data presented in this dissertation is from co-first authored work published in Ref. [18].

## Chapter 2: Introduction to 2D Materials

### 2.1 Overview

To give a brief introduction to the intriguing field of 2D materials and their many interesting properties, I will begin with graphene. The commonly used substance known as graphite is composed of many atomically thin sheets of carbon atoms arranged in a hexagonal lattice held together via van der Waals (vdW) forces [19]. These single atomic thick sheets, called graphene, were generally thought to be unstable in monolayer form and would never be experimentally realized. The discovery that graphene could be mechanically exfoliated from a graphite crystal using only sticky tape had deep ramifications in physics and led to the now flourishing research of many other materials that can also be mechanically exfoliated into monolayer form [21]. The technique of isolating monolayer graphene opened the field of 2D device physics and was awarded the Nobel Prize in 2010.

Unlike pseudo two-dimensional systems, such as GaAs quantum wells, 2D materials exhibit a true two-dimensional nature. Reaching this limit leads to intriguing physical properties such as graphene's linear carrier dispersion due to its carriers' massless nature [21, 22]. Although graphene is an interesting material for studying all kinds of physical phenomena as well as being an excellent conductor with extremely high



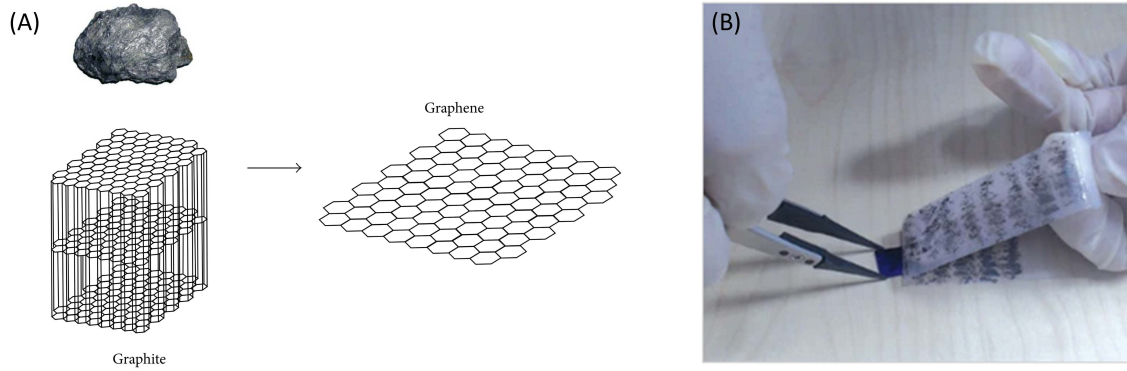


Figure 2.1: (A) A graphite crystal is composed of many single atomic sheets of carbon held together with van der Waals forces. In monolayer form, a single sheet is called graphene [19]. (B) The sticky tape technique to mechanically exfoliate graphene involves the procedure of pulling apart a flake of graphite with sticky tape on either side until the van der Waals forces are broken and a single layer of graphene remains on the tape. The monolayers are removed by placing the tape on a substrate ( $\text{SiO}_2$ , sapphire, glass, etc.) and peeling back the tape [20].

carrier mobilities, it does not have an intrinsic band gap. This makes it a poor choice for building transistors or studying optical excitations. As the 2D material community grew so did the discovery of other materials with similar dispersion relations to graphene, but also with intrinsic band gaps [1]. Some of these materials are listed in Fig. 2.2(A).

## 2.2 Other 2D Materials

One material in particular, hexagonal boron nitride (hBN), is probably even more important than the discovery of graphene. hBN retains graphene's honeycomb lattice (with very similar lattice constants), except that the carbon atoms are replaced with boron and nitrogen. This gives hBN a very large band gap ( $\sim 6$  eV) making it very insulating and transparent to low energy light fields, including the visible spectrum [23]. There

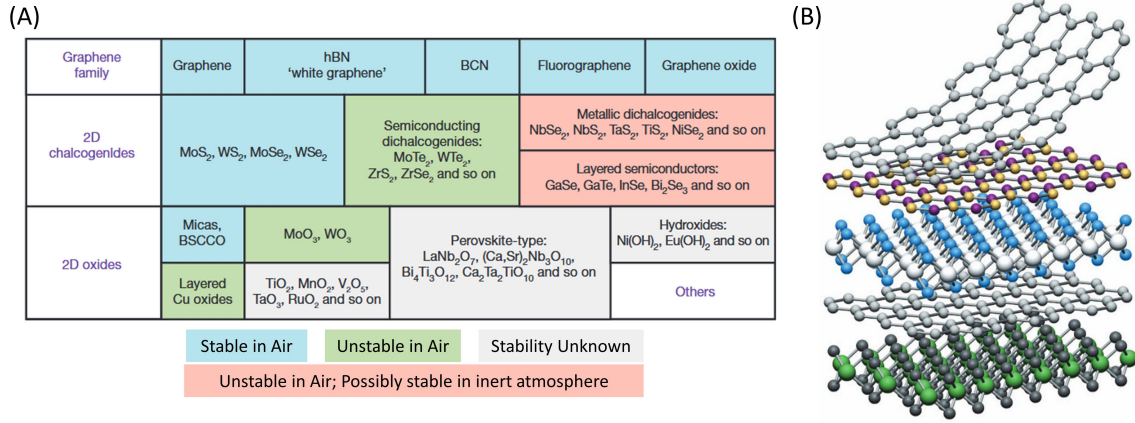


Figure 2.2: Figures from Ref. [1]. (A) Table of some of the different 2D materials that have been discovered and their many different properties. (B) Ref. [1] proposed the ability to stack any combination of these materials and making unique devices.

are entire laboratories dedicated to optimizing its growth for the 2D material community because device fabrication very often relies on the encapsulation of the 2D material of interest between flakes of hBN. Nearly every device follows this prescription because many of these materials will quickly degrade when exposed to air [1]. hBN encapsulation protects them from such exposure and greatly reduces their degradation [24]. In addition to protecting the sample, hBN's insulating properties make it an excellent dielectric for gating or isolating electronic leads. In our device, hBN is used for both of these properties.

The group of 2D materials we focus on in our measurements are the transition metal dichalcogenides (TMDs). These materials differ from graphene and hBN because they are three atoms thick, but exhibit a very similar honeycomb lattice when viewed from the top or bottom [25], Fig. 2.3. The resulting band structure for TMDs is that of a massive Dirac material with a direct band gap in the visible light regime at the  $\pm K$  points [26]. This

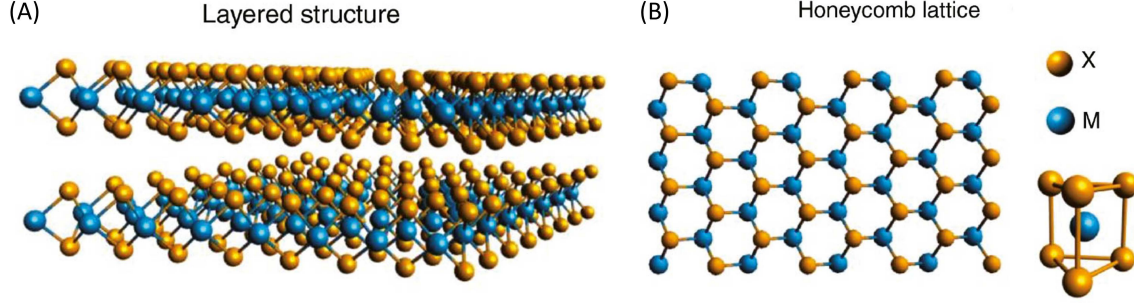


Figure 2.3: Figure from Ref. [25] of the lattice structure of Transition Metal Dichalcogenides (TMDs). (A) Side profile of a monolayer of a TMD. Unlike graphene or hBN, TMDs have a three layer molecular structure with a chalcogen,  $X$ , on the top and bottom of the sheet and a transition metal,  $M$ , atom in the middle. In the case of  $\text{WSe}_2$ , the transition metal is tungsten,  $\text{W}$ , and the chalcogen is selenium,  $\text{Se}$ . (B) The profile of the three-layer 2D material still forms a honeycomb lattice. In monolayer form, the unit cell of a TMD lacks inversion symmetry which leads to a strong spin splitting of the bands. [28, 38].

makes them easy to optically probe using commercially available optics and detectors.

TMDs also exhibit strong spin-orbit coupling [27–30], circular dichroism [27, 30, 31], and very strong exciton binding energies [32–34]. Strong spin-orbit coupling breaks the spin-degeneracy of both the conduction and valence bands while circular dichroism allows for the addressing of individual valleys through the polarization of the light field [30, 35]. The strong binding energies of the exciton states ( $>100\text{meV}$  for the  $1s$  exciton species) allows for these materials to remain optically active at room temperature [36, 37]. All of these properties make TMDs excellent candidates for probing exciton bound states and their associated Rydberg series.

## 2.3 2D Material Possibilities

Many of the 2D materials have very different and interesting properties, but all of them can be processed using similar mechanical exfoliation and staking techniques. This allows for the possibility of easily constructing devices out of almost any combination of these materials and experimentally realizing the results [1], as shown in Fig. 2.2(B). The method of stacking has been heavily developed and substantial advancements have allowed for the realizations of high quality devices made from these materials.

One specific development is the squeegee method that was developed by our collaborators at NRL [39]. This allows for TMDs encapsulated in hBN to be "squeegeed" of any residue that may remain between the hBN and the TMD flake during the staking process by dragging an AFM tip across the surface. The procedure has other uses such as the ability to selectively generate single-quantum emitters [40].

The field of 2D materials is a new and exciting field filled with many possibilities.

## Chapter 3: Physical Properties of Transition Metal Dichalgeniodes

### 3.1 Overview

TMDs are a very interesting group of 2D materials because of their many optical properties such as the opening of a direct band gap in monolayer form, circular dichroism, and strong spin-orbit coupling. In this chapter, we will explore these properties and their ramifications for our optical measurements.

### 3.2 In-direct vs Direct Bandgap

As the thickness of TMDs are reduced from bulk to the monolayer limit, the material transitions from an indirect to a direct band. This is depicted in Fig. 3.1(A), in which the band structure for different thicknesses of MoS<sub>2</sub> is calculated using DFT [26]. The results are consistent with the other TMDs including WSe<sub>2</sub> [41]. Thus, only when a TMD is in it's monolayer limit does it exhibit a direct band gap at the high symmetry  $\pm K$  points.

The absorption of a photon cannot change the crystal momentum or spin of a carrier. It can only provide additional energy. As a result, for a carrier in an indirect band gap material to transition from the valence to the conduction band (or vice versa), it would

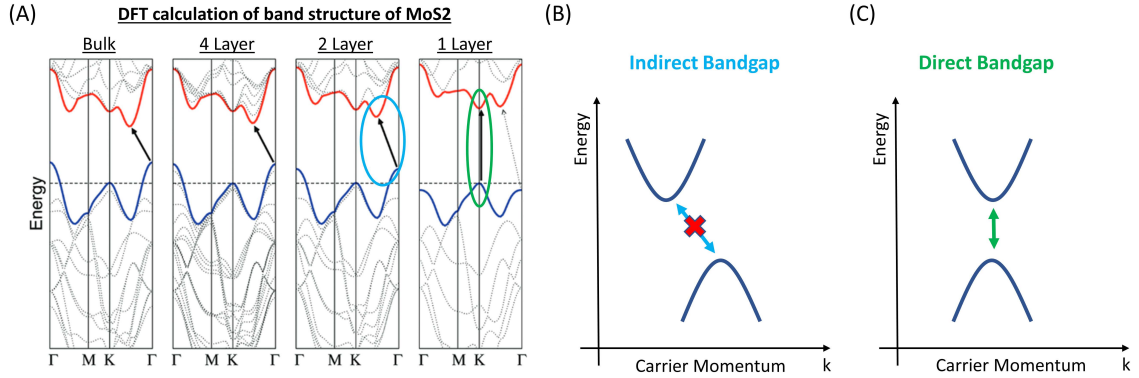


Figure 3.1: (A) DFT calculation by Ref. [26] of the band structure of MoS<sub>2</sub> from bulk to the monolayer limit. In monolayer form, the band gap changes from indirect to direct at the high symmetry  $\pm K$  points of the honeycomb lattice. The same transformation occurs in all TMDs including WSe<sub>2</sub>. (B) In the bulk case when there is an indirect band gap, carriers are required to change their crystal momentum to transition between the conduction and valence bands. Since the emission/absorption of a photon is unable to change the momentum of the carriers in the crystal, such transitions would require coupling to a phonon mode. This is a higher order effect. Therefore, indirect band gaps are considered optically dark. (C) In the monolayer limit when there is a direct band gap at the  $\pm K$  points, the carriers no longer need to change their crystal momentum to transition across bands and can do so through the emission/absorption of a photon. This is considered optically bright.

need to absorb or emit a photon to change its energy as well as couple to a phonon mode that would change its crystal momentum. Such a transition is considered optically dark to first order, Fig. 3.1(B). Therefore, the significance of an indirect band gap is that photon emission and absorption by carriers in the crystal is forbidden by conservation of crystal momentum [42].

For a material with a direct band gap, carriers can transition between the valence and conduction bands without changing their crystal momentum which can be done exclusively through the emission or absorption of a photon. Such transitions are considered optically bright, Fig. 3.1(B).

In monolayer form, TMDs have a direct band gap and are optically bright. Also, since the band gap is direct, we can approximate the carrier transitions to only small values of  $k$  around the  $\pm K$  points. In the next section, we will derive the light-matter selection rules using this approximation to show circular dichroism.

### 3.3 Circular Dichroism in TMDs

If we zoom in on the bottom of the conduction band and top of the valence band of a monolayer TMD's band structure, Fig. 3.2, we can make an approximation for only small  $k$  transitions because of the direct band (i.e. carriers do not need to change their crystal momentum to transition between the valence and conduction bands). This section examines the light-matter interaction of TMDs and finds they exhibit a phenomenon known as circular dichroism that allows optical transitions of carriers in the  $\pm K$  valleys to be individually addressed through the polarization of the light field used to excite

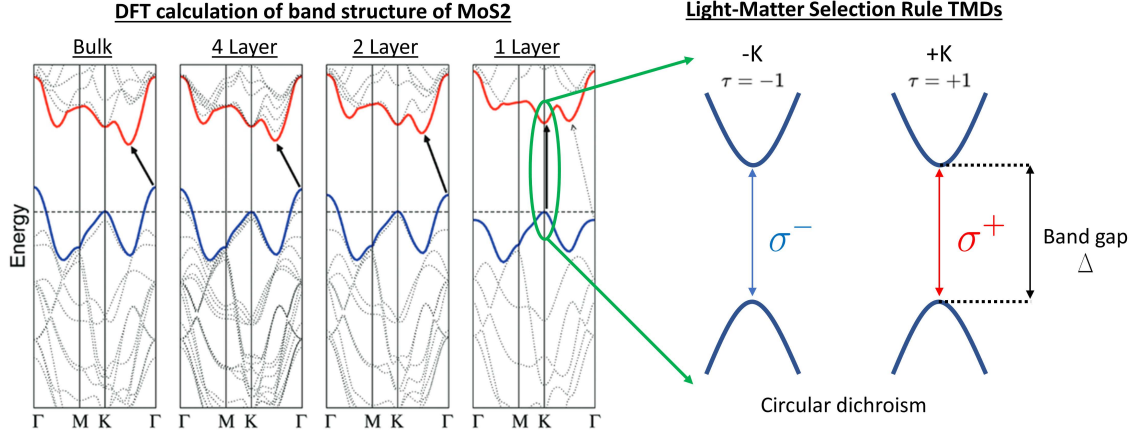


Figure 3.2: Schematic of circular dichroism in monolayer TMDs. Band structure calculated via DFT by Ref. [26]. Approximating for small  $k$  optical transitions at the  $\pm K$  points, we are able to derive selection rules showing a coupling of only  $\sigma^\pm$  polarized light for transitions in the  $\pm K$  valley. This is known as circular dichroism and allows for the addressing of carriers in only one valley through the polarization of the light-field.

them [30, 31, 43].

TMDs can be modeled as a massive Dirac system for carriers with small  $k$  around the  $\pm K$  points. We begin with the general Dirac Hamiltonian with the inclusion of a band gap [43]

$$\vec{H}_0 = v_F(\tau k_x \sigma_x + k_y \sigma_y + \Delta \sigma_z),$$

where  $v_F$  is the Fermi velocity,  $\tau \in \{1, -1\}$  is the valley parameter corresponding to  $\pm K$  valleys,  $\vec{k} = (k_x, k_y)$  is the wave number of the carriers with respect to the  $\pm K$ -points,  $\sigma_i$  are the Pauli matrices, and  $2\Delta$  is the energy of the band gap [31]. This approximation provides the description of the band structure near the  $\pm K$ -points for small  $k$ -values, i.e.  $k \sim \frac{1}{a_B} < 1$  ( $a_B$  is the Bohr radius of the exciton). Although DFT calculations are necessary for a more complete picture of the band structure, this approach highlights



important details of the light-matter interaction for s-type excitons which are the focus of this dissertation.

To describe the interaction of TMDs around the  $\pm K$ -points with a light field, the vector potential must be incorporated into the interaction Hamiltonian [43]. This substitutes  $\vec{k} \rightarrow \vec{k} + e\vec{A}$ , where  $\vec{A}$  is the vector potential of the light and  $e$  is the charge of the carrier, giving

$$\vec{H} = v_F(\tau k_x \sigma_x + k_y \sigma_y + e\tau A_x \sigma_x + eA_y \sigma_y + \Delta \sigma_z) \quad (3.1)$$

$$\equiv \vec{H}_0 + \vec{H}_{int}, \quad (3.2)$$

where

$$\vec{H}_0 \equiv v_F(\tau k_x \sigma_x + k_y \sigma_y + \Delta \sigma_z) \quad (3.3)$$

$$\vec{H}_{int} \equiv ev_F(\tau A_x \sigma_x + A_y \sigma_y). \quad (3.4)$$

$\vec{H}_{int}$  is the interaction Hamiltonian that describes the light-matter interaction of TMDs. (For simplicity, we will define  $e, v_F \equiv 1$  as these constants do not play a role in the derivation of the selection rules.)

The general selection rules for a chiral Dirac systems can be derived from the interaction Hamiltonian. By substituting the Pauli matrices into  $\vec{H}_{int}$ ,

$$\vec{H}_{int} = \begin{pmatrix} 0 & \tau A_x - iA_y \\ \tau A_x + iA_y & 0 \end{pmatrix}. \quad (3.5)$$

We have the following basis transformation relationship from the circular polarization basis to linear,  $|\sigma^\pm\rangle = |x\rangle \pm i |y\rangle$ . Therefore,

$$\vec{A} = A_0^{(+)} |\sigma^+\rangle + A_0^{(-)} |\sigma^-\rangle \quad (3.6)$$

$$= A_0^{(+)} (|x\rangle + i |y\rangle) + A_0^{(-)} (|x\rangle - i |y\rangle) \quad (3.7)$$

$$= (A_0^{(+)} + A_0^{(-)}) |x\rangle + i(A_0^{(+)} - A_0^{(-)}) |y\rangle \quad (3.8)$$

$$= A_x |x\rangle + A_y |y\rangle, \quad (3.9)$$

where  $A_0^{(\pm)}$  are the amplitude of the  $\sigma^\pm$  circular polarization components of the incoming photon. Making this substitution gives

$$\vec{H}_{int} = \begin{pmatrix} 0 & (\tau + 1)A_0^{(+)} + (\tau - 1)A_0^{(-)} \\ (\tau - 1)A_0^{(+)} + (\tau + 1)A_0^{(-)} & 0 \end{pmatrix}. \quad (3.10)$$

Since  $\tau \in \{1, -1\}$  corresponds to each valley, we obtain the following two results for  $\vec{H}_{int}$  that describe the light-matter interaction in the  $\pm K$  valleys:

| Valley Index ( $\tau$ )  | $\vec{H}_{int}$  |
|--------------------------|--|
| $\tau = 1; \mathbf{K}$   | $\begin{pmatrix} 0 & 2A_0^{(+)} \\ 2A_0^{(-)} & 0 \end{pmatrix}$   |
| $\tau = -1; -\mathbf{K}$ | $\begin{pmatrix} 0 & -2A_0^{(-)} \\ -2A_0^{(+)} & 0 \end{pmatrix}$ |

The following wave functions describe the carriers in the valence and conduction band that the light will interact with:

$$|c\rangle = \begin{pmatrix} \phi_{\tilde{m}}^c \\ \phi_{\tilde{m}-1}^c \end{pmatrix} \quad and \quad |v\rangle = \begin{pmatrix} \phi_{m+1}^v \\ \phi_m^v \end{pmatrix}, \quad (3.11)$$

where  $\tilde{m}$  and  $m$  are the quantum numbers of angular momentum in the conduction and valence bands, respectively. Therefore, the probability of an electron absorbing a photon and being excited from the valence band to the conduction band is given by

$$\langle c | H_{int} | v \rangle = \begin{pmatrix} \phi_{\tilde{m}}^c & \phi_{\tilde{m}-1}^c \end{pmatrix} \begin{pmatrix} 0 & \tau 2A_0^{(\tau)} \\ \tau 2A_0^{(-\tau)} & 0 \end{pmatrix} \begin{pmatrix} \phi_{m+1}^v \\ \phi_m^v \end{pmatrix}. \quad (3.12)$$

The selection rules only depend on the angular part of these integrals which allows us to

extract two allowed optical transitions given by

$$\int \phi_{\tilde{m}}^* A_0^{(\tau)} \phi_m d^2r \rightarrow \int e^{-i\tilde{m}\phi} e^{im\phi} d\phi = \delta_{\tilde{m},m} \quad (3.13)$$

$$\int \phi_{\tilde{m}-1}^* A_0^{(-\tau)} \phi_{m+1} d^2r \rightarrow \int e^{-i(\tilde{m}-1)\phi} e^{i(m+1)\phi} d\phi = \delta_{\tilde{m}-1,m+1}. \quad (3.14)$$

These relationships say that there are two possible optical transitions of an electron from the valence band to the conduction band. The first is when  $\tilde{m} - m = 0$ . Such a transition will form an s-type exciton. The second is when  $\tilde{m} - 1 = m + 1 \Leftrightarrow \tilde{m} - m = 2$ . This corresponds to the formation of a d-type exciton. [31] In our approximation, we assumed that the carriers have small k-values around the  $\pm K$ -points; i.e. the momentum of the carriers relative to the  $\pm K$ -points is very close to zero for this description to hold. Therefore, in the  $k \cdot p$  approximation to first order,  $\phi_{m+1}^v \ll \phi_m^v$ , i.e.

$$|v\rangle = \begin{pmatrix} \phi_{m+1}^v \\ \phi_m^v \end{pmatrix} \sim \begin{pmatrix} k e^{i\phi_k} \\ 1 - k^2 \end{pmatrix}. \quad (3.15)$$

For very small values of k, the  $\phi_m^v$  component is the primary active transition and we are primarily only generating s-type excitons because of the direct band gap of the material allowing us to make the following approximation

$$\begin{pmatrix} \phi_m^c & 0 \end{pmatrix} \begin{pmatrix} 0 & \tau 2A_0^{(\tau)} \\ \tau 2A_0^{(-\tau)} & 0 \end{pmatrix} \begin{pmatrix} 0 \\ \phi_m^v \end{pmatrix}. \quad (3.16)$$

This shows that  $\tau$  determines which polarization couples  $\phi_m^v$  to  $\phi_m^c$ . Hence, the

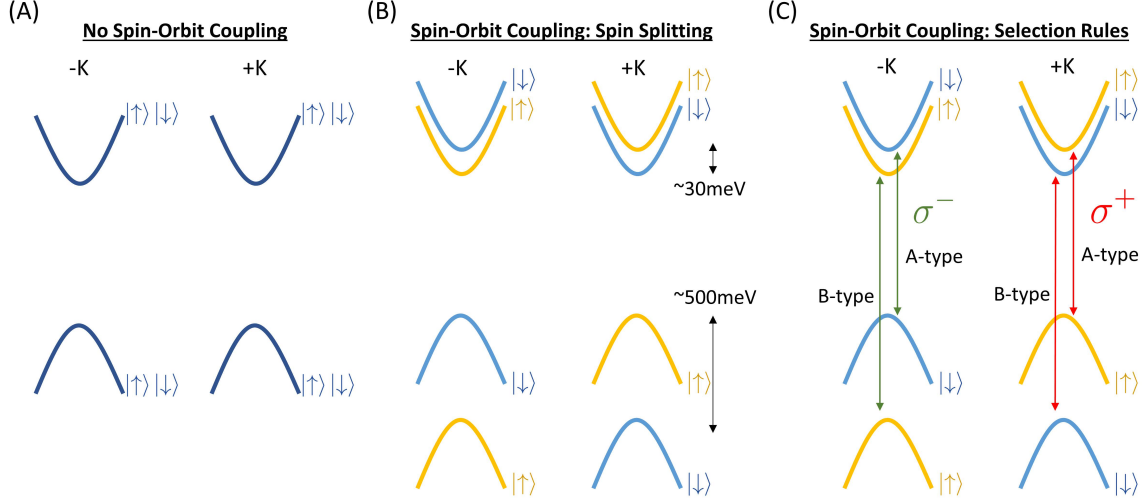


Figure 3.3: (A) In the case when there is no spin-orbit coupling, the spin of the carriers in the valence and conduction bands are degenerate in energy. (B) Due to the strong spin-orbit coupling in WSe<sub>2</sub>, the spin degeneracy is broken. The conduction band exhibits a spin splitting of  $\sim 30 \text{ meV}$  while the valence band is  $\sim 500 \text{ meV}$ . The spin splitting is equal in magnitude, but opposite in spin for  $\pm K$  valleys. (C) Including the optical selection rules, there are two types of allowed s-type optical transitions. Since a photon cannot flip a carrier's spin, the lowest energy transition in WSe<sub>2</sub> is between the upper valence band and upper conduction band. This is called an A-type transition. The higher energy B-type transition is between the lower valence band and the lower conduction.

circular polarization basis couples directly to the valleys of the TMD:  $\tau = +1 \leftrightarrow |\sigma^+\rangle$  and  $\tau = -1 \leftrightarrow |\sigma^-\rangle$ . Refer to Fig. 3.2 for a schematic of the polarization selection rules.

### 3.4 Spin-Orbit Coupling

In addition to exhibiting circular dichroism, TMDs also experience significant spin-orbit coupling (SOC) resulting in a breaking of spin degeneracy for both the conduction and valence bands. This is a result of the transition metal in the molecular structure and the role its d-orbitals play in the formation of the bands [44].

The importance of SOC in these materials is illustrated in Fig. 3.3. In a material with no SOC, Fig. 3.3(A), the spin of the carriers is degenerate in energy. Therefore, we are unable to distinguish the spin of the carriers involved in the optical transitions. When strong SOC is incorporated into the band structure, there is a significant energy splitting of the spin states in the valence and conduction bands. In WSe<sub>2</sub>, the conduction band experiences a SOC splitting of  $\sim 30$  meV, while the valence band's spin splitting is an order of magnitude greater at about  $\sim 500$  meV [27]. Also, the spin splitting is equal in magnitude, but opposite in spin between the  $\pm K$ -valleys, Fig. 3.3(B).

Interestingly enough, TMDs formed out of the transition metal molybdenum, Mo, have opposite spin splitting of the conduction band than those formed out of tungsten, W. Therefore, in MoS<sub>2</sub> and MoSe<sub>2</sub>, the lower conduction band and the upper valence band have the same spin. Since we exclusively focus on WSe<sub>2</sub> in our measurements, the spin splitting schematic presented in Fig. 3.3(B) is for the SOC of tungsten based TMDs.

In this model that includes SOC, we can have two possible optical transitions, Fig. 3.3(C). The reason there are only two possible transitions is the result of the absorption/emission of a photon being unable to change the spin of a carrier. Therefore, carriers can only transition to and from bands with the same spin. This limits possible transitions to two types labeled A-type and B-type.

A-type transitions are between the upper valence bands and upper conduction bands while B-type transitions are also possible between the lower valence bands and the lower conduction bands. Due to the significant splitting of the valence band, B-type transitions are much higher in energy than A-type transitions. In our measurements, we limit ourselves to A-type optical transitions.

By incorporating the selection rules derived in the previous section, Fig.3.3(C), we note that we can selectively address both the spin state of the carriers and their momentum through the polarization of the applied light field. This will be of importance in our measurements of the valley Zeeman splitting and our extraction of a corresponding  $g$ -factor for the excitons in  $\text{WSe}_2$ .

## Chapter 4: WSe<sub>2</sub> Device Details

### 4.1 WSe<sub>2</sub> Stacking Procedure

Our sample was assembled by our collaborators at the Naval Research Laboratory (NRL) and their techniques are detailed in Ref. [39]. Encapsulation was performed via the wet capillary action method and interlayer contamination was removed via the nano-squeegee method, both outlined in Ref. [39].

A cross-sectional schematic of the field effect device (FED) used in all measurements presented in this dissertation is depicted in Fig. 4.1(A). The device is a CVD grown flake of WSe<sub>2</sub> encapsulated between two mechanically exfoliated hBN flakes. Two few-layer graphite sheets were placed on either side of the WSe<sub>2</sub> flake as electrical contacts. Graphene's similar crystal structure to TMDs makes it an ideal material for making electrical contact to WSe<sub>2</sub>, especially in the n-doped regime [45]. Electrical contacts with metallic electrodes on monolayer WSe<sub>2</sub> have been studied and shown to not be as reliable [46].

The WSe<sub>2</sub> device is then placed upon a few-layer graphite gate. In this configuration, the sample forms a FED with the bottom hBN acting as the dielectric insulator ( $\sim 15$  nm thick). The step-by-step assembly of this device is shown in Fig. 4.2(A-E). After the stack had been assembled, a region labeled on Fig. 4.2(F) had been nano-



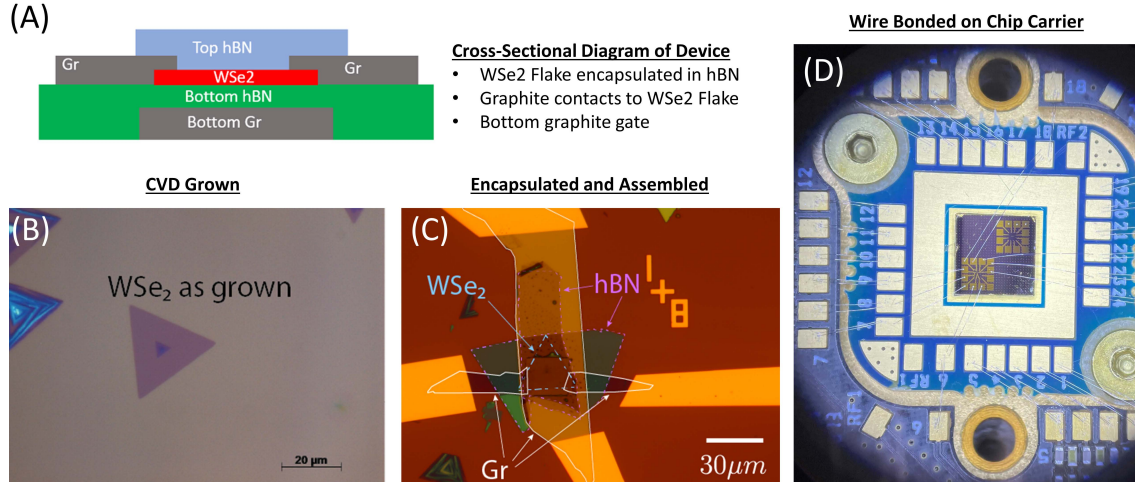


Figure 4.1: (A) Cross-sectional schematic of the WSe<sub>2</sub> FED used in all of the measurements of this thesis. This illustration was provided by H.-J. Chuang who assembled the device. (B) The CVD grown WSe<sub>2</sub> flake prior to encapsulation on the surface of SiO<sub>2</sub> substrate. A nucleation point is observed in the center of the flake corresponding to the growth of multi-layer WSe<sub>2</sub>. Due to the nature of optical measurements being able to locally probe a  $\sim 1$   $\mu\text{m}$  spot on the sample, we can conduct all of our measurements away from the nucleation point and only in the monolayer region. (C) The sample after the device had been assembled in the configuration outlined in (A). Each layer of material is labeled. (D) The sample after Cr/Au electrodes have been fabricated to each of the few-layer graphite contacts. The Cr/Au electrodes are then wire bonded to our chip carrier and carriage measurement system.

squeegeed of residue polymer left behind during the stacking process. Nano-squeegeeing utilizes an AFM to drag any polymer residue remaining between the layers to the sides of the sample. The nano-squeegeed region becomes very flat while the other regions on the sample remain spotted and rough. The nano-squeegeed region is clearly visible as a rectangular region in the center of the device. Fig. 4.2(G) is an AFM image of the nano-squeegeed region. Fig. 4.2(H) is a measurement of PL intensity from the sample while being illuminated via 532 nm light. The nano-squeegeed region appears very uniform in PL intensity while the top of the WSe<sub>2</sub> flake that had not been nano-squeegeed is very bright and varied in intensity. This is due to the non-uniform disorder profile in this region from residue left behind during the assembly of the device. The PL response from the few-layer graphite contacts is very dark which is a good indication that the WSe<sub>2</sub> flake and the few-layer graphite are in physical and electrical contact.

Our device allows for the grounding of the WSe<sub>2</sub> flake while a voltage is applied to the graphite bottom gate. An applied electric field to the device will shift the conduction and valence bands of the sample, effectively changing the Fermi level and the concentrations of the charge carriers in the sample to either be depleted (p-doped) or injected (n-doped) [47]. This allows for the study of more exotic quasiparticle states that only form outside of charge neutrality.

To pattern metallic contacts to the few-layer graphite, the sample was spun with a mask of PMMA and a mask was patterned using an Elionix 100 keV eBeam lithography system. After developing the PMMA mask, 3 nm chromium (Cr) /50 nm gold (Au) was deposited via thermal evaporation. The remaining PMMA mask was lifted-off in a room temperature bath of acetone for 1 hour. The final device is shown in Fig. 4.1(C,D) with

metallic contacts connecting the few-layer graphite leads and gate to the pre-patterned Au bond pad.

The device was then placed in our custom chip carrier/carriage system for wire bonding, Fig. 4.1(D). The gold bond pads are visible on the surface of the sample in the middle of the chip carrier. The sample was wire bonded and then placed in our BlueFors dilution refrigerator for measurements.

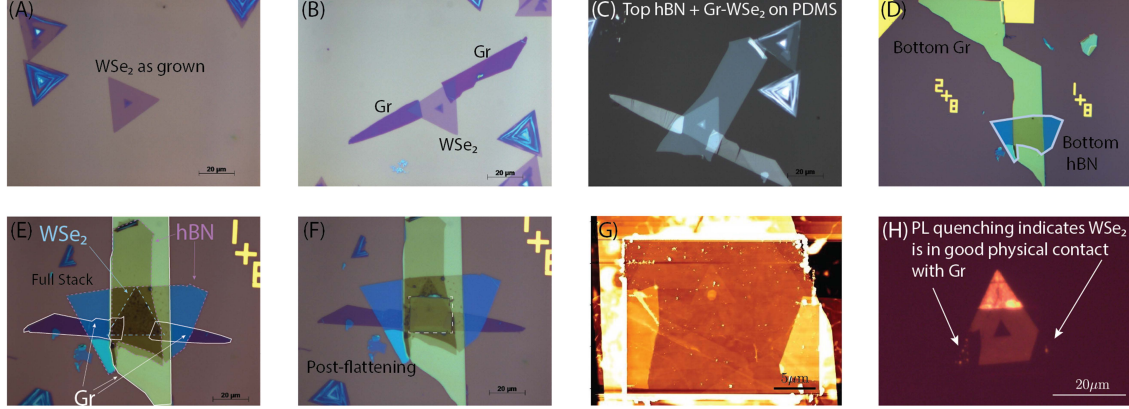


Figure 4.2: The device was fabricated by our collaborators at NRL using techniques laid-out in Ref. [18, 39]. These images were provided by H.-J. Chuang who assembled the device and they outline the step-by-step procedure involved in making the device. (A) The CVD grown  $\text{WSe}_2$  flake prior to encapsulation on the surface of a  $\text{SiO}_2$  substrate. A nucleation point is observed in the center of the flake corresponding to the growth of multi-layer  $\text{WSe}_2$ . (B) The few-layer graphite contacts are placed on either side of the  $\text{WSe}_2$  flake. (C) The contacts and flake are then picked-up using a few-layer hBN flake ( $\sim 12$  nm thick) shown here with the stack attached to the PDMS stamp used in the assembly procedure. (D) A few-layer hBN flake ( $\sim 15$  nm thick) is placed on top of a few-layer graphite bottom gate. (E) The hBN/ $\text{WSe}_2$  and few-layer graphite contacts are placed on the hBN/few-layer graphite bottom gate, and completes the assembly of the device. (F) Using a technique developed in Ref. [39], a region in the center of the device is squeegeed with an AFM tip to remove residue between the layers of hBN and  $\text{WSe}_2$  flakes. This region is clearly visible as a rectangular indentation in the middle of the device. (G) AFM image of the device post-squeegee. (H) PL response from the sample indicates the photoresponse of the sample at 300k. The bright top region of the device is due to the large amount of disorder from residue pressing against the  $\text{WSe}_2$  flake since this region was not nano-squeegeed.

## Chapter 5: Photoluminescence Measurements

### 5.1 Introduction

When a semiconductor with a direct band gap is illuminated with photons of sufficient energy, an electron can absorb one of these photons and excite out of the valence band into the conduction band, leaving a hole behind [42]. In analogy to hydrogen, the electron and hole pair can form a bound state known as an exciton. Excitons are one of the most fundamental quasiparticles that can form in a solid-state system. In this chapter, I will explain their formation through a technique known as photoluminescence.

### 5.2 Exciton formation through Photoluminescence (PL)

The equilibrium electronic configuration of a semiconductor material with a finite band gap is to have a filled valence band and an empty conduction band. In a material with a direct band gap, such as monolayer TMDs, electrons can be optically excited out of the valence band and into the conduction band. These now free electrons and holes can form bound quasiparticle states that eventually recombine and emit photons with energies equivalent to their bound state energies [42]. Detecting the energies of these photons is a signature that the bound states existed. This type of optical measurement is known

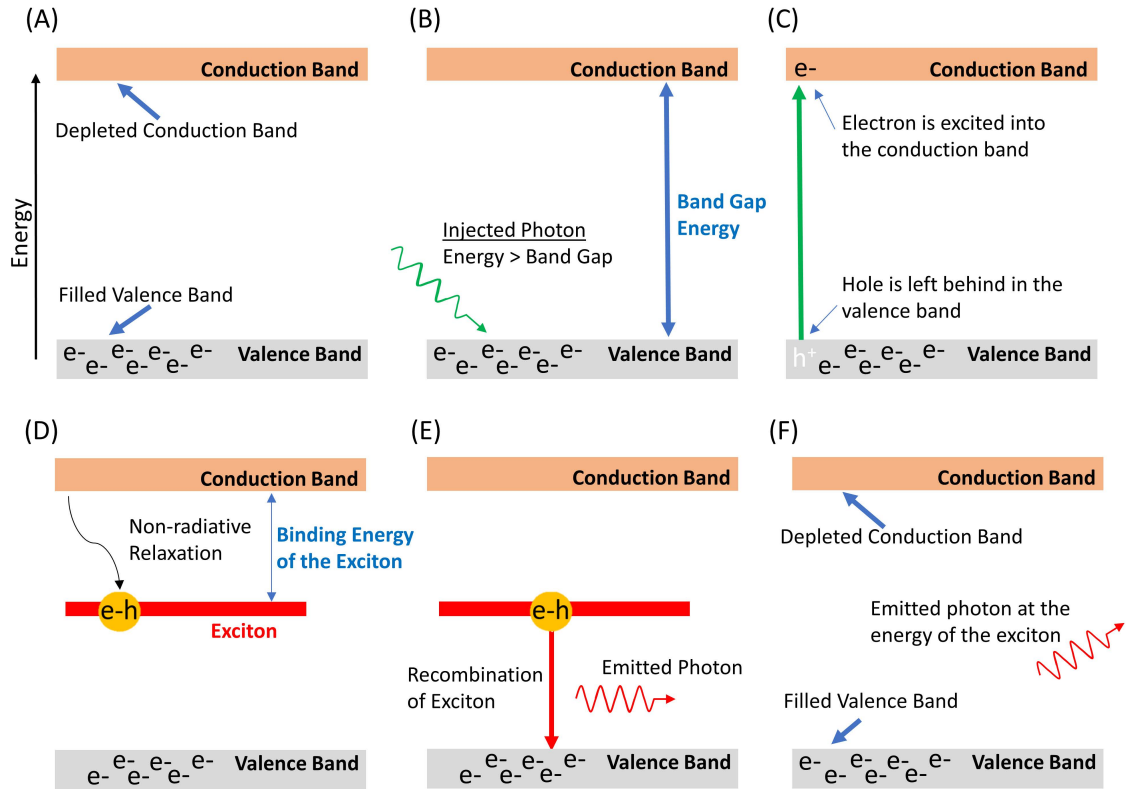


Figure 5.1: Schematic of the excitation of an electron and hole via photoluminescence and the formation to recombination of an exciton bound state. (A) In the charge neutral regime, a semiconductor has a full valence band and a depleted conduction band. (B,C) When a photon of energy larger than the band gap is absorbed by an electron in the valence band, it is excited into the conduction band and leaves behind a hole in the valence band. (D) The electron's attraction to the hole along with repulsion from other electrons in the material instigates the non-radiative relaxation of the two free particles into a bound exciton. The difference in energy between the conduction band and the bound exciton is defined as its binding energy. (E) The exciton bound state has a finite lifetime, as it is still an excitation of the system, and the electron and hole will eventually recombination. This is done radiatively through the emission of a photon at the energy of the exciton. (F) The system returns to its ground state equilibrium with the exception of the emitted photon with an energy equal to the energy of the bound exciton state.

as photoluminescence (PL) and is one of the most fundamental optical measurements conducted on semiconductor systems.

One such quasiparticle state is when a free electron in the conduction band and hole in the valence band form a bound state known as a neutral exciton,  $X_0$  [42]. The generation of a neutral exciton is depicted in Fig. 5.1. In  $\text{WSe}_2$ , this is the primary quasiparticle state formed in the charge neutrality regime (full valence band; deplete conduction band).  $\text{WSe}_2$ 's direct band gap at the  $\pm K$  points means an electron in the valence band can be excited into the conduction band if it absorbs a photon of energy equal to or greater than the band gap. This also results in the formation of a vacancy in the valence band with opposite spin and charge of the electron known as a hole. Such an excitation pushes the system out of equilibrium with a free electron in the conduction band and a free hole in the valence band, Fig. 5.1(C). In analogy to how a free electron and proton can lower their energy by forming a bound hydrogen atom, the free electron and hole may reduce their energy by forming a bound exciton state, Fig. 5.1(D). The exciton's energy is defined by its binding energy with respect to the conduction band.

The exciton bound state is still an excitation of the material and will eventually lower its energy further through the recombination of the electron and hole resulting in the emission of a photon, Fig. 5.1(E). The exciton's binding energy means the emitted photon's energy will be less than the energy of the band gap between the conduction and valence band, Fig. 5.1(F). Detecting the emission of photons at energies lower than the band gap of the material is an indication that these bound states formed. This is how we measure the existence of the exciton states through PL. Also, since this emitted photon's energy is always lower than the energy of the excitation laser in a PL measurement, it's

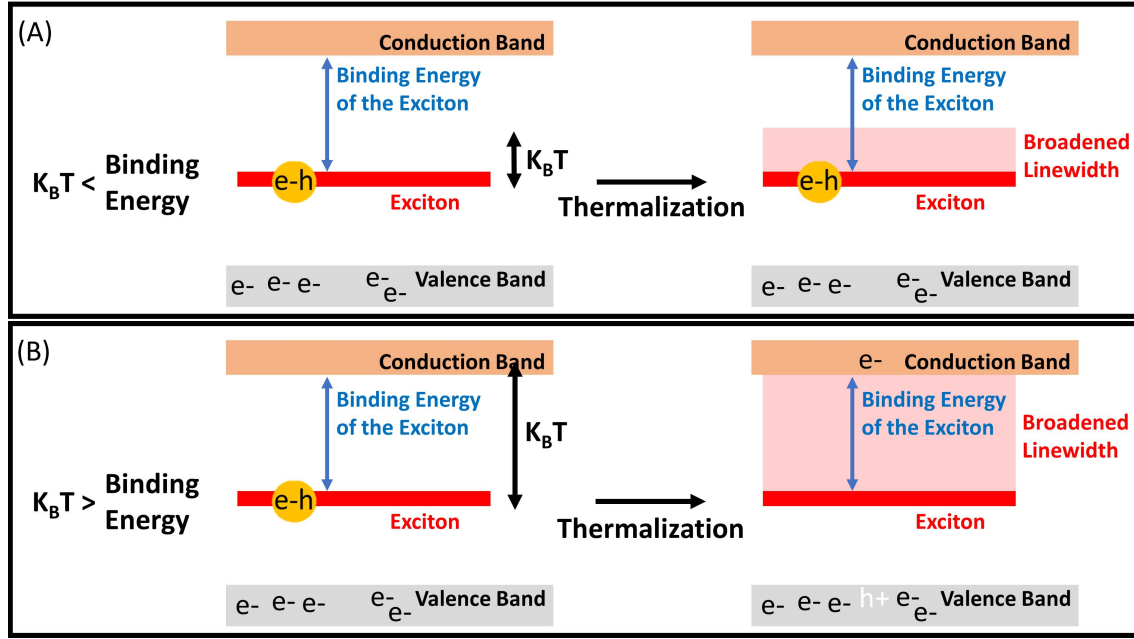


Figure 5.2: (A) If the temperature of the sample is low enough such that  $K_B T$  is less than the binding energy of an exciton, bound state excitons can form and remain bound until they radiatively recombine. Thermalization effects will broaden the linewidth of the exciton because of the possibility of excitons recombining with the added thermal energy [42]. (B) When  $K_B T$  is larger than the binding energy, electrons and holes that form bound exciton states will be quickly thermally excited back into free particles. This is illustrated as the exciton's linewidth broadening into the conduction band. If there is no energy gap between the bound state and the conduction band, we cannot spectrally resolve the recombination of individual exciton states [48].

emission can be easily isolated from the reflected laser light through the use of an optical low-pass filter.

The value of an exciton's binding energy is a very important characteristic for not only identifying the exciton species, but also for knowing what temperature is required for its formation [42]. If  $k_B T$  is greater than the binding energy of the bound state, the exciton will no longer be able to form because the bound electron and hole will be thermally excited back into free particles, Fig. 5.2(B). Therefore, in materials with small exciton



binding energies, very low temperatures are required to resolve their emission. TMDs are unique because of their large binding energies with the  $1s$  neutral exciton having a binding energy  $>100$  meV. This allows for the formation of bound neutral excitons even at room temperature ( $k_B T \approx 25$  meV). We conduct all of our measurements at low temperature to narrow the exciton emission linewidths to observe the charged exciton states and to measure the Rydberg series which have smaller binding energies;  $K_B T$  reduces to  $\sim 0.34$  meV at 4 K and  $\sim 0.025$  meV at 300 mK. The ideal scenario is for  $K_B T \ll E_{\text{binding}}$  of the exciton.

Of course, in a real experiment, we are not dealing with a single excitation and a single emission. The illumination light is from a laser that contains many photons which are absorbed by many electrons in the system. This results in the formation of many excitons that radiatively recombine and emit photons of energies equal to their bound state configuration that we then collect and monitor. Since continuous-wave (CW) lasers are used exclusively in our measurements, we are generating a steady-state of excitons that emit at some rate depending on the laser power. Such a configuration is depicted in Fig. 5.3(A).

A typical PL signature of an exciton's emission is depicted in Fig. 5.3(B). This would be the emission signature of a single exciton state as depicted in Fig. 5.3(A). The x-axis is the emission energy from the sample and the y-axis is the number of counts detected by our camera. The free-particle band gap corresponds to the energy separation of the valence and conduction band. The excitation laser's energy is selected to be greater than the free-particle band gap to generate free carriers. A lower energy peak on the x-axis labeled the optical band gap corresponds to the energy of the photons emitted from

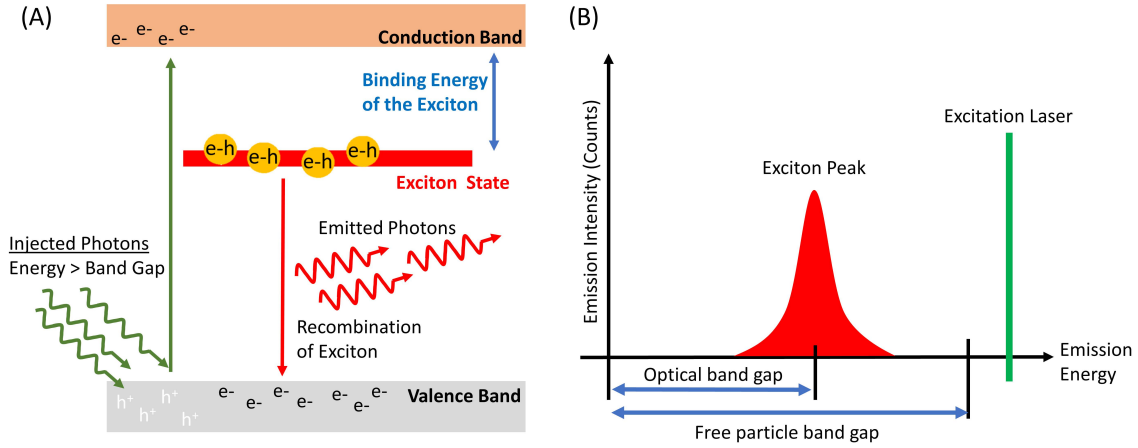


Figure 5.3: (A) PL using a CW laser source on a system with only one bound exciton state. A steady state of free electrons, free holes, and bound excitons is created. (B) PL signature from the recombination of excitons in a system with only one bound state, as modeled in (A).

the recombination of the excitons in the system. The optical band gap means that there are no bound states formed below this energy. The measurement of a lower energy peak is a signature of the existence of a bound exciton state, and its energy with respect to the free particle band gap is the exciton's binding energy.

### 5.3 Experimental Realization

The optical configuration for a PL spectroscopy measurement is typically a confocal microscope. A schematic of a confocal assembly is depicted in Fig. 5.4(A-D). A collimated laser source is illuminated on a sample through an objective. Photons from the laser are absorbed by electrons at the illumination spot in the sample and generate bound excitons. As the excitons recombine, their emission photons are collected by the objective and collimated back along the laser's path. A beamsplitter reflects the light

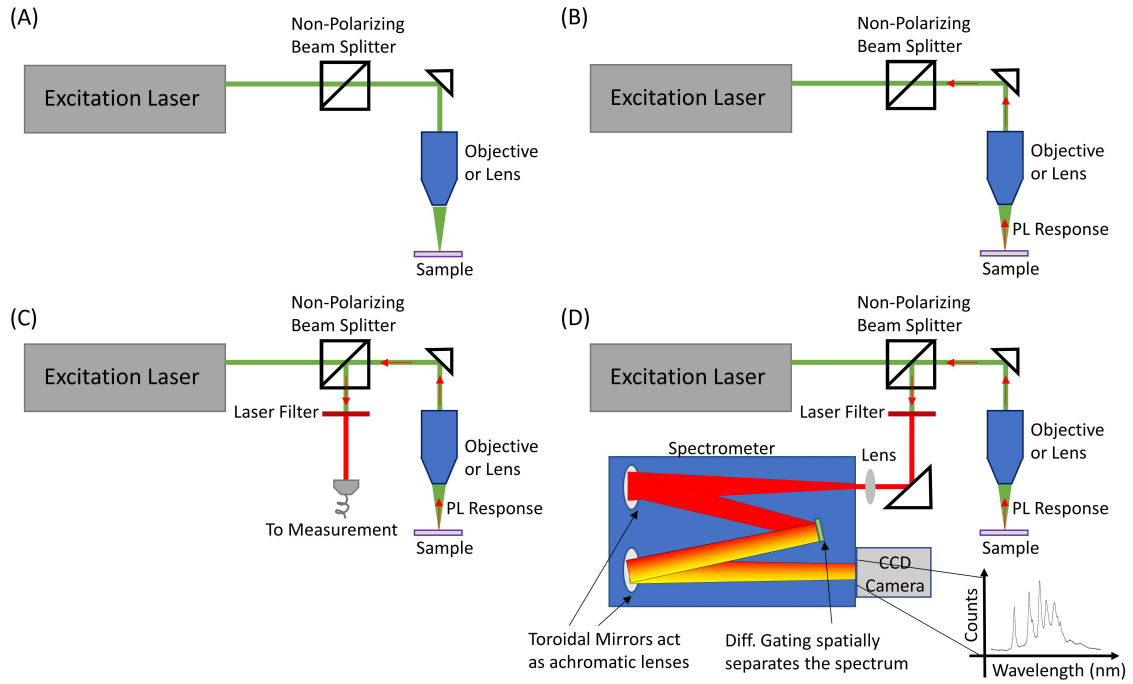


Figure 5.4: Schematic of a photoluminescence measurement in a confocal configuration. (A) A collimated laser is aligned to an objective that focuses the laser light on the sample. (B) The PL response emitted by the sample is collected by the objective, collimated, and directed back along the laser path. (C) The beamsplitter will direct only light that has been collected by the objective toward our measurement optics. To filter out scattered laser light, a low-pass filter is placed after the beamsplitter and before the measurement optics. Now, only the light emitted by the sample at energies lower than the laser reaches the detector. (D) In a standard spectroscopy measurement, the light is directed into a spectrometer. The spectrometer spatially separates the spectrum of the inputted light using a diffraction grating and then focuses the spatially separated light onto a CCD camera. In this configuration, each pixel on the camera corresponds to a different wavelength calibrated by the grating. The camera will also register the intensity of a given wavelength as counts; i.e. more photons at a given wavelength corresponds to more counts on the corresponding pixel of the camera. This setup is utilized for all measurements presented in this thesis.

collected from the sample toward our measurement detector, Fig. 5.4(D).

Before the collected light reaches our detector, a low pass filter is used to filter out the laser light that was reflected off the surface of the sample. It is important that our excitation laser is selected such that a commercially available low pass filter can be used to block the reflected laser light. If the laser's energy is too close to the energy of the excitons, the low-pass filter may not be able to successfully filter the laser from the exciton signal. If this is the case, a higher energy laser would be needed.

In a spectroscopy measurement, the exciton emission photons are sent to a spectrometer where their spectrum is spatially separated using a diffraction grating, Fig. 5.4(D). A single photon detection camera is used to collect the photons and read out their energy. The resulting data from the camera is shown in Fig. 5.4(D). A peak in counts means there is an exciton bound state at that energy that radiatively recombined and emitted a photon that was collected. Zero count dips mean there is either no exciton bound state at that energy or it is not radiatively active.

## 5.4 Rydberg Series

The neutral exciton also exhibits an additional similarity to a hydrogen atom in the existence of a Rydberg series of higher energy bound states [42]. It's generally difficult to measure the higher principal quantum number  $n$  exciton states in pseudo-2D material systems, such as GaAs quantum wells, due to their reduced binding energy with increasing  $n$ . Since the  $1s$  neutral exciton in GaAs quantum wells already has a binding energy less than  $\sim 10$  meV [49], the Rydberg series is very difficult to observe without

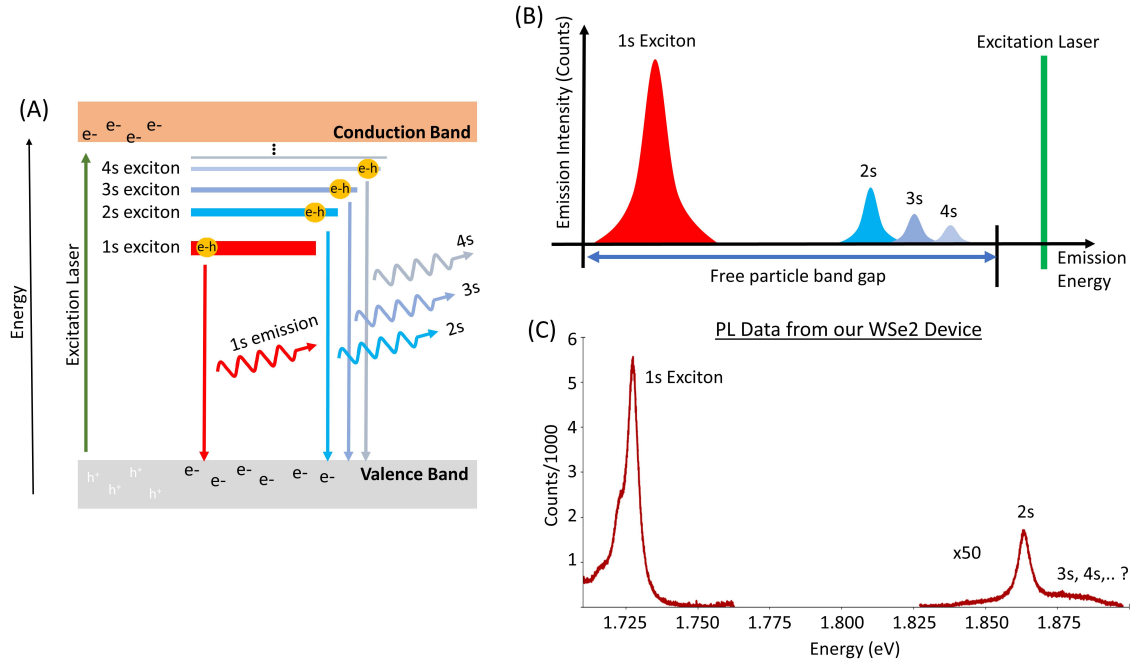


Figure 5.5: Schematic of a photoluminescence measurement including the Rydberg series of excitons. (A) PL excitation of free electrons into the conduction band that form bound Rydberg excitons with their hole counterparts. These higher principal number exciton states can either radiatively recombine and emit a photon or non-radiatively relax into lower principal number excitons. (B) Illustration of the a PL spectrum including emission from the Rydberg series of the exciton. (C) Data collected from our WSe<sub>2</sub> device at a temperature of  $<300$  mK. The sample is illuminated with 532 nm laser light at a power of 70  $\mu$ W and spot size of 1  $\mu$ m. The emission from the 1s exciton was collected with a 60 second exposure time. PL from the energy range of the 2s and 3s Rydberg neutral excitons was collected with a 3000 second exposure time. The only distinguishable PL signature is from the 2s neutral exciton. There is some signal from higher energies, but not enough emission to identify any peaks from higher  $n$ s.

very low temperatures. TMDs are an excellent platform to observe and study Rydberg excitons because of their extremely high exciton binding energies,  $>100$  meV, that allow for the Rydberg series to be spectrally resolved.

The fuller picture of PL with the inclusion of the Rydberg series of bound exciton states is illustrated in Fig. 5.5(A). An electron in the valence band absorbs a photon and is excited into the conduction band, leaving behind a hole in the valence band. If we make the assumption that there is no non-radiative relaxation between Rydberg exciton states in our system, the electron and hole can form any of these exciton states and eventually radiatively recombine by emitting a photon at the energy corresponding to that  $n$ s Rydberg exciton. Such a PL emission spectrum would be similar to that shown in Fig. 5.5(B).

The relaxation of higher  $n$  Rydberg excitons in TMDs have been extensively studied in Ref. [16, 50–52]. These reports found that very strong non-radiative mechanisms in TMDs cause rapid cascading of higher  $n$  state excitons into  $1$ s excitons. In Fig. 5.6(A), the most prominent cascade channels are outlined. The time scale of the cascade is presented in Fig. 5.6(B) for a 300 fs laser excitation pulse [16]. A large number of free electrons and holes are generated that quickly form high  $n$  Rydberg excitons. They quickly non-radiatively relax into lower  $n$  Rydberg excitons until nearly all the remaining excitons are of the  $1$ s variety.

This means the non-radiative relaxation time scales are much faster than the radiative recombination of the higher  $n$  Rydberg excitons. Such a characterization of a bound state in solid-state physics is known as the state's oscillator strength. The low oscillator strength of the higher  $n$  excitons drastically decreases the likelihood of being

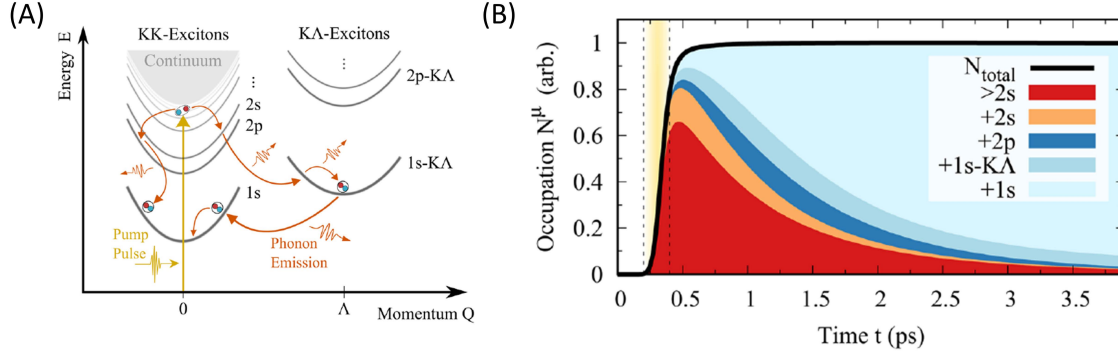


Figure 5.6: Figures from Ref. [16] depicting the non-radiative relaxation channels of Rydberg excitons in TMDs and their time scales. (A) Schematic of the primary phonon relaxation channels of higher  $n$  Rydberg excitons. (B) Populations of the Rydberg excitons in a TMD as a function of time after an excitation pulse. The populations of excitons with  $n > 2$  quickly rise after the initial laser pulse and then quickly decrease as they cascade along the non-radiative relaxation channels outlined in (A). The lifetime of a delocalized  $1s$  exciton in a TMD is on the order of a few picoseconds [16, 52].

able to monitor their emission through PL. Therefore, a more accurate depiction of the formation of Rydberg excitons through PL is that the free electrons and holes quickly form large  $n$  Rydberg excitons due to their low binding energies [16]. These large  $n$  excitons have very low oscillator strengths which makes it unlikely they will radiatively recombine before the much faster non-radiative mechanisms relax them into lower and lower  $n$  Rydberg exciton states, causing the cascade. At each  $n$ , the exciton has some probability of radiatively recombining and emitting a photon (which is our only means of detecting their existence in PL), but this is a very rare occurrence. Therefore, only the lowest  $n$  Rydberg excitons are observable using PL with the  $1s$  exciton being the brightest.

PL data from our WSe<sub>2</sub> sample, Fig. 5.5(C), shows the weak emission from the  $2s$

neutral exciton and near non-existent emission from the larger  $n$  Rydberg neutral exciton series. This makes PL a poor choice for monitoring the dynamics of Rydberg excitons with  $n > 2$ .

In photochemistry, this phenomenon is commonly known as Kasha's rule which states that non-radiative relaxations of higher  $n$  excitons dominate over radiative recombination [5, 15, 17]. This is due to the much faster time scales of the non-radiative relaxation mechanisms in comparison to the increasing with  $n$  lifetime of a Rydberg exciton before it radiatively recombines [16]. Therefore, the PL signature from an  $n > 1$  exciton is expected to be strongly suppressed and the only appreciable emission lines are from the  $1s$  state excitons. Although this rule has been shown to loosen for high-quality samples measured at low temperatures [5, 17], the  $n > 1$  exciton states remain far dimmer than the  $1s$  excitons.

As will be discussed in the next section, WSe<sub>2</sub> has many bright  $1s$  exciton states (neutral exciton, triplet and singlet charged excitons, dark excitons, intravalley excitons, replica excitons, etc.). In principal, there is a Rydberg series associated with each of these exciton species that may also recombine and emit photons at their corresponding energies. Being able to excite these states is dictated by their oscillator strengths and the neutral Rydberg series has proven to be the easiest to investigate due to its relatively high oscillator strength. The oscillator strength of the Rydberg series decreases rapidly for increasing principal quantum number  $n$ . The reduction of oscillator strength coupled with increased influence from disorder (increasing  $n$  also corresponds to increasing Bohr radius) makes radiative recombination of high  $n$  states less likely. We have to utilize a different optical measurement technique known as photoluminescence excitation (PLE)



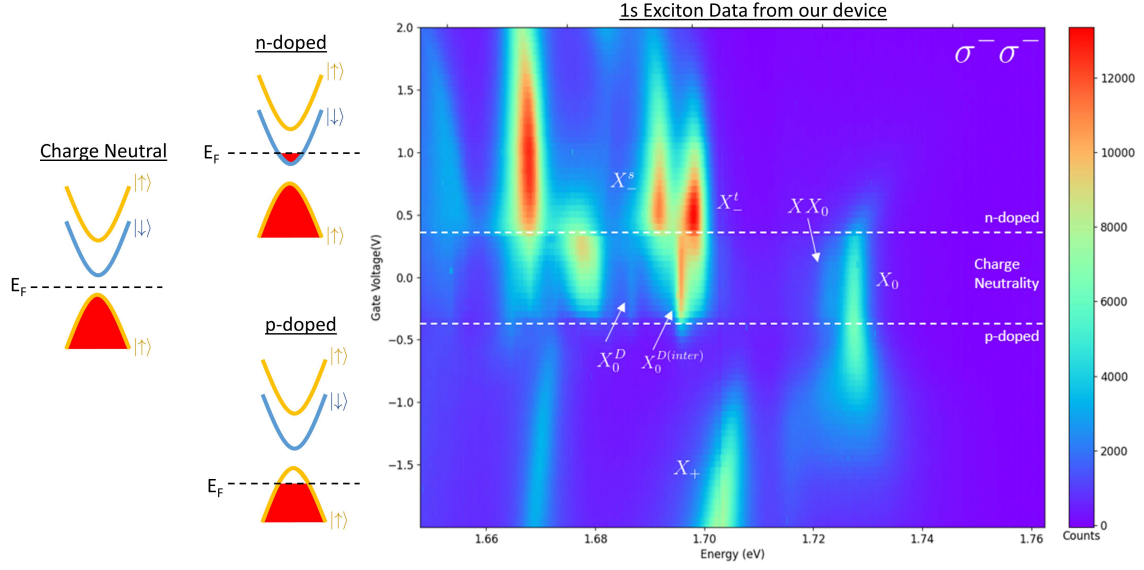


Figure 5.7: PL vs gate voltage of our WSe<sub>2</sub> sample. Sample is illuminated with a 633 nm laser focused to a 1  $\mu$ m spot with power of 70  $\mu$ W [18]. Only signatures from the 1s exciton species are observed here. Six exciton species of interest are labeled: the neutral exciton,  $X_0$ , the biexciton,  $XX_0$ , the two charge excitons,  $X_-^t$  and  $X_-^s$ , and two dark excitons,  $X_0^D$  and  $X_0^{D(inter)}$ . There are three charge transition regions identified: charge neutrality (Fermi level in the band gap), n-doped (Fermi level in the lower conduction band), p-doped (Fermi level in the upper valence band).

to study these states, as discussed in the next chapters.

## 5.5 Other Exciton Species

In addition to the neutral exciton, other exciton species can be formed in WSe<sub>2</sub> and are optically active. To instigate the formation of these other exciton species, we can control the carrier concentration via the back gate of the sample. In Fig. 5.7(A), we note three regions of distinctly different exciton emission spectrums. The first is labeled charge neutrality. In the charge neutral regime, PL primarily results in the creation of

neutral excitons. Their formation and life was discussed in the prior sections. There are a number of other lower energy emission signatures in the charge neutral regime besides the neutral exciton. These have been explored in great detail in the literature [53–57]. We are able to identify a bi-exciton and two dark excitons corresponding to the intra- and intervalley dark excitons. We also note that there is a clear signature of a charged exciton state,  $X_-^t$ . Its formation in charge neutrality is not a surprise because the neutral exciton is able to couple to localized charges on the sample and form a charged exciton. There are also less understood lower energy states that have been explored in other literature, but are beyond the scope of this work.

As the gate is swept to positive voltages, the electron density of the sample increases. Until we reach about +0.3 V, not much changes in the exciton signature. This is due to localized disorder in the device that allows for localized charging [47]. If the sample had a perfect band gap with no localized states, the next electron added to the system would enter the lower conduction band and charge neutrality would be a single value at 0 V. Localized disorder allows for electron occupation of energy states in the band gap. The gate voltage range between  $\pm 0.3$  V corresponds to the Fermi level being set within the band gap of the material. Since TMDs typically have a lot of disorder, there are many localized energy states on the sample with occupation energies in the band gap. Therefore, charge neutrality has a finite gate voltage range. Added or subtracted electrons in this gate voltage range do not affect the overall electronic behavior of the system. This is why the exciton signatures that do not depend on localized charging ( $X_0$ ,  $XX_0$ ,  $X_0^{D(inter)}$ ,  $X_0^D$ ) are unchanged in charge neutral regime. Other localized emission lines show significant changes in intensity indicating that their formation depends on the

localized disorder.

Once the gate voltage crosses the +0.3 V threshold, all of the localized charge defects in the system have been filled with electrons and the Fermi level enters WSe<sub>2</sub>'s lower conduction band. This transition takes the sample from being charge neutral to n-doped [47, 55, 58]. The excess free electrons form a Fermi sea and strongly influence the behavior of the exciton emission. We immediately see a swift drop in the intensity of the neutral exciton as the sample becomes more n-doped with increasing gate voltage. This is due to a shift in oscillator strength toward the formation of the two lower energy exciton states known as the singlet and triplet charged excitons (sometimes called trions in the literature) [47, 58]. Due to the growing sea of free electrons in the lower conduction band, the preferred bound states shift from the neutral exciton to the three-body charge excitons. This new quasi-particle state consists of the excited electron and hole pairing with a free electron from the now populated lower conduction band.

WSe<sub>2</sub>'s SOC splitting results in the lower conduction band having opposite spin from the upper conduction band. The two possible negatively charged exciton states are defined by the spin of the second electron [47, 55, 58]. These are detailed in Fig. 5.8. The first is the singlet which is an intravalley charge exciton because all carrier components of this three-body quasiparticle are in the same valley. This means the spin of the two electrons in this configuration have opposite spins and hence why the singlet charged exciton has lower energy. The second is the triplet which is an intervalley charge exciton because the second electron comes from the lower conduction band of the other valley meaning both electrons have the same spin.

On the other side of charge neutrality, starting at around -0.3 V, the Fermi level

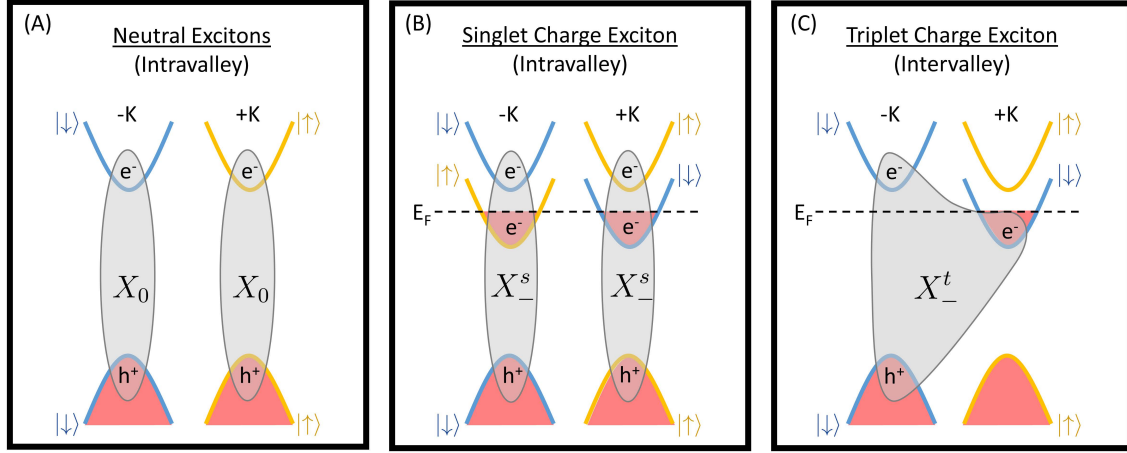


Figure 5.8: Illustration of the neutral and charged exciton bound states [59]. Red illustrates electron occupied states. Grey regions illustrate the bound state configuration of the exciton species. (A) The primary exciton formed in charge neutrality is the neutral exciton. It is the bound state between an excited electron in the upper conduction band and a hole in the upper valence band for  $\text{WSe}_2$ . The spin of both bands involved in the formation of this exciton are the same. (The lower conduction bands are intentionally left out to avoid confusion.) (B) As the sample is gated into the n-doped regime, the Fermi level enters the lower conduction band and free electrons begin to occupy these states. The singlet charged exciton is the bound state between an excited electron in the upper conduction band, a hole in the upper valence band, and a free electron from the lower conduction band. Because this bound state is formed in the same valley, the spin of the two electrons is opposite; i.e. a singlet configuration. This is the lowest energy charged exciton configuration. (C) The triplet charged exciton is a bound state between an excited electron in the upper conduction band, a hole in the upper valence band, and a free electron from the lower conduction band of the opposite valley. In this configuration, the spin of the two electrons is the same. Hence, it has a higher energy than the singlet configuration due to exchange. (The lower conduction band of the  $-K$  valley is intentionally left out to avoid confusion.)

begins to enter the upper valence band. This is the p-doped regime and results in the formation of the positively charged exciton composed of two holes and one electron [47]. For the purposes of this work, we note the existence of this state, but do not conduct any additional measurements on it.

## 5.6 Extraction of Carrier Concentration

Using a standard capacitive model, we estimate the carrier density as a function of gate voltage via the following relation [47, 60],

$$\Delta n = \frac{\Delta V \epsilon_0 \epsilon}{eL} \quad (5.1)$$

Here,  $\epsilon_0$  is the permittivity of free space,  $e$  is the elementary charge,  $L$  is the thickness of the dielectric spacer,  $\epsilon$  is the relative permittivity of the dielectric spacer, and  $\Delta V$  is the difference between our gate voltage from charge neutrality. In our case, the dielectric spacer is the hBN between the graphite back gate and our sample, which is estimated to be 15 nm thick. The thickness was measured using atomic force microscopy (AFM) and is expected to have a margin of error of approximately 5%. The average dielectric background for the hBN is given as  $\epsilon_{\perp} \approx 2.5$  [61]. We estimate the charge neutrality region based on the extension of neutral states in Fig. 5.7, which extends from  $V_g = -0.3$  to  $+0.3$  V. Fig. 5.9(A) shows the results of applying Eqn. 5.1 with our system parameters.

We can use the carrier density to extract an approximate associated Fermi level in

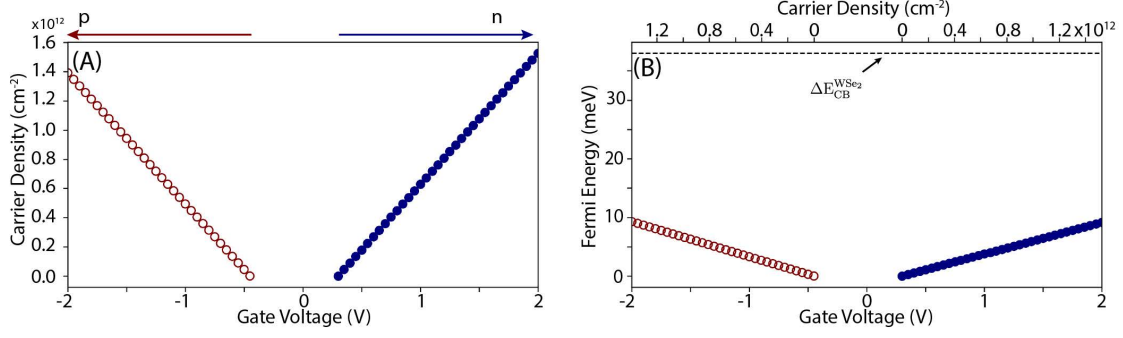


Figure 5.9: (A) Extracted carrier density as a function of applied gate voltage in a capacitive model [18]. (B) Calculated Fermi energy from carrier dependence with gate voltage. The energy corresponding to the conduction band spin-splitting is noted.

the sample. Here, we estimate the Fermi energy based on the carrier density as:

$$E_F = \frac{n}{\rho(E)} = \frac{n}{m^*/(\pi\hbar^2)}, \quad (5.2)$$

with  $\rho(E) = m^*/(\pi\hbar^2)$  as the density of available states when the the Fermi level is below the upper conduction band. We take the effective mass of the electron  $m_e^* = 0.4m_e$  [44] and the effective mass of the hole to be  $m_h^* = 0.36m_e$  [62]. WSe<sub>2</sub> transitions from a degenerate to a non-degenerate state as the Fermi level enters the upper conduction band. This results in the density of states becoming  $\rho(E) = m^*/(2\pi\hbar^2)$ . The Fermi energy is measured from the bottom of the lower conduction band at B=0T. Using these physical parameters, we generate 5.9(B) and indicate that the splitting of the upper and lower conduction bands for our system is  $\Delta E_{CB}^{WSe_2} = 38 \text{ meV}$  [44].

We estimate that the carrier concentration in the system is  $n_e \approx 4.6 \times 10^{10} \text{ cm}^{-2}$  at  $V_g = +0.35 \text{ V}$  and  $n_e \approx 2.7 \times 10^{11} \text{ cm}^{-2}$  at  $V_g = +0.6 \text{ V}$ .

## 5.7 2s Negatively Charged Excitons

In its simplest description, a charged exciton can be modeled similarly to a charged hydrogen ion,  $H^-$ . Although this particular model has been shown to have only one bound state [9], in the past decade it was theoretically proposed that the charged exciton may have bound Rydberg states [10]. Only recently has their existence been experimentally confirmed [11–14]. In this section we further confirm the existence of a negatively charged 2s exciton state in WSe<sub>2</sub> using PL.

Fig. 5.10(A) depicts a diagram of what the energy landscape would look like with the inclusion of a 2s charged exciton state. This diagram is in the low n-doped regime to allow for an overlap between favorable formation of the neutral and charged exciton states (between +0.3 V and +0.5 V on Fig. 5.7). The binding energy of  $X_-^s$  and  $X_-^t$  being greater than  $X_0$  indicates that the 2s charged exciton would also have a binding energy larger than  $X_0^{2s}$ , putting its emission energy between  $X_0$  and  $X_0^{2s}$ , as depicted in Fig. 5.10(B) [11–13].

Therefore, the two defining characteristics of a 2s charged exciton state in PL is that it should only be observable in the n-doped regime and have an emission energy below  $X_0^{2s}$  [11–13]. We conducted a similar PL vs gate voltage sweep in the energy range of both the 1s and 2s exciton species in Fig. 5.11. We limit ourselves here to only include gate voltages in the charge neutral and n-doped regimes. Fig. 5.11(A) includes emission energies of the  $X_0$ ,  $X_-^t$ , and  $X_-^s$ . Fig. 5.11(C) includes the emission energy of the  $X_0^{2s}$ . We note that  $X_0$  and  $X_0^{2s}$  have the same gate voltage dependence as the carrier density crosses the n-doped threshold. This further confirms that this higher energy signature corresponds to the 2s Rydberg exciton of the neutral exciton. Fig. 5.11(B) is the energy

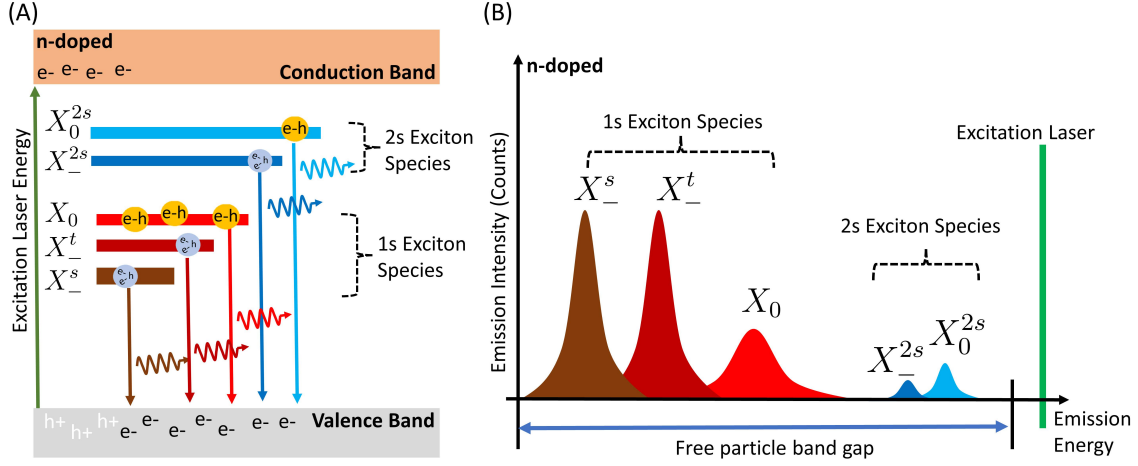


Figure 5.10: (A) Energy diagram of the binding energy relationships of the neutral excitons and the charged excitons. (B) Radiative signatures of each exciton species in (A) when measured in PL.

regime between  $X_0$  and  $X_0^{2s}$ . We can clearly see the onset of a new peak emerge only in the n-doped regime. To the best of our knowledge, this is the first measurement of the radiative recombination of  $X_-^{2s}$  through PL.

Since the  $2s$  charged exciton is expected to be a doublet, as observed for the  $1s$  charged excitons, the signature of  $X_-^{2s}$  is an average.  $X_-^t$  and  $X_-^s$  have a narrow linewidth and a strong intervalley exchange interaction that splits them ( $\sim 6$  meV [63,64]) which allows for them to be spectrally resolved. However, the broadness of the  $2s$  states combined with a reduced intervalley exchange energy (theoretically predicted to be  $\sim 1$  meV [12, 63]), prevents us from resolving the doublet of the  $2s$  charged exciton. The nomenclature of  $X_-^{2s}$  is used to describe signatures from both spin configurations.

To illustrate the onset of the  $X_-^{2s}$  signature as the sample enters the n-doped regime, we integrate the total number of counts in the emission spectrum of  $X_-^{2s}$  and plot it as a function of gate voltage. This is presented in Fig. 5.12(A,B). We see a clear jump in the



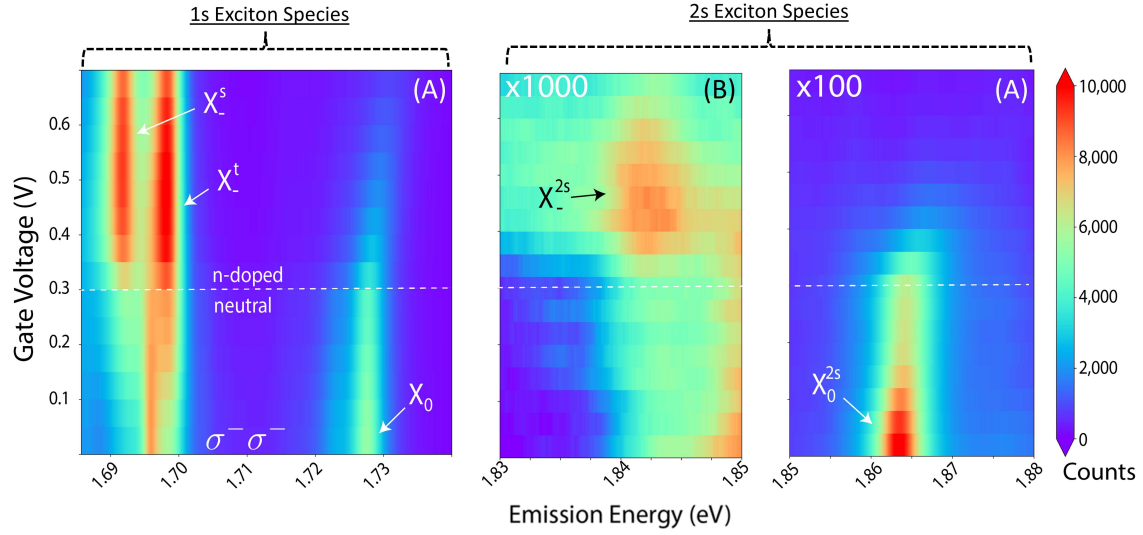


Figure 5.11: PL data of three emission energy regimes [18]. Sample is illuminated with a 532 nm laser focused to a 1  $\mu\text{m}$  spot with power of 70  $\mu\text{W}$ . All data is scaled to the same color bar with the scaling labeled on the plot. (A) Is the same energy range of the data of the 1s excitons presented in Fig. 5.7. It is limited to only show gate voltages in the charge neutral and n-doped regimes, and emission energies between  $X_-^s$  and  $X_0$ . (B) In the energy regime below the  $X_0^{2s}$ , another emission signature emerges only in the n-doped regime. This is the 2s negatively charged exciton,  $X_-^{2s}$ . (C) The energy regime of  $X_0^{2s}$ .

total number of counts as soon as the gate voltage crosses the +0.3 V threshold and exits charge neutrality. On the other hand, examining  $X_0^{2s}$  in the same manner, Fig. 5.12(C,D), shows a strong downward kink at +0.3 V. This analysis further confirms the emergence of the  $X_-^{2s}$  peak in our emission spectrum and demonstrates a shift from  $X_0^{2s}$  being the most favorable 2s bound state in charge neutrality toward  $X_-^{2s}$  in the n-doped regime. This is in agreement with the behavior of the 1s exciton species.

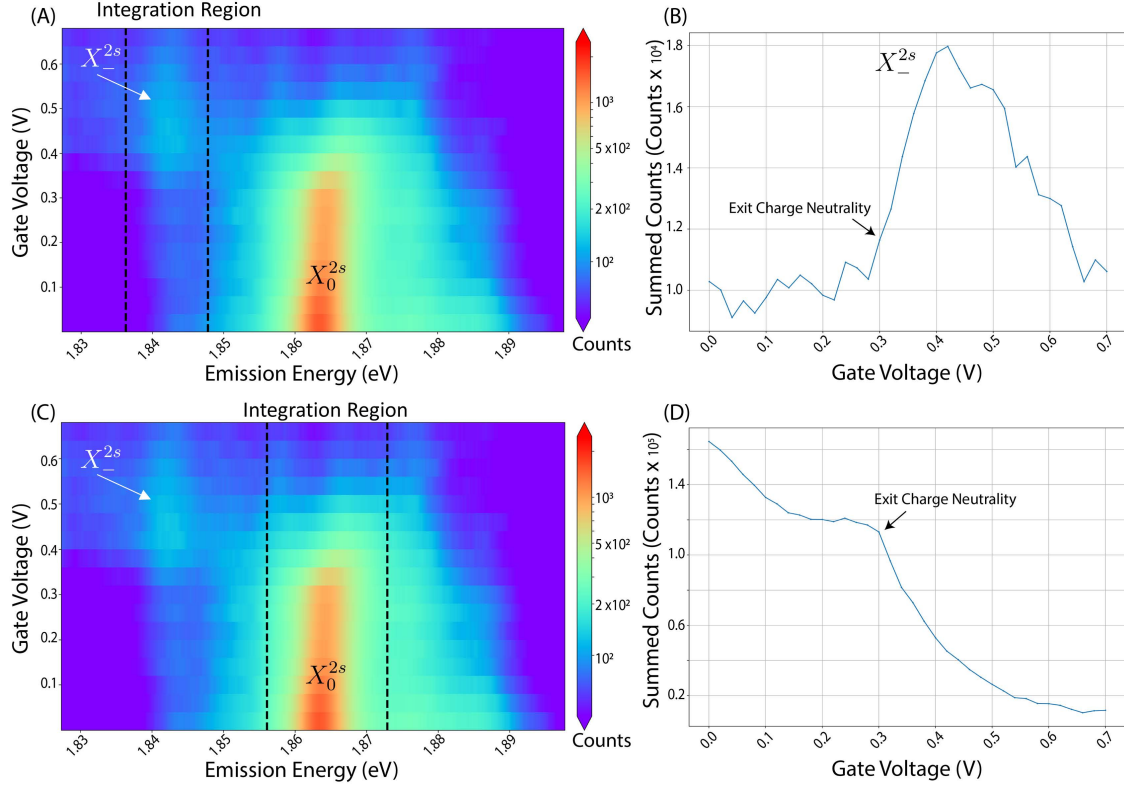


Figure 5.12: Additional analysis of  $X_0^{2s}$  and  $X_-^{2s}$  and their gate voltage dependence. (A) An integration spectrum is set around the  $X_-^{2s}$  peak and the total counts are summed for each gate voltages. This gives the plot presented in (B). As the gate voltage exits charge neutrality and enters the n-doped regime ( $\sim 0.3$  V), the emission intensity from the  $X_-^{2s}$  rapidly increases. (C) An integration spectrum is set around  $X_0^{2s}$  and the total counts are summed for each gate voltage. This gives the plot presented in (D). As the gate voltage exits charge neutrality and enters the n-doped regime ( $\sim 0.3$  V), the emission intensity from the  $X_0^{2s}$  experiences a kink and swiftly drops.

## Chapter 6: Photoluminescence Excitation Measurements

### 6.1 Overview

In PL, a laser of energy greater than the band gap of the material is used to generate free electrons and holes. We then rely on non-radiative relaxation channels for formation of bound exciton states. Their radiatively recombination emits a photon at the energy of the bound state which we can measure. As detailed in the previous chapter, non-radiatively relaxation to the lower  $n$  Rydberg states is far more likely for the large  $n$  excitons than radiatively recombination [16]. While measuring radiative emission from  $X_0^{2s}$  and  $X_-^{2s}$  is possible, it is exceedingly weak as shown in Fig. 5.11. Their PL signatures have a very poor signal-to-noise ratio making them difficult to analyze for changes. In this chapter, we utilize a different measurement technique known as photoluminescence excitation (PLE) that allows for a much higher signal-to-noise ratio of the spectral profile for the  $2s$  exciton species with even  $X_0^{3s}$  being identifiable. I will outline how PLE works and our measurements of  $X_0^{2s}$ ,  $X_0^{3s}$ , and  $X_-^{2s}$ .

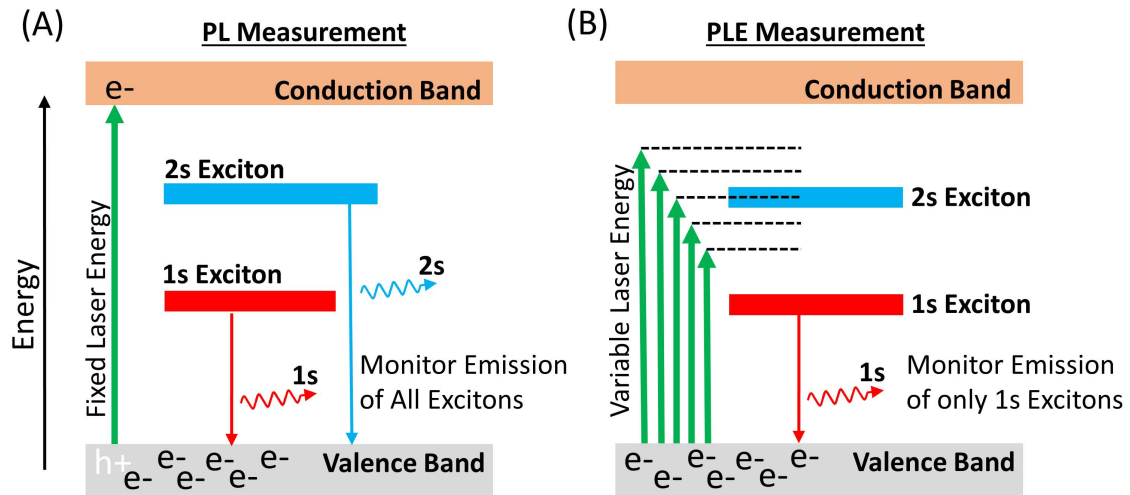


Figure 6.1: (A) In PL, the excitation laser's energy is fixed and greater than the band gap of the material. Free electrons and holes cascade into bound exciton states and radiatively recombine. The monitored emission photons are from all radiative exciton species. (B) In PLE, the excitation laser's energy is variable and less than the band gap. Only the emission photons from the  $1s$  exciton are monitored as the laser's energy is swept across the  $n > 1$  Rydberg excitons. We collect the emission intensity of the  $1s$  exciton as an indicator for whether the laser is in resonance with an  $n > 1$  Rydberg exciton.

## 6.2 Photoluminescence Excitation

In PL, the energy of the excitation laser remains constant at an energy greater than the band gap of the material. This generates a steady state of free electrons and holes that cascade into lower energy bound state excitons. We monitor the radiative emission of all exciton states within the band gap. If an emission peak is detected at a certain energy, this corresponds to an exciton state radiatively recombining. As outlined in the previous chapter, many of the higher  $n$  Rydberg excitons are unlikely to ever radiatively recombine and preferentially lower their energies through non-radiative relaxation into lower  $n$  Rydberg excitons [16]. This makes it very difficult to measure any Rydberg states above  $2s$ .

PLE adds another knob to the PL measurement that controls the energy of the excitation laser. The difference between the two optical measurement techniques is illustrated in Fig. 6.1. It is also important that the variable laser's energy is within the band gap of the material; i.e. no free electrons and holes are being formed in PLE. When the laser's energy is off-resonant with any bound state energy, as depicted in Fig. 6.2(A), the photons do not provide enough energy to form free electrons nor the right amount of energy to form a bound state. Therefore, when the laser's energy is off-resonant with any bound states, and within the band gap of the material, the system doesn't interact with the laser light and there is zero to minimal PL emission from the  $1s$  excitons, as shown in Fig. 6.2(B). (The exciton bound states have tails for finite temperature and have some very small probability of forming in the off-resonant case.)

By tuning the laser's energy to the energy of a bound exciton state, electrons can

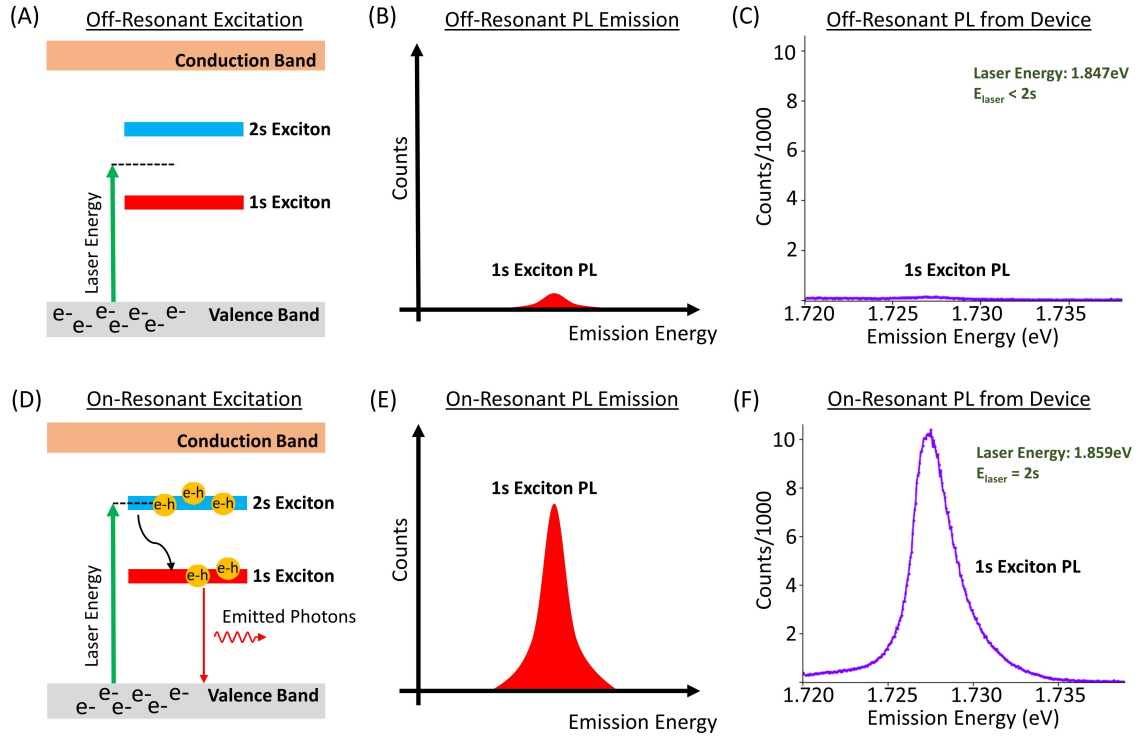


Figure 6.2: There are two possible laser energy scenarios in PLE. The first is when the laser is off-resonant with any exciton state and the second is when the laser is on-resonant with an exciton state. (A) When the laser is set to an energy that doesn't match any of the exciton states in the system, the electrons in the valence band are unable to form bound states and the material does not absorb the laser photons. Although there is still some probability that an exciton will form because of the tails of the  $2s$  state extending broadly, there will be very few. Therefore, we expect to measure very few photons from the  $1s$  exciton as depicted in (B). We see that this is in accordance with data from our measurement presented in (C). (D) In the second case, when the laser's energy is on-resonance with an exciton state, the electrons in the valence band will be able to absorb a photon with the exact amount of energy required to form this exciton bound state with its hole counterpart. The system will become heavily populated with  $2s$  excitons that will non-radiatively relax into  $1s$  exciton that will radiatively recombine. In this scenario, we expect to see a bright peak in the emission spectrum for the  $1s$  exciton as depicted in (E). We see that this is in accordance with data from our measurement presented in (F).

absorb a photon and have the exact energy required to form a bound exciton as depicted in Fig. 6.2(D). In the on-resonant case, the population of  $2s$  excitons will increase. Since we are unable to monitor the radiative recombination of the  $2s$  excitons because we can't separate the illuminated laser light from the signal, we rely on non-radiatively relaxation of this large population of  $2s$  excitons into  $1s$  excitons. The population of the  $1s$  excitons will radiatively recombine and emit photons at their energy, as shown in Fig. 6.2(E). Since the  $1s$  excitons are at a lower energy than the on-resonant excitons, we can filter the laser's light and monitor their radiative recombination.

Watching the  $1s$  exciton's emission intensity tells us whether or not the laser's excitation energy is in resonance with a Rydberg exciton state. When the intensity is low, the laser is creating only a few  $2s$  excitons, hence the laser is off-resonant with the state, Fig. 6.2(B). When the intensity is high, the laser is in-resonance with an excited exciton state, Fig. 6.2(E). When we conduct this experiment on our  $\text{WSe}_2$  sample, Fig. 6.2(C,F), we see the exact same results as illustrated, Fig. 6.2(B,E). In Fig. 6.2(C), the laser's energy is tuned between the  $2s$  and  $1s$  exciton states and we measure very little emission from the  $1s$  exciton. In Fig. 6.2(F), the laser's energy is tuned to the  $2s$  exciton's energy and we measure a large increase in the emission from the  $1s$  exciton.

PLE has proven to be a very reliable technique in measuring non-radiative higher  $n$  Rydberg neutral excitons. This is demonstrated in Fig. 6.3(A-C). The previously indistinguishable  $3s$  neutral exciton can be identified in our PLE measurement, as shown in Fig. 6.3(C). To demonstrate this further, we can simplify our PLE data by summing the counts within an integrated spectral range around the monitored emission energy (the energy of  $X_0$  in this case.) This energy range is shown in Fig. 6.3(D). This allows us to



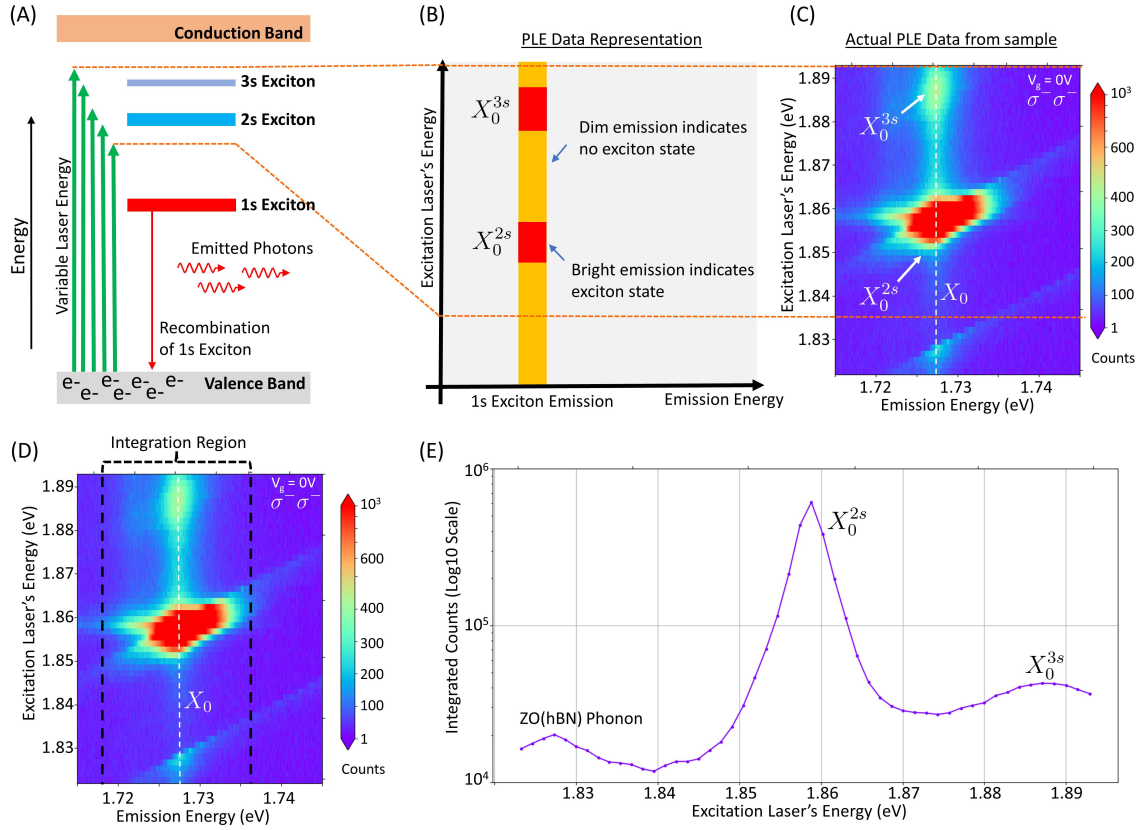


Figure 6.3: To demonstrate the value of PLE, we scan our laser across the energy range of the  $2s$  and  $3s$  neutral excitons while the sample is in charge neutrality,  $V_g = 0$  V. In a standard PL measurement of the neutral Rydberg series, we were unable to distinguish any emission peak corresponding to the  $3s$  neutral exciton as demonstrated in Fig. 5.5(C). Here we show a measurement of both the  $3s$  and  $2s$  neutral excitons using PLE. (A) The energy of the excitation laser is swept across the energy range of  $X_0^{2s}$  and  $X_0^{3s}$ . (B) When the laser is in resonance with a Rydberg exciton state, we expect an increase in emission intensity of the  $1s$  exciton. In this representation of the expected data, the y-axis is the energy of the excitation laser and the x-axis is the emission energy of the monitored  $1s$  state. The emission energy is fixed at the energy of the monitored emission channel as the excitation energy is swept. (C) Actual data from our WSe<sub>2</sub> sample. The monitored emission channel is  $X_0$  in this PLE data. Two clear intensity peaks appear that we have identified as  $X_0^{2s}$  and  $X_0^{3s}$  based on their binding energies. (Laser power fixed at 70 uW, spot size of 1  $\mu$ m, and collection time of 60 seconds.) (D) We can further process the data by integrate the counts around the emission peak to simplify the PLE response to the plot in (E) with the x-axis as the excitation laser's energy and the y-axis as the total integrated counts.

visualize the data in the 2D plot presented in Fig. 6.3(E). We can see three clear peaks in the integrated data. The first corresponds to the ZO(hBN) phonon mode that will be discussed in more detail later. The other two peaks correspond to  $X_0^{2s}$  and  $X_0^{3s}$ . The integrated counts (y-axis) is presented in a  $\log_{10}$  format.

### 6.3 PLE Gate Voltage Dependence

Similarly to the PL vs. gate voltage data presented in Fig. 5.11, we also collected PLE data at different gate voltages. The charge neutral and n-doped carrier density regimes are illustrated and discussed in Fig. 6.4. In the charge neutral case, only the neutral excitons can favorably form in the system. Therefore, we are only able to excite  $X_0^{2s}$  and monitor its resonance through the emission of  $X_0$ . The data presented here was also previously discussed in Fig. 6.3. As the carrier density is gated into the n-doped regime, the charged exciton states start to favorably form [47]. While the gate voltage is in the n-doped regime, but still near the charge neutrality threshold of  $V_g = +0.3$  V (as discussed in Fig. 5.7), the neutral exciton can still form, but its oscillator strength begins to diminish as  $X_-^s$  and  $X_-^t$  become the dominant exciton states. Since there is still finite oscillator strength for both the neutral and charged excitons in the low carrier density regime, the  $X_0^{2s}$  resonance appears in all three of the  $1s$  excitons' emission intensities, as labeled in Fig. 6.4(D). We also notice the emergence of a lower energy resonance at 1.838 eV in the n-doped PLE data that matches the binding energy of the  $X_-^{2s}$  measured in Fig. 5.11(B).

A more detailed analysis of the gate voltage dependence of the lower energy resonance as well as the  $X_0^{2s}$  resonance is conducted in Fig. 6.5. We monitored two

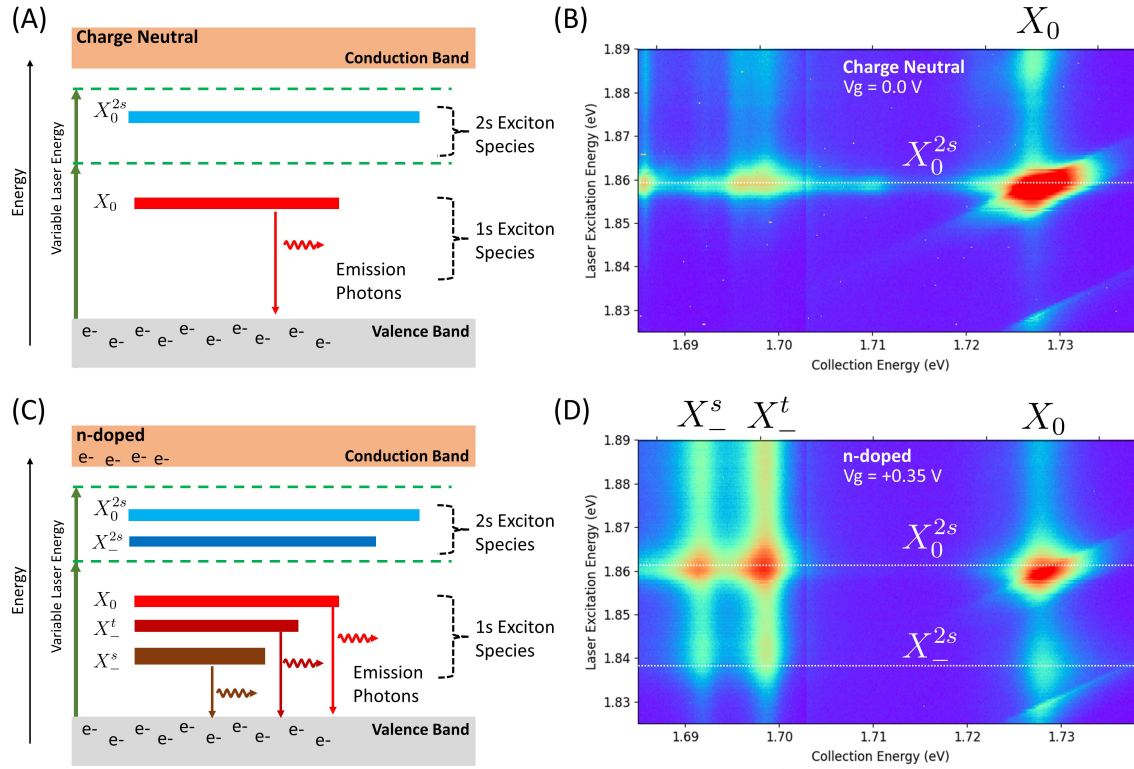


Figure 6.4: (A) In charge neutrality, we expect only neutral Rydberg excitons to have appreciable oscillator strengths. Therefore, sweeping the laser's energy across the  $2s$  energy range will only result in one resonance at the energy of  $X_0^{2s}$ , which is shown in (B). Since the charged excitons are unable to form in charge neutrality, the primary emission peak is the  $1s$  neutral exciton,  $X_0$ . There is enhancement of all radiative states in  $\text{WSe}_2$  at the  $X_0^{2s}$  resonance due to the large increase in exciton population, but outside of this resonance, these states are inactive. (C) As the carrier population is gated into the n-doped regime, the charged exciton states become favorable (as discussed in the previous chapter.) Therefore, we are able to form  $X_-^{s/t}$  and  $X_-^{2s}$ . (D) The PL data for a near-threshold gate voltage of  $V_g = +0.35$  V is shown here. (The carrier density is very low around  $4.6 \times 10^{10} \text{ cm}^{-2}$ , extracted from the capacitive model.) The emission signatures also change as we gate through the n-doping threshold with  $X_-^{s/t}$  becoming much brighter, as discussed in Fig. 5.11. Laser power fixed at 70  $\mu\text{W}$ , spot size of 1  $\mu\text{m}$ , and collection time of 60 seconds.

emission signatures ( $X_0$  and  $X_-^{2s}$ ) to demonstrate that the  $2s$  resonances are independent of which  $1s$  exciton we choose to monitor. We do note that because the  $X_0$  exciton dims in the n-doped regime, it becomes a less reliable emission channel than  $X_-^{s/t}$  as the gate voltage is increased.

The labeling and identification of the new low energy state as the  $2s$  charged exciton  $X_-^{2s}$  is based on two observations:

(I)  $V_g = +0.3$  V corresponds to the transition of the sample from charge neutrality to n-doped and the emergence of the negatively charged  $1s$  excitons  $X_-^t/X_-^s$ . The  $X_-^{2s}$  resonance displays a similar onset at  $V_g = +0.3$  V indicating a similar negative charge character. (II) When the  $X_-^{2s}$  resonance first appears at  $V_g = +0.3$  V, we find that  $\Delta E_{(X_0^{2s}-X_-^{2s})} = 21\text{meV}$  while  $\Delta E_{(X_0-X_-^t)} = 29\text{meV}$  and  $\Delta E_{(X_0-X_-^s)} = 35\text{meV}$ . This reduction indicates that the  $2s$  charged exciton is less tightly bound than its  $1s$  state counterpart. This is in accordance with other observations in the literature [11–14] and consistent with the fact that Rydberg states display a reduction in relative binding energy with each increasing  $n$ .

Since the  $2s$  charged exciton is expected to be a doublet, as observed for the  $1s$  charged excitons, the extracted position of  $X_-^{2s}$  is an average.  $X_-^t$  and  $X_-^s$  have a narrow linewidth and a strong intervalley exchange interaction that splits them ( $\approx 6$  meV [63,64]) which allows us to spectrally resolve them. However, the broadness of the  $2s$  states combined with a reduced intervalley exchange energy (theoretically predicted to be  $\approx 1\text{meV}$  [12,63]), prevents us from resolving the doublet of the  $2s$  charged exciton. There is, however, indication of the two states in the asymmetric lineshape of the  $X_-^{2s}$  peak, similar to the observation by Ref. [11,12].

In Fig. 6.5(A,B), we see the spectral dependence of  $X_0^{2s}$  and  $X_-^{2s}$  with carrier density while monitoring emission from  $X_0$ . As the  $n_e$ -doping increases with increasing gate voltage, the  $X_0^{2s}$  resonance broadens, decreases in intensity, and spectrally blueshifts. The broadening and loss of spectral intensity are consistent with more rapid decoherence from interaction with the Fermi sea. The blueshift results from the competing effects of band gap and binding energy renormalization due to decreased  $e^- - e^-$  and  $e^- - h^+$  interaction from screening by the Fermi sea [11, 65, 66].

In contrast,  $X_-^{2s}$  peak grows in intensity and experiences minimal spectral drift with increased carrier density. In the case of a three-body quasiparticle, one expects a redshift that is linearly dependent on the charge concentration in the system resulting from momentum conservation [65, 67, 68]. This competes with the effects of band gap and binding energy renormalization previously discussed for the neutral excitons that favor a blueshift [65], and leads to the minimal spectral drift observed. Both the increase in intensity and small spectral shift are consistent with the behavior of  $1s$  and  $2s$  charged excitons previously observed [11, 65, 66].

Since  $X_-^{2s}$  emerges in the  $n$ -doped regime, we expect  $X_-^t$  and  $X_-^s$  to be the most prominent emission channels for  $2s$  exciton species (see Fig. 5.7). To verify this, we monitor the  $X_-^t$  emission channel in a similar manner to  $X_0$  and show the results as a function of  $V_g$  in Fig. 6.5(C,D). We confirm that the behavior (spectral position, shift with gate, etc.) of  $X_0^{2s}$  and  $X_-^{2s}$  is independent of the monitored decay channel.

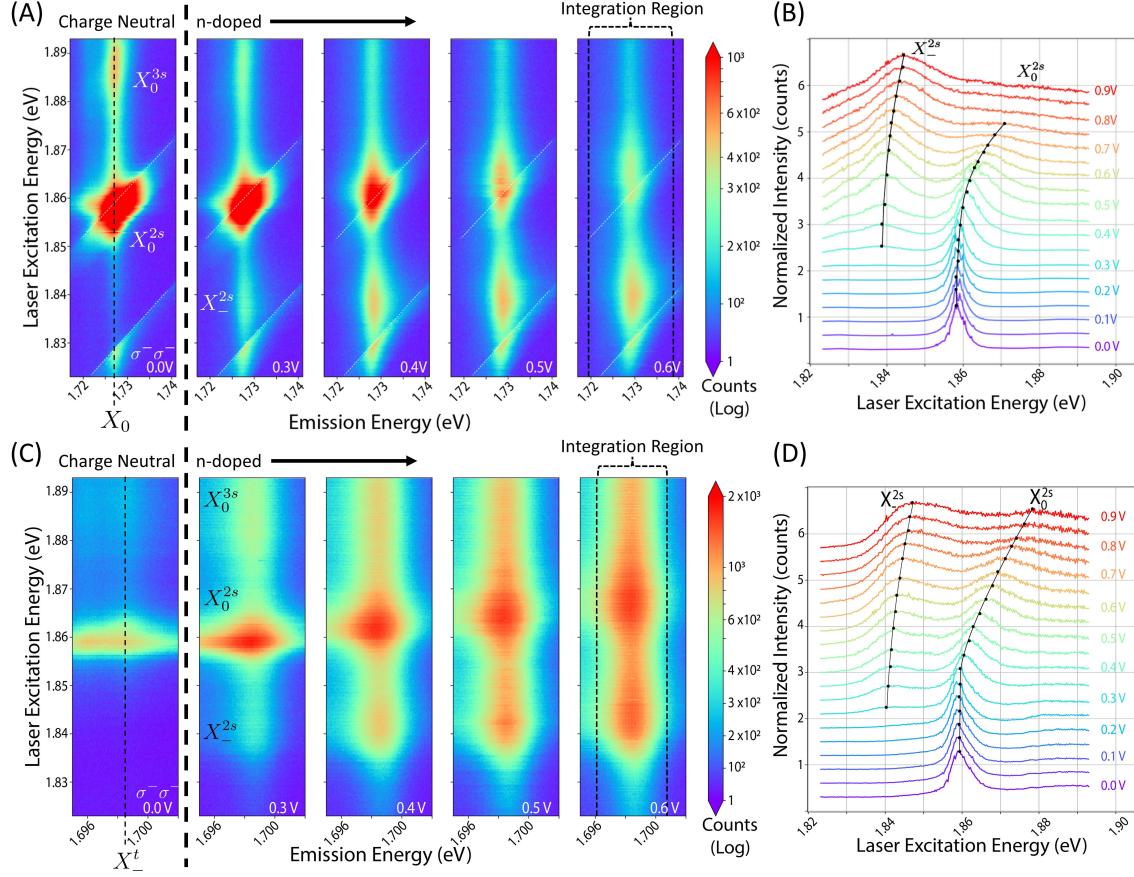


Figure 6.5: (A) PLE data with increasing  $n_e$ -doping while monitoring the  $X_0$  recombination channel in the -K-valley ( $\sigma^- \sigma^-$ ) [18]. (B) Waterfall plot of vertical cross-sections from  $V_g = 0 - 0.9V$ . The integration region is annotated in panel (A). The counts were summed over the emission width for each excitation energy. (C) PLE data with increasing  $n_e$ -doping while monitoring the  $X_0^t$  recombination channel ( $\sigma^- \sigma^-$ ) [18]. (D) The waterfall plot corresponds to vertical cross-sections from  $V_g = 0 - 0.9V$ . Laser power fixed at 70 uW, spot size of 1  $\mu m$ , and collection time of 60 seconds.



## 6.4 Phonon Modes

Previous reports exploring the  $X_0^{2s}$ - $X_0^{3s}$  energy regime using PLE have demonstrated strong electron-phonon coupling between a WSe<sub>2</sub> monolayer and its environment [69–71]. These investigations have shown that there are two prominent Raman modes in hBN/WSe<sub>2</sub>/hBN heterostructures that become bright when their emission energies match that of the  $X_0$ ; both are labeled in Fig. 6.5(A) and Fig. 6.6(D). The first is the enhancement of an optical phonon, ZO(hBN), that is silent in pure hBN and becomes prominent only when in close proximity to WSe<sub>2</sub> [69–71]. The second phonon line is a combined Raman mode of ZO(hBN) and an out-of-plane optical vibrational mode in WSe<sub>2</sub>,  $A_{1g}$ (WSe<sub>2</sub>) [71]. We measure the spectral displacement of this phonon line from the ZO(hBN) line to be 31 meV, which is in good agreement with prior reports for the energy of the  $A_{1g}$ (WSe<sub>2</sub>) phonon [72].

When the Raman emission from the ZO(hBN) +  $A_{1g}$ (WSe<sub>2</sub>) phonon is resonant with  $X_0$ , the signal becomes increasingly dominant and orders of magnitude brighter than any other signal from the sample. This is attributed to the degeneracy between the phonon's line intercept with  $X_0$  and the energy gap between the  $X_0$  and the  $X_0^{2s}$  [73]. This degeneracy can be broken through gating as the  $X_0^{2s}$  state blue-shifts with increasing carrier density. Fig. 6.5(A) depicts this shift, showing the spectral isolation of  $X_0^{2s}$  from the ZO(hBN)+ $A_{1g}$ (WSe<sub>2</sub>).

This overlap of the phonon energies with the emission energy of  $X_0$  makes  $X_0$  a poor choice for analyzing PLE data because of this added complexity. Therefore,  $X_-^t$  or  $X_-^s$  are both better emission energies to monitor for  $2s$  PLE resonances. Since we have

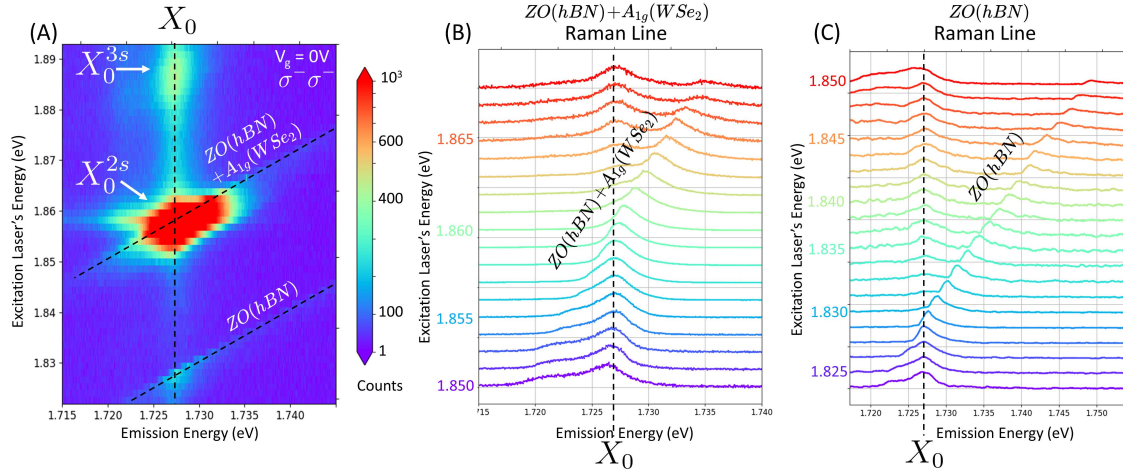


Figure 6.6: (A) Labeling of the two prominent phonon modes that overlap with the  $X_0$  emission in the PLE data of our  $WSe_2$  sample.  $ZO(hBN)$  corresponds to a phonon energy of 101 meV or  $819\text{ cm}^{-1}$ .  $ZO(hBN) + A_{1g}(WSe_2)$  corresponds to a phonon energy of 132 meV or  $1066\text{ cm}^{-1}$ . Both values are in close agreement with those reported in Ref. [71]. (B) PL trace of the  $ZO(hBN) + A_{1g}(WSe_2)$  phonon. (C) PL trace of the  $ZO(hBN)$  phonon. Laser power fixed at 70 uW, spot size of 1  $\mu\text{m}$ , and collection time of 60 seconds.



shown that the PLE signatures for  $X_0^{2s}$  and  $X_-^{2s}$  are the same for  $X_0$  and  $X_-^t$  in Fig. 6.5, we monitored  $X_-^t$  in our reported magnetic field study of the  $2s$  excitons in  $\text{WSe}_2$ .

## Chapter 7: Magnetic Field Dependence of Exciton States

### 7.1 Introduction

In this chapter, we measure and analyze the magnetic field dependence of the  $2s$  exciton species,  $X_0^{2s}$  and  $X_-^{2s}$ . Magneto-optical characterization of newly identified quasiparticle species has proven to be an important tool in semiconductor systems for identifying the composite configurations of excitons and distinguishing their replica states [74, 75]. It also directly measures the spin-valley character of an exciton state [30, 53, 58, 76, 77] and its influence by many-body interaction with free charges or disorder [60, 78, 79].

### 7.2 Valley Zeeman Splitting

Since TMDs exhibit strong SOC, their spin configurations are well defined in both the conduction and valence bands. This means that the spin dependent magneto-response at the direct transition for the  $\pm K$  valleys is expected to be the same for both bands; i.e. either they both shift up or down in energy. If this was the only contribution to the magnetic moment in these materials, it would mean that applying a non-zero perpendicular magnetic field would not break the band gap degeneracy of the  $\pm K$  valleys.

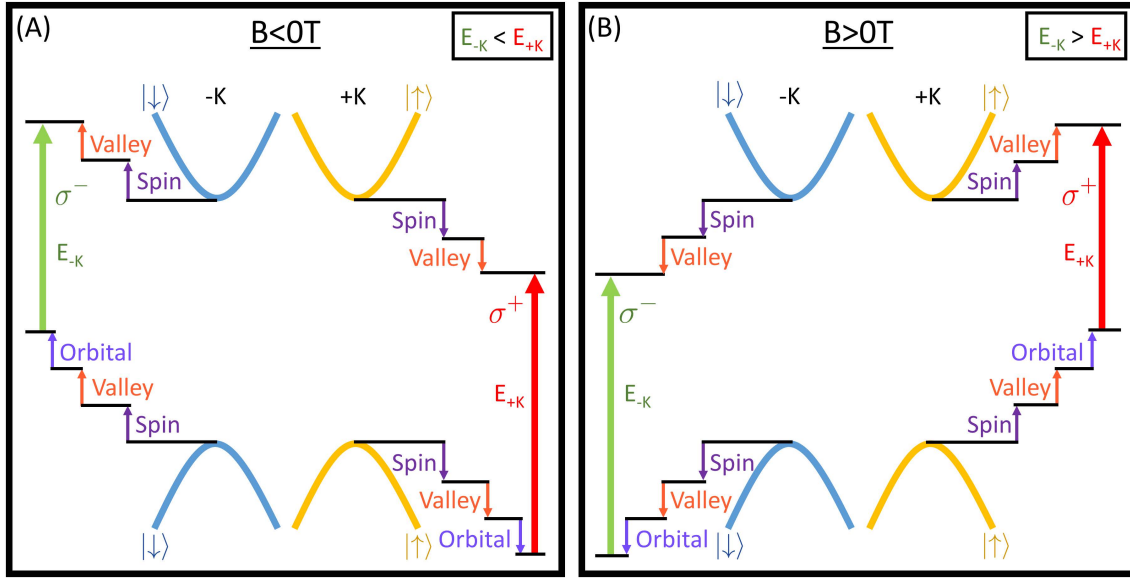


Figure 7.1: Illustration of the energy shift of the conduction and valence bands in  $\text{WSe}_2$  in the presence of a non-zero perpendicular magnetic field. Each magnetic moment contribution to the energy shift of each band is acknowledged with the labeling following the derivation in Ref. [35].

To fully understand the magneto-photo response of TMDs, we need to include the magnetic moment components of the bands themselves. These are the valley, or inter-cellular, and orbital, or intra-cellular, magnetic moments [30, 35] and they do result in the breaking of the band gap degeneracy of the  $\pm K$  valleys in the presence of a non-zero perpendicular magnetic field.

The valley magnetic moment is determined by the Berry curvature of the bands which can also be thought of as the mass of the carriers [30, 35]. This term is approximately equal, to first order, in both the conduction and valence bands. Therefore, its contribution has little to no effect on the band gap and only accounts for small corrections to the magnetic response [35].

The orbital magnetic moment has a more significant effect. In TMDs, the states in the conduction and valence bands are primarily formed from the d-orbitals of the transition metal, in our case tungsten (W) [30, 35, 80, 81]. DFT calculations show that the  $d_{z^2}$  orbital contributes most to the conduction band, while the  $d_{x^2-y^2}$ ,  $d_{xy}$  orbitals contribute most to the valence band [35, 80, 81]. Hence, in the presence of a perpendicular magnetic field ( $B_z$ ), the valence band experiences a significant magnetic response while the conduction band is unaffected.

Therefore, in this model, the conduction band only has contributions from the valley magnetic moment, while the valence band has contributions from both the valley and orbital magnetic moments [30, 35]. This is illustrated in Fig. 7.1 following the derivation in Ref. [35]. The orbital magnetic moment ends up dictating the shift in the band gaps of the  $\pm K$  valleys because it only influences the valence band while the spin and valley magnetic moments affect both bands equally.

To calculate the change in energy of the band gap for each valley independently, we have  $\Delta E_{\pm K} = (\mu_{\pm K,c} - \mu_{\pm K,v})B_Z$  [35, 82]. Since the spin and valley magnet moments are the same in the valence and conduction bands, the only contributing component comes from the orbital magnetic moment. The orbital magnetic moment of each band is given by  $\mu_{\pm K}^{orbital} = l_z \mu_B$ , where  $l_z$  is the angular momentum of the d-orbitals that form the band [30, 35, 82].  $l_z=0$  for the conduction band because it is formed from the  $d_{z^2}$  orbital while  $l_z=\pm 2$  for the valence band because it is formed from  $d_{x^2+y^2}$ ,  $d_{xy}$  orbitals [35]. Therefore, the only non-zero contribution is  $\mu_{\pm K,v}^{orbital} = \pm 2\mu_B$  which gives the change in band gap as  $\Delta E_{\pm K} = (0 - \pm 2)\mu_B B_Z = \mp 2\mu_B B_Z$ . We can extract a  $g$ -factor using the relationship for the valley Zeeman splitting given by  $\Delta E_{ValleyZeeman} = \Delta E_{+K} - \Delta E_{-K} = gB$  [30, 35, 82]. From this, we get a  $g$ -factor of  $-4\mu_B$ .

The resulting energy shift of the band gaps in the  $\pm K$  valleys for  $\pm B$  fields is illustrated in Fig. 7.2 [35, 82]. If the exciton exhibits no other magnetic field dependent energy shifts, its energy will follow the valley Zeeman shift of the bands and we will measure  $g_{X_0} = -4\mu_B$ . This would be the case in the single particle interpretation of the exciton [30, 35, 82].

A  $g$ -factor of  $-4\mu_B$  has been shown for  $X_0$  in  $WSe_2$  while the carrier density is charge neutral. This has been reported by many groups including, but limited to Ref. [4–7, 30, 35, 82] and has been verified in our own measurements. More exotic exciton states, such as charged excitons, have been shown to have  $g$ -factors that differ from this model [30, 58, 83, 84] and there are now reports that show interesting changes in  $g$ -factor with carrier density for all exciton states (including the neutral exciton) [14, 78, 79].

**Spin-Orbit Coupling: Selection Rules**

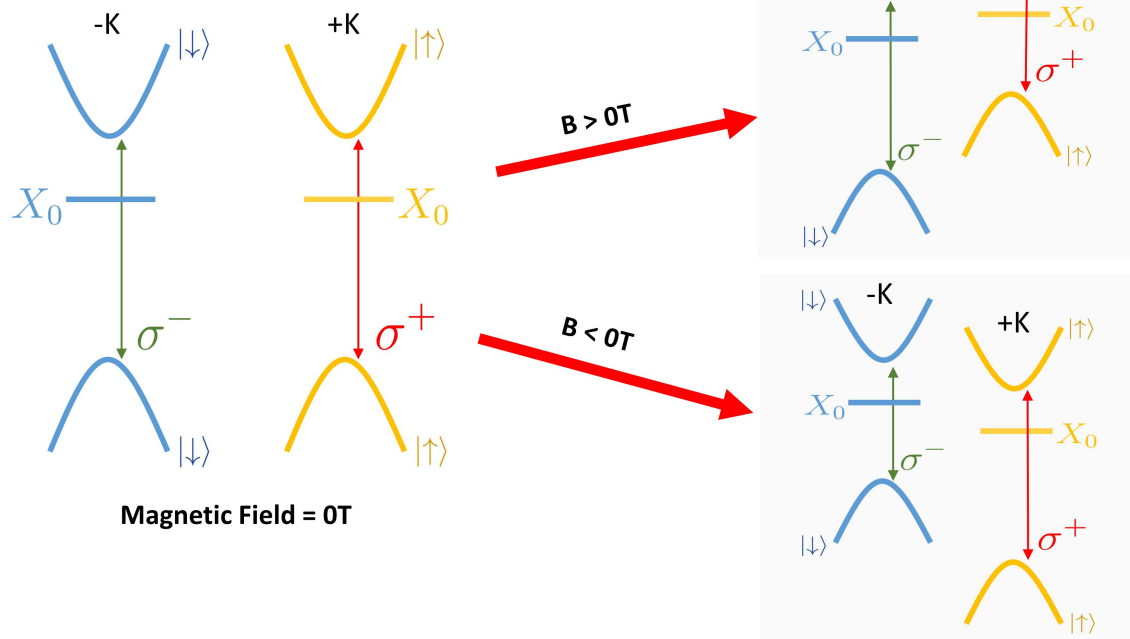


Figure 7.2: Illustration of the valley Zeeman splitting in a TMD following the model in Fig. 7.1.

### 7.3 PLE Magnetic Field Dependence

In all of our magnetic field PLE data probing the  $2s$  excitons, we chose  $V_g = +0.6$  V because both the neutral and charge excitons have comparable resonance intensity, Fig. 6.5. This corresponds to a carrier density of  $n_e \approx 2.7 \times 10^{11} \text{cm}^{-2}$ . This choice of carrier density allows us to measure the valley Zeeman splitting of both  $2s$  states in the same PLE data.

Since PLE has two independent energy axes, the data's response to valley Zeeman shifts is more complicated than if we were monitoring the exciton states using PL or reflectivity. In PL or reflectivity, shifts in the emission energy directly correlate with shifts in the exciton energy. Since in PLE we are monitoring the emission of a second, lower energy, exciton state that also experiences valley Zeeman energy shifts, both the x-axis and y-axis shift in energy. This is illustrated in Fig. 7.3(A,B). If we assume (for the purposes of this illustration) that both the  $2s$  excitons that we are exciting and the  $1s$  excitons we are monitoring have a  $g$ -factor of  $-4\mu_B$ , they will both shift in energy equally with changing magnetic field; i.e. both the excitation energy at which the laser resonantly excites a  $2s$  exciton and the emission energy of the monitored  $X_0$  exciton shift equally with magnetic field. This will appear as a shift of the emission energy of the  $X_0$  exciton along the x-axis and a shift in the  $2s$  PLE intensity resonances along the y-axis, Fig. 7.3(C,D). The assumption of  $g$ -factor being close to  $-4\mu_B$  for both the  $2s$  and  $1s$  states means the energy shift of the  $2s$  resonances will have a near 45 deg linear slope. Note that the magnetic field energy shift is opposite and equal in the  $\pm K$  valleys.

If we were to plot the valley Zeeman PLE for the  $\pm K$  valleys with fixed non-zero

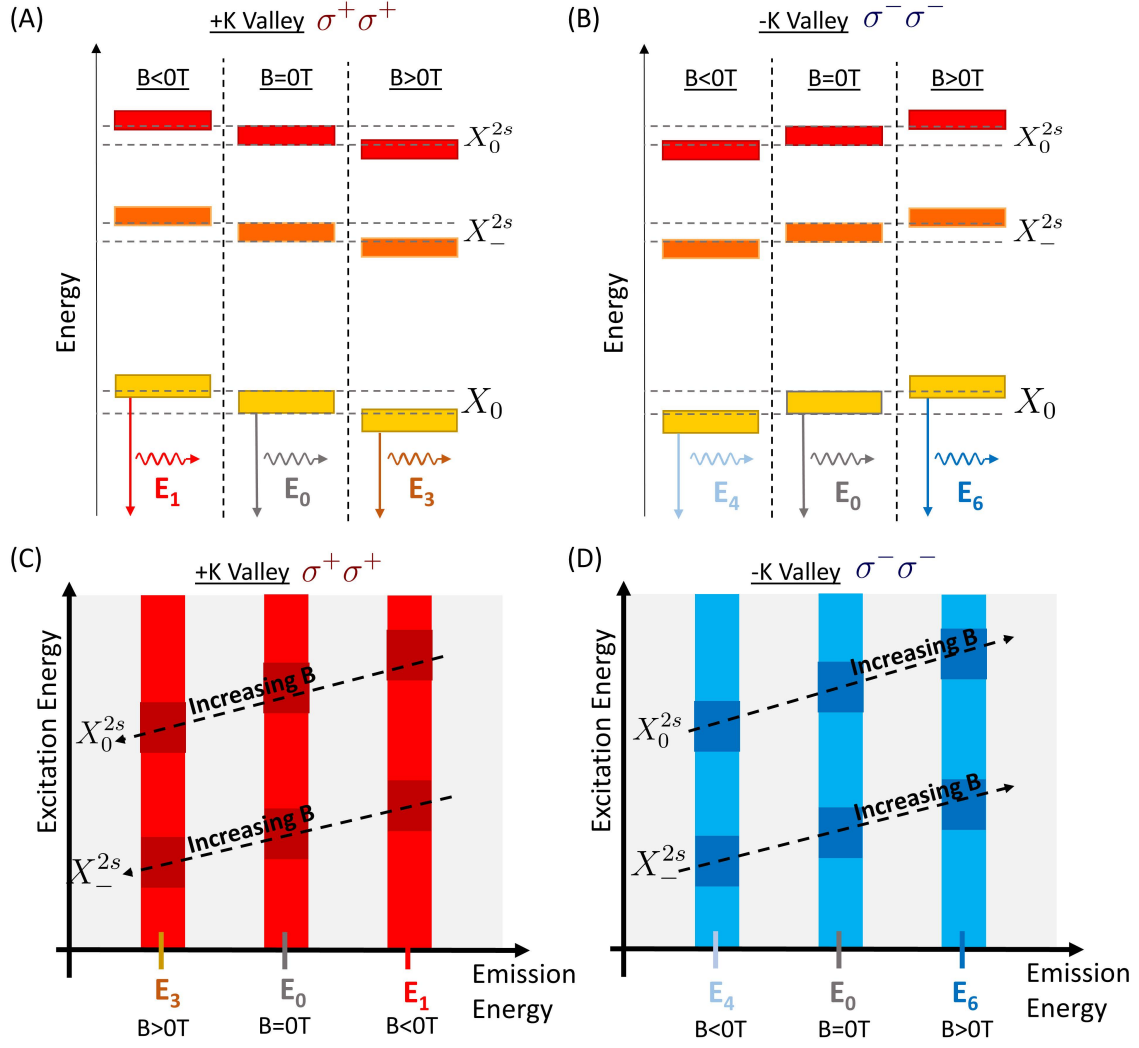


Figure 7.3: Illustration of the valley Zeeman splitting PLE response for the  $\pm K$  valley. (A, B) As detailed in Fig. 7.2, a perpendicular magnetic field applied to a TMD results in the band gap of the material shifting in equal and opposite for the  $\pm K$  valleys. If the  $g$ -factors of the exciton species are similar, this shift in the band gap will appear as the exciton energies shifting equally in energy. This is demonstrated in this diagram for  $\pm B$  fields with respect to the degenerate case when  $B=0T$  ( $X_0$ 's emission energy labeled  $E_0$ ). (C, D) Plotting the PLE data on top of itself should appear as illustrated here. We expect the emission spectrum of the monitored  $1s$  exciton ( $X_0$  shown here) to shift in its emission energy with magnetic field as well as the  $2s$  resonances shifting on the y-axis. Therefore, in this plotting configuration we expect a 45 deg linear slope in the emission intensity peak of the  $2s$  resonances. This is denoted by the dotted line labeled increasing  $B$ . The slope is negative for the  $+K$  valley and positive for the  $-K$  valley.



magnetic fields, we would expect data similar to the illustrations in Fig. 7.4. Plotting the PLE data in this configuration is a good check as to whether we are indeed observing a valley Zeeman splitting in our magnetic field dependent PLE data. This is precisely what we see in Fig. 7.5 which monitors the emission of  $X_0$ . To plot the  $\pm K$  valley PLE data together, we subtract the  $+K$  data from the  $-K$  data with a colorbar defined such that blue is for only positive counts ( $-K$ ) and red is for only negative counts ( $+K$ ). White regions mean the counts are equal for both of the  $\pm K$  valleys. Plotting the data in this manner shows the  $2s$  resonances on top of each other at  $B = 0T$ , but then they quickly shift apart (in both the  $x$  and  $y$  directions). The same response is shown while monitoring the emission from  $X_-^t$  in Fig. 7.6. From this, we can extract the valley Zeeman splitting of both the  $2s$  and  $1s$  exciton states and their corresponding  $g$ -factors.

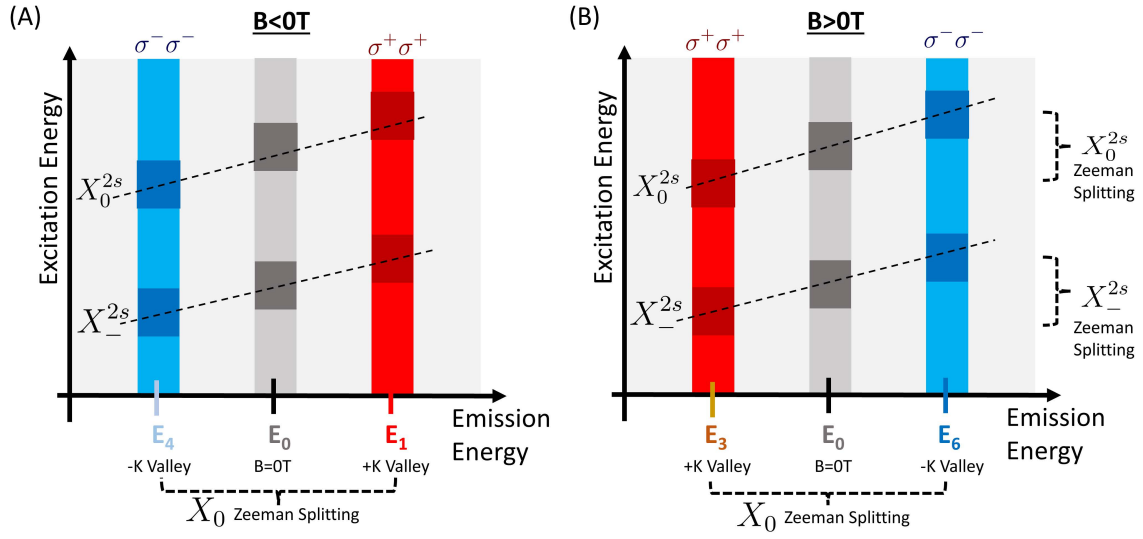


Figure 7.4: Plotting the expected valley splittings in the PLE data illustrated in Fig. 7.3(C, D) and plotting them for fixed magnetic fields. Since the x-axis and y-axis in PLE are decoupled (the energy of the emission line does not affect the resonances of the laser excitation), we can extract the valley Zeeman splitting for  $X_0$ , our monitored emission energy, on the x-axis and the valley Zeeman splitting for  $X_0^{2s}$  and  $X_-^{2s}$  on the y-axis.

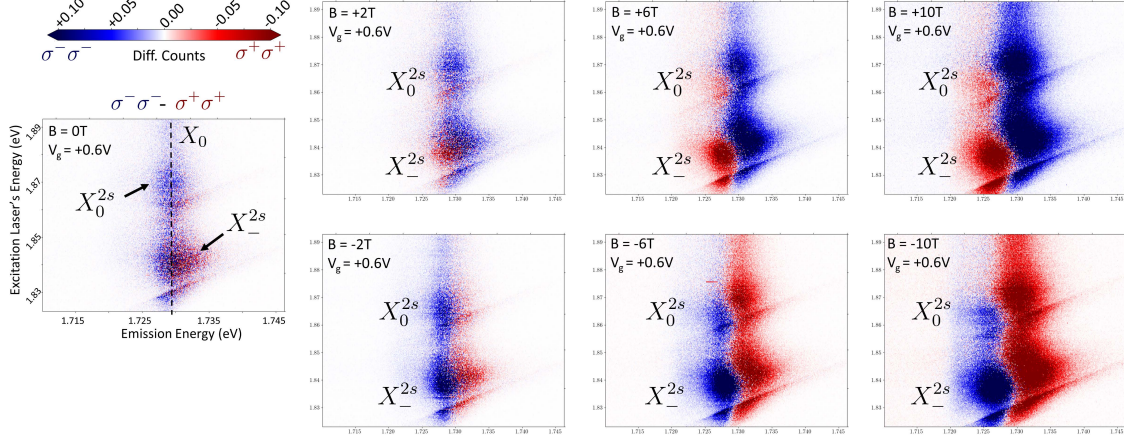


Figure 7.5: Data from our WSe<sub>2</sub> sample demonstrating the effect illustrated in Fig. 7.4. To present the data in this way, the PLe data for each valley was first power sharpened to the power of 3. Power sharpening is a technique that kills off the background signal and noise of the data and leaves only the most prominent peaks. Then the PLe data from the +K valley ( $\sigma^+\sigma^+$ ) is subtracted from the PLe data from the -K valley ( $\sigma^-\sigma^-$ ). The colorbar was set to have 0 be white, positive counts be blue (-K valley counts), and negative counts be red (+K valley counts). Whenever the plots overlap with one another, the total number of counts should be small (close to zero). This is the case when  $B=0\text{T}$  (left most plot). We see the two PLe signatures from the two valleys overlap and the total number of counts is small. As the magnetic field is increased (decreased), shown in the top (bottom) data plots, we see that the valley energy degeneracy of the  $2s$  resonances is broken. The splitting flips for  $\pm B$  fields. The energy splitting is clearest for high magnetic fields, our highest field is  $\pm 10\text{T}$ . We also observe that not only did the x-axis emission spectrum for the monitored  $X_0$  exciton shift, but there is a clear y-axis shift in the  $2s$  resonances. This matches the illustration of what the valley Zeeman splitting should look like in PLe in Fig. 7.4. Laser power fixed at 70 uW, spot size of 1  $\mu\text{m}$ , and collection time of 60 seconds.

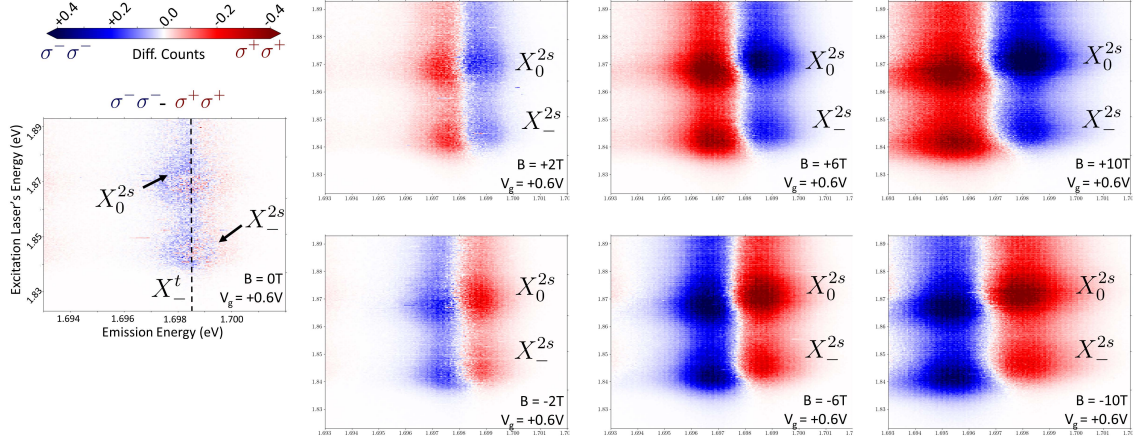


Figure 7.6: Same data presented in Fig. 7.5 except while monitoring the  $X_-^t$  emission energy. We see the exact same behavior, but without contamination from the phonon lines that are present in the  $X_0$  data. Laser power fixed at 70 uW, spot size of 1 um, and collection time of 60 seconds.

## 7.4 Magneto-photoresponse of the 2s Exciton Species

We turn our attention to extracting the behavior of the  $X_0^{2s}$  and  $X_-^{2s}$  from the PLE data with applied magnetic field presented in Fig. 7.6. Integrated vertical cross-sections of the  $X_-^t$  emission channel presented in Fig. 7.7(A, B) show the response of the  $\pm K(\sigma^\pm\sigma^\pm)$  valleys with an applied external magnetic field. The extracted peak centers from fitting the peaks to a voigt profile are marked with black dots [18]. Applying a magnetic field breaks the time-reversal symmetry in the system, and results in a red/blue shift with positive field for the  $+K/-K$  valley and vice versa with applied negative field [30, 60].

Using the definition for the Zeeman splitting in terms of polarization components,

$$\Delta E_Z = E^{\sigma^+\sigma^+} - E^{\sigma^-\sigma^-} = g\mu_B B, \quad (7.1)$$

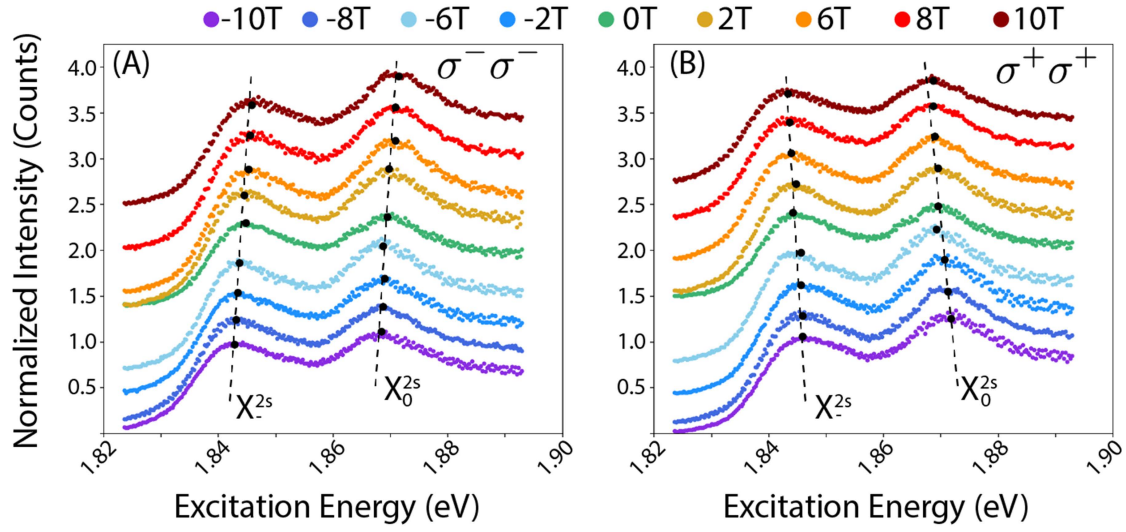


Figure 7.7: Vertical cross-sections from the  $X_t$  emission channel as a function of field for (A)  $(\sigma^- \sigma^-)$  and (B)  $(\sigma^+ \sigma^+)$  marked with the corresponding peak positions (black dots) for the  $X_0^{2s}$  and  $X_-^{2s}$  states from fitting with the dashed line serving as a guide to the eye [18].

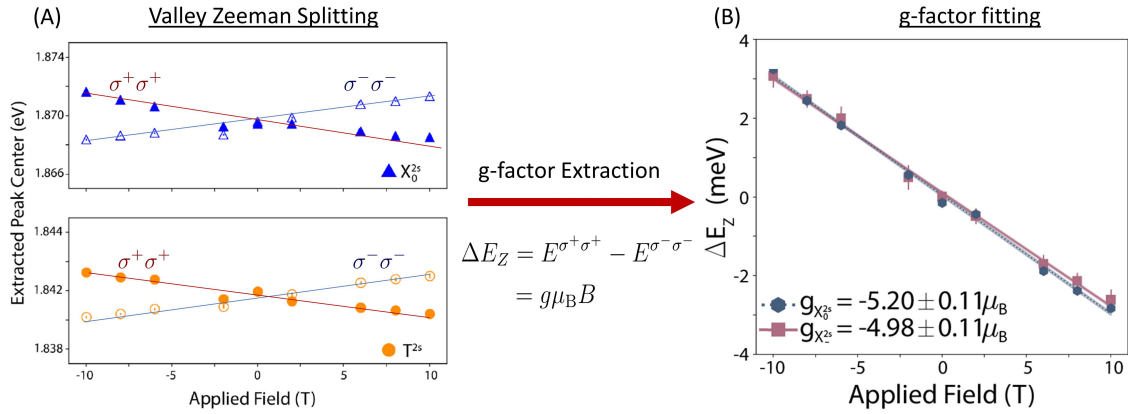


Figure 7.8: (A) Extracted peak positions for  $X_0^{2s}$  and  $X_-^{2s}$  vs magnetic field from data presented in Fig. 7.7. This is the valley Zeeman splitting of both  $2s$  exciton species. (B) Extracted  $g$ -factors for  $X_0^{2s}$  and  $X_-^{2s}$  states. The thickness of the fit line in panel (B) corresponds to the error in the fit [18].

we fit a linear model to our data and extract a  $g$ -factor of  $-5.20 \pm 0.11 \mu_B$  and  $-4.98 \pm 0.11 \mu_B$  for  $X_0^{2s}$  and  $X_-^{2s}$ , respectively. This fit and extracted difference is shown in Fig. 7.8(C). Results that agreed within experimental error were found for both  $X_0^{2s}$  and  $X_-^{2s}$  for a similar analysis of the  $X_-^s$  emission channel, Fig. 7.9.

Frequently, a single-particle model is used to interpret the  $g$ -factor for  $1s$  excitons. In this model, the contributions to the Zeeman splitting are defined as  $\Delta E_Z = -\vec{\mu} \cdot \vec{B}$ . The magnetic moment  $\vec{\mu}$  is composed of additive terms for the orbital and spin contributions (intracellular components  $\mu_O, \mu_S$ ) along with a correction for the effects of the finite Berry curvature in the system (valley or intercellular component  $\mu_V$ ) [35, 63, 76, 77, 85] in each relevant band. Within this interpretation, we expect  $g_{X_0} \approx -4.4 \mu_B$  and  $-11 \mu_B < g_{X_-^{t/s}} < -4 \mu_B$  (depending on the method used to calculate  $\mu_V$ , and whether the doublet is resolved [30, 58, 74]).

To serve as a reference point between the literature and our  $2s$  results, we also extracted the  $g$ -factors for  $X_0$  and  $X_-^{t/s}$ , Fig. 7.10. These values are  $g_{X_0} = -4.22 \pm 0.04 \mu_B$ ,  $g_{X_-^t} = -4.12 \pm 0.04 \mu_B$ , and  $g_{X_-^s} = -3.86 \pm 0.05 \mu_B$  in our system at  $V_g = 0.6$  V. They are consistent with the results from the single particle interpretation, but highlight a distinct increase in our  $2s$   $g$ -factors with respect to the corresponding  $1s$  states. We discuss two possible contributions to this enhancement.

(I) Enhancement of the  $g$ -factor for the  $2s$  neutral exciton has been observed in magnetic Rydberg measurements in both intrinsic and electrostatically neutral samples [5, 7, 86]. Since the observation in neutral samples rules out doping effects, the divergence from  $g_{X_0} \approx -4.4 \mu_B$  has been attributed to enhanced intercellular contributions arising from the increased  $k$ -space localization of the wavefunctions with each subsequent  $n$

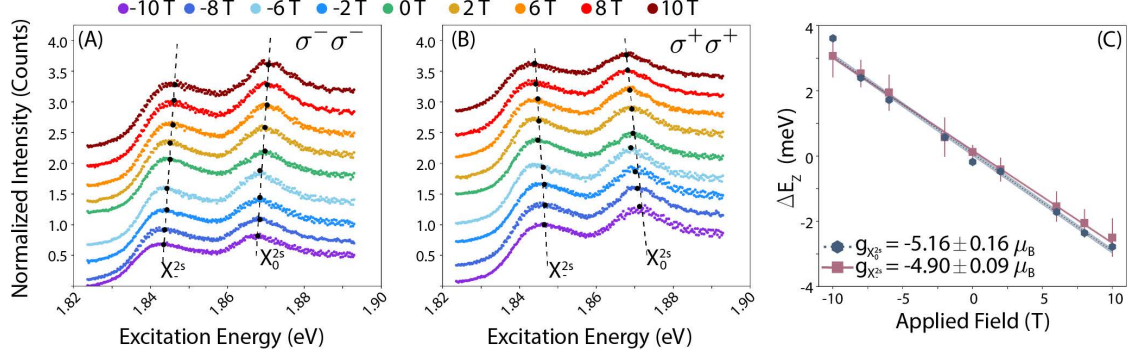


Figure 7.9: Vertical cross-sections from the  $X_s$  emission channel as a function of field for (A)  $(\sigma^-\sigma^-)$  and (B)  $(\sigma^+\sigma^+)$  marked with the corresponding peak positions (black dots) for the  $X_0^{2s}$  and  $X_-^{2s}$  states from fitting with the dashed line serving as a guide to the eye [18] (C) Extracted  $g$ -factors for  $X_0^{2s}$  and  $X_-^{2s}$  states. The thickness of the fit line in panel (B) corresponds to the error in the fit [18].

[5]. Extending this technique to charged excitons gives an intercellular component that *decreases* as the Bohr radius *increases*. This is compounded by an increased  $k$ -space localization of the charged exciton [18]. While this model could explain the results for  $X_0^{2s}$  it would underestimate the  $g$ -factor for  $X_-^{2s}$ .

(II) A second possibility is the onset of many-body interaction (polaron picture) between the excitons and the emerging Fermi sea from electrostatic gating. Many-body interactions are expected to be very favorable in  $\text{WSe}_2$  which has a Wigner-Seitz radius greater than 1 even at extremely high densities [79, 87]. The interaction strength will vary with the Fermi sea's population and the Bohr radius, and induces Fermi sea polarization. Carrier dependent enhancement of the  $g$ -factor in TMDs has been documented for many materials/quasiparticles, with the strength of enhancement dictated by the degree of the induced Fermi sea polarization [53, 60, 78, 79].

In the many-body picture, it has been observed that as doping levels are varied there



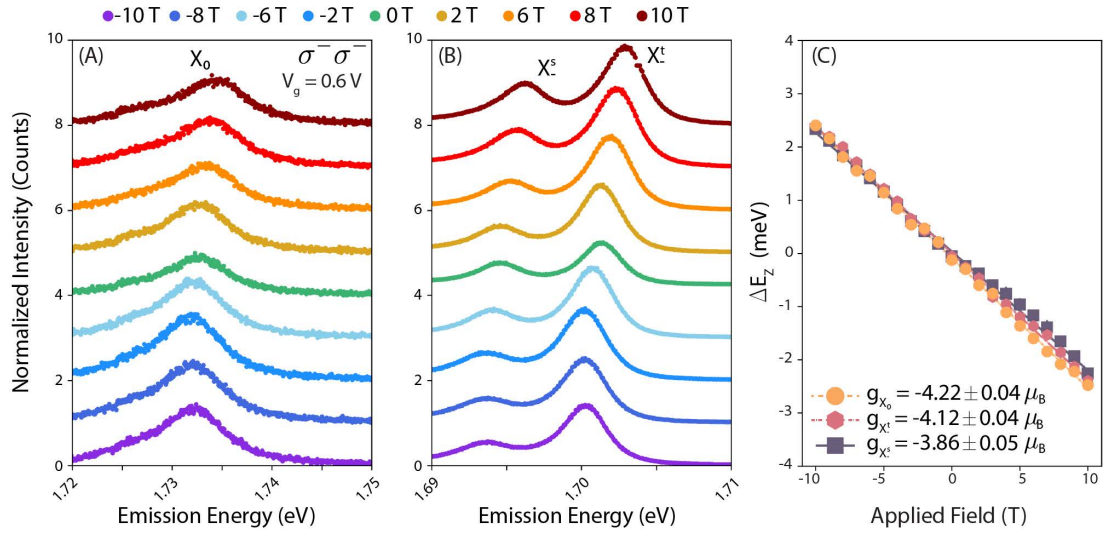


Figure 7.10: (A)  $1s$  exciton emission PL at  $V_g = 0.6$  V for  $X_0$ , (A), and  $X_{t,s}^-$ , (B). Valley Zeeman splitting was extracted from the peak positions and plotted in (C) from which their  $g$ -factors are extracted [18]. Data collected using a 633 nm HeNe with its power fixed at 70 uW, spot size of 1  $\mu$ m, and collection time of 60 seconds.



is a convergence of the  $g$ -factor between competing quasiparticles (e.g.  $X_0$  and  $X^-$ ) in regions in which they coexist. In analogy to the Kondo effect, the impurity (exciton) is dressed with either an attractive or repulsive interaction with the Fermi sea. As carrier density increases, the state dressing will become more similar for all exciton species – regardless of the type of interaction – resulting in a convergence of the  $g$ -factors [78] for  $X_0$ -like and  $X_-$ -like excitons. Such behavior is not expected to be limited to the  $1s$  state excitons and can explain the convergence of our extracted values of  $g$  for the  $X_0^{2s}$  and  $X_-^{2s}$  within experimental error.

## Chapter 8: Conclusion

In this dissertation, we have confirmed the existence of a negatively charged  $2s$  exciton with finite oscillator strength using both PL and PLE. As PLE has been shown to have superior signal-to-noise ratio to PL, we conducted magnetic dependent PLE measurements of the  $2s$  neutral and negatively charged exciton. From this, we were able to extract a corresponding  $g$ -factor for these states.

Our results serve as the first marker in mapping the behavior of the  $2s$  charged state,  $X_{-}^{2s}$ , with magnetic field in TMDs. The stability of the  $X_{-}^{2s}$  state offers a possible medium for studying the cross-over from exciton Rydberg physics to the quantum Hall regime for charged species at high magnetic fields. Recent work by Klein *et al.* used carrier density dependent  $g$ -factor measurements to demonstrate tunable many-body physics through all  $1s$  exciton species in  $\text{MoS}_2$  [78]. Our initial results indicate that it would be possible to produce this type of map for  $2s$  species with access to higher magnetic fields and devices with larger dynamic carrier density range. This opens up a unique opportunity to study many-body interactions in higher energy exciton species that is generally limited in traditional semiconductors systems with smaller exciton binding – like GaAs quantum wells.

In addition to the extraction of the  $g$ -factor of the  $2s$  excitons in the  $n$ -doped regime,

significant effort was placed in the design and construction of the state-of-the-art ultra-low temperature free space dilution refrigerator capable of making optical measurements at  $< 30$  mK. The design and assembly of all of our custom probe system, our custom sample holder, and the non-magnetic aluminum optical breadboard are described in detail in the appendices. We spent years constructing and optimizing our ultra-low temperature optics lab. I am happy to report the results discussed in this dissertation as they represent the culmination of all of the time and effort we put into the design of our measurement laboratory. From designing and optimizing the BlueFors dilution refrigerator, monitoring equipment to avoid magnetic path shifts of our optics, and re-assembling and programming a 13-year old dye laser, each step slowly got us closer to our goal of making these measurements possible. I look forward to seeing all of the future results that will come out of this lab.

## Appendix A: BlueFors Procedures

### A.1 Introduction to BlueFors

The BlueFors dilution refrigerator is currently the most important measurement system in our lab and was used in all of the measurements in the main text. Knowing how to operate and modify this system is crucial for future measurements with this system. In this Appendix, I will outline all of the procedures necessary to operate the BlueFors dilution refrigerator and make non-warranty specific modifications. Note that any procedure that involves the main cryostat should have two people to disassemble (or assemble) the BlueFors to avoid damage.

If there are any issues that are not covered in this dissertation, contact **support@Bluefors.com**. Note: They do not have any optics experience and are unable to provide any support involving such measurements (this may one day change, but currently this is the case.)

All optics in the systems are custom designed, machined, and gold-plated by our lab. Additional optical components will require similar effort to add to the system. The Markforged Onyx 3D printer is your ally in designing new components. Onyx is the only plastic that works reliably at low temperatures and can be used to prototype designs before having them machined out of copper and then gold-plated.

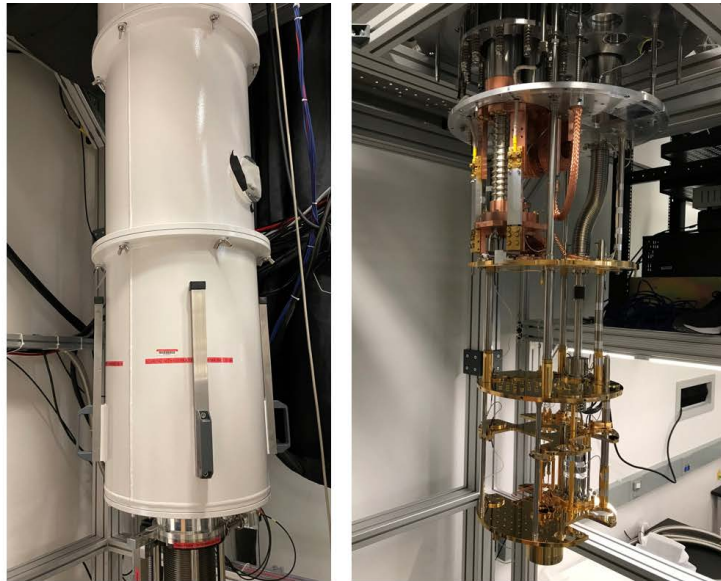


Figure A.1: Images of the BlueFors dilution refrigerator fully sealed and fully open.

Tools and equipment utilized in these procedures should be located on the wall to the left of the BlueFors and are shown in Fig. A.2. The most commonly utilized tools are the electric drill and the items located in the probe screw holder. The holder was 3D printed to hold the probe screws, the hex drivers for the drill, and the graphite used to lubricate the probe. The drill should be set to a torque of 12-15 when tightening screws. Currently, there is a laptop with all of the BlueFors software that is connected to the BlueFors controller cabinet. This computer can be operated remotely.

If anything is missing, the remaining tools for the BlueFors that are less commonly used are in the black tool cabinet in the corridor. There are also the tools necessary to work on the Cryomech compressor in this cabinet.

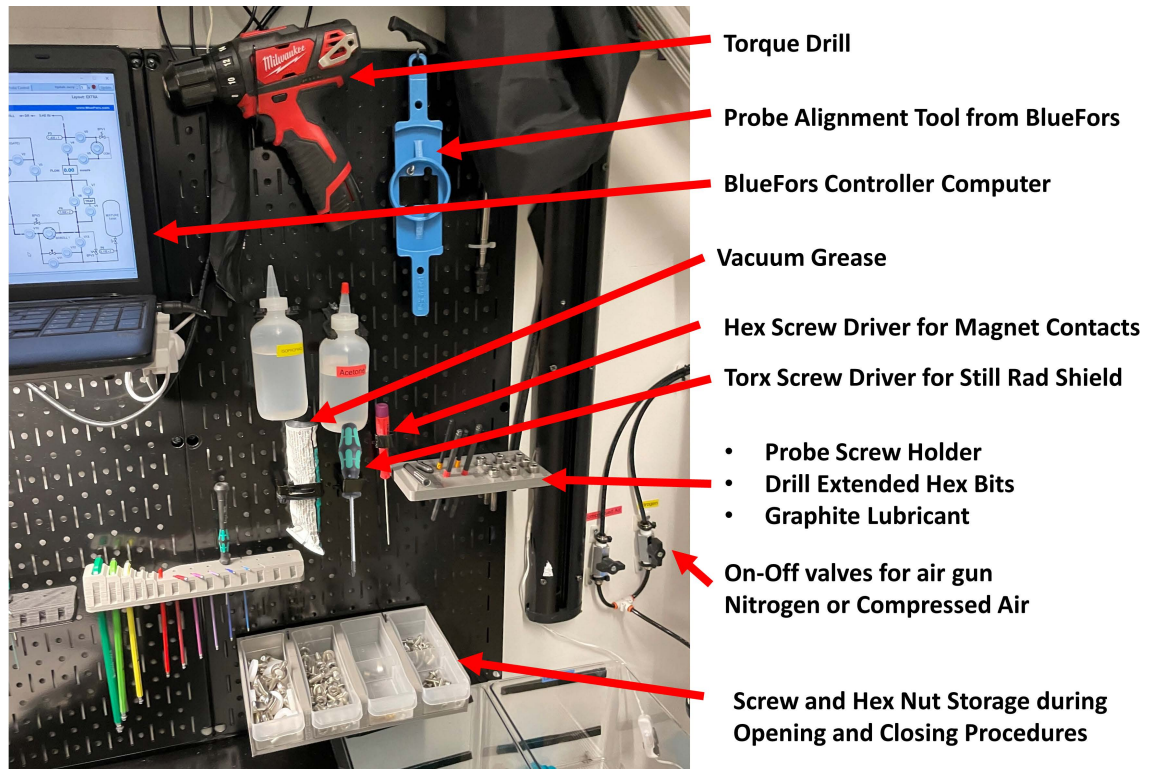


Figure A.2: Various tools that are used while working on the BlueFors.

## A.2 Gas Handling System Configurations and Schematics

This section outlines some of the most commonly used pump and valve configurations of the the Gas Handling System (GHS) in the BlueFors procedures discussed in the next few sections.

1. Fig. [A.3](#) – **All Valves Off**
2. Fig. [A.4](#) – **Start Condensing**
3. Fig. [A.5](#) – **Normal Circulation**
4. Fig. [A.6](#) – **Stop Condensing**
5. Fig. [A.7](#) – **Pump Probe Bellows**
6. Fig. [A.8](#) – **Vent Probe Bellows**
7. Fig. [A.9](#) – **Pump Vacuum Can**
8. Fig. [A.10](#) – **Vent Vacuum Can**
9. Fig. [A.11](#) – **Pump LN2 Trap**

ALL VALVES OFF

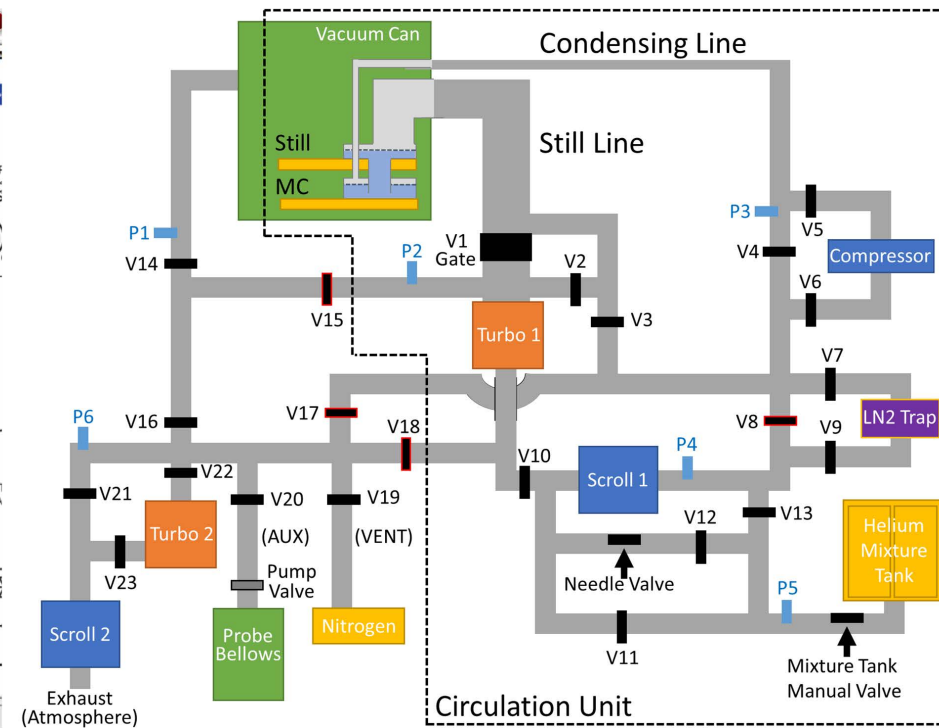
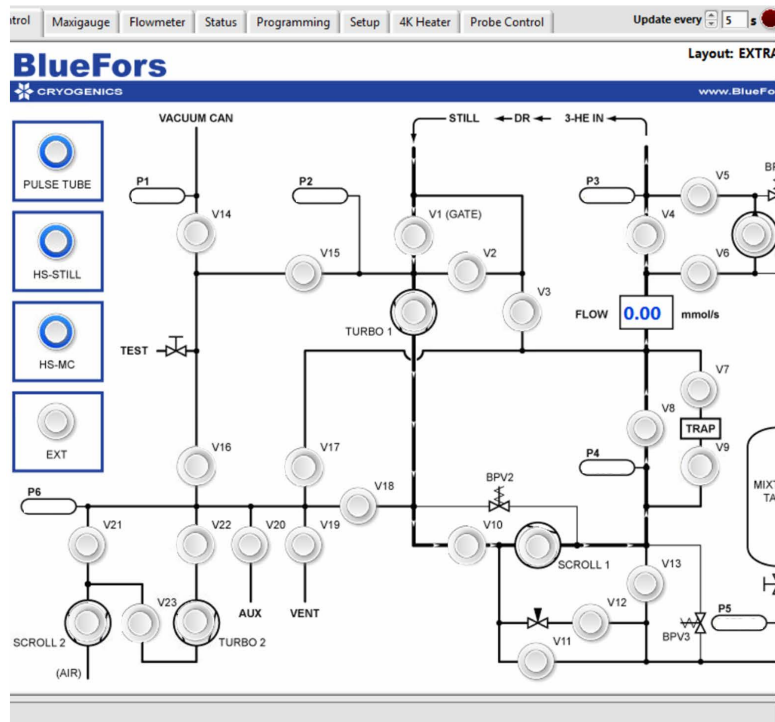


Figure A.3: GHS with all valves closed.



### Start Condensing

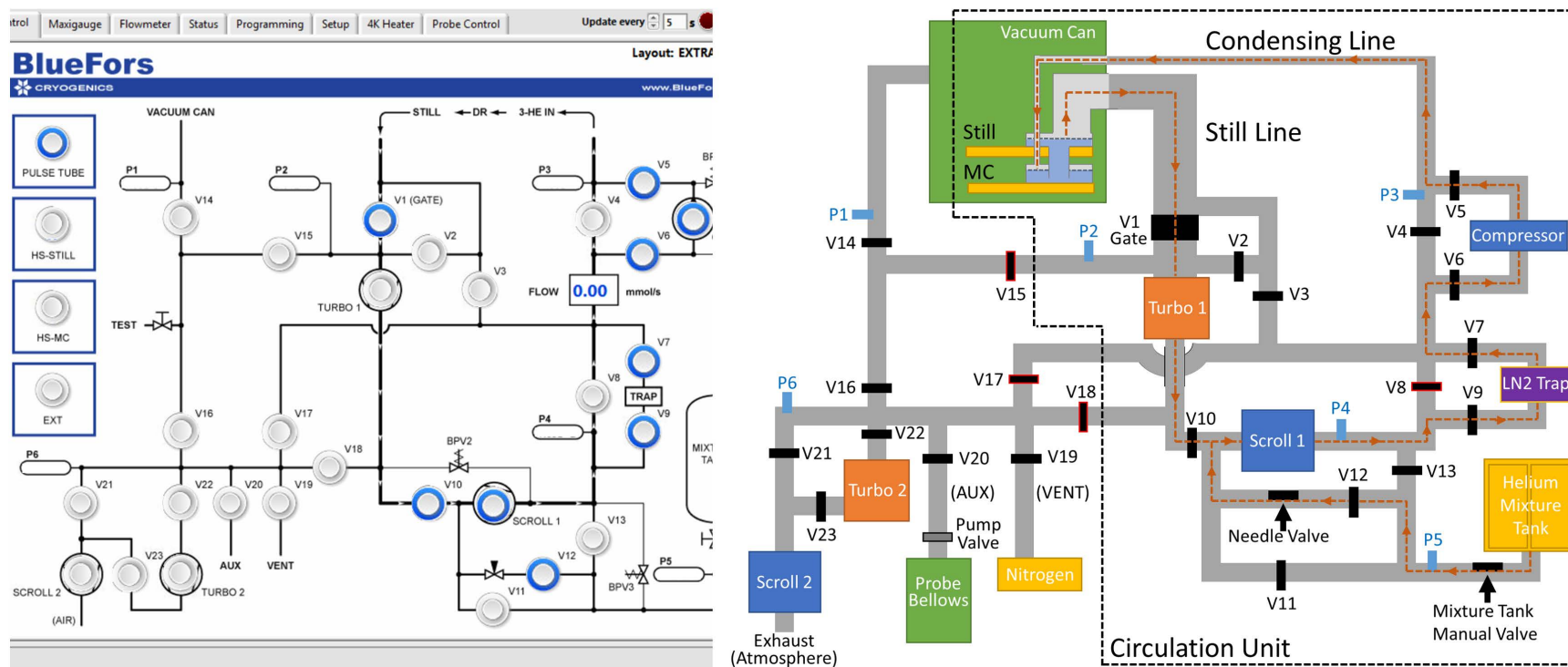


Figure A.4: GHS configuration to start condensing the helium mixture into the Still and Mixing Chamber. This procedure is automated and does not need to be done manually unless there is some issue.

### Normal Circulation

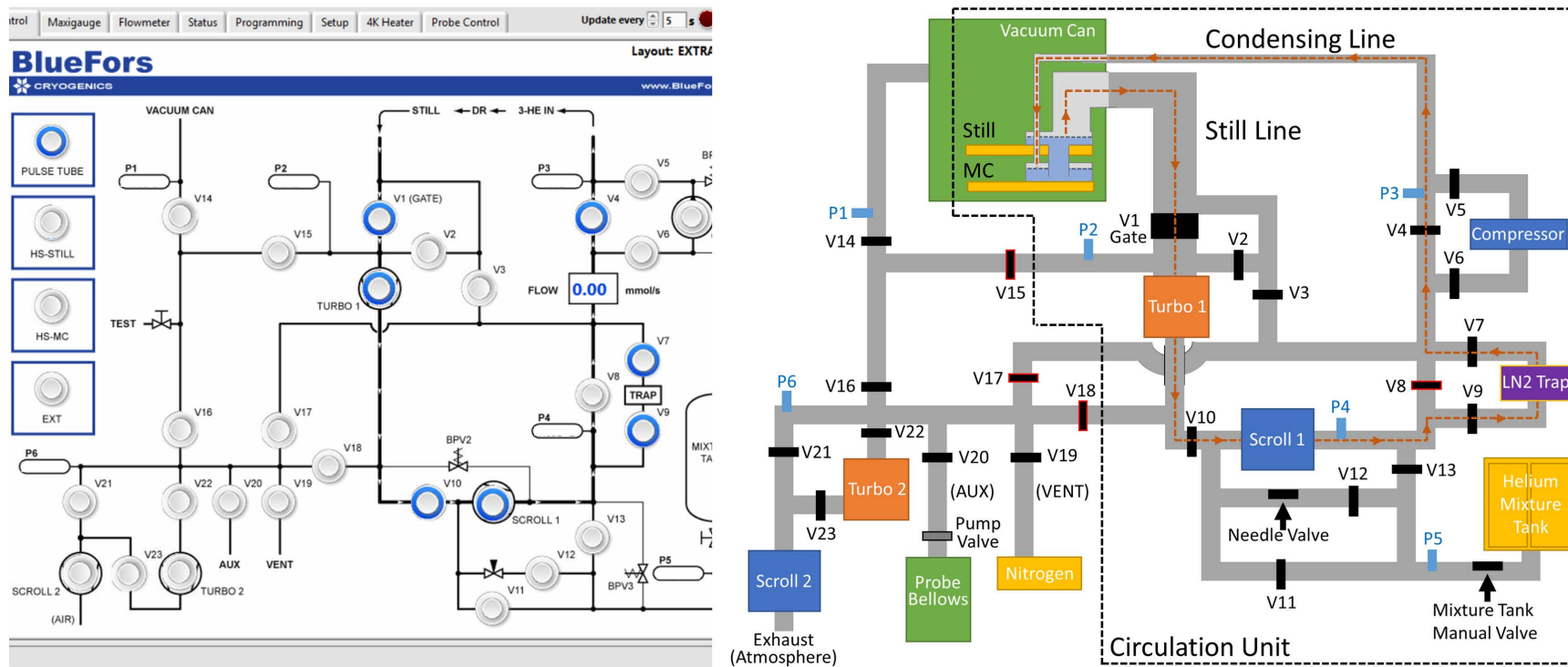


Figure A.5: GHS configuration as the dilution unit circulates  $^3\text{He}$  in normal circulation.

## Stop Condensing

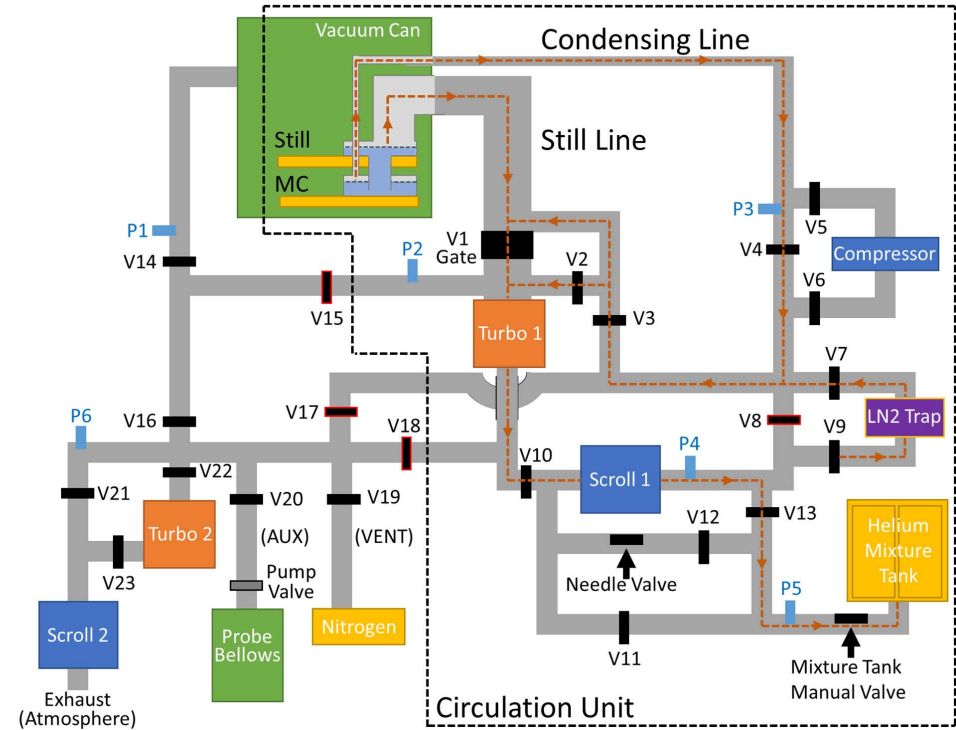
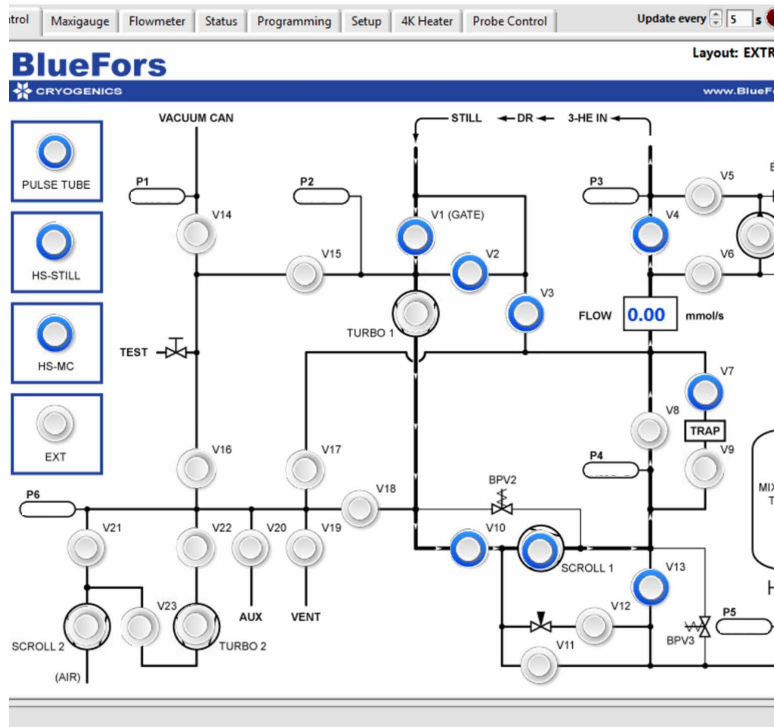


Figure A.6: GHS configuration to stop condensing. The helium mixture is being pumped out of the Still and Mixing Chamber and back into the helium reservoir.

## Pump Probe Bellows

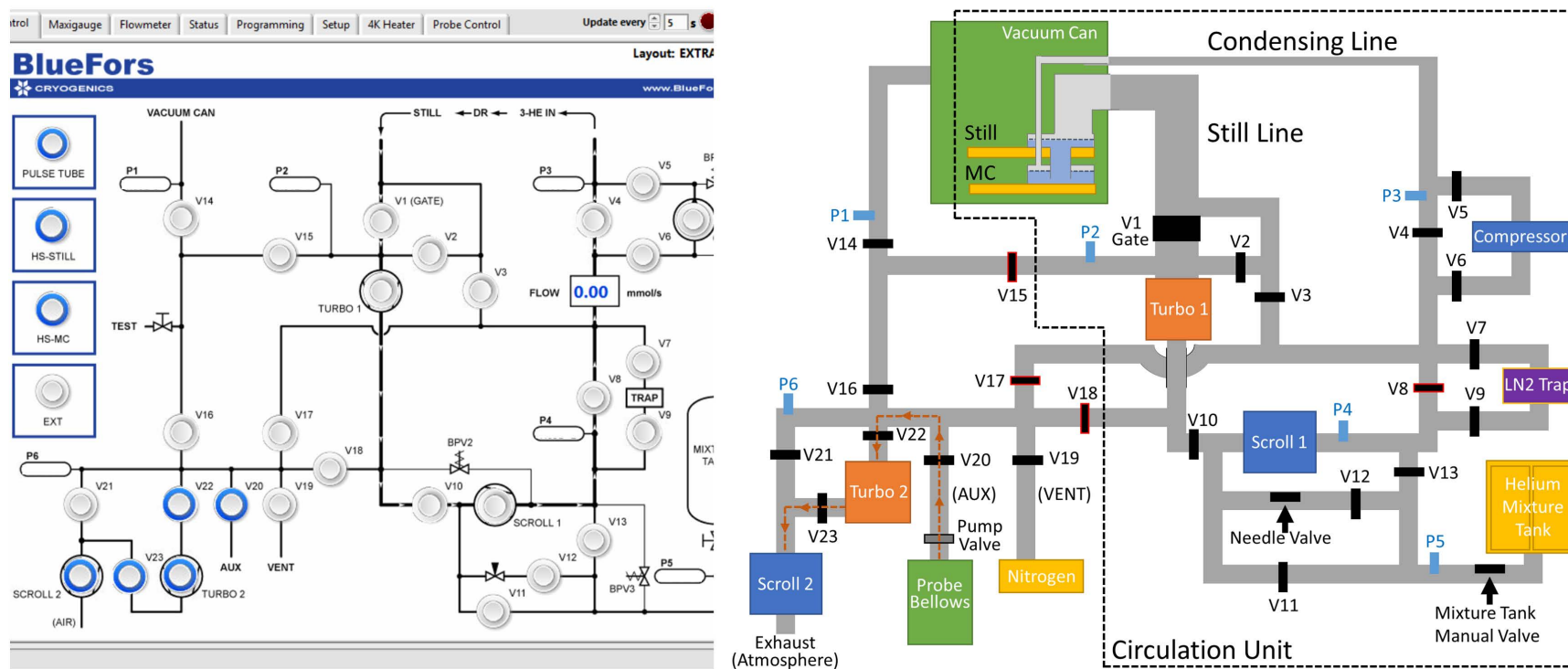


Figure A.7: GHS configuration to pump on the probe bellows. Note: You must also open the Pump Valve from the Probe Control tab on the software.

## Vent Probe Bellows

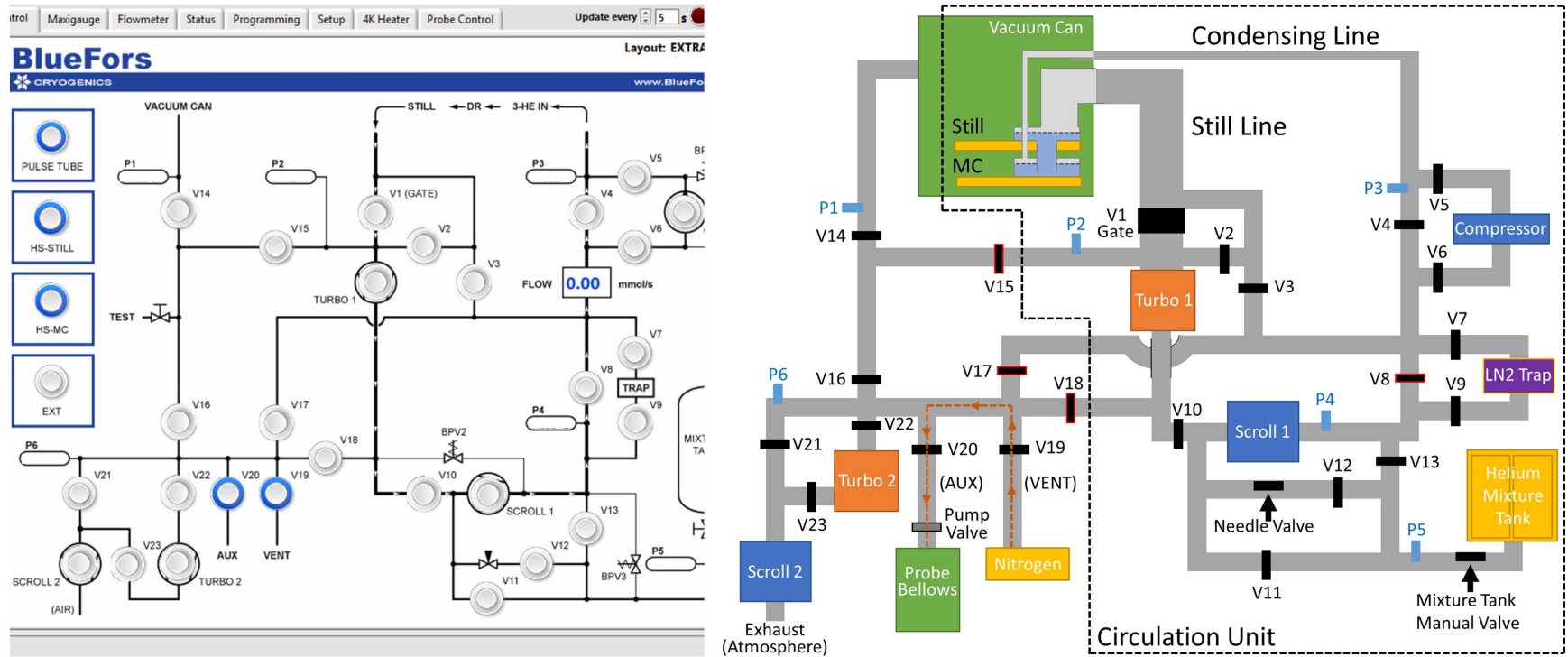


Figure A.8: GHS configuration to vent the probe bellows. Note: You must also open the Pump Valve from the Probe Control tab on the software and the Nitrogen needle valve must be manually opened.

### Pump Vacuum Can

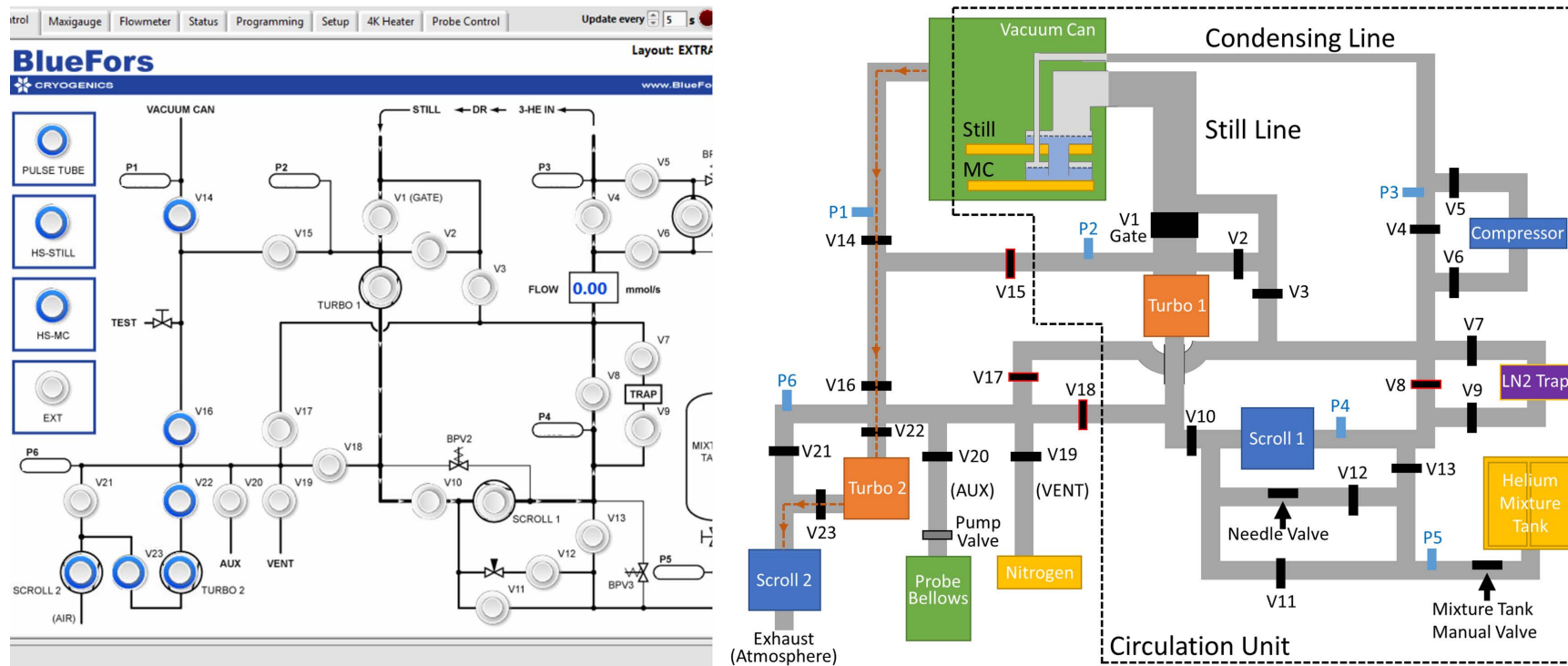


Figure A.9: GHS configuration to pump the vacuum can.

### Vent Vacuum Can

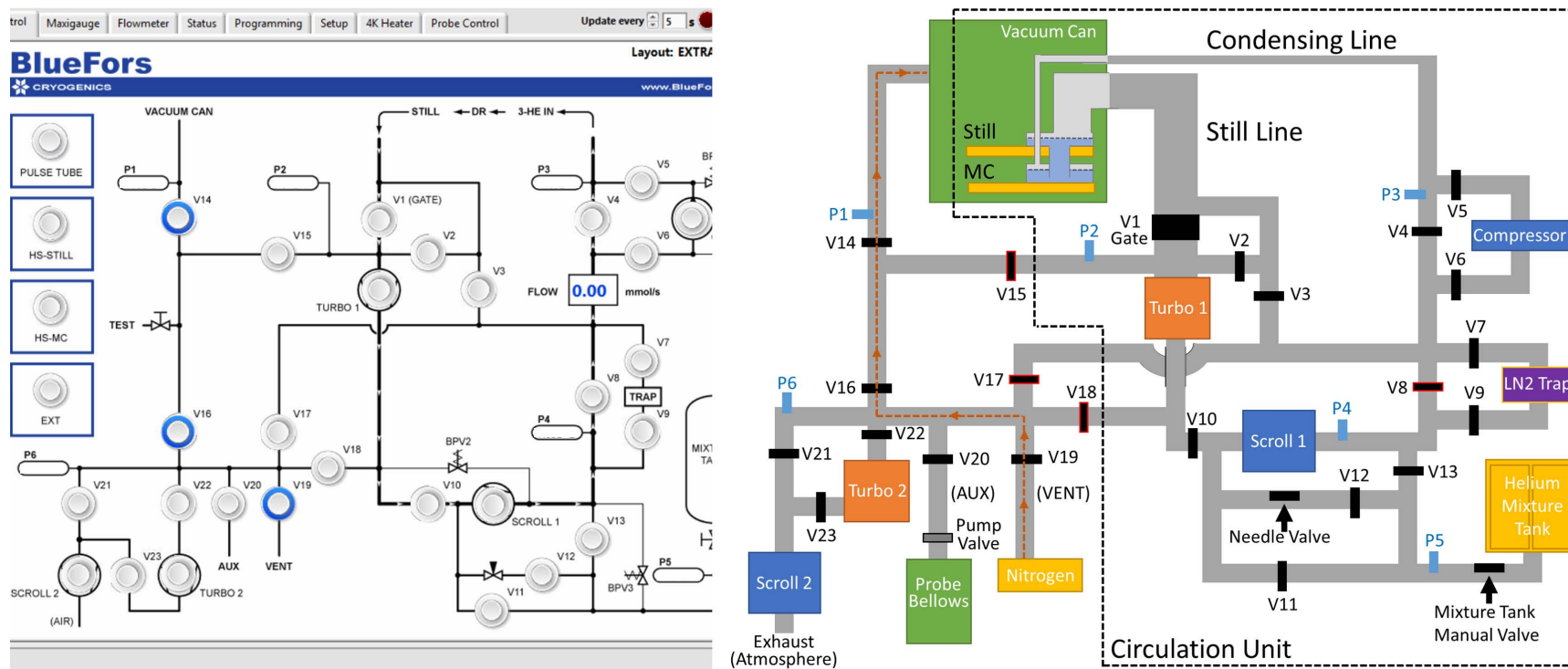


Figure A.10: GHS configuration to vent the vacuum can. Note: P1 should be off and the Nitrogen needle valve must be manually opened.



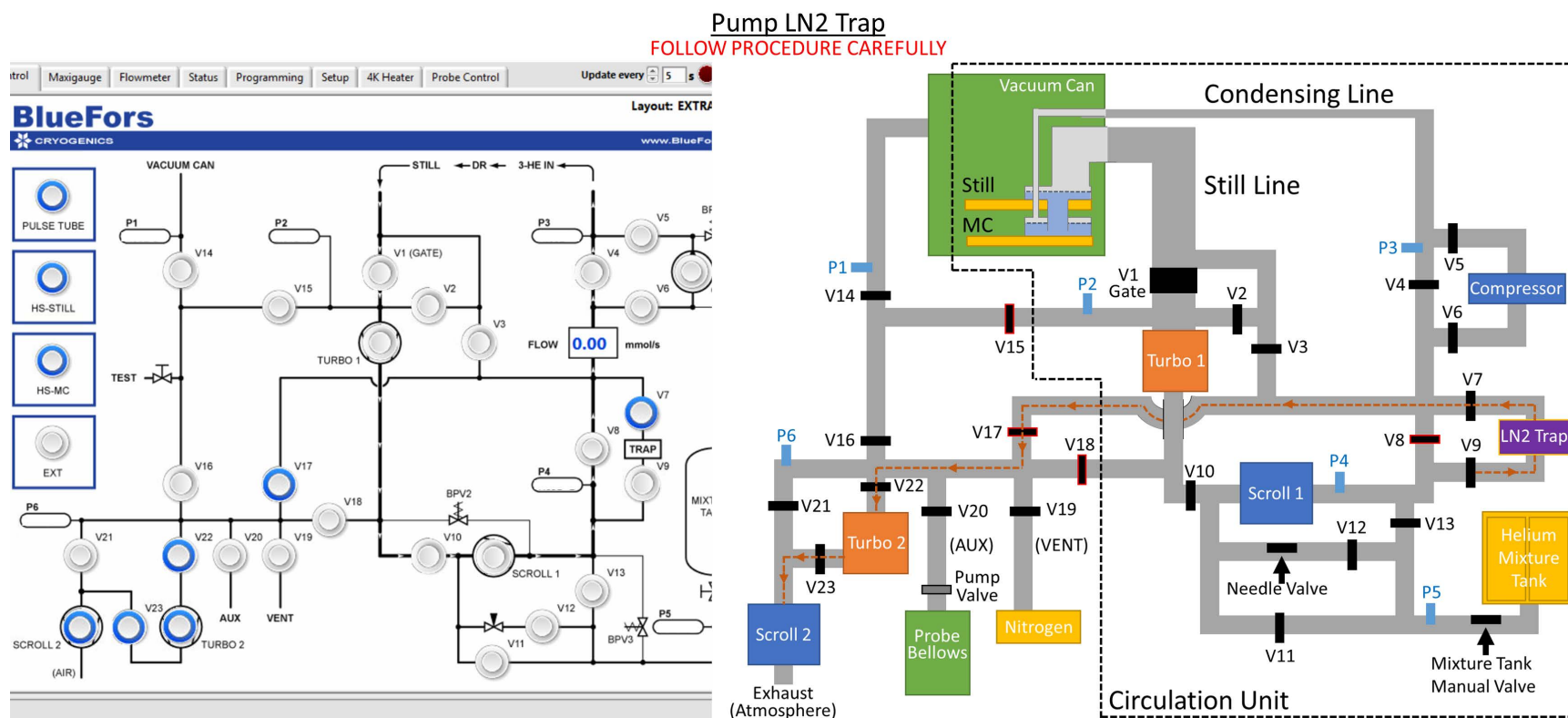


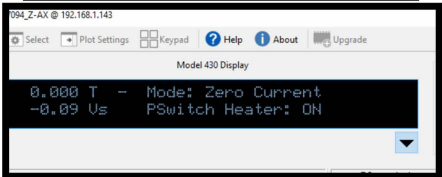
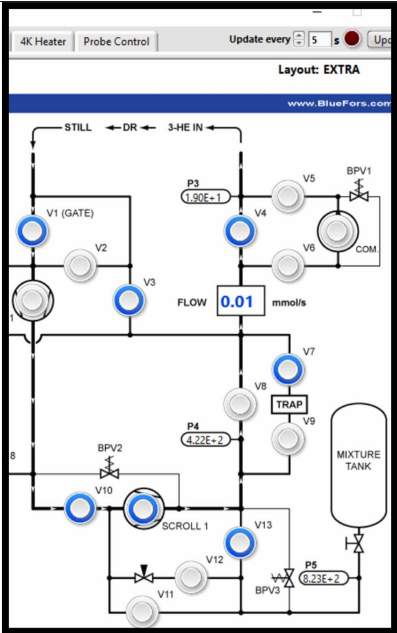
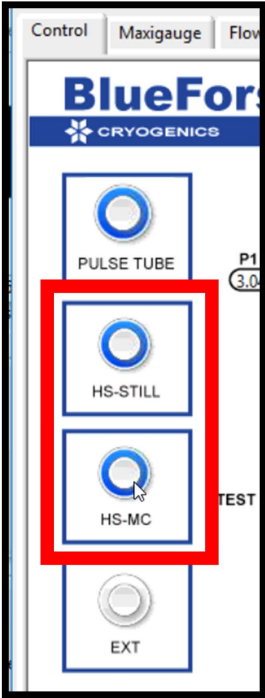
Figure A.11: GHS configuration to pump the LN2 trap when it needs to be cleaned. This is a dangerous configuration because it connects Turbo 2 and Scroll 2 to the closed circulation unit. If you are not careful, helium mixture can be lost. Be sure to follow the steps carefully in the procedure.



### A.3 Probe Procedures:

The first two procedures that I will outline are for unloading and loading the probe from the BlueFors. As these are the two most common procedures used, please follow the checklists each time to avoid making mistakes that might damage the probe system. The checklists can be found at the end of this appendix. The procedures laid out here are meant to clarify details on the checklist that may be unclear. This is not meant as a substitute for the checklist. Be sure to follow the checklist to prevent mistakes from being made during the procedures.

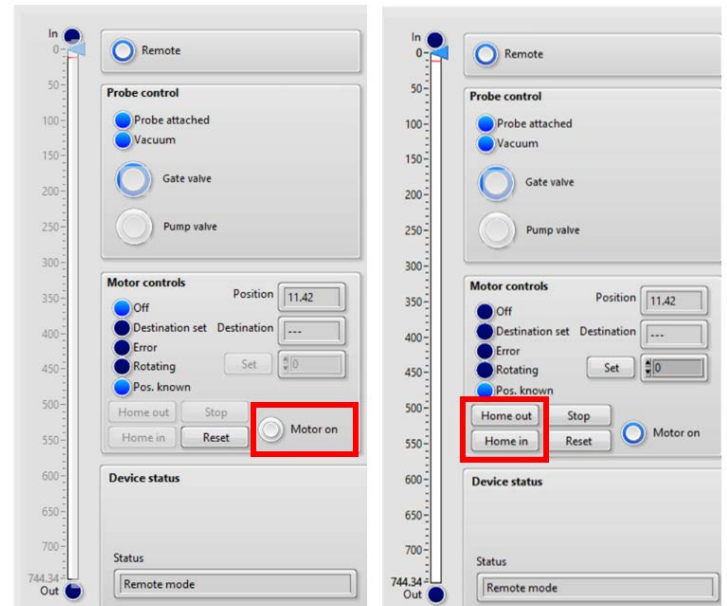
A.3.1 Unloading the Probe

| Details   | Images   |
|---|--|
| <p>1. Make sure that the Dilution Refrigerator is no longer condensing /circulating or the mixture tank is open. Also check that the magnet is set to 0T. Removing the probe will heat up the system and can cause the magnet to quench.</p> <p>(Configuration shown here is pumping any remaining helium in the mixing chamber into the mixture tank.)</p> | <div></div> <div></div> |

2. While the probe is loaded into the BlueFors, it will be isolated from the rest of the probe housing and hanging from the Mixing Chamber flange. This is typically indicated by the probe position being set to 11.43 mm.

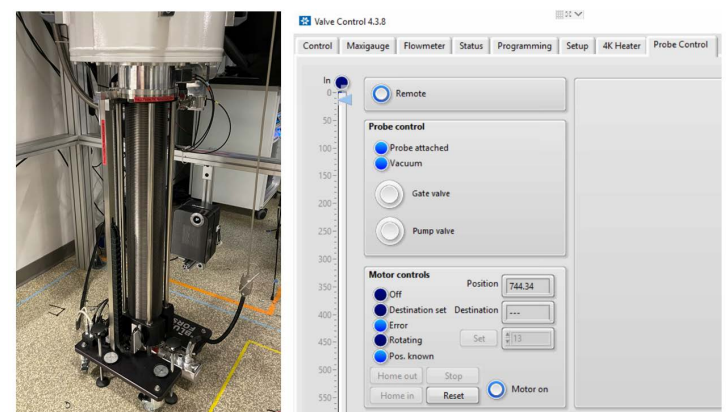
To reconnect the probe to the probe housing, turn on the probe motor and click **Home In**. This will push the probe system to its maximum position inside the BlueFors chamber and reattach the probe to the rest of the probe system, allowing for it to be removed.

**DO NOT PRESS HOME OUT BEFORE THIS STEP!** Doing so would cause the probe to be removed without being re-attached and can severely damage the detachment mechanism.



3. After the probe is reattached, it can be safely removed from the BlueFors. Select **Home Out** and wait until the probe is fully removed from the BlueFors (motor position >744 mm.)

Press the Gate Valve button to close the bottom gate valve. This will isolate the probe bellows from the BlueFors vacuum chamber.

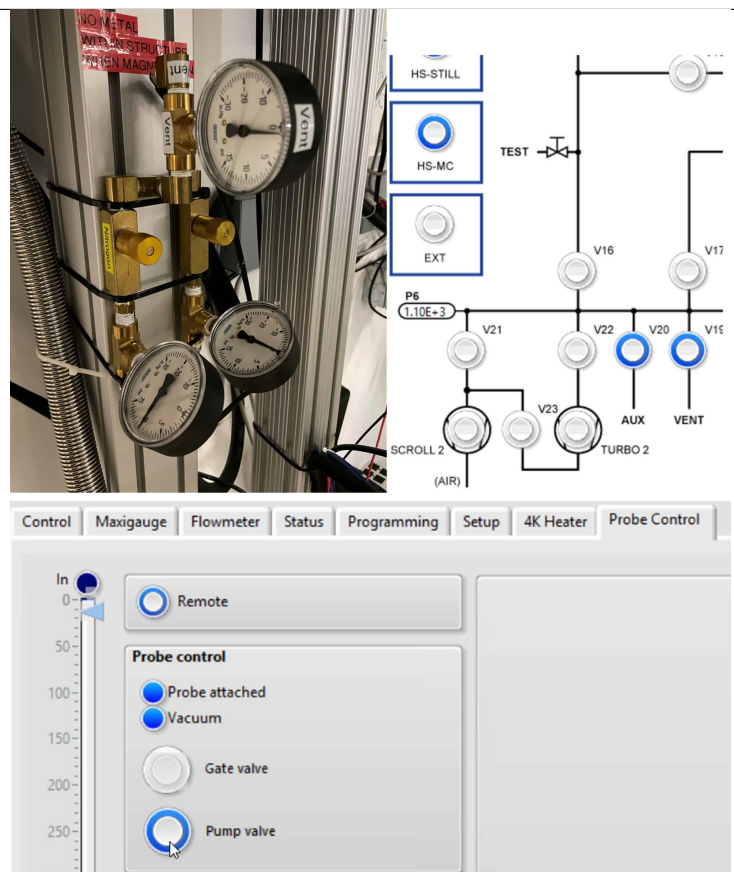


4. There are two methods to warm up the probe:

a) Wait for the Probe to warm in vacuum (one day).

b) Open the **pump valve**, **V19**, and **V20** to inject  $\sim 100$  mBar of nitrogen into the probe bellows. If you are injecting nitrogen, close **V19** when the 100 mBar pressure is reached. The pressure in the probe bellows can be monitored on P6.

After waiting the appropriate amount of time to warm the probe, open the **pump valve**, **V20**, and **V19**. Open the nitrogen needle valve and monitor P6 until it reaches  $>1100$  mBar. Do not over-pressurize the probe bellows.



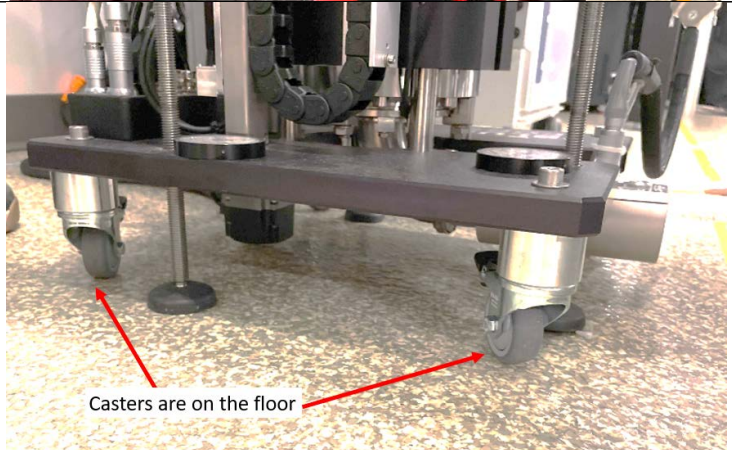
5. Now that the probe is warm and the probe bellows is at atmospheric pressure, lower the three feet to the ground.



6. Unscrew the 6 screws holding the Probe Bellows to the Gate Valve. These screws are M8. Use the red Hex key.

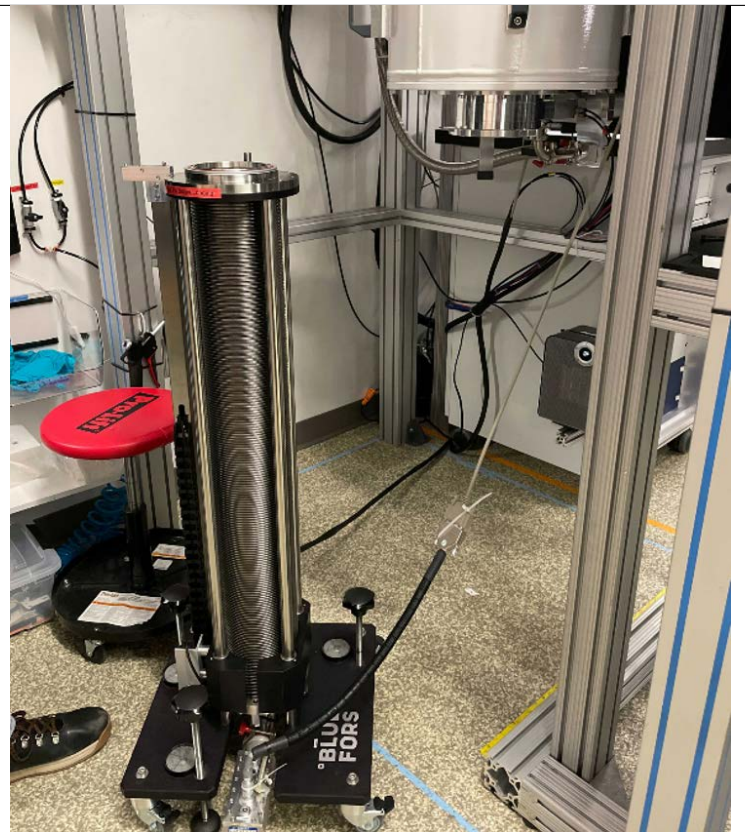


7. Raise the feet (systematically so that they don't get stuck) until the Probe Bellows is on casters and can be moved out from under the BlueFors.



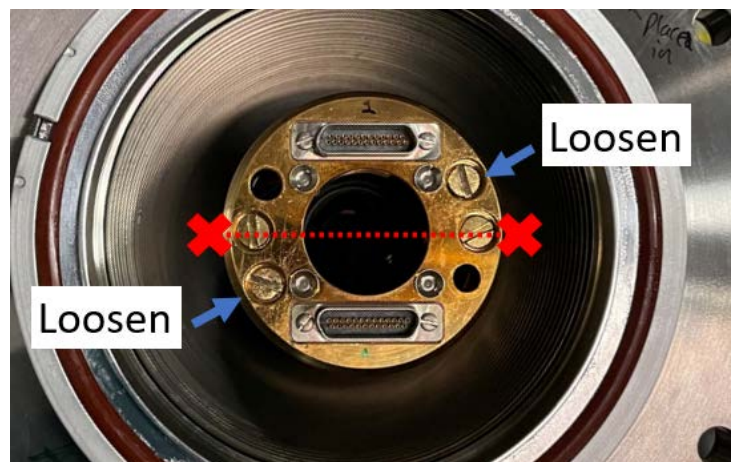


8. Roll the Probe Bellows out from under the BlueFors. Make sure there is clearance above the probe for it to be taken out.



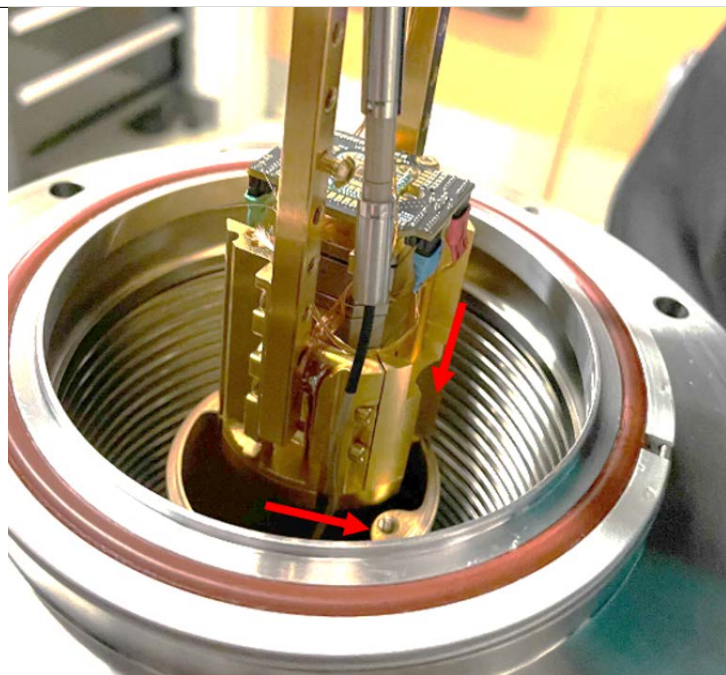
9. Unscrew the two screws that hold the probe head to the radiation shield. These are the off-diagonal screws labeled in the figure. If you look through the viewport of the probe, you can see that screws extend down to the probe's radiation shield.

**NOTE: Make sure to disconnect the correct screws. The other two will drop the probe!**



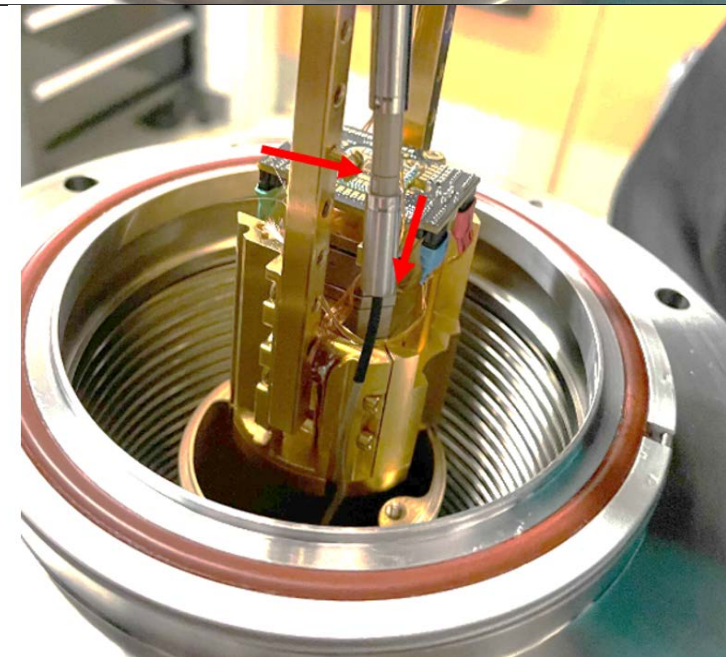
10. Be sure that the orientation of the Attocube holder is correct to be able to remove the probe without hitting the two screw slots on the top of the radiation shield.

**Do not fully remove the Probe just yet!**



11. You must remove the thermometer connector before fully removing the probe. Pull down on the bottom connector.

**NOTE: Do not drop the connector after disconnecting.**





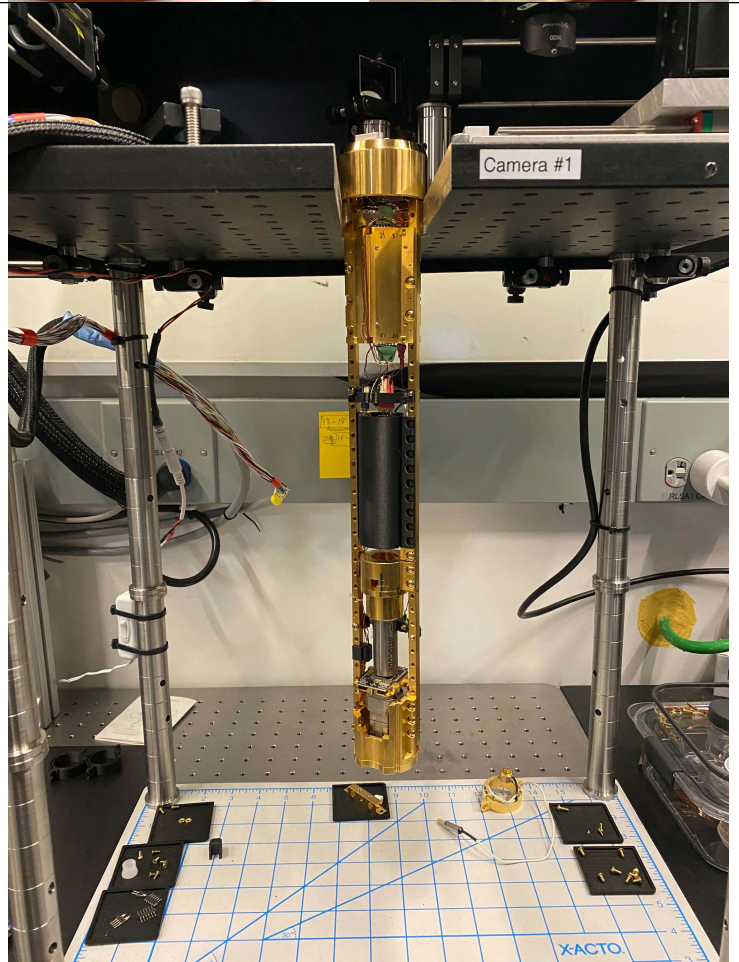
12. Place the bottom connector such that it hangs over the radiation shield and does not fall inside.



13. Place the probe in the machined breadboard. There are two tapped holes on this breadboard that allow for the probe to be securely mounted to the optical breadboard while it is worked on.

This breadboard contains the optics necessary to image through the objective.

**This completes the probe unloading procedure.**





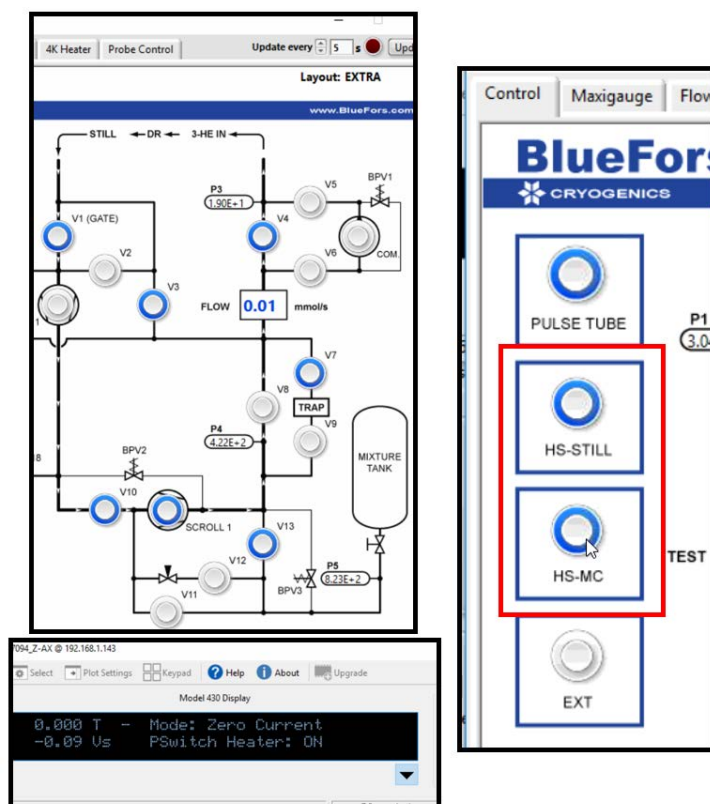
### A.3.2 Loading the Probe

#### Details

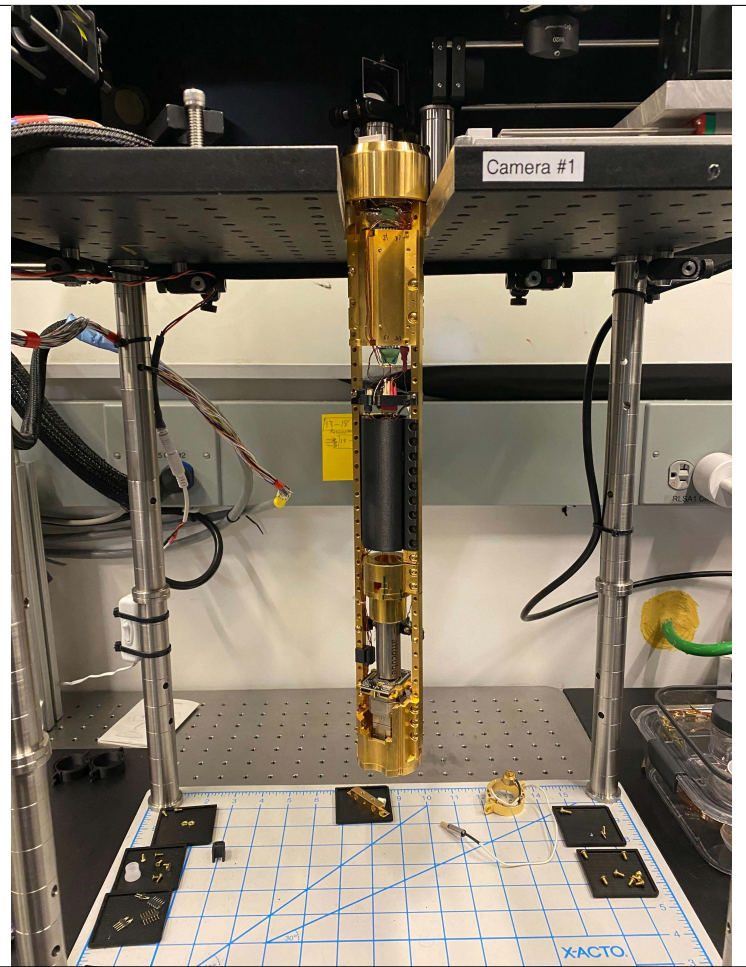
1. Although the system should not be circulating helium nor at a non-zero magnetic field, make sure that it is not condensing /circulating and that the magnet is set to 0T. Loading the probe will heat up the system and can cause the magnet to quench.

Check that heaters **HS-STILL** and **HS-MC** are on. These heaters make thermal contact between the 4k flange and all flanges below it (Still, Mixing Chamber). If they are not ON, the still, mixing chamber, and probe will not cool down to 4k.

#### Images



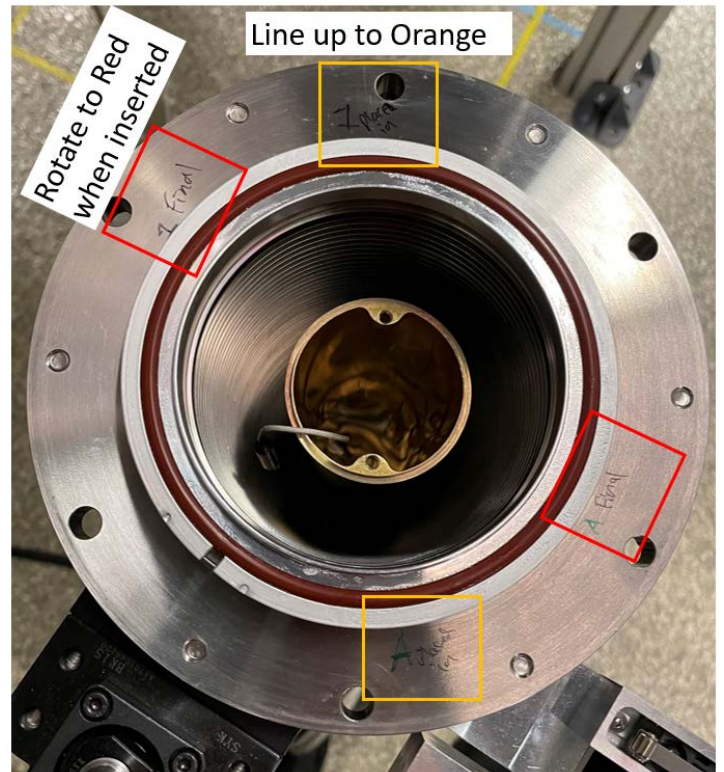
2. Remove the probe from the optical breadboard and carry it to the probe bellows.



3. Notice the orientation of the probe prior to loading it into the bellows. The green **A** and **1** must line up with the green **A** and **1** labeled on the top of the probe when it is inserted. Follow the guides drawn on the top of the probe and on the probe bellows for orienting the probe correctly when loading.

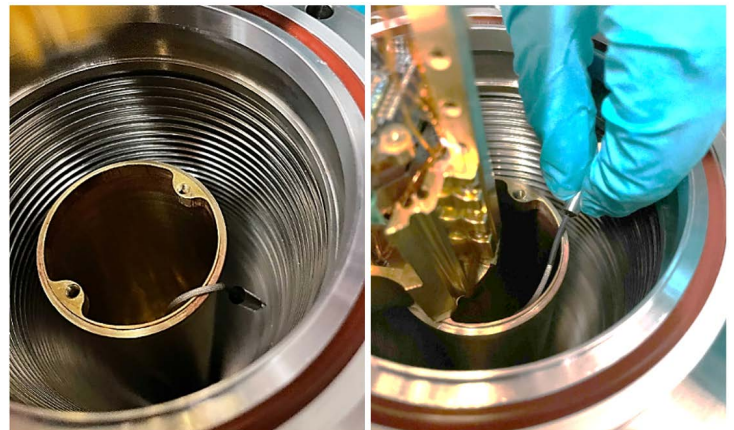
If these are not correct, the probe will not connect to the mixing chamber flange and you will have to unload the probe to re-orient.

A blue 3D printed part supplied by BlueFors can also be used to assure that the alignment is correct.



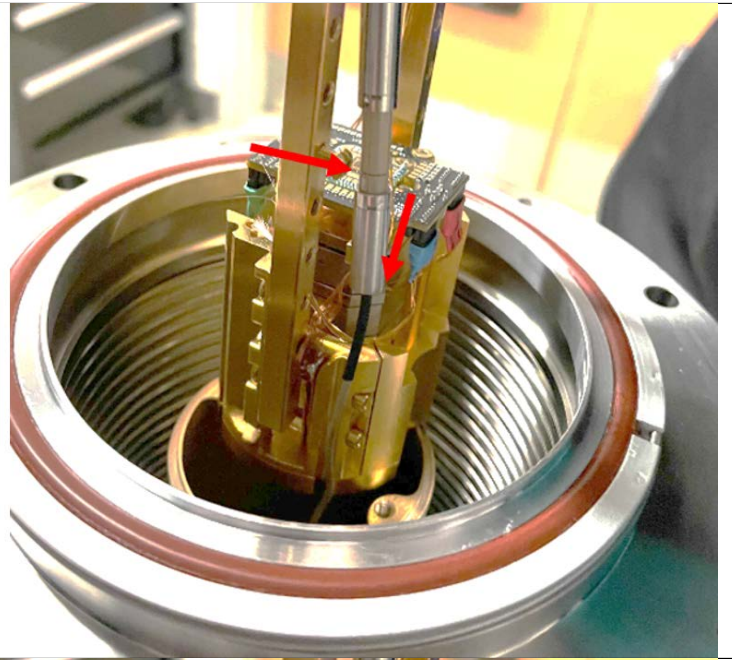
4. Locate the thermometer cable that should have been placed hanging over the probe radiation shield (if you are using the heater, there should also be a heater cable.)

If the cable is not there, it must have fallen into the radiation shield. You can use a magnetic extension arm to retrieve it or you may have to unscrew the radiation shield.

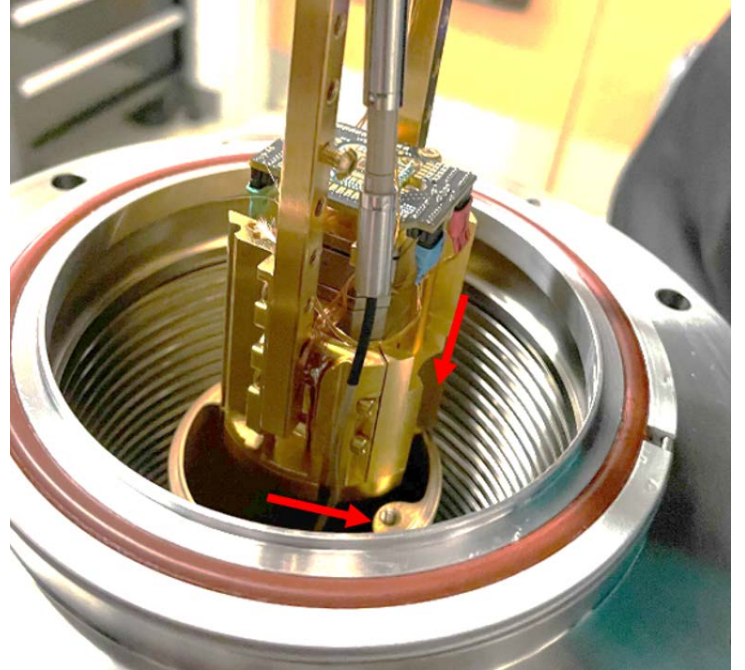




5. Connect the thermometer connectors together. This may be tricky with only one person, but can be done with practice.



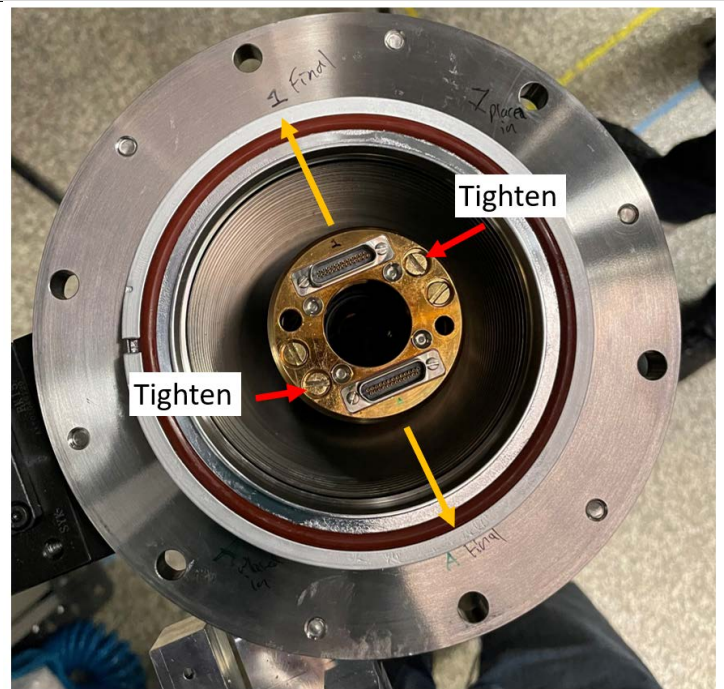
6. Line up the probe such that the bottom piece fits into the radiation shield. Be careful that the two intruding tapped parts do not catch on the sample carriage while loading. This could damage the sample, attocubes, or objective.



7. Twist the probe into place such that the screws on the probe head line up with the tapped holes on the radiation shield.

Note whether or not the **A** and **1** on the probe head and the probe bellows match.

Tighten these screws with a properly sized flat head screw drive.

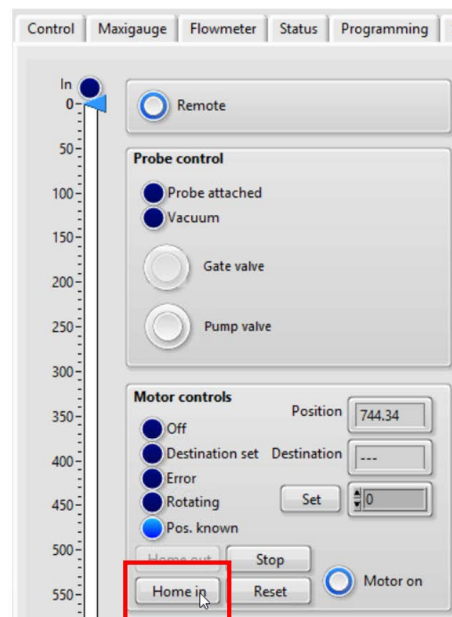


8. Raise the probe to **Home In** until it reaches its full height. There are two important things that must be done while the probe is fully extended out:

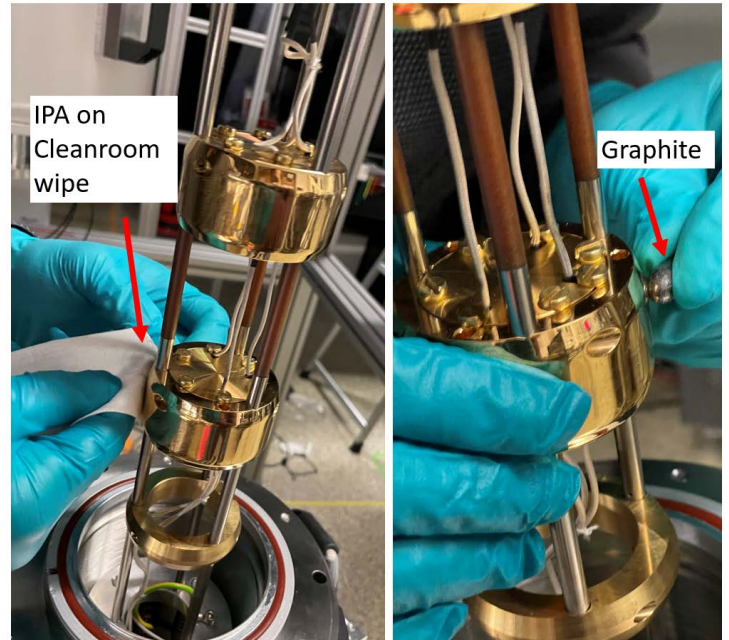
a) Clean each flange with IPA and then coat it with graphite as a lubricant that prevents long term damage to the probe contacts.

b) Locking the detachment pin into place.

These are covered in the next two steps.



9. Clean each flange of the probe assembly with a cleanroom wipe and IPA. Then take the graphite rod and rub it diagonally along the side of each flange. The graphite acts as a lubricant as the probe is loaded into the main chamber. The probe is always slightly misaligned while entering the BlueFors and must be redirected to the correct orientation determined by the internal radiation shields. Most importantly, the graphite prevents scratching of the smooth metallic surfaces on the probe head. The more scratched the probe head becomes, the less thermal contact and the lower its cooling power.

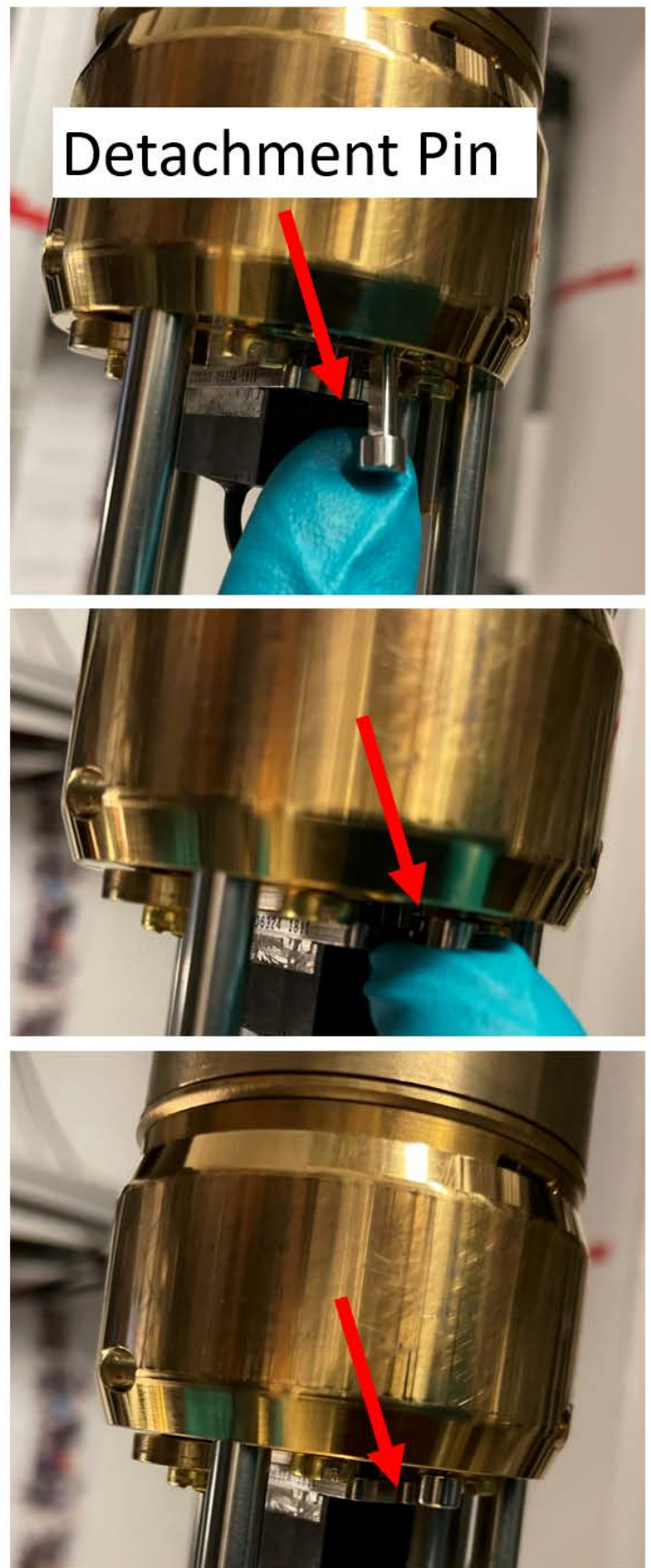




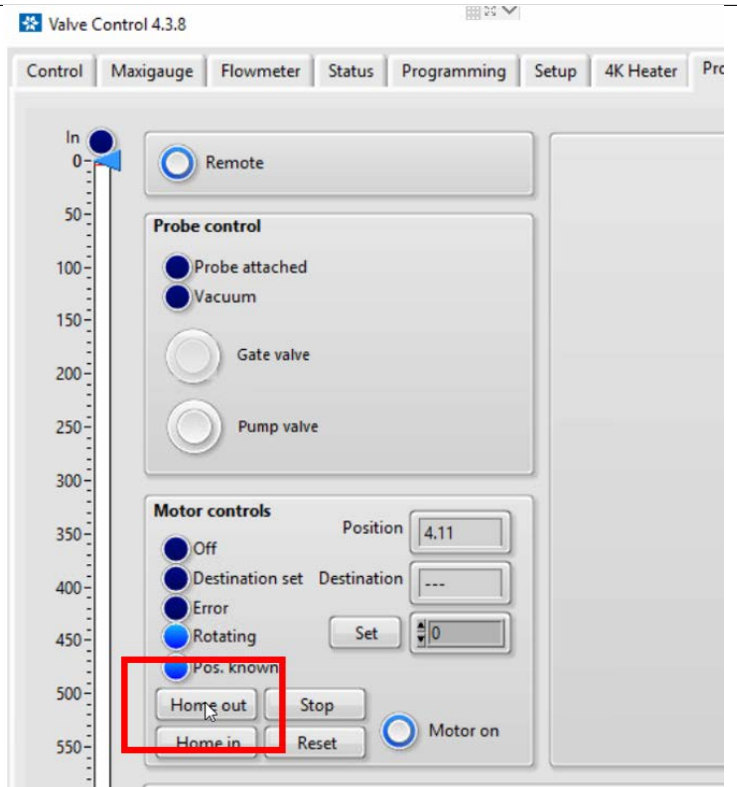
10. This is the most important step in the probe loading procedure!

The **detachment pin** can be found directly underneath the probe radiation shield. This pin **must** be pressed upwards during this step. If the pin is loosely hanging and the probe is loaded into the BlueFors, it will not detach with the assembly. This will significantly reduce the cooling power and add all of the vibrations from the probe assembly.

This step is easy to forget if you don't follow the checklist. If you do not press the **detachment pin**, you will need to remove the probe and start over.



11. Lower the probe to **Home Out**.

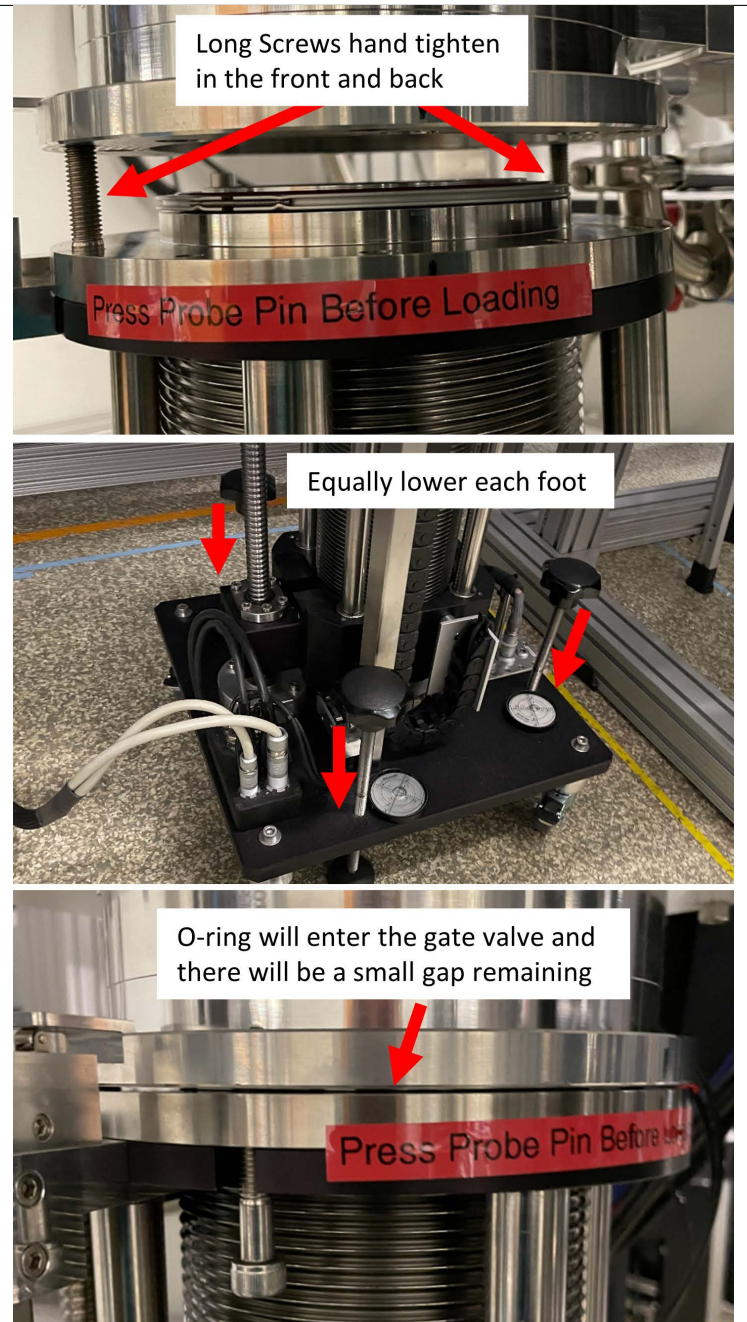


12. Once the probe is inside of the probe bellows, remove the top O-ring and clean it with IPA. Graphite tends to build up on this O-ring and it has to be regularly cleaned. Apply a fresh coat of vacuum grease to this O-ring and clean the flange that it sits on with IPA. Then return the O-ring back to the flange.



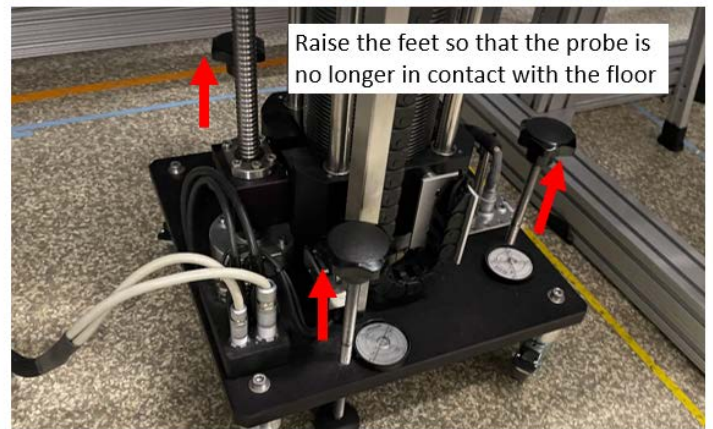


13. Move the probe bellows beneath the gate valve and insert two long M8 screws on either side. These screws do not need to be tight, they are only used to guide the probe toward the gate valve while the feet are raised. Lower the feet systematically down until the top of the probe bellows enters the gate valve and the O-ring is no longer visible. If one of the feet gets too tight, the probe assembly is likely tilted. Loosen the other two feet until all three feet are no longer tight.



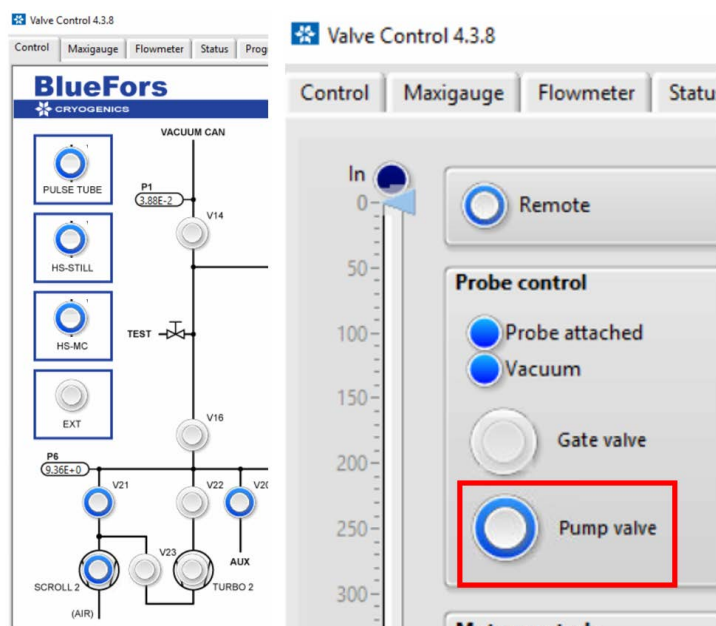
14. Remove the two long guide screws and using the red electric drill, secure the probe bellows to the gate valve with the 6 smaller M8 screws. Be sure the electric drill is set to a torque between 12 and 15.

Finally, the feet should be raised such that the probe is hanging from the gate valve and not touching the floor.



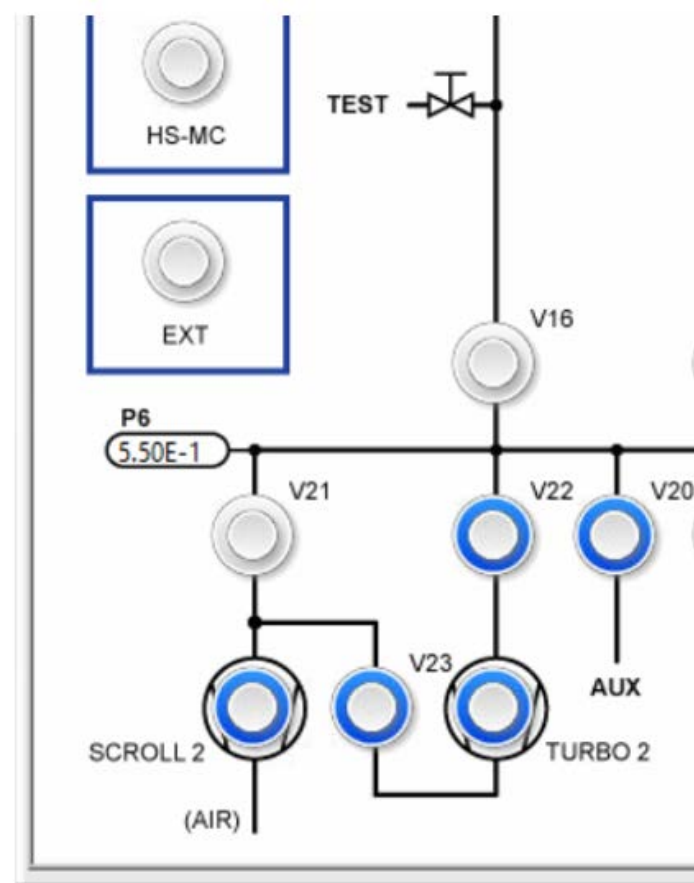
15. Now the probe bellows must be evacuated using Scroll 2, as shown here.

**Note:** If the probe has been exposed to atmosphere for more than a few days, it may take a while to reach minimum pressure. This time can be reduced by purging the bellows with nitrogen while the probe is being pumped with Scroll 2 (NEVER WHILE THE TURBO IS ON).



16. Turbo 2 can be turned on when **P6** drops below 1 mBar. When **P6** has reached  $<5e-4$  mBar, the probe can be inserted into the BlueFors.

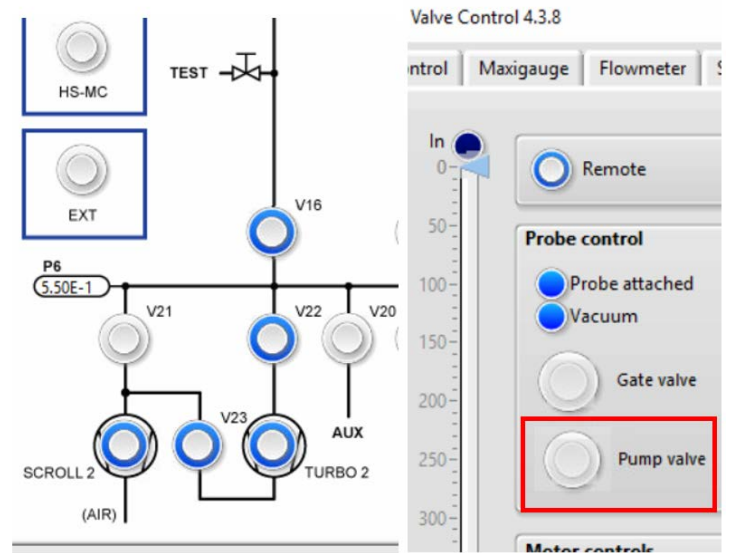
**Note:** It is not necessary to wait for this pressure, but each time the probe is loaded into the BlueFors, any gas left in the probe bellows will be trapped in the main vacuum chamber and become much more difficult to pump out. Eventually, this gas will reduce the cooling power of the cryostat and the main chamber will need to be warmed up to pump out the accumulated gas.



17. As the probe is loaded into the BlueFors it will heat up the system and cause the chamber to out-gas. Gas in the vacuum chamber provides a thermal link from the 300k radiation shield to the other flanges. This will heavily increase the cooling time of the system, and it may never reach 4k. This may also cause the optical windows to ice.

Scroll 2 and turbo 2 are used to pump out this excess gas from the vacuum chamber. The program listed in the next step has been modified to always pump out the vacuum chamber after the probe has been inserted into the BlueFors. Always use this program when loading the probe.

From the previous step, only close the Pump Valve and V20. If scroll 2 and Turbo 2 are not currently on, the program will automatically turn them on when it is started to pump the vacuum lines to a low enough pressure to pump on the vacuum can. Once the probe is fully loaded, the program will open V14 and start pumping on the vacuum.



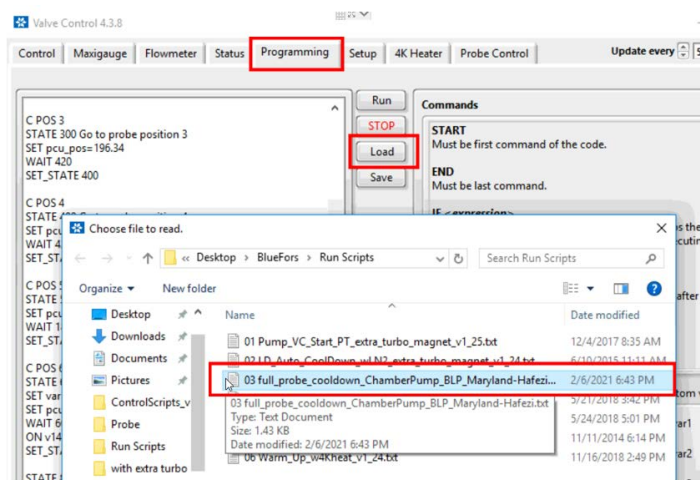


18. Navigate to the Programming tab and load the program shown here. Once the program is loaded, press

Run to begin loading the probe into the chamber.

**Note:** If the Pump Valve is not closed, the Gate Valve will not open and the script will quit.

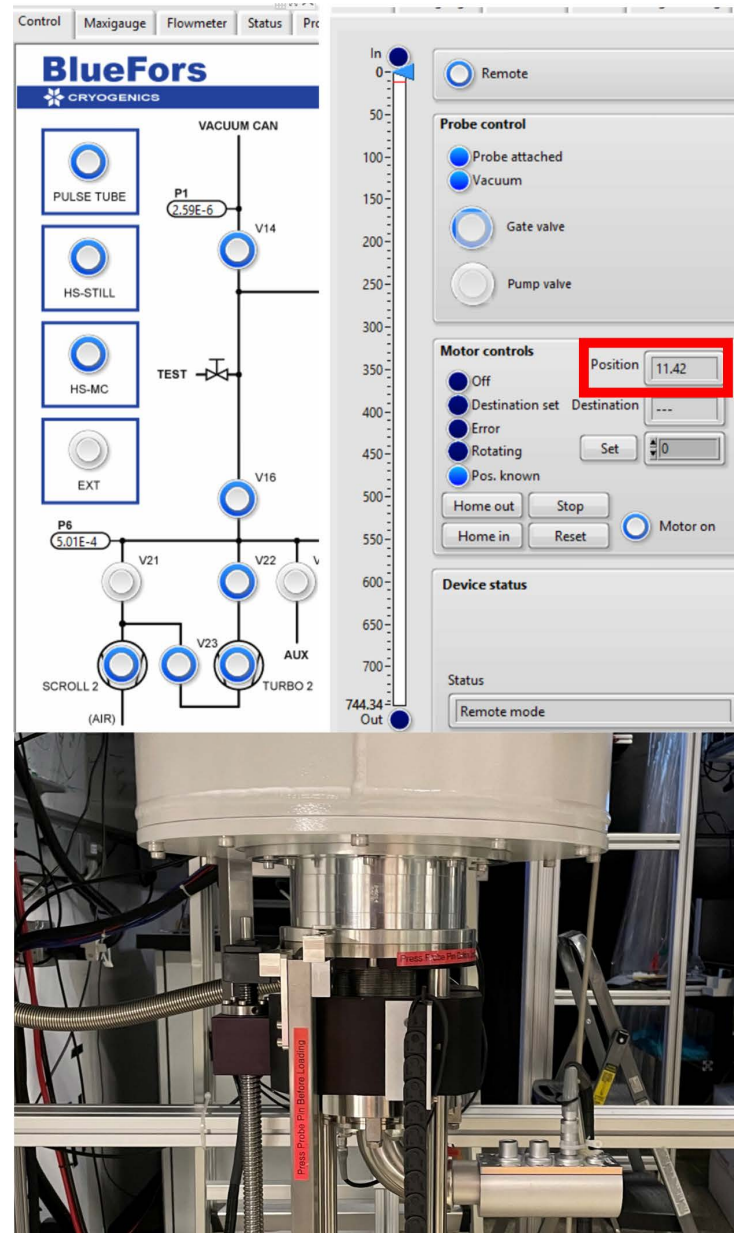
The probe will be loaded in steps. The program opens the gate valve and loads the probe head to the first radiation shield. It waits some amount of time (calibrated by BlueFors) and then moves to the next radiation shield until the probe finally reaches the mixing chamber flange. The step-by-step cooling is necessary because only the 50k and 4k flanges have direct cooling from the Cryomech compressor. This helps reduce cooling time.



19. Once the probe reaches the mixing chamber flange, it must be detached from the probe assembly. This is automatically done by the program in the last step when it pulls the probe back 11.42mm (calibrated by BlueFors). This is after it has made contact with the mixing chamber flange. The force holding the probe to the mixing chamber is strong enough that the detachment mechanism dislodges and the probe assembly disconnects from the probe.

The probe is now hanging from the mixing chamber plate. The program will also open V14 to be pumped on the vacuum can while the probe cools.

**Note:** After the detachment mechanism is used once, it cannot be used again until the probe is removed. You cannot re-attach the probe and then attempt to detach it again.



20. Once the probe's temperature reaches 4K, you can stop pumping on the vacuum can by turning off V14, V16, V22, Turbo 2, V23, Scroll 2.

**This completes the probe loading procedure.**

## A.4 Condensing

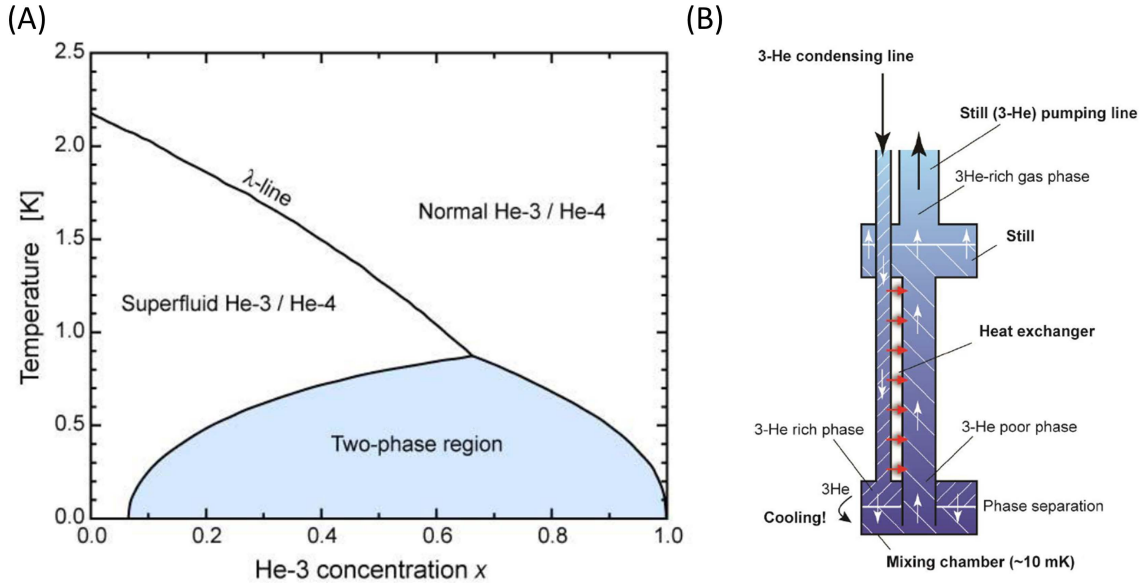


Figure A.12: (A) Phase transition of 3-He/4-He mixture [88]. (B) Schematic of a dilution refrigerator mixing chamber and still.

To reach the low temperatures accessible with a dilution refrigerator, you must condense the 3-He/4-He mixture into the mixing chamber. The gas handling system will then pump 3-He out of the still and recirculate it back into the mixing chamber.

I will briefly explain how the dilution refrigerator works, but refer to the user manual [88] for a more in depth discussion. Once the 3-He/4-He mixture drops below  $\sim 800$  mK, the mixture separates into two different phases, depicted in Fig. A.12(A). The first phase is called the dilute or 3-He poor phase and it contains 6.4% 3-He diluted in 4-He. The second phase is a near pure 3-He called the 3-He rich phase and it consists almost entirely of 3-He.

Gravity causes the 3-He poor phase to sit at the bottom of the mixing chamber because it contains heavier 4-He isotopes. By engineering the dilution unit such that the



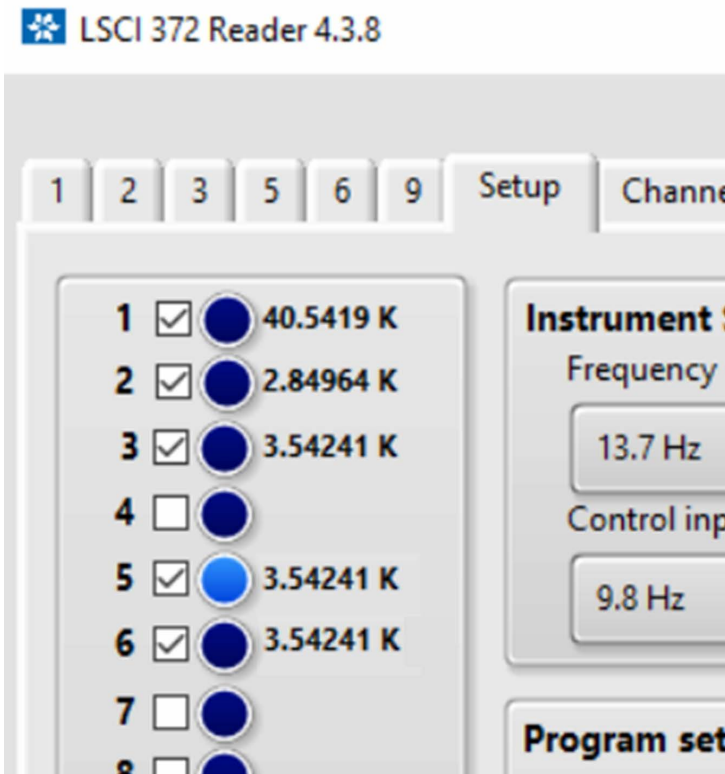
still and the mixing chamber are separated by the 3-He poor phase mixture, we can utilize the two phases to cool down the mixing chamber.

To walk through how this works, we start with the 3-He poor phase fully condensed in the mixing chamber, as shown in Fig. A.12(B). As we circulate, 3-He rich phase gas is pumped out of the still and condensed into the mixing chamber. This means the system is always out of equilibrium and causes the 3-He poor phase mixture to out-gas 3-He into the still while absorbing 3-He from the mixing chamber to keep the concentration fixed at 6.4% 3-He.

The condensed 3-He headed to the mixing chamber is cooled through a series of heat exchangers by the 3-He poor phase headed to the still. This cools the condensed 3-He to the base temperature of the mixing chamber. Cooling power is determined by how much 3-He is transferred across the phase boundary on the still side. This can be increased by warming up the Still with the Still heater. The heat on the still will increase the transfer of 3-He from poor phase to rich phase. We put 15 mW on the Still to keep its temperature around 1 K and to maximize our cooling power.

The condensing procedure is pretty straightforward and is mostly automated. The only requirements to start condensing is that the probe is loaded into the BlueFors and all of the flanges are  $\leq 4$  K.

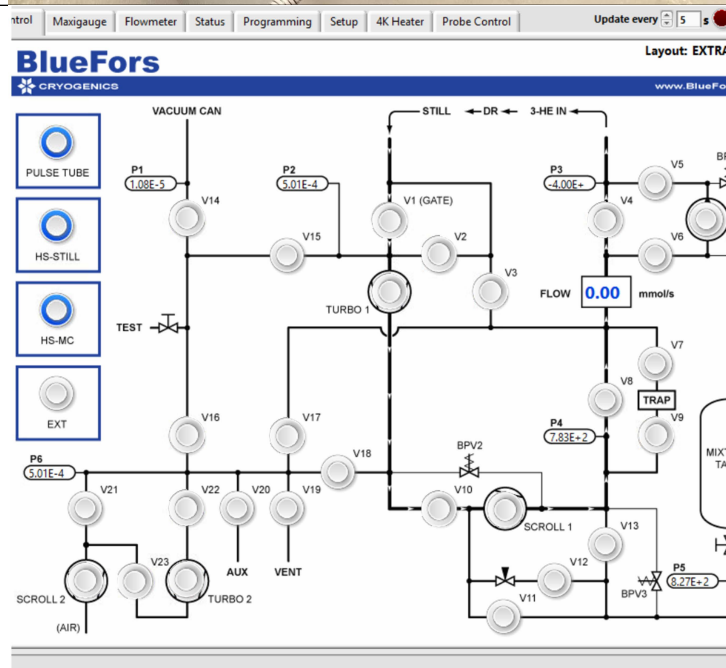
A.4.1 Condensing Procedure:

| Details   | Images  |                 |         |                 |   |                                     |         |   |                                     |         |   |                                     |         |   |                          |   |   |                                     |         |   |                                     |         |   |                          |   |   |                          |   |
|---|---|-----------------|---------|-----------------|---|-------------------------------------|---------|---|-------------------------------------|---------|---|-------------------------------------|---------|---|--------------------------|---|---|-------------------------------------|---------|---|-------------------------------------|---------|---|--------------------------|---|---|--------------------------|---|
| <p>1. Make sure that the flanges have reached their minimum temperatures. With the exception of the 50k flange, they should be <math>\leq 4</math> K prior to condensing.</p> |  <p>The screenshot shows the LSCI 372 Reader 4.3.8 software interface. At the top, there are tabs for '1', '2', '3', '5', '6', '9', 'Setup', and 'Channel'. Below the tabs, there is a list of channels with checkboxes and temperature readings in Kelvin (K). Channel 1 is checked and shows 40.5419 K. Channel 2 is checked and shows 2.84964 K. Channel 3 is checked and shows 3.54241 K. Channel 4 is unchecked and shows a dark blue circle. Channel 5 is checked and shows 3.54241 K. Channel 6 is checked and shows 3.54241 K. Channel 7 is unchecked and shows a dark blue circle. Channel 8 is unchecked and shows a dark blue circle. To the right of the channel list, there are buttons for 'Instrument', 'Frequency' (13.7 Hz), 'Control inp' (9.8 Hz), and 'Program set'.</p> <table><tr><th>Channel</th><th>Checked</th><th>Temperature (K)</th></tr><tr><td>1</td><td><input checked="" type="checkbox"/></td><td>40.5419</td></tr><tr><td>2</td><td><input checked="" type="checkbox"/></td><td>2.84964</td></tr><tr><td>3</td><td><input checked="" type="checkbox"/></td><td>3.54241</td></tr><tr><td>4</td><td><input type="checkbox"/></td><td>-</td></tr><tr><td>5</td><td><input checked="" type="checkbox"/></td><td>3.54241</td></tr><tr><td>6</td><td><input checked="" type="checkbox"/></td><td>3.54241</td></tr><tr><td>7</td><td><input type="checkbox"/></td><td>-</td></tr><tr><td>8</td><td><input type="checkbox"/></td><td>-</td></tr></table> | Channel         | Checked | Temperature (K) | 1 | <input checked="" type="checkbox"/> | 40.5419 | 2 | <input checked="" type="checkbox"/> | 2.84964 | 3 | <input checked="" type="checkbox"/> | 3.54241 | 4 | <input type="checkbox"/> | - | 5 | <input checked="" type="checkbox"/> | 3.54241 | 6 | <input checked="" type="checkbox"/> | 3.54241 | 7 | <input type="checkbox"/> | - | 8 | <input type="checkbox"/> | - |
| Channel   | Checked   | Temperature (K) |         |                 |   |                                     |         |   |                                     |         |   |                                     |         |   |                          |   |   |                                     |         |   |                                     |         |   |                          |   |   |                          |   |
| 1   | <input checked="" type="checkbox"/>   | 40.5419         |         |                 |   |                                     |         |   |                                     |         |   |                                     |         |   |                          |   |   |                                     |         |   |                                     |         |   |                          |   |   |                          |   |
| 2   | <input checked="" type="checkbox"/>   | 2.84964         |         |                 |   |                                     |         |   |                                     |         |   |                                     |         |   |                          |   |   |                                     |         |   |                                     |         |   |                          |   |   |                          |   |
| 3   | <input checked="" type="checkbox"/>   | 3.54241         |         |                 |   |                                     |         |   |                                     |         |   |                                     |         |   |                          |   |   |                                     |         |   |                                     |         |   |                          |   |   |                          |   |
| 4   | <input type="checkbox"/>  | -               |         |                 |   |                                     |         |   |                                     |         |   |                                     |         |   |                          |   |   |                                     |         |   |                                     |         |   |                          |   |   |                          |   |
| 5   | <input checked="" type="checkbox"/>   | 3.54241         |         |                 |   |                                     |         |   |                                     |         |   |                                     |         |   |                          |   |   |                                     |         |   |                                     |         |   |                          |   |   |                          |   |
| 6   | <input checked="" type="checkbox"/>   | 3.54241         |         |                 |   |                                     |         |   |                                     |         |   |                                     |         |   |                          |   |   |                                     |         |   |                                     |         |   |                          |   |   |                          |   |
| 7   | <input type="checkbox"/>  | -               |         |                 |   |                                     |         |   |                                     |         |   |                                     |         |   |                          |   |   |                                     |         |   |                                     |         |   |                          |   |   |                          |   |
| 8   | <input type="checkbox"/>  | -               |         |                 |   |                                     |         |   |                                     |         |   |                                     |         |   |                          |   |   |                                     |         |   |                                     |         |   |                          |   |   |                          |   |

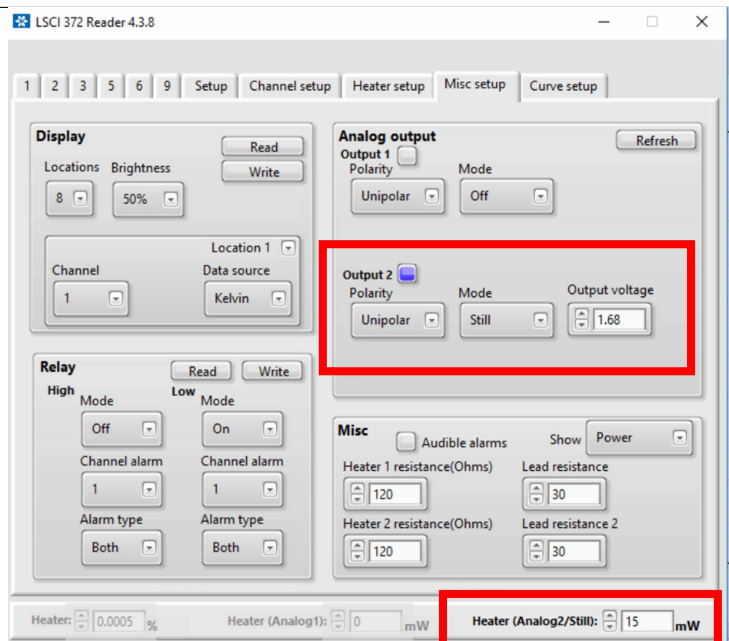
2. Refill the LN2 dewar that contains the trap. Be sure that it is full before starting the condensing procedure. All of the mixture gas will be pumped through the trap. This will cause a lot of the LN2 to boil off in the first hours of the condensing procedure. Be sure that the dewar remains full. Once the mixture has been condensed into the mixing chamber, you will only need to refill the LN2 dewar about once a week.



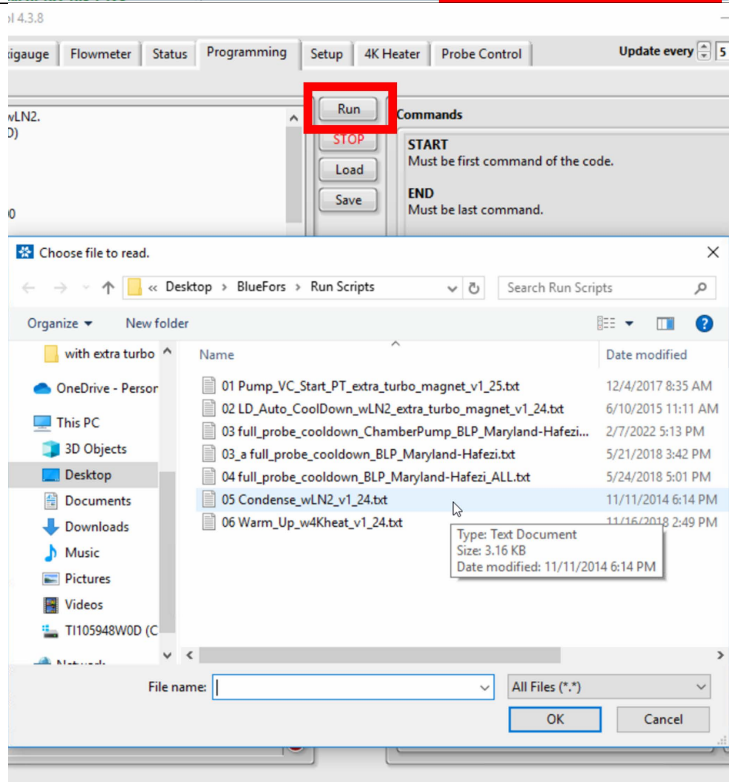
3. All of the valves should be off. Only the PulseTube, HS-Still, and HS-MC should be On.



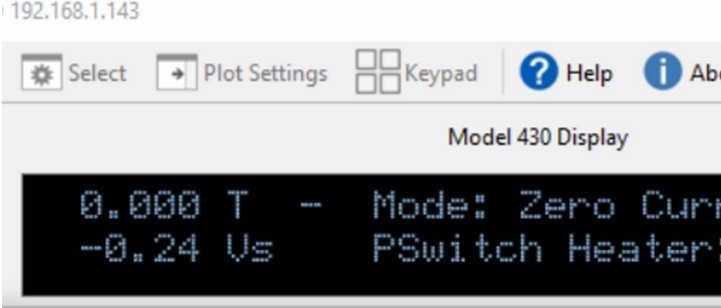
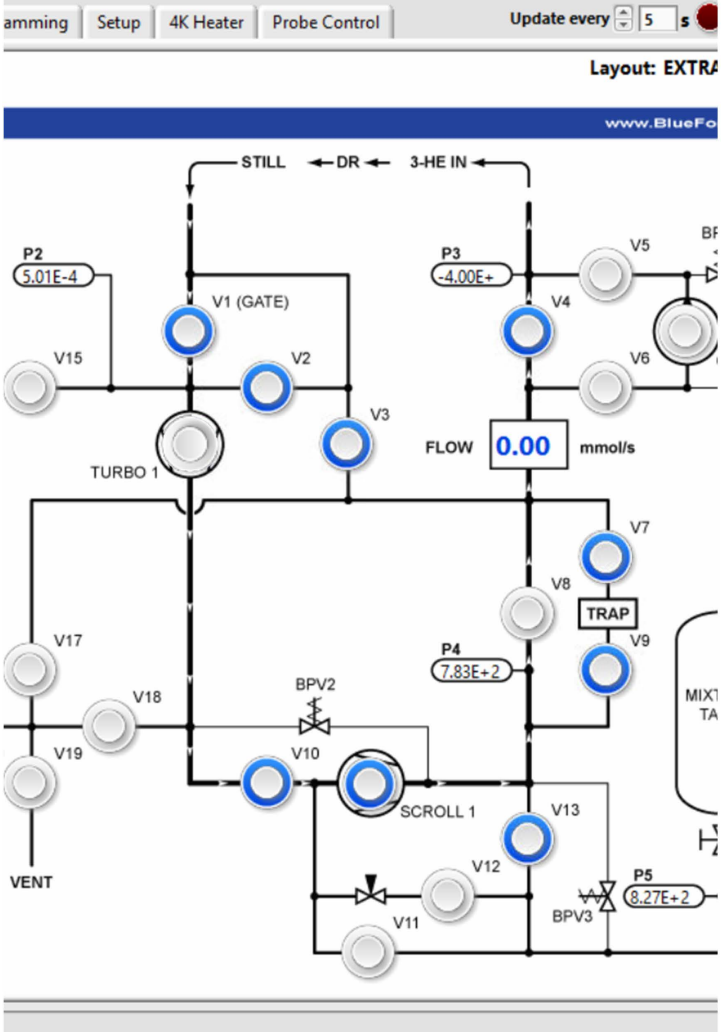
4. Set the Still heater to 15 mW. Be sure to press Enter on the keyboard after entering the value otherwise it will not change. This is Output 2 on the BlueFors temperature controller. Make sure that it is turned ON under the Misc Setup tab.



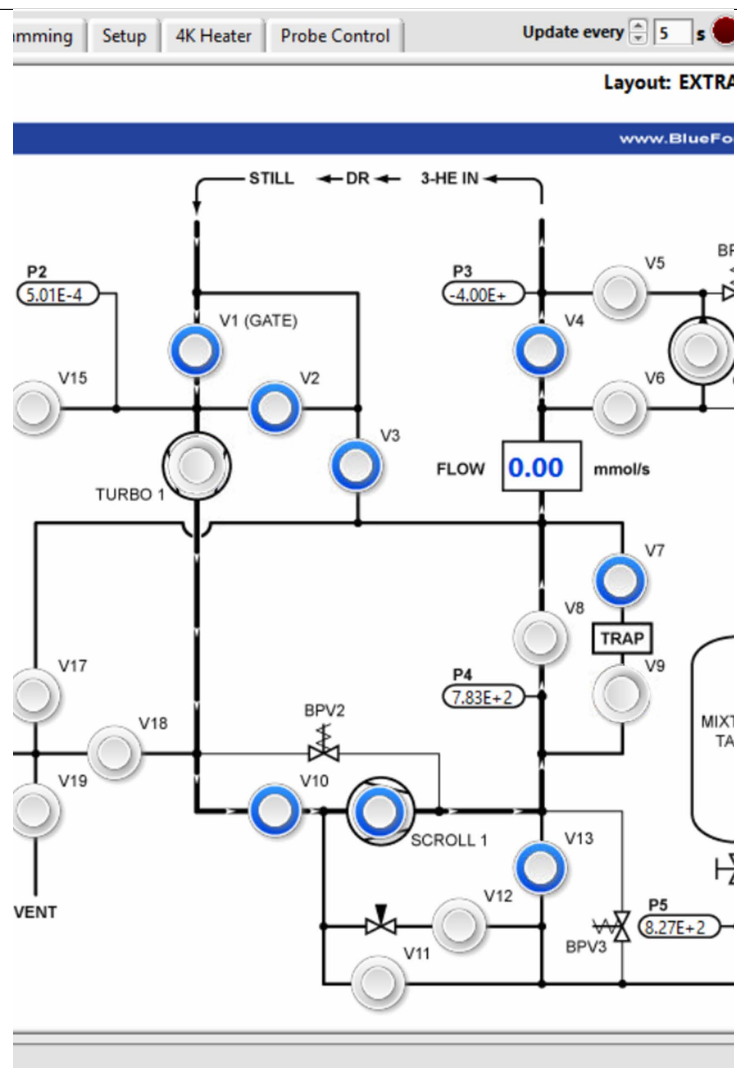
5. Open the program **05 Condense\_wLN2.v1\_24.txt** and click Run to begin the automated condensing procedure. The procedure will start by slowly releasing the 3-He/4-He mixture into circulation until most of the gas condenses in the mixing chamber. Once the Mixture Tank is nearly depleted ( $\sim 5$  mBar left in P5), it will begin circulating 3-He and cooling the cryostat to base temperature. The entire process will take a few hours before base temperature is reached.



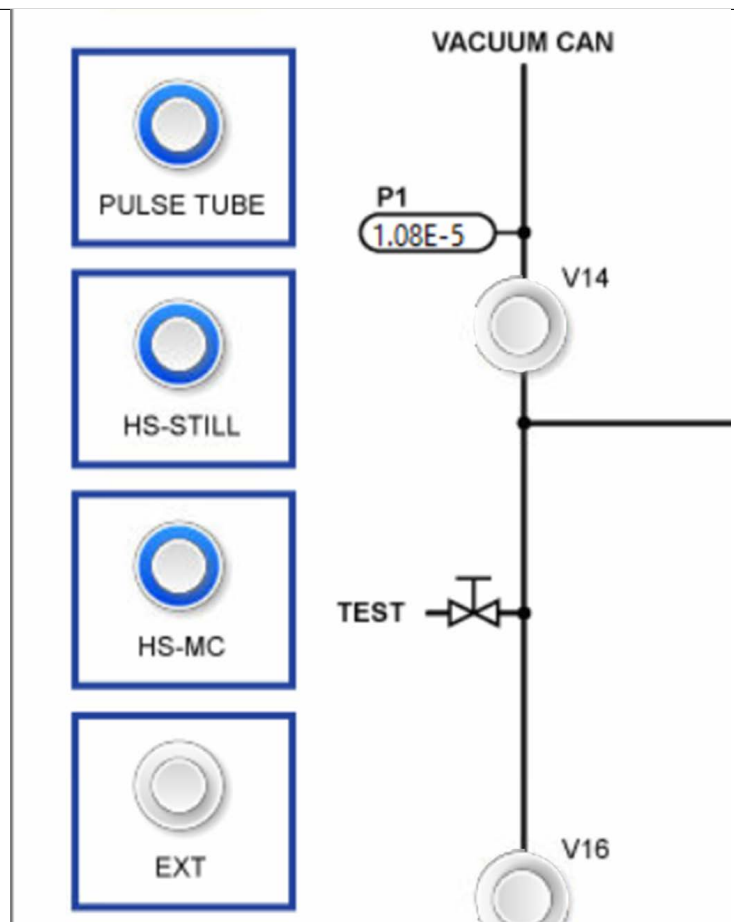
## A.4.2 Stop Condensing Procedure:

| Details  | Images  |
|--|---|
| <p>1. Check that the magnet is back to 0T before you stop condensing.</p>  |  <p>The screenshot shows a digital display with the following text: "0.000 T - Mode: Zero Curr", "-0.24 Us PSwitch Heater". The interface includes buttons for "Select", "Plot Settings", "Keypad", "Help", and "Abt". The IP address "192.168.1.143" is visible at the top left.</p>   |
| <p>2. Turn off Turbo 1 and open V13 to start pulling 3-He out of the mixing chamber and into the Mixture Tank. Wait about 5 minutes after turning off the turbo before the next step to allow it to ramp down.</p> |  <p>The schematic diagram illustrates the 3-He system. Key components include:         <ul style="list-style-type: none"> <li><b>Valves:</b> V1 (GATE), V2, V3, V4, V5, V6, V7, V8, V9, V10, V11, V12, V13, V15, V17, V18, V19.</li> <li><b>Pumps:</b> TURBO 1, SCROLL 1.</li> <li><b>Pressure Gauges:</b> P2 (5.01E-4), P3 (-4.00E+), P4 (7.83E+2), P5 (8.27E+2).</li> <li><b>Other Components:</b> BPV2, BPV3, TRAP, MIX1 TA, VENT, STILL, DR, 3-HE IN.</li> <li><b>Flow Rate:</b> A digital readout shows "FLOW 0.00 mmol/s".</li> <li><b>Interface:</b> The diagram is part of a software interface with tabs for "Pumping", "Setup", "4K Heater", and "Probe Control". It includes an "Update every 5 s" setting and a "Layout: EXTRA" label.</li> </ul> </p> |

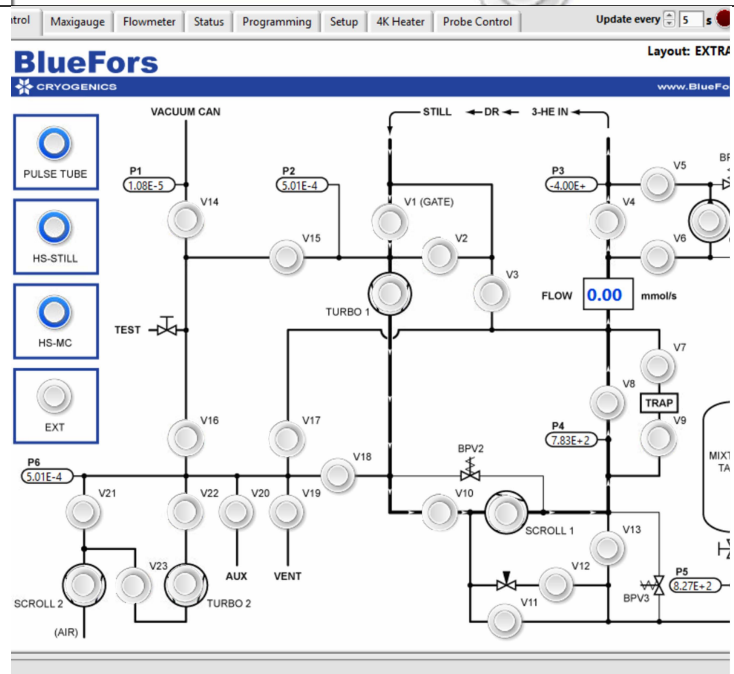
3. Close V9 and Open V3 and V2. This will allow for the helium mixture to be pulled from both the condensing and the still side of the mixing chamber. Closing V9 stops the circulation of helium and forces it to collect in the Mixture Tank.



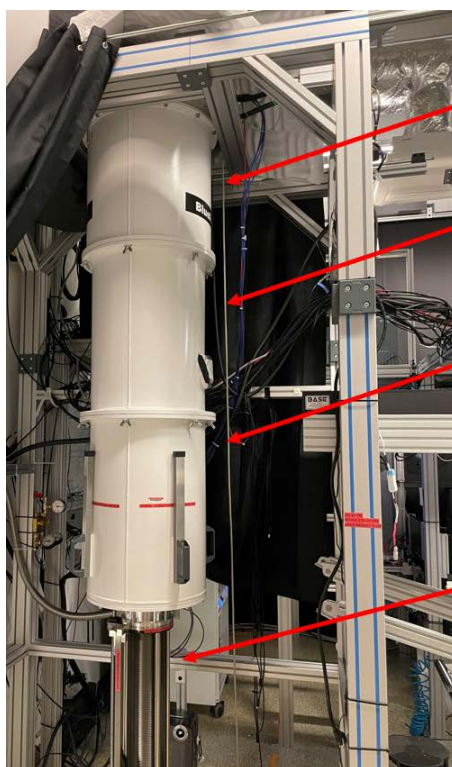
4. Turn on HS-STILL and HS-MC to bridge thermal contact between these flanges and the 4k plate. This will start to heat up the mixture and speed up the collection as well as keeping the flanges cold below 4 K after the mixture is removed.



5. Once P5 is  $>820$  mBar, P2 is  $<5.01E-4$  mBar, and P3 is  $\sim 4$  mBar, the mixture has been fully removed from the mixing chamber and entirely in the Mixture tank. You can turn off the circulation by closing the following valves in order: V7, V4, V3, V1, V10, V13, Scroll 1. You can also turn off Output 2 for the Still Heater on the temperature controller program.







**Top Vacuum Can**– Doesn't have to be removed unless access to the PulseTube or top flanges is necessary

**Middle Vacuum Can**– Contains optical access window and must be handled with care

**Bottom Vacuum Can**– Contains gate valve for probe loading and legs that keep the radiation shield off the ground

1. The Legs must be flipped downward
2. The gate valve bellows and high-pressure tubing must be removed (follow instructions ahead)

**Probe Bellows** – Attaches to the gate valve on the bottom vacuum can.

Figure A.13: Details of the BlueFors dilution refrigerator.

## A.5 Opening/Closing the System

Before we begin the procedure of removing the radiation shields, I want to acknowledge two components that must be disassembled carefully to avoid damaging the system.

The first is making sure that all of the middle radiation shields are handled such that the optical view ports are protected from damage. The optical view ports are glass and will break if they hit something or if the middle radiation shields are dropped.

The second is the magnet. The first concern is the wiring that must be disconnected before it can be removed, The second concern is that the magnet requires a lift to be placed



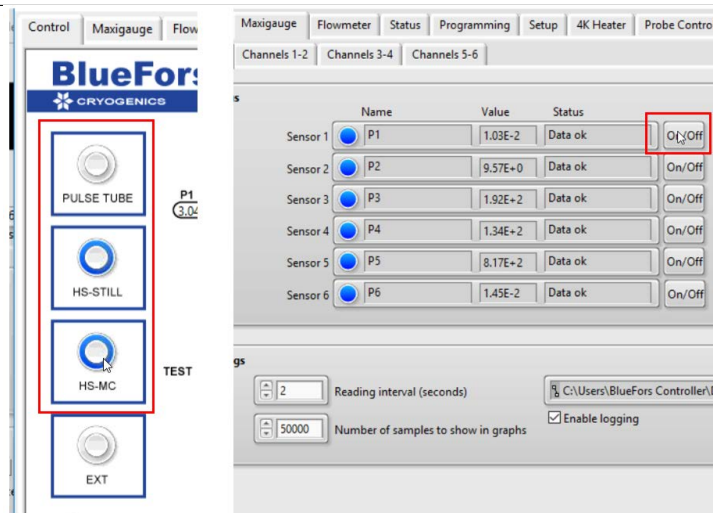
underneath it to allow for a smooth removal. The innermost radiation shield (connected to the still) is inside the magnet's bore. If the magnet is tilted too much while being removed, it can cause severe damage to this radiation shield. It is crucial that the magnet is removed slowly and perfectly downward. The same is true for when the magnet is being lifted back into place.

The magnet is also the only flange in the system that does not have a twist safe guard that protects it from falling when all the screws are removed. If a lift is being used, be sure that it is in a locked setting so that when all of the magnet's weight falls on it, the lift will be able to handle it. (If the red jack with foam is being used, the lift is locked as long as you don't press on the release foot pedal. If a different lift is used in the future, be sure to confirm that it is locked when the magnet is unscrewed from the 4k flange.)

A.5.1 Warm-up Procedure:

| Details  | Images   |
|--|--|
| <p>1. The magnet must be at 0T and the dilution unit should not be condensing.</p> | <div><p>Layout: EXTRA</p><p>www.BlueFors.com</p><p>Model 430 Display</p><p>0.000 T - Mode: Zero Current<br/>-0.09 Us PSwitch Heater: ON</p><p>75 samples/sec</p></div> |

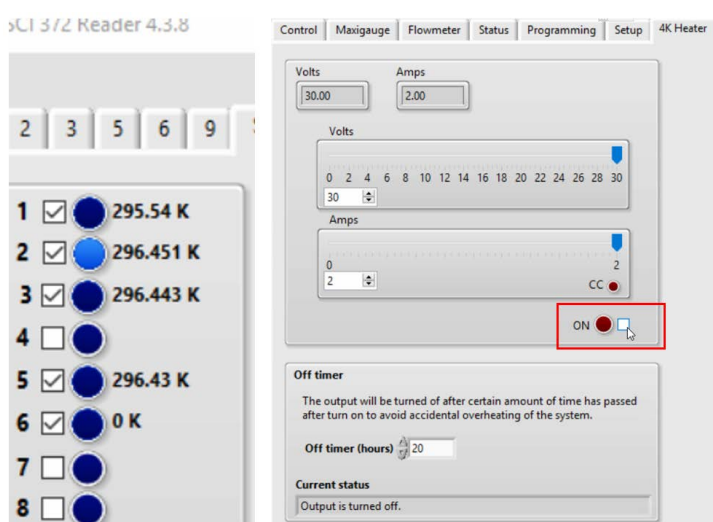
2. Turn off pressure gauge **P1** (the ion gauge can be damaged if the pressure rises) and the **PulseTube**. Turn on **HS-STILL** and **HS-MC**. This will bridge thermal contact between the mixing chamber flange, still flange, and 4k plate.




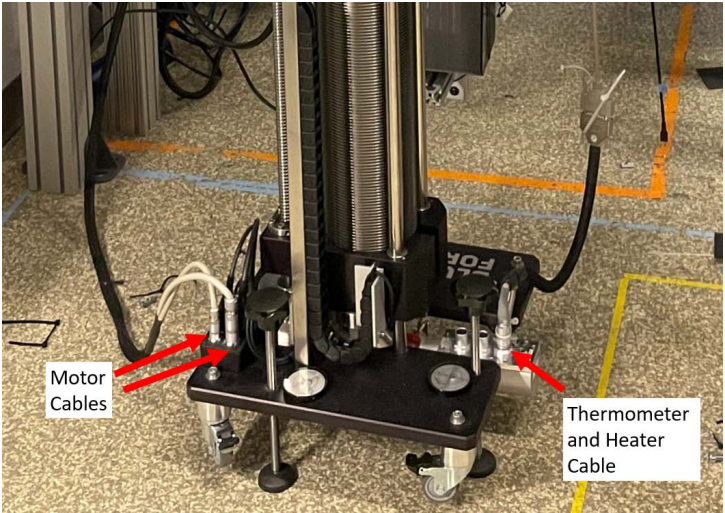
3. Turn on the 4k heaters for 20 hours. If the system hasn't reached  $>290\text{K}$  on all thermometers by the end of the first 20 hours, turn the heaters on again. Monitor the temperature such that it never gets too hot. Note: the probe and mixing chamber thermometers are not calibrated above 100 K and will read 0 K.

**Optional:** Nitrogen can be added to the vacuum chamber to decrease the warm-up time, but since this BlueFors has optical windows, doing so will cause condensation on the outermost window. I prefer to warm-up under vacuum to avoid this.

**This concludes the warm-up procedure.**



### A.5.2 Opening Procedure:

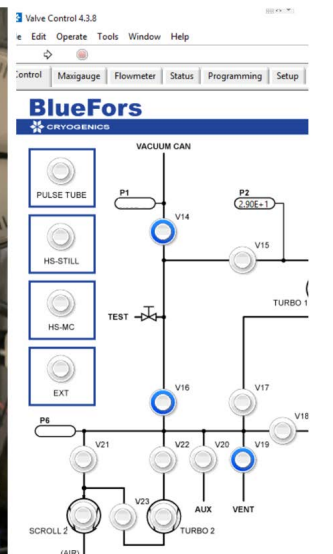
| Details   | Images  |
|---|---|
| <p>1. Remove any optics attached to the BlueFors's vacuum can side-axis flange and cover the optical window with optical paper to avoid damage.</p>   |  A close-up photograph of a white, cylindrical vacuum chamber. A circular flange on the side is covered with a piece of white optical paper, secured by black tape. Several colored cables (blue, red, black) are visible in the background.   |
| <p>2. Following the <b>Unloading Probe</b> procedure, remove the probe bellows from underneath the BlueFors. The three connectors on the probe must be unplugged from the probe assembly to allow for the probe to be completely moved out.</p> <p>Place the probe somewhere in the lab away from the BlueFors.</p> |  A photograph of the BlueFors probe assembly on a lab floor. The assembly consists of a black base with various cables and connectors. Two red arrows point to specific cables: one labeled 'Motor Cables' and another labeled 'Thermometer and Heater Cable'. The probe is positioned next to a large, silver, corrugated metal bellows. |

3. Turn all of the legs on the bottom vacuum can to the downward position. These legs are used to elevate the radiation shield off the ground and protect the gate valve.



4. The vacuum can must be brought to atmospheric pressure before it can be opened. Open the following valves: V19, V16, V14. This will open the vent line to the vacuum can. Open the nitrogen needle valve to begin filling the vacuum chamber with nitrogen. Monitor P6 until it reaches  $>1100\text{mBar}$ . Do not over pressurize the chamber.

**Turn off V19, V16, V14 after this step is completed.**





5. Before this step, make sure that no valves are open.

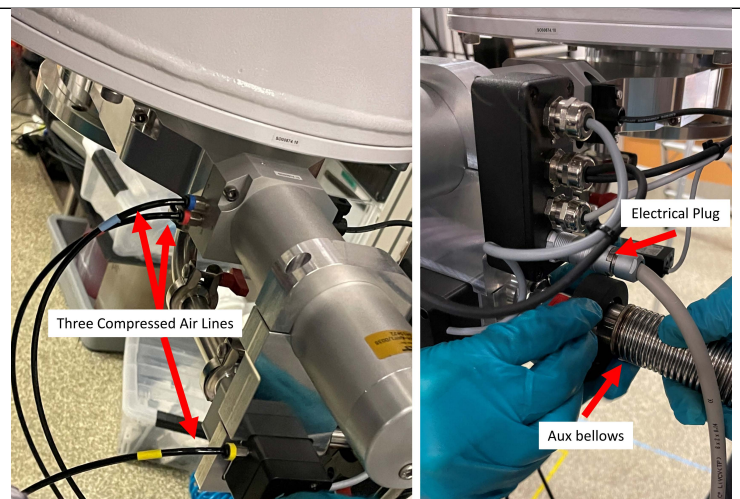
All valves require compressed air to be opened and the compressed air must be turned off to remove the gate valve.

Behind the BlueFors controller, there is a regulator for the compressed air. Turn the top until the gauge reads 0 (shown here). This turns off the compressed air to the controller and the gate valve can now be removed.

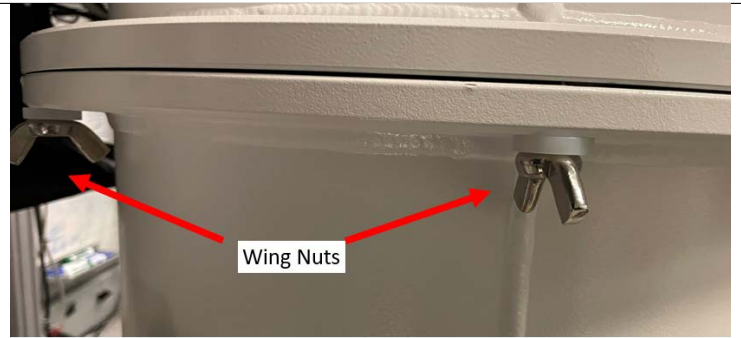
**None of the valves in the gas handling system can be opened while the compressed air is off.**



6. Disconnect the **three compressed air lines**, the **electrical plug**, and the **Aux bellows** from the gate valve.



7. Remove the bottom wing nuts that connect the bottom vacuum can to the middle vacuum can. The can will **not** fall when all of the wing nuts are removed. The vacuum can must be rotated and lowered down. Be careful to not hit the gate valve on the back t-slot support.



8. Place the bottom vacuum can somewhere safe in the lab.



9. Repeat the same procedure on the middle vacuum can.

Note that there is an optical window on this vacuum can and it must be handled with more care. Place the middle vacuum can on top of the bottom vacuum can.

The top radiation shields are ignored in this procedure because they do not need to be removed to access the important flanges of the cryostat. If the top flange must be removed, refer to the manual supplied by BlueFors or contact [support@bluefors.com](mailto:support@bluefors.com).



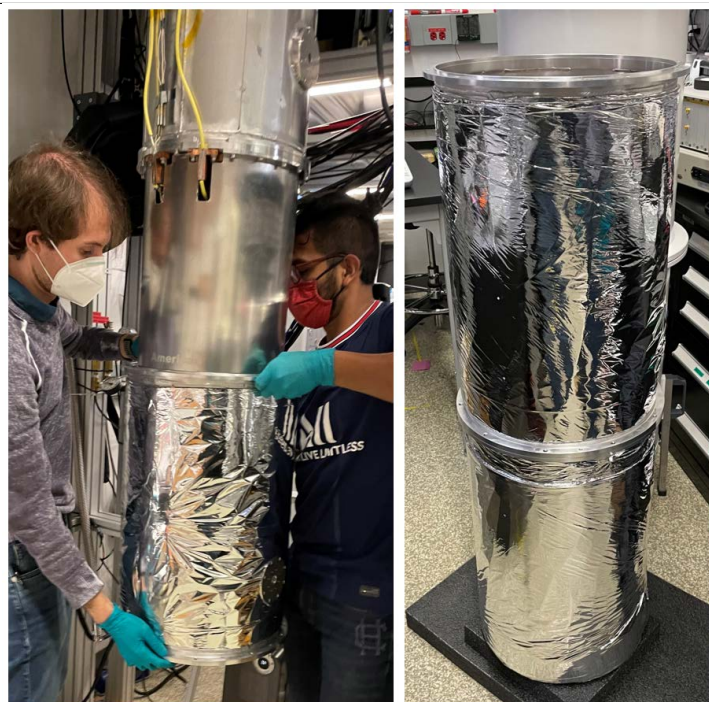
10. Using the electric drill or hex key, remove the screws securing the bottom 50k radiation shield to the middle 50k radiation shield. This radiation shield will not fall when all screws have been removed. Twist the radiation shield and remove it.

Because of the probe contact extruding from the bottom of the 50k radiation shield, place it in foam with a hole cut out of the center as shown here.



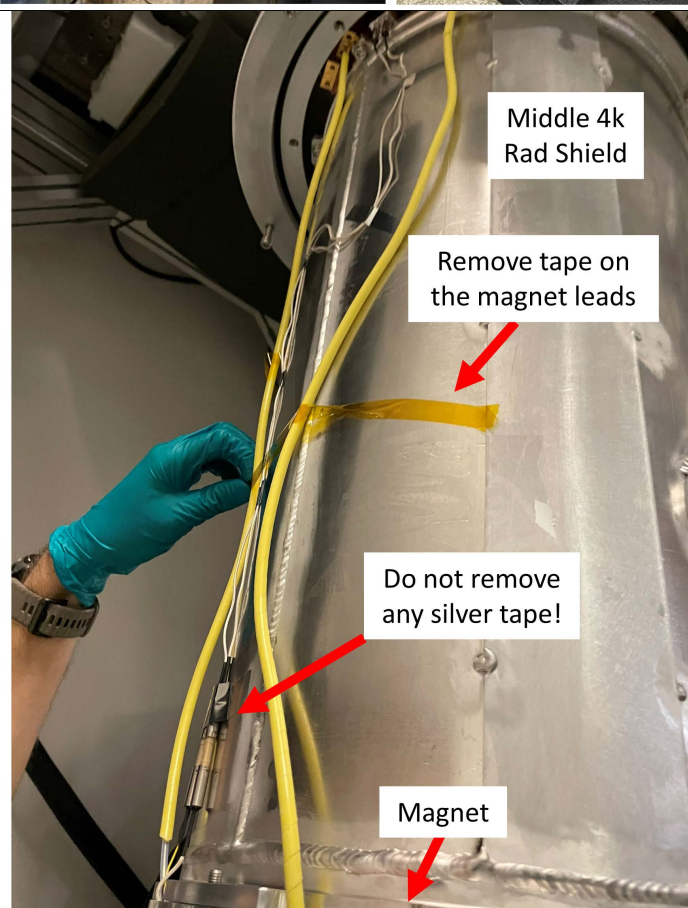


11. Similarly, remove the screws securing the middle 50k radiation shield. Handle this radiation shield with care as it has optical windows. Place it upon the bottom 50k radiation shield.

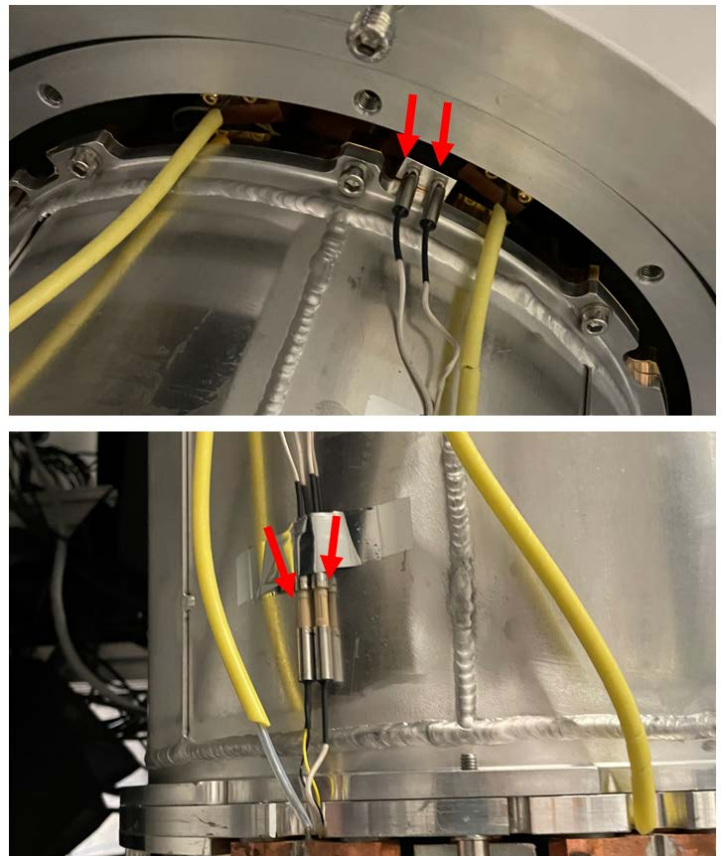


12. Attached to the bottom of the now exposed 4k radiation shield is the magnet. It must be handled with care because of its mass and electrical wiring. Before removing the magnet, the thermometer and heater connectors must be disconnected as well as the magnet leads.

Proceed to the next step.

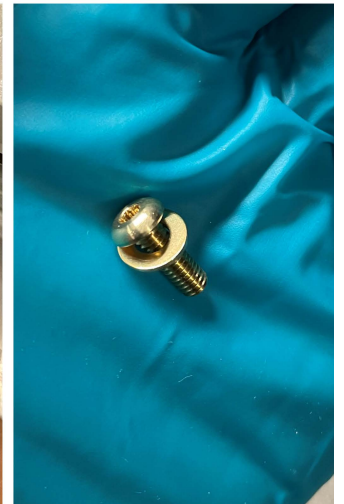


13. First remove the thermometer and heater cables to the magnet. Each of these connectors is unique, so don't worry about labeling them. Disconnect the bottom connectors and the top connectors.

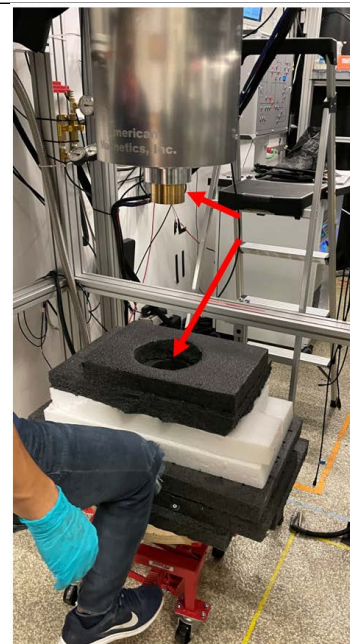


14. Now remove the magnet leads. These are the two rigid wires that are wrapped in plastic shielding. If they are taped to the middle 4k radiation shield, remove the tape. The contacts for the magnet leads are a little difficult to reach because they are just underneath the top radiation shield. They can still be accessed, but one must be very careful while removing the screws securing the two contacts.

There are two brass screws securing each magnet contact (total of 4). Each one must be carefully removed.



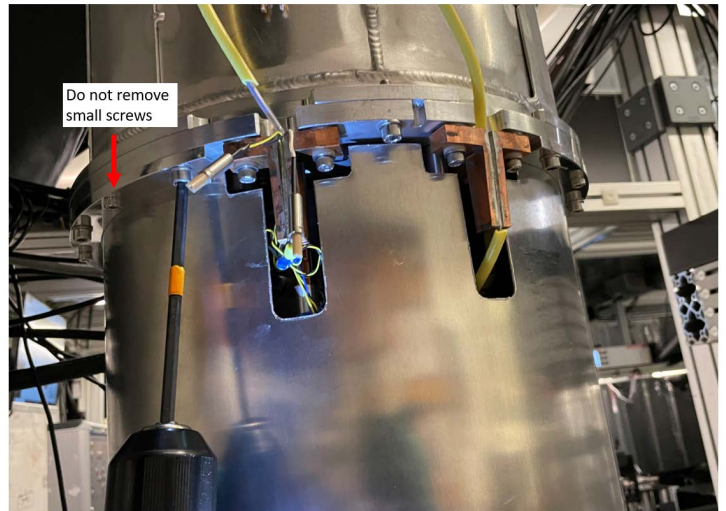
15. The magnet is now ready to be removed. Unlike all of the other radiation shields, the magnet will fall if all the screws are removed. Therefore, place the jack underneath the magnet before removing any screws. If using the red jack, be sure that the foam hole is centered on the probe extrusion at the bottom of the magnet. Raise the jack until it is in contact with the magnet.





16. Remove all screws securing the magnet to the middle 4k radiation shield. **NOTE:** there are two types of screws. Only remove the larger ones that secure the magnet to the middle 4k radiation shield. The smaller ones hold the magnet together and should never be removed.

The entire weight of the magnet will fall onto whatever jack is holding it. Be sure that the jack is locked and can handle this load before beginning this step. If using the red jack, it is automatically locked unless the release foot pedal is pressed.

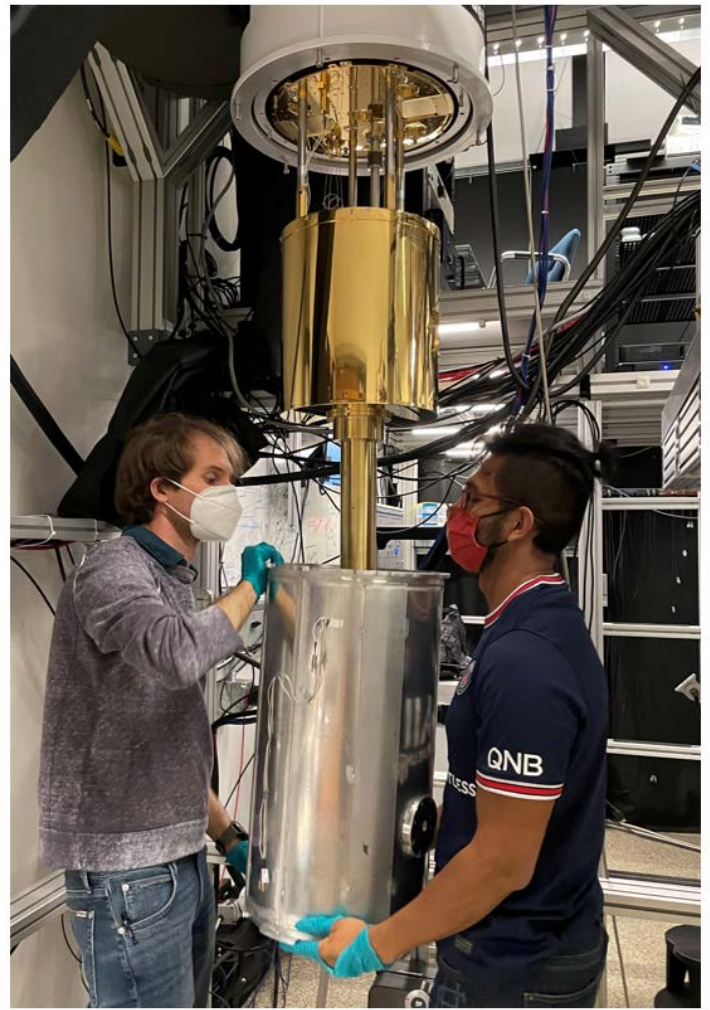


17. Slowly lower the magnet, trying to keep it as straight as possible. Inside of the magnet's bore is another radiation shield that can be easily bent if the magnet is tilted while being removed.

Keeping the magnet on the lift, place it somewhere safe in the lab and **do not bend the magnet leads.**



18. Remove the screws securing the middle 4k radiation shield to the top 4k radiation shield. This radiation shield will not fall when all of the screws have been removed. Rotate it and carefully remove it from the cryostat. Place it on some foam in the lab.



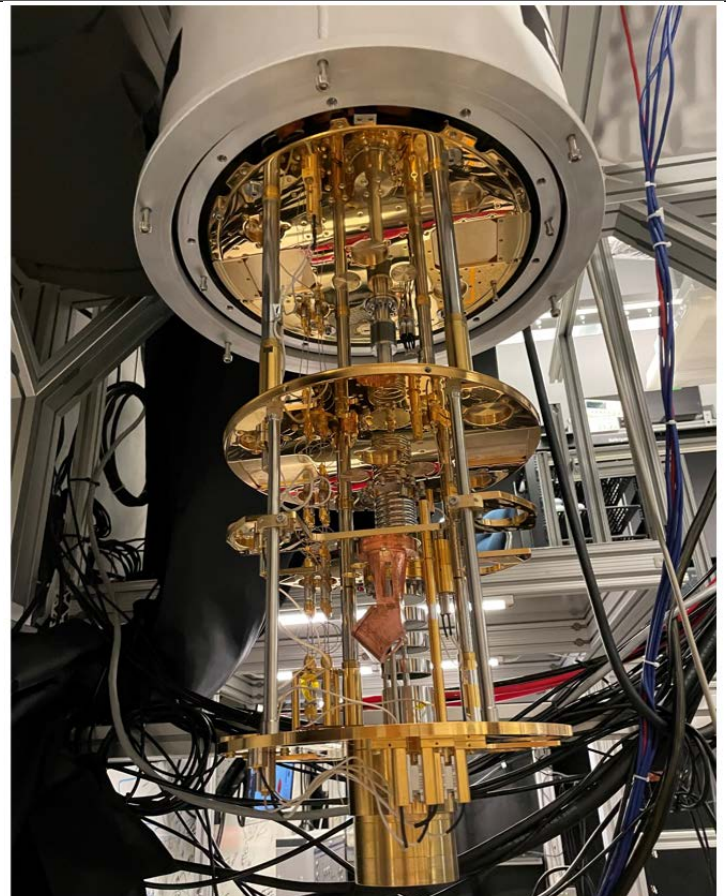


19. The gold plated still radiation shield is the last radiation shield in the BlueFors. It is secured to the still flange via Torx conical screws. This radiation shield will fall if all of the screws are removed. Remove all screws except two and then be sure that someone is holding the radiation shield while the last two are removed.

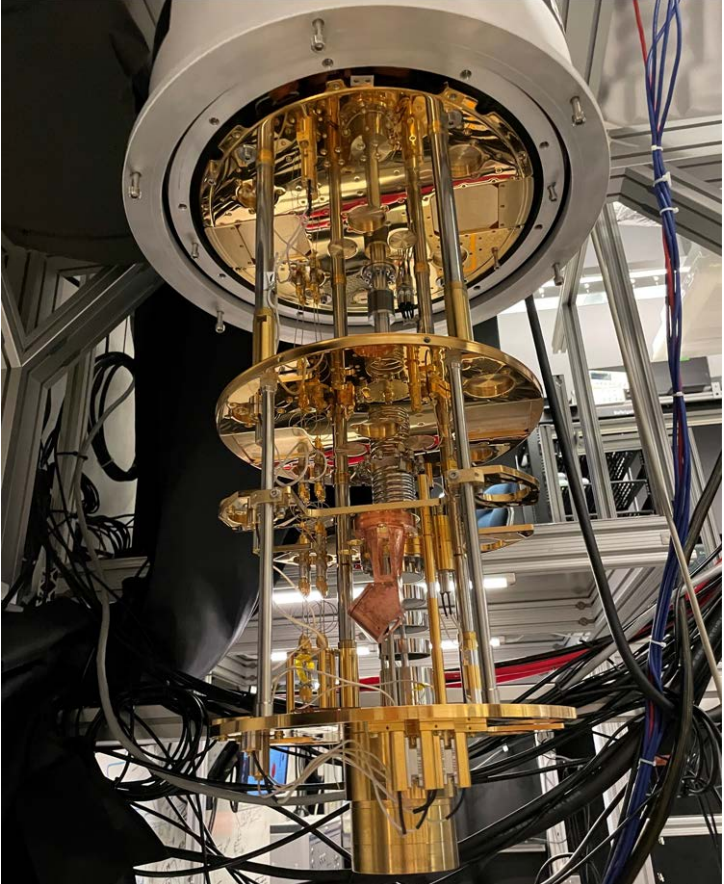

Remove the radiation shield and place it upside-down on foam somewhere safe in the lab.



20. **The opening procedure is now complete.**

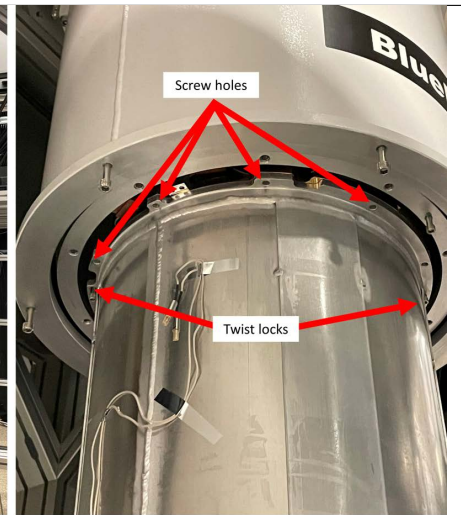


### A.5.3 Closing Procedure:

| Details  | Images   |
|--|--|
| <p>1. Start with the open BlueFors (with the top radiation shield still installed). Note the side of the optical path (located on the right shown in this image). This is the side all of the optical windows must be facing for the middle radiation shields.</p> |   |
| <p>2. While someone lifts the still radiation shield, secure it to the still flange. This radiation shield does not have twist locks that prevent it from falling.</p> <p>The screws used to secure this radiation shield have a Torx conical head.</p>            |  |



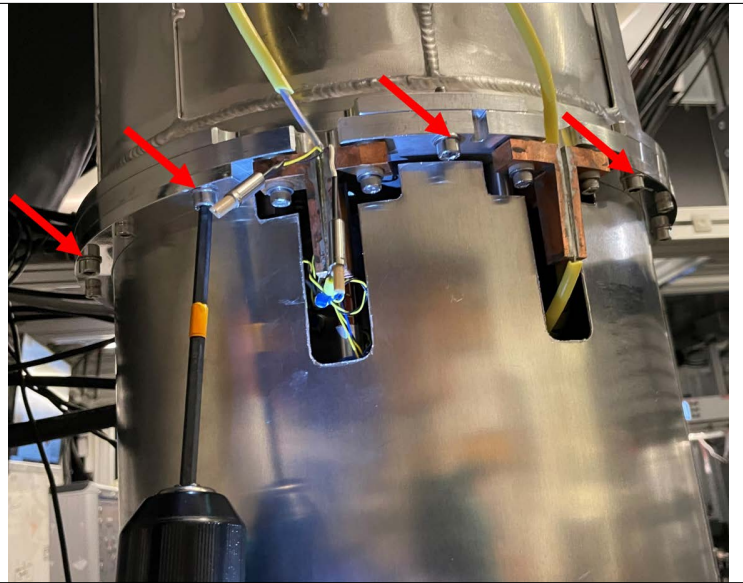
3. Lift the 4k middle radiation shield to the 4k flange and twist it into place. The two twist-lock screws will keep it from falling. Secure it to the top 4k radiation shield with the proper screws.



4. Place the magnet underneath the BlueFors and slowly raise it. The bore of the magnet is just the right diameter so that the still radiation shield will fit. You must be very careful while raising the magnet because there is a lip that the still radiation shield can get caught on inside the magnet bore. Be sure that you guide the magnet up and that the still radiation shield stays in the center.

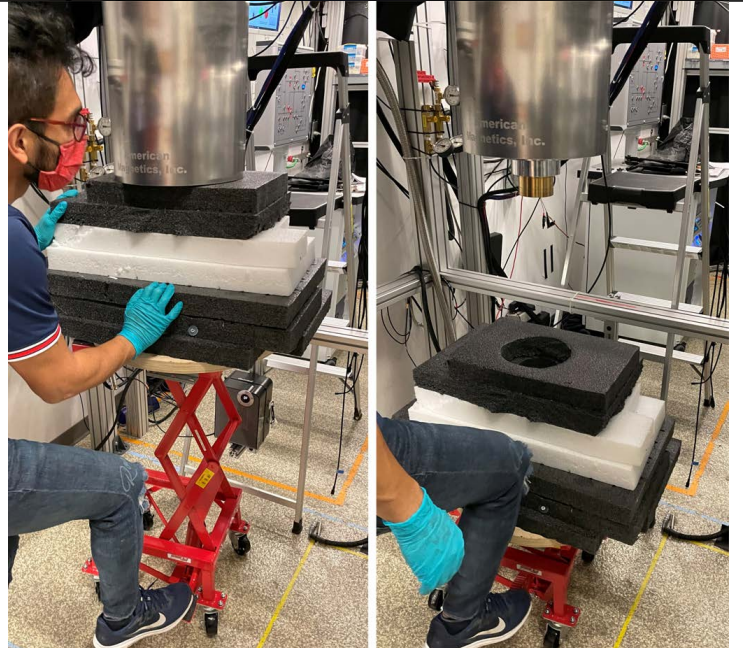


5. Secure the magnet to the 4k middle radiation shield using the proper screws.



6. Lower the lift out of the way.

**BE SURE THE MAGNET IS SECURE TO THE 4K MIDDLE RADIATION SHIELD!**

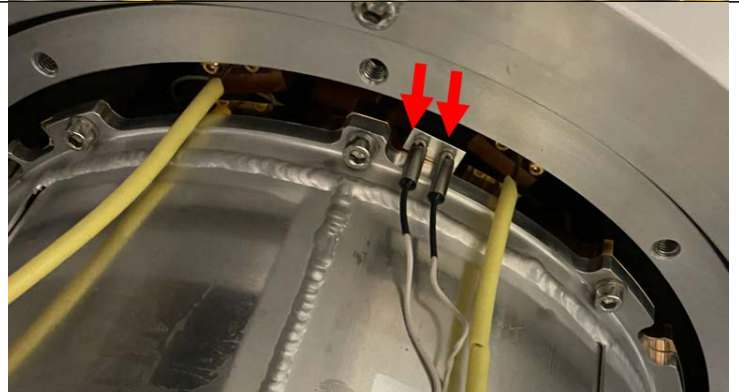




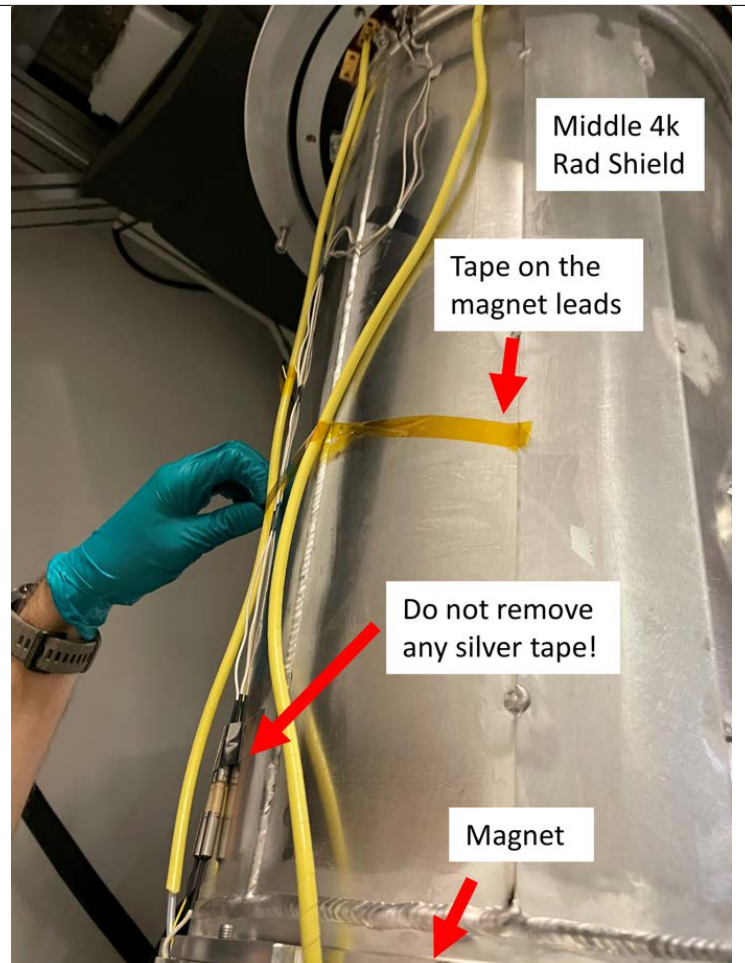
7. Using the proper brass screws, connect the magnet leads to the metal contacts located just underneath the upper radiation shield.



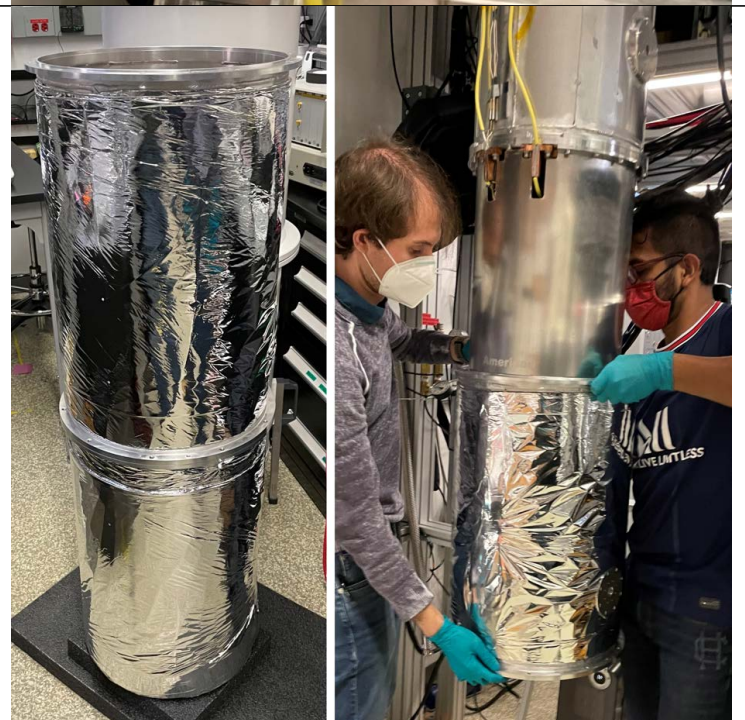
8. Connect the thermometer and heater DC connectors at the top and bottom of the 4k middle radiation shield. Each is unique so there is no confusion which is which.



9. Tape down the magnet leads so that they do not touch the middle 50k radiation shield. Use Kapton tape.



10. Raise the middle 50k radiation shield and twist it into place using the twist lock screws on either side (next step).





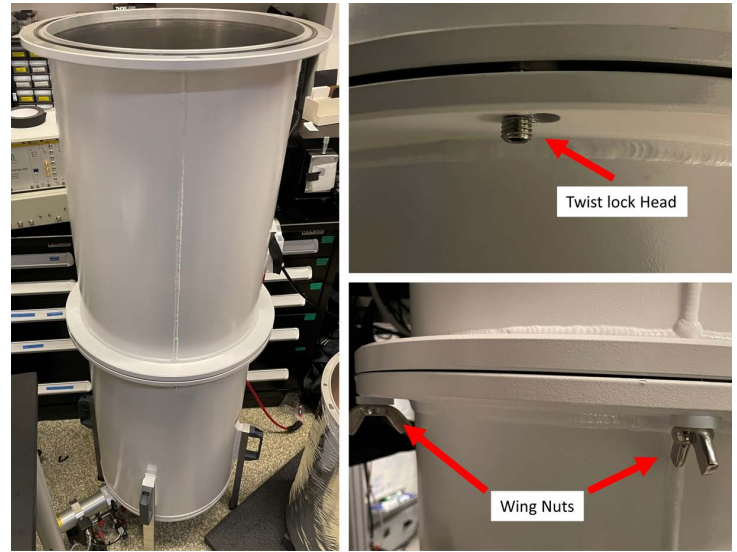
11. Secure the middle 50k radiation shield to the top 50k radiation shield.



12. Secure the bottom 50k radiation shield to the middle 50k radiation shield.



13. Clean the o-ring for the middle vacuum can and apply vacuum grease uniformly along the o-ring. Raise the middle vacuum can to the top vacuum can and twist it into place. The screws will keep it from falling. Using the wing nuts, secure the middle vacuum can to the top vacuum can by uniformly tightening the wing nuts around the cryostat. Only hand tighten.



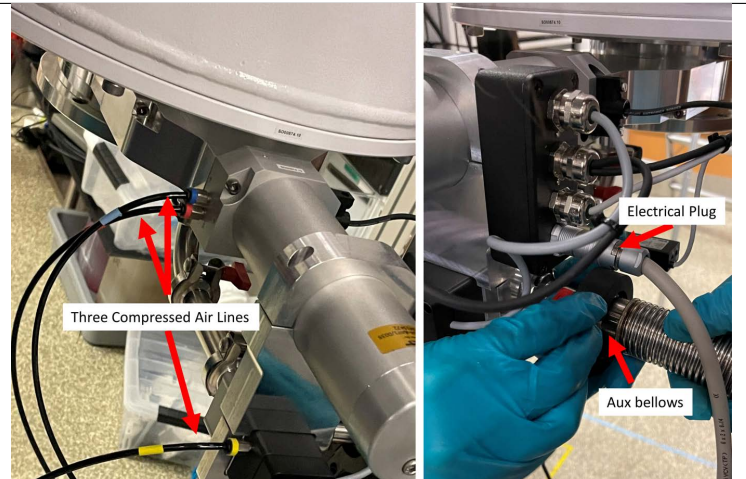
14. Clean the o-ring for the bottom vacuum can and apply vacuum grease uniformly along the o-ring. Make sure to be careful with the gate valve. It may hit on the t-slot frame when lifted. Raise the bottom vacuum can to the middle vacuum can and twist it into place. The screws will keep it from falling. Using the wing nuts, secure the bottom vacuum can to the middle vacuum can by uniformly tightening the wing nuts around the cryostat. Only hand tighten.

Flip the feet upwards so that the probe can be easily installed underneath the BlueFors.

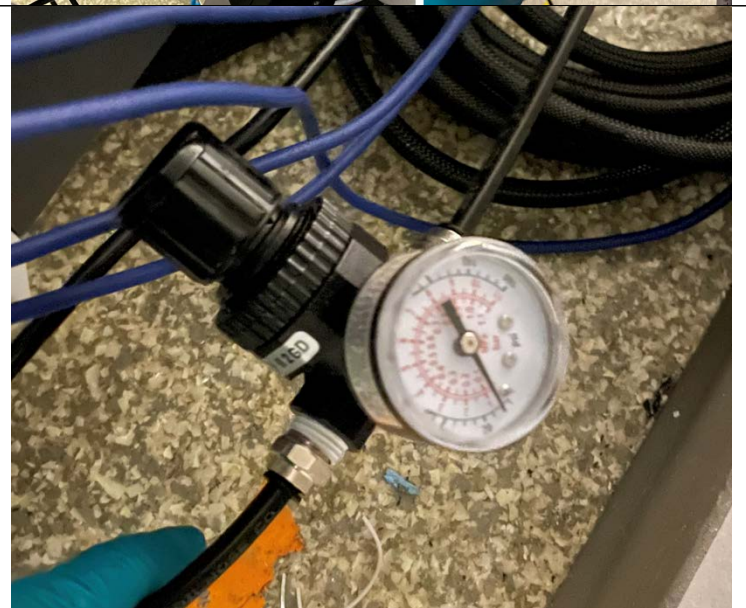




15. Reconnect all of the tubing and wiring for the gate valve.

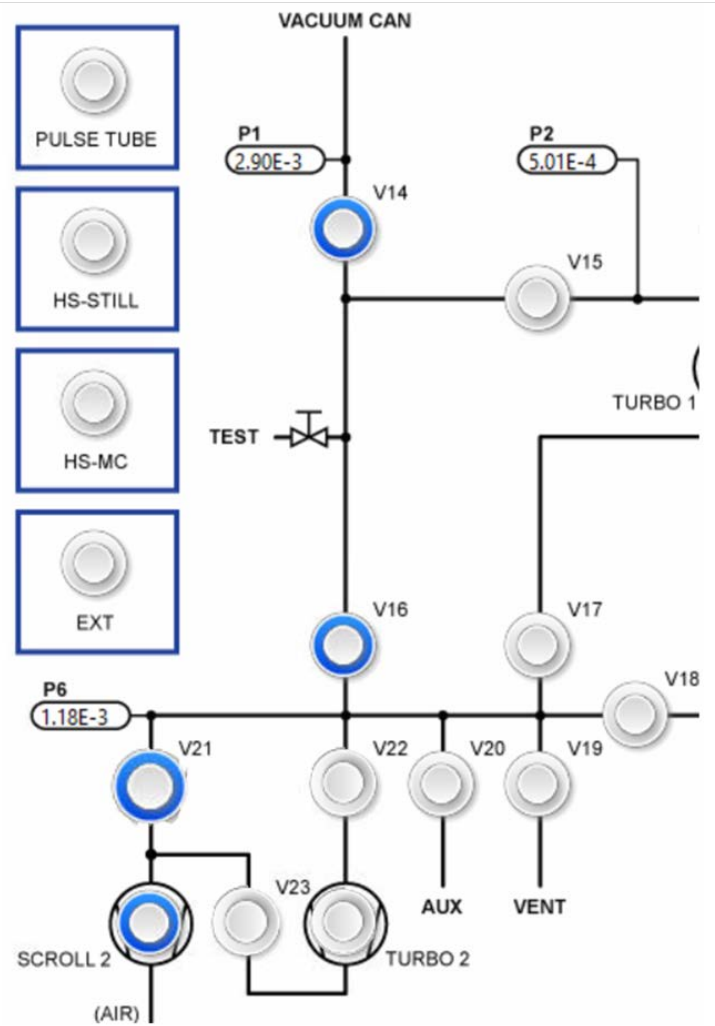


16. Open the pressure to the GHS system so that the valves can be used.



17. Pump on the vacuum can with Scroll 2 using the valve configuration shown here. Wait until P6 reads less than 1 mBar before moving to the next step.

Check the wing nuts on the middle and bottom vacuum cans. Tighten any that are now loose.

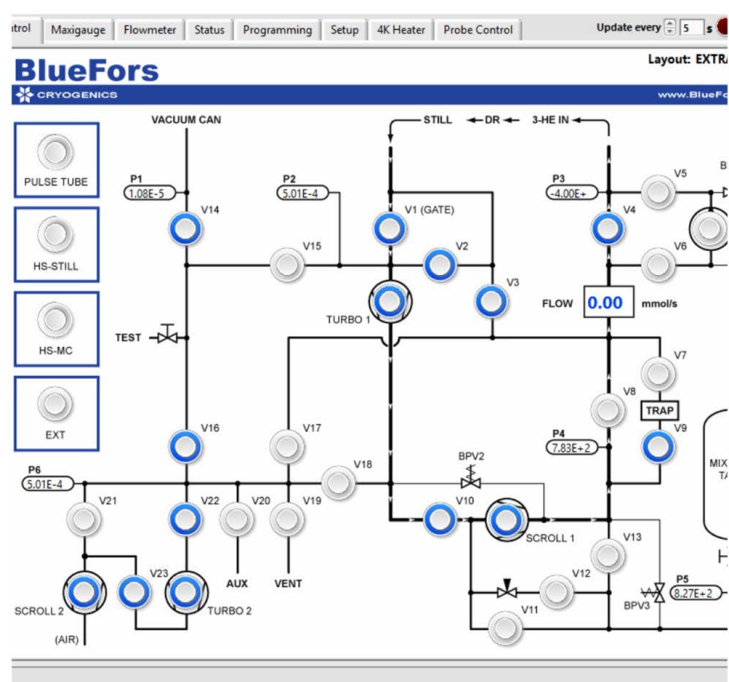


18. Pump on the vacuum can with Turbo 2 using the valve configuration shown here. Turn on pressure gauge P1 to measure the true pressure inside the vacuum can.

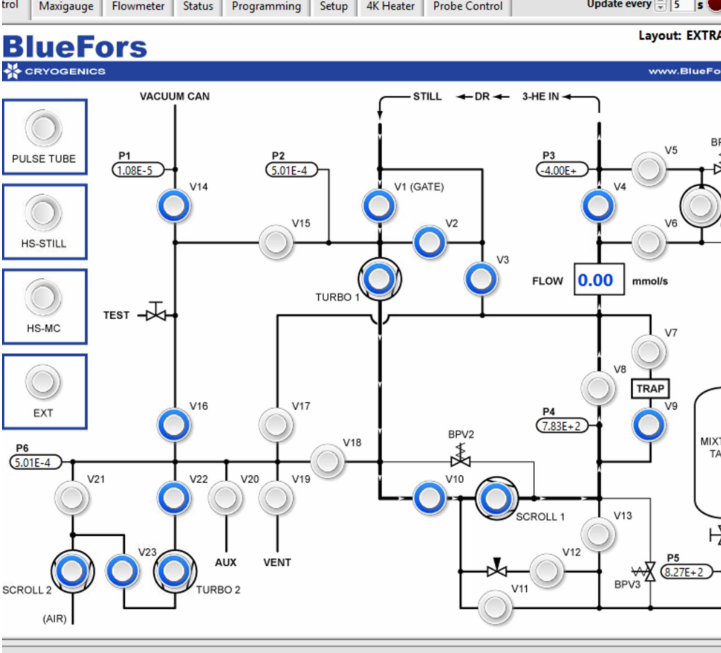
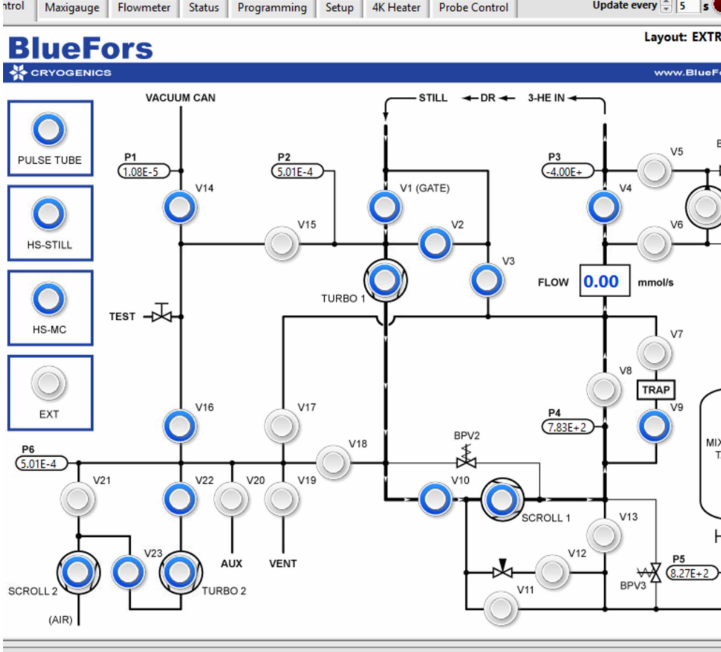
This can be turned on under the Maxigauge tab. Wait until P1 reads less than  $<2 \times 10^{-3}$  mBar before starting to cool down the cryostat.

Also begin pumping out the dilution unit inside the cryostat using the configuration shown here. You need to make sure the helium lines are at vacuum before cooling is started.

**This completes the closing procedure.**



## A.5.4 Cool-down Procedure:

| Details   | Images   |
|---|--|
| <p>1. The vacuum can should be pumped with Scroll 2 until P1 reads <math>&lt;2\text{E}-3</math> mBar.</p>   |   |
| <p>2. Turn on PulseTube, HS-Still, and HS-MC. You should hear the helium pump start to pulse. If not, check the Cryomech compressor panel to make sure that it is running correctly.</p> <p>Wait a few days until all temperatures except the 50k flange reach <math>&lt;4</math> K. The mixing chamber and probe will read 0 K until they are below 100 K.</p> |  |

## A.6 BlueFors Traps

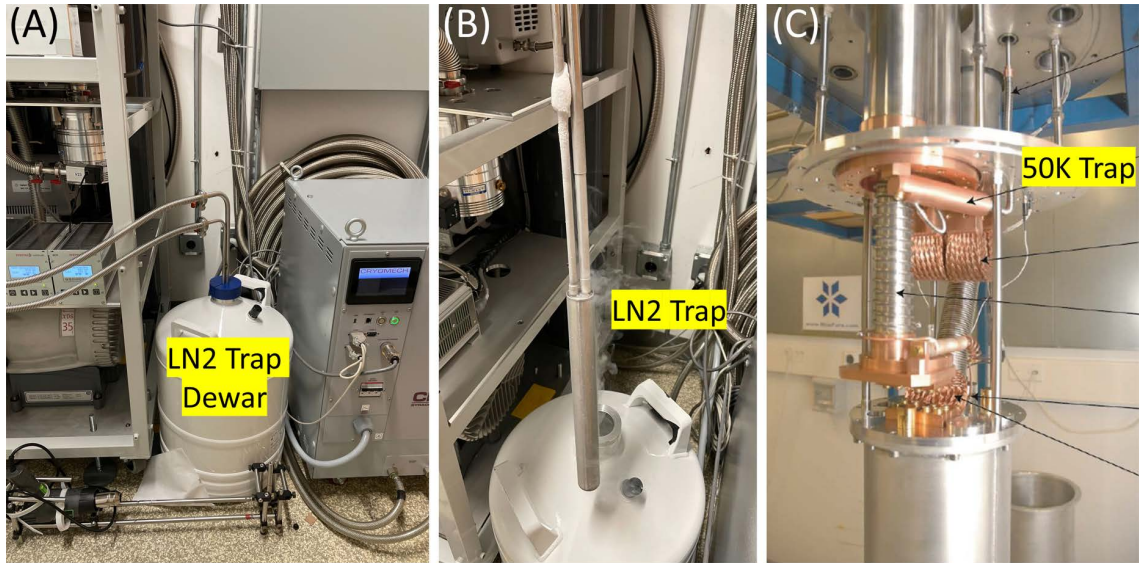


Figure A.14: (A) The first trap resides in a LN2 dewar and is accessible to users. (B) The trap is a carbon filter that provides a large amount of surface area for contamination gases to ice; i.e. anything other than helium. The trap enclosure is shown here. The trap must be submerged in LN2 so that the carbon trap is cold enough for nitrogen, oxygen, and water to freeze. (C) There is a secondary trap inside of the cryostat on the 50 K plate. This is the final filter that can freeze-out any remaining contamination gases that are not helium. It also acts as a heat exchanger and is the first stage of the cooling of the helium mixture. This image is from the BlueFors manual, but they took the image from a different fridge design [88]. I am not sure where this is located on our system.

The gas handling system for the BlueFors is designed to always keep the pressure below 1 atm (1013.25 mBar). Hence, if there is a leak, it will suck air into the lines instead of 3-He/4-He mixture being lost. The consequence of this design choice is that air will constantly leak into the circulation plumbing. If these atmospheric gases enter the condensing lines in the cryostat, they will freeze and clog the lines. This will prevent helium from circulating and the entire dilution unit will need to be warmed up to unclog the icing.

Therefore, to avoid icing in the condensing lines, there are two carbon traps

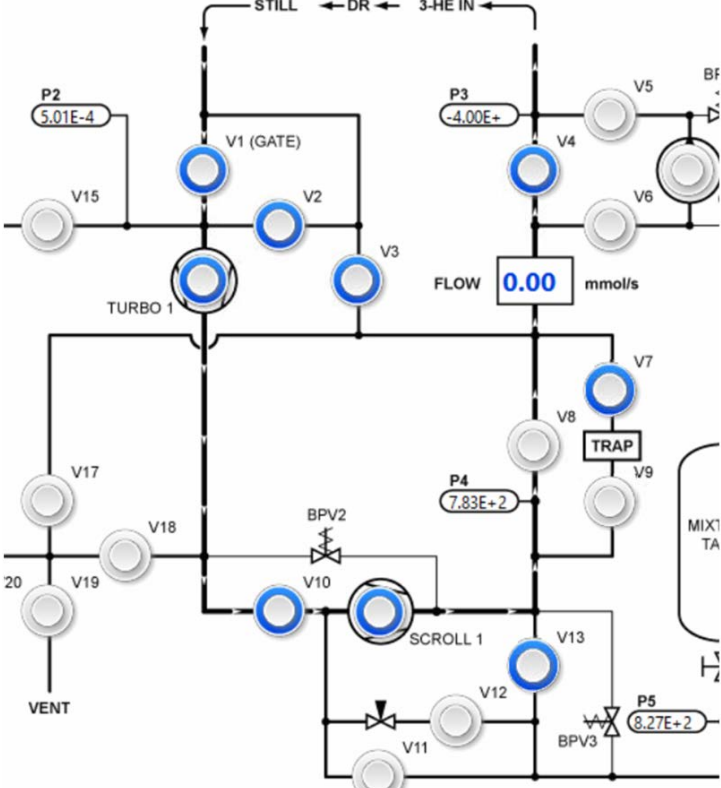
designed to collect any contamination gases that may have leaked into the gas handling system. The first one is the LN2 trap, Fig. [A.14\(A,B\)](#) and the second one is inside of the cryostat on the 50k flange, Fig. [A.14\(C\)](#). The 50K trap is inaccessible to users and is a final filter to prevent icing in the condensing lines. Therefore, we will only focus on the LN2 trap that is accessible to users.

The LN2 trap resided in a LN2 dewar, picture in Fig. [A.14\(A\)](#). This dewar must be constantly refilled about once a week with LN2. If this is not maintained, the trap can warm up and contaminated gas will boil off and into the gas handling system, potentially clogging the condensing lines. If this happens, the entire cryostat will need to be warmed up to pump out the contaminated gases.

The LN2 trap may become clogged after months of continuous condensing. This will be noticeable if the base temperature and/or the P4 pressure begin to rise. The clogging of the carbon filter prevents helium from being able to pass through the LN2 trap and reduces the cooling power of the dilution refrigerator. The following procedure outlines how to clean the traps. There is also a check sheet that should be followed while completing this procedure.

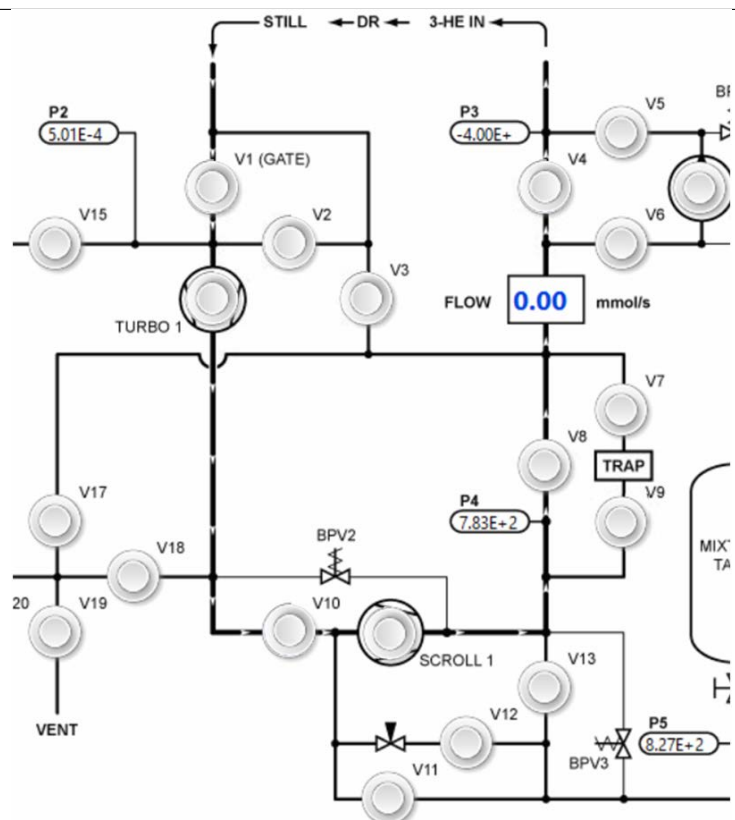


## A.6.1 LN2 Trap Cleaning Procedure:

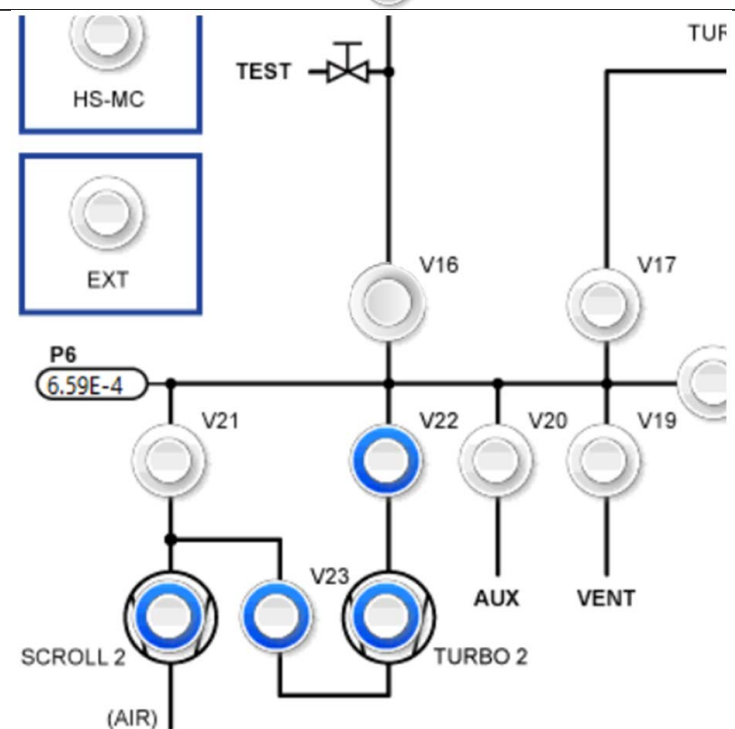
| Details  | Images  |
|--|---|
| <p>1. While the trap is still in the LN2 dewar and cold, pump all of the 3-He/4-He mixture back into the mixture tank.</p> |  |

2. Once the pressures of P3 and P4 reach their minimum and saturate ( $P3 \sim -4$  and  $P4 < 5.01E-4$ ), close all of the valves in the following sequence: V7, V4, V3, V2, V1, Turbo 1, V10, V13, Scroll 1.

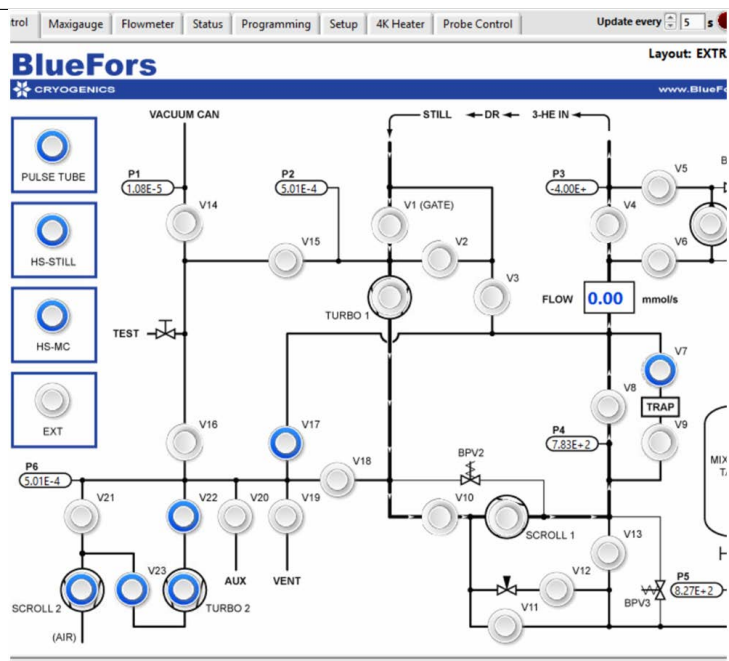
Note:  $P3 = -4$  mBar means the pressure is below the calibration range of the pressure gauge.



3. Turn on Scroll 2, V23, Turbo 2, and V22 to pump on the lines. The pressure on P6 should reach  $< 5.01E-4$  before they are used to pump out the traps. To be careful, you should wait at least 30 minutes after P6 reaches this pressure before pumping on the trap. The trap should be kept in the LN2 during this step.



4. Now open V17. The program will ask you again with a warning box. Press continue and then open V7.



5. Remove the trap from the LN2 dewar.



6. Place the trap in the heat gun assembly on the floor.

The heat gun is set at the correct distance from the trap such that you can leave it running at low power and it won't damage the trap. Set the heat gun to I.

Wait for P6 to reach  $<5.01\text{E-}4$ . This may take some time.

The carbon will warm up in stages and you will see the P6 pressure pulse as gas is released.

Place trap in this holder against the middle rod



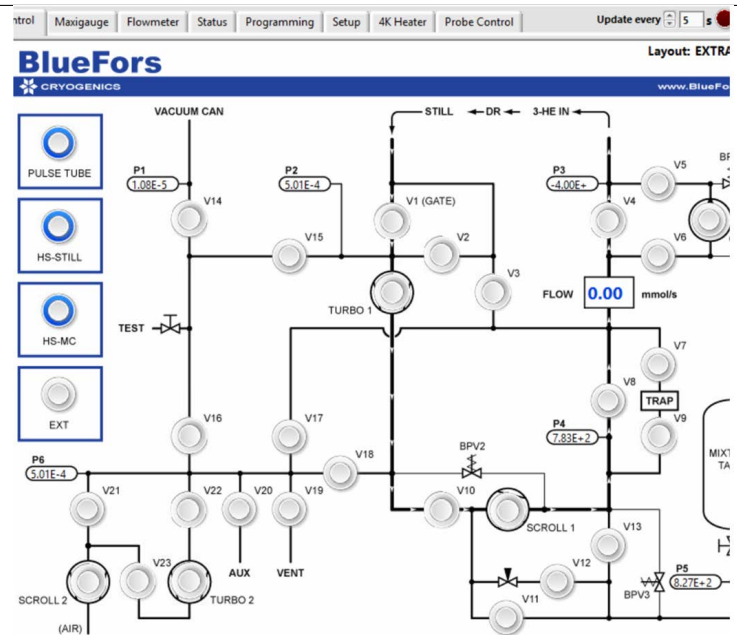
7. Turn off the heat gun and close **V7** and **V17**. Slowly place the trap back inside of the LN2 dewar. Refill the dewar as needed until the trap is cold.



8. Close V22, Turbo 2, V23, and Scroll 2.

Since the trap is still warm right now, it will take some time to cool back down to LN2 temperatures. Wait approximately 30 minutes for the trap to cool down.

**This Completes The Trap Cleaning Procedure**



## A.7 Procedure Check Sheets

All of the procedure check sheets I've written to operate the BlueFors are listed in this section. They can be printed and used as guides for the procedures listed above. These check sheets are intended to walk a user through the basic procedures to operate the BlueFors and to help track any changes that might have occurred over time. As I am the one who wrote these check sheets, these steps are customized for our current BlueFors system. There are many procedures (such as long term maintenance) that are not included in these check sheets and users should reference the BlueFors manual [88] for such details. If the shared Google Drive is still being used by this lab, the PDF or Word versions of the check sheets can be found in the directory: `G:\Shared drives\2DM\03 Equipment\04 BlueFors\00 Binder Logs`.

The primary goal of these check sheets is to avoid mistakes and damage to the BlueFors, and to document changes throughout its use. They should not be treated as absolutes and as the lab changes and new experiments are developed, these check sheets should be adapted as well.



## Probe Loading Check Sheet

User: \_\_\_\_\_ Date: \_\_\_\_\_

01) Is the Dilution Unit cold? ☐Yes ☐No

If "Yes," what are the plate temperatures and pressures?

50k Plate \_\_\_\_\_k Magnet \_\_\_\_\_k MXC Plate \_\_\_\_\_k P4 \_\_\_\_\_mBar

4k Plate \_\_\_\_\_k Still Plate \_\_\_\_\_k P1 \_\_\_\_\_mBar P5 \_\_\_\_\_mBar

If "No," proceed to (Full Cool Down Check Sheet) or continue loading the probe warm.

02) What equipment is installed on the probe?

Sapphire Boards: ☐Yes ☐No Number: \_\_\_\_\_ Wire Holder: ☐Yes ☐No Number: \_\_\_\_\_

DC Wires: ☐Yes ☐No Number: \_\_\_\_\_ RF Cables: ☐Yes ☐No Number: \_\_\_\_\_

Lens Mount: ☐Yes ☐No Lens: \_\_\_\_\_ Objective Mount: ☐Yes ☐No Objective: \_\_\_\_\_

Attocube Stage: ☐Yes ☐No Attocube Holder: ☐Yes ☐No

Sample Holder: ☐Yes ☐No Sample Name: \_\_\_\_\_ Thermometer and Heater: ☐Yes ☐No

Ground Wiring: ☐Yes ☐No Other: \_\_\_\_\_

03) Have the probe thermometer and heater connectors been plugged together? ☐Yes ☐No

04) Has the probe been checked for the proper orientation with the blue alignment piece? ☐Yes ☐No

05) Has the probe been screwed into the radiation shield? ☐Yes ☐No

06) Has the probe been raised to "Home In?" ☐Yes ☐No

07) Have the probe contacts been cleaned with IPA and Graphite? ☐Yes ☐No

08) Has the probe pin been pressed upward at the bottom? ☐Yes ☐No

09) Has the probe been lowered to "Home Out?" ☐Yes ☐No

10) Has the probe O-ring been cleaned on the probe bellows? ☐Yes ☐No

11) Have the probe bellows casters been raised and attached to the gate valve flange? ☐Yes ☐No

12) Has Scroll 2, V21, V20 (AUX), and "pump valve" been opened pumped to P6 <1mBar? ☐Yes ☐No

13) Has V21 been closed and V23, V22, and Turbo 2 been opened to pump P6 <5e-4mBar? ☐Yes ☐No

14) Have the "pump valve," V20, V22, Turbo 2, V23, and Scroll 2 been closed been turned off? ☐Yes ☐No ☐Pumping  
-If Pumping Vacuum Can during probe loading, only close "pump valve" and V20 at this step. Vacuum Can

15) Has the Trap Dewar been filled with LN2? ☐Yes ☐No

16) Has the script 03a full\_probe\_cooldown\_BLP\_Maryland-Hafezi.txt been loaded on the Programming Tab? ☐Yes ☐No

-If Pumping Vacuum Can, use the script: 03 full\_probe\_cooldown\_ChamberPump\_BLP\_Maryland-Hafezi.txt

Click **Run** to start loading sequence.

Date: \_\_\_\_\_ Time: \_\_\_\_\_

**Note (if not Pumping Vacuum Can):** If the P1 pressure rises above 1e-5mBar, the system will not reach <4k.

-Turn on **Scroll 2** and open **V23, V22, V16** and wait until **P6** pressure drops below **1mBar**

-Turn on **Turbo 2** and wait until **P6** drops below **5e-4mBar**

-Open **V14** to pump out the Vacuum Can

-When the MXC temperature reaches <4k, close **V14, V16, V22, Turbo 2, V23, V21, Scroll 2**.

## Probe Unloading Check Sheet User: \_\_\_\_\_ Date: \_\_\_\_\_

**01)** Is the Dilution Unit Condensing? ☐Yes ☐No

If "Yes," what are the plate temperatures and pressures?

**50k Plate** \_\_\_\_\_k **Magnet** \_\_\_\_\_k **MXC Plate** \_\_\_\_\_k **P4** \_\_\_\_\_mBar

**4k Plate** \_\_\_\_\_k **Still Plate** \_\_\_\_\_k **Probe** \_\_\_\_\_k **P5** \_\_\_\_\_mBar

If "No," proceed to (4).

**02)** Has "Turbo 1" been turned off? ☐Yes ☐No ☐ No Condensing

Wait 5 minutes as the Turbos ramp down before proceeding.

**03)** Has V13 been opened? ☐Yes ☐No ☐ No Condensing

**04)** Is the Magnet at 0 Tesla? ☐Yes ☐No

If "No," wait until the Magnet has been ramped to 0 Tesla.

**05)** Has the Pellicle BS been placed back in the imaging system and the sample image been found? ☐Yes ☐No

**06)** Has the Motor been turned On in the "Probe Control" menu? ☐Yes ☐No

**07)** Has the Probe been raised to "Home In" to lock the probe head? ☐Yes ☐No

**08)** Has the Probe been lowered to "Home Out?" ☐Yes ☐No

**09)** Has the "Gate Valve" been closed? ☐Yes ☐No

**10)** Has V9 been closed and V3 opened? ☐Yes ☐No ☐ No Condensing

**11)** Have HS-STILL and HS-MC been turned on? ☐Yes ☐No ☐ No Condensing

**12)** Are V14, V16, V22, Turbo 2, V23, V21, Scroll 2 Turned Off? ☐Yes ☐No

**13)** Has the "aux" and "vent" been pumped out with "Scroll 2" to ~1mBar on P6? ☐Yes ☐No

**14)** Has V21 been closed and "Scroll 2" been turned off? ☐Yes ☐No

**15)** Has the "pump valve" been opened? ☐Yes ☐No

**16)** Has the Probe Bellows been filled with ~100mBar on P6 with N2 through the "vent" to the "aux?" ☐Yes ☐No

**17)** Has V19 been closed? ☐Yes ☐No

Date: \_\_\_\_\_ Time: \_\_\_\_\_

Wait approximately 3 hours to warm-up the Probe to room temperature. Monitor P6 pressure.

**18)** Has the P6 pressure risen to >800mBar through "Aux?" ☐Yes ☐No

**19)** Has the Probe Bellows been filled to ~1100mBar on P6 with N2 through the "vent" to the "aux?" ☐Yes ☐No

**20)** Have the Probe Bellows feet been lower to the floor? ☐Yes ☐No

**21)** Have the 6 screws securing the Probe Bellows to the Gate Valve been removed? ☐Yes ☐No

**22)** Have the Probe Bellows feet been risen such that the casters are movable? ☐Yes ☐No

**23)** Has the Probe Bellows been moved out from underneath the fridge? ☐Yes ☐No

**24)** Has the "pump valve" been closed? ☐Yes ☐No

**25)** Has the "Scroll 2" been used to pump P6 and "aux" below 1e-1mBar? ☐Yes ☐No

**Condensing Check Sheet**    User: \_\_\_\_\_ Date: \_\_\_\_\_

**01)** Is the Probe loaded into the BlueFors? ☐Yes ☐No

**02)** Is the Magnet at 0 Tesla? ☐Yes ☐No

If "Yes," wait until the Magnet has been ramped to 0 Tesla.

**03)** Is the Dilution Unit Cold? ☐Yes ☐No

If "Yes," what are the plate temperatures and pressures?

**50k Plate** \_\_\_\_\_k    **Magnet** \_\_\_\_\_k    **MXC Plate** \_\_\_\_\_k    **P1** \_\_\_\_\_mBar

**4k Plate** \_\_\_\_\_k    **Still Plate** \_\_\_\_\_k    **Probe** \_\_\_\_\_k

**P2** \_\_\_\_\_mBar    **P3** \_\_\_\_\_mBar    **P4** \_\_\_\_\_mBar    **P5** \_\_\_\_\_mBar

If "No," the system must be cold before condensing.

**04)** Has the Trap Dewar been filled with LN2? ☐Yes ☐No

**05)** Has **Still Heater** been set to **15mW** and **Output 2** under **Misc setup** on the software been turned **On**? ☐Yes ☐No

**06)** Has the **Condense\_wLN2\_v1\_24.txt** script been loaded into the BlueFors software? ☐Yes ☐No

**07)** To begin condensing, click **Run** on the software.

Date: \_\_\_\_\_ Time: \_\_\_\_\_

It will take approximately 2 hours for the BlueFors to reach base temperature.

**08)** Has the system reached base temperature while condensing?

**50k Plate** \_\_\_\_\_k    **Magnet** \_\_\_\_\_k    **MXC Plate** \_\_\_\_\_k    **P1** \_\_\_\_\_mBar

**4k Plate** \_\_\_\_\_k    **Still Plate** \_\_\_\_\_k    **Probe** \_\_\_\_\_k

**P2** \_\_\_\_\_mBar    **P3** \_\_\_\_\_mBar    **P4** \_\_\_\_\_mBar    **P5** \_\_\_\_\_mBar

**Notes:**

If the Attocube controller is running with a large sensor voltage, the probe temperature will never reach base temperature. With Sensor Voltage = 2V (No Lockin), the temperature will remain around 800mk. Set the Sensor Voltage = 100mV (Lockin) to reach base temperature of <20mk.

Monitoring the Still temperature will give some indication of the base temperature of the probe. The Still should be around 1k. If the Still is below 1k, that indicates there is a heat load on the probe and/or MXC.

The LED and Laser will raise the probe temperature according to how much power they dump into the sample and sample holder.

**Stop Condensing Check Sheet**    User: \_\_\_\_\_ Date: \_\_\_\_\_

**01)** Is the Dilution Unit Condensing? ☐Yes ☐No

If "Yes," what are the plate temperatures and pressures?

**50k Plate** \_\_\_\_\_k    **Magnet** \_\_\_\_\_k    **MXC Plate** \_\_\_\_\_k    **P4** \_\_\_\_\_mBar

**4k Plate** \_\_\_\_\_k    **Still Plate** \_\_\_\_\_k    **Probe** \_\_\_\_\_k    **P5** \_\_\_\_\_mBar

If "No," proceed to (5).

**02)** Is the Magnet at 0 Tesla? ☐Yes ☐No

If "Yes," wait until the Magnet has been ramped to 0 Tesla.

**03)** Has "Turbo 1" been turned off? ☐Yes ☐No

**04)** Has V13 been opened? ☐Yes ☐No

Wait 5 minutes as the Turbos ramp down before proceeding.

**05)** Has V9 been closed and V3 opened? ☐Yes ☐No

**06)** Have HS-STILL and HS-MC been turned on? ☐Yes ☐No

**07)** Has P5 reached >830mBar? ☐Yes ☐No

**08)** Have V7, V4, V3 been turned off in order? ☐Yes ☐No

**09)** Have V1, V10, V13, Scroll 1 been turned off in order? ☐Yes ☐No

**10)** What are the final pressures?

**P1** \_\_\_\_\_mBar    **P3** \_\_\_\_\_mBar    **P5** \_\_\_\_\_mBar

**P2** \_\_\_\_\_mBar    **P4** \_\_\_\_\_mBar

### Cleaning Trap Check Sheet

User: \_\_\_\_\_ Date: \_\_\_\_\_

- 01) Are all of the Dilution Unit's valves closed and pumps off? ☐ Yes ☐ No
- 02) Is P5 >830mBar? ☐ Yes ☐ No
- 03) Have Scroll 2, V23, Turbo 2, and V22 been opened or turned on? ☐ Yes ☐ No
- 04) Has P6 reached <5e-4mBar and been pumping for an additional 30 minutes? ☐ Yes ☐ No
- 05) Has V17 been opened and then V7 opened? ☐ Yes ☐ No
- 06) Has the Trap been removed from the LN2 Dewar and placed on the floor? ☐ Yes ☐ No
- 07) Has the Heat Gun been turned on and positioned toward the middle of the Trap (Low Heat)? ☐ Yes ☐ No
  - Position the Heat Gun far enough away that it doesn't burn your hand when placed near the trap.
- 08) Has the Trap been pumped until P6 reads <5e-4mBar? ☐ Yes ☐ No
- 09) Has the LN2 Dewar been filled with LN2? ☐ Yes ☐ No
- 10) Has the Heat Gun been turned off? ☐ Yes ☐ No
- 11) Has V7 then V17 been closed? ☐ Yes ☐ No
- 12) Has the Trap been placed (slowly) into the LN2 Dewar? ☐ Yes ☐ No
- 13) Have V22, Turbo 2, V23, and Scroll 2 been closed or turned off? ☐ Yes ☐ No
  - Wait at least 30 minutes before condensing to allow for the Trap to cool.

**Opening BlueFors Check Sheet** User: \_\_\_\_\_ Date: \_\_\_\_\_

01) Is the Dilution Unit Condensing? ☐Yes ☐No

If "Yes," follow the Warm-Up Procedure before proceeding.

02) Has the Still temperature reached >290k? ☐Yes ☐No

03) Have the HS-STILL and HS-MC heaters been turned Off? ☐Yes ☐No

04) Has the Vacuum Can been vented to >1100mBar on P6 via V19, V16, and V14? ☐Yes ☐No

05) Has the Aux bellows been vented to >1100mBar via V20? ☐Yes ☐No

06) Have V19, V16, V14, V20 been closed? ☐Yes ☐No

07) Has the compressed air regulator on the wall behind the control unit been closed? ☐Yes ☐No

**Note: None of the valves can be turned on when the compressed air is closed.**

08) Have the three black compressed air lines, one electrical line, and Aux bellows been disconnected from the Gate Valve? ☐Yes ☐No

09) Have all the legs on the BlueFors Bottom Can been turned to extend toward the floor? ☐Yes ☐No

10) Have the Wing Nuts and Washers on the Bottom Can been removed? ☐Yes ☐No

11) Has the Bottom Can been twisted and removed? ☐Yes ☐No

12) Have the Wing Nuts and Washers on the Middle Can been removed? ☐Yes ☐No

13) Has the Middle Can been twisted, removed, and placed on top of the Bottom Can for storage? ☐Yes ☐No

**If the Cage System is still attached, be careful to avoid hitting the optical breadboard.**

14) Have the screws on the Bottom 50K Shield been removed (Red Metric Key)? ☐Yes ☐No

15) Has the Bottom 50K Shield been twisted, removed, and placed onto foam with a hole? ☐Yes ☐No

16) Have the screws on the Middle 50K Shield been removed (Red Metric Key)? ☐Yes ☐No

17) Has the Middle 50K Shield been twisted, removed, and placed on foam? ☐Yes ☐No

18) Have the 4 Magnet Contact Brass Screws been removed (Using SwissTools M2.5 driver)? ☐Yes ☐No

19) Have the Heater and Thermometer been unplugged from the Magnet and above the Middle 4K Shield? ☐Yes ☐No

20) Has the Lift Jack been raised underneath the Magnet with the probe support entering foam hole? ☐Yes ☐No

21) Have the 10 Magnet support screws been removed (Orange Metric Key)? ☐Yes ☐No

22) Has the Magnet been SLOWLY removed from the fridge? ☐Yes ☐No

**Be careful with the lift jack; it can lower quickly. Avoid this!**

23) Has the Magnet, on the lift jack, been placed somewhere safe in the lab? ☐Yes ☐No

24) Have the screws on the Middle 4K Shield been removed (Orange Metric Key)? ☐Yes ☐No

25) Has the Middle 4K Shield been twisted, removed, and placed on foam? ☐Yes ☐No

25) Has the Still Shield been HELD IN PLACE while the Torx screws are removed? ☐Yes ☐No

**Note: The Shield will FALL if not held while unscrewing**

26) Has the Still Shield been placed upside-down on foam? ☐Yes ☐No



## Warm-Up Check Sheet

User: \_\_\_\_\_ Date: \_\_\_\_\_

**01)** Is the Dilution Unit Condensing? ☐Yes ☐No

If "Yes," follow the Probe Unloading Procedure before proceeding.

If "No," proceed to (4).

**02)** Has the P5 pressure reached 840mBar,  
P4 pressure reached >780mBar, and P2 and P3 pressures dropped below 0.1mBar? ☐Yes ☐No

**03)** Have V7, V4, V3, V1, V10, V13 and Scroll 1 (in this order) been turned Off? ☐Yes ☐No

**04)** Has Heater (Analog/Still) been set to 0mW (press Enter after changing number)? ☐Yes ☐No

**05)** Has the P1 pressure gauge been turned Off? ☐Yes ☐No

**06)** Has the PulseTube been turned Off? ☐Yes ☐No

**07)** Has the 4k Heater been turned on and set to 30V, 2A? ☐Yes ☐No

Date: \_\_\_\_\_ Time: \_\_\_\_\_ (Note: 4K Heater turns off after 15 hours)

### Instructions for Nitrogen exchange gas:

**08)** Has the Still temperature reached >100K? ☐Yes ☐No

**09)** Has Scroll 2, V21, V16, and V19 been turned On? ☐Yes ☐No

**10)** Has P6 reached <1mBar and the N2 line been purged? ☐Yes ☐No

**11)** Have V21 and Scroll 2 been turned Off? ☐Yes ☐No

**12)** Has V14 been opened? ☐Yes ☐No

**13)** Has 100mBar of N2 been vented into the Vacuum Can?" ☐Yes ☐No

**14)** Has V19 been closed? ☐Yes ☐No

Date: \_\_\_\_\_ Time: \_\_\_\_\_ (Monitor that P6 pressure stays <1100mBar)

## Cool-Down Check Sheet User: \_\_\_\_\_ Date: \_\_\_\_\_

01) Are the 50K, 4K, Magnet, and Still temperatures >290k? ☐Yes ☐No

50k Plate \_\_\_\_\_ k Magnet \_\_\_\_\_ k P1 \_\_\_\_\_ mBar P2 \_\_\_\_\_ mBar P4 \_\_\_\_\_ mBar

4k Plate \_\_\_\_\_ k Still Plate \_\_\_\_\_ k P6 \_\_\_\_\_ mBar P3 \_\_\_\_\_ mBar P5 \_\_\_\_\_ mBar

02) Has the 4K Heater been turned Off? ☐Yes ☐No

03) Has Scroll 2, V21, V16, and V14 been turned On? ☐Yes ☐No

04) Has P6 pressure reached <1mBar? ☐Yes ☐No

05) Has P1 pressure gauge been turned On? ☐Yes ☐No

06) Has V21 been closed and V23, Turbo 2, and V22 been turned On? ☐Yes ☐No

Date: \_\_\_\_\_ Time: \_\_\_\_\_

### Process for cleaning the Dilution Unit Lines of contaminates (Assumes all Dilution Unit Valves are Off)

07) Has the Trap Dewar been filled with LN2? ☐Yes ☐No

08) Is V9 turned On? ☐Yes ☐No P2 \_\_\_\_\_ mBar P3 \_\_\_\_\_ mBar P4 \_\_\_\_\_ mBar

09) Has Scroll 1, V10, V1, V2, V3, and V4 been turned On in that order? ☐Yes ☐No

13) Has P2 pressure reached <5mBar? ☐Yes ☐No P2 \_\_\_\_\_ mBar P3 \_\_\_\_\_ mBar P4 \_\_\_\_\_ mBar

14) Has Turbo 1 been turned On? ☐Yes ☐No

- Proceed once P2 is <5e-4mBar. P2 \_\_\_\_\_ mBar P3 \_\_\_\_\_ mBar P4 \_\_\_\_\_ mBar

- Continue pumping on the Dilution Unit throughout the next steps.

- Upon completion on the these steps, it may be necessary to pump the traps. See that form for instructions.

15) Has P1 pressure reached <2.0e-3mBar? ☐Yes ☐No

50k Plate \_\_\_\_\_ k Magnet \_\_\_\_\_ k P1 \_\_\_\_\_ mBar P2 \_\_\_\_\_ mBar P4 \_\_\_\_\_ mBar

4k Plate \_\_\_\_\_ k Still Plate \_\_\_\_\_ k P6 \_\_\_\_\_ mBar P3 \_\_\_\_\_ mBar P5 \_\_\_\_\_ mBar

16) Have the HS-STILL and HS-MC been turned On? ☐Yes ☐No

17) Has the PulseTube been turned On? ☐Yes ☐No

Date: \_\_\_\_\_ Time: \_\_\_\_\_

18) Are the 4K, Magnet, and Still temperatures <5k? ☐Yes ☐No

-Since the Probe isn't installed, these plates are always hotter than 4k during the first cool down.

50k Plate \_\_\_\_\_ k Magnet \_\_\_\_\_ k MXC Plate \_\_\_\_\_ k P2 \_\_\_\_\_ mBar P4 \_\_\_\_\_ mBar

4k Plate \_\_\_\_\_ k Still Plate \_\_\_\_\_ k P1 \_\_\_\_\_ mBar P3 \_\_\_\_\_ mBar P5 \_\_\_\_\_ mBar

Date: \_\_\_\_\_ Time: \_\_\_\_\_

19) Have V14, V16, V22, Turbo 2, V23, Scroll 2 been turned Off in that order? ☐Yes ☐No

20) Have V4, V3, V2, V1, Turbo 1, V10, V9, and Scroll 1 been turned Off in that order? ☐Yes ☐No

## Appendix B: BlueFors Probe

### B.1 Summary

The probe assembly supplied by BlueFors does not include any parts that are necessary for making low temperature optical measurements, see CAD design supplied by BlueFors in Fig. B.1. The only parts fabricated by BlueFors for the probe are the side rods with M3 taps spaced every 10 mm. These allow for equipment to be mounted to the probe, but all of that equipment must be custom designed, machined, and gold-plated by the users. This appendix is meant to outline all of the parts that have been custom-designed for the probe so that free-space optical measurements could be easily made with the BlueFors. All parts were machined by the company Protolabs and gold-plated without an immersion layer (gold on copper) by Alexandria Metal Finishers.

I want to express a special thanks to Daniel Stone who helped in many of these designs. I am grateful to have had his engineering intuition and design skills while we were designing and machining these parts. Also, thanks to Deric Session who spent many hours helping with the soldering and epoxying of the connectors used in the probe.



## B.2 Wiring on the Probe

### B.2.1 Type of Wire Used for the Probe

There are a total of 48 DC lines that can be used in the BlueFors probe. The first set of 24 lines is for the Attocube positioners and the second set is for the DC wiring that connects to the samples. Attocube has their own wiring requirements because of the voltage necessary to drive their positioners. Either contact Attocube to ask for their exact requirements or only use the wire that is supplied by Attocube in their kit.

For the 24 DC lines in the probe, typically the lowest gauge wire available should be used to reduce heat flow. We tried using 36 AWG twisted pair wires from LakeShore (part number: WDT-36-25), but this wire is very difficult to work with without the proper equipment. The difficulty comes from the insulating coating. Using traditional wire stripping methods will always induce some damage to the wire itself. Even if the wire is soldered into place and epoxied with Stycast, the wire eventually breaks. This can be difficult to diagnose especially if it only happens at cryogenic temperature. LakeShore suggests the use of a stripping wheel (part number: ERASER RT2S Wire Stripper). This machine uses a rotating fiberglass wheel to remove the coating on the wire and doesn't induce any damage to the wire itself. If one wants to use this smaller gauge of wire, this machine is necessary.

Instead, we used 32 AWG single strand wire from LakeShore (part number: WSL-32-100) for all of the DC contacts. This wire is much easier to strip without damaging the wire itself and has been working well up to this point.

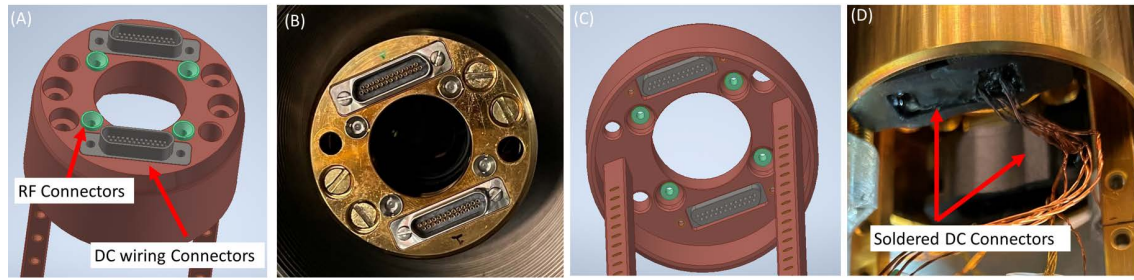


Figure B.2: (A, B) 3D CAD and image of the top of probe head. The 4 RF connectors are shown in green and the two Micro D-Sub 25-pin connectors are shown in grey. The Micro D-Sub connectors on the top of the probe head are **Socket** type. (C, D) 3D CAD and image of the bottom of the probe head. The Micro D-Sub connectors on the bottom of the probe head are **Plug** type.

### B.2.2 On Probe Wiring Configuration

The current wiring configuration of the probe is outlined in Fig. B.4. There are two 25-pin Micro D-Sub connectors for all of the DC wiring utilized in the probe. One connector is exclusively for the Attocube positioners and the other is exclusively for measurements. The break-out connectors needed to be soldered and epoxied so that the wires were accessible for use. This section discusses how this is currently done. Fig. B.4 outlines three important sections on the probe for the wiring.

At the top of the probe, shown in Fig. B.2, there are two 25-pin Micro D-sub **Socket** connectors. These socket connectors plug into the corresponding 25-pin Micro D-sub **Plug** connectors inside of the BlueFors on the Mixing Chamber flange, Fig. D.3(D).

Inside of the probe, there are two 25-pin Micro D-sub **Plug** connectors. These feed-through connectors are used for the breakout of the Attocube and DC wiring. Using 25-pin micro D-sub **Socket** (part number: DCDM-25SSBN-LF), we can solder breakout



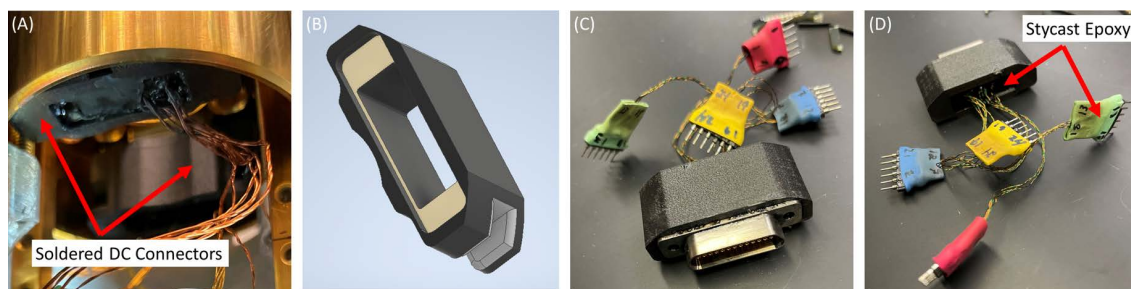


Figure B.3: (A) Image of the bottom of probe head. The black connectors shown here are designed to protect the solder joints on the 25-pin Micro D-Sub breakout connectors. (B) A 3D CAD depiction of this custom adapter. This adapter is printed using Onyx. After the 25-pin Micro D-Sub socket connector has been soldered, it is placed inside of the inset shown here. Then the back of the adapter is filled with Stycast epoxy to secure the solder joints. (C, D) An old version of this breakout connector. This adapter used the wrong wires. We found that the 36 AWG twisted-pair wire is too brittle and often cracks inside of the cryostat. Only use the 32 AWG single strand wire.

wiring. To protect this wiring, we 3D printed adapters that wrap around the connector. These adapters are shown in Fig. B.3(C,D). The backside of the adapter is filled with Stycast 2850 FT cryogenic epoxy to prevent any strain on the solder joints and to help thermalize the wires. This epoxy should be placed on any solder joints for any wiring used in the cryostat. We have had a lot of experience with connectors breaking at the solder joint when this epoxy was not used.

The D-sub connector for the Attocube wiring breaks out into three 5-pin 2mm pitch SIP connectors (part number: BLY1.50Z). These are shown in Fig. B.4(C). They connect to their corresponding Attocube plugs at this junction. The bottom wiring connects to the Attocube positioners. Each of the Attocube positioner's wiring is color coded. To add additional Attocube components, a new D-sub connector will need to be made because the current one only has the break-out wiring for the three positioners.

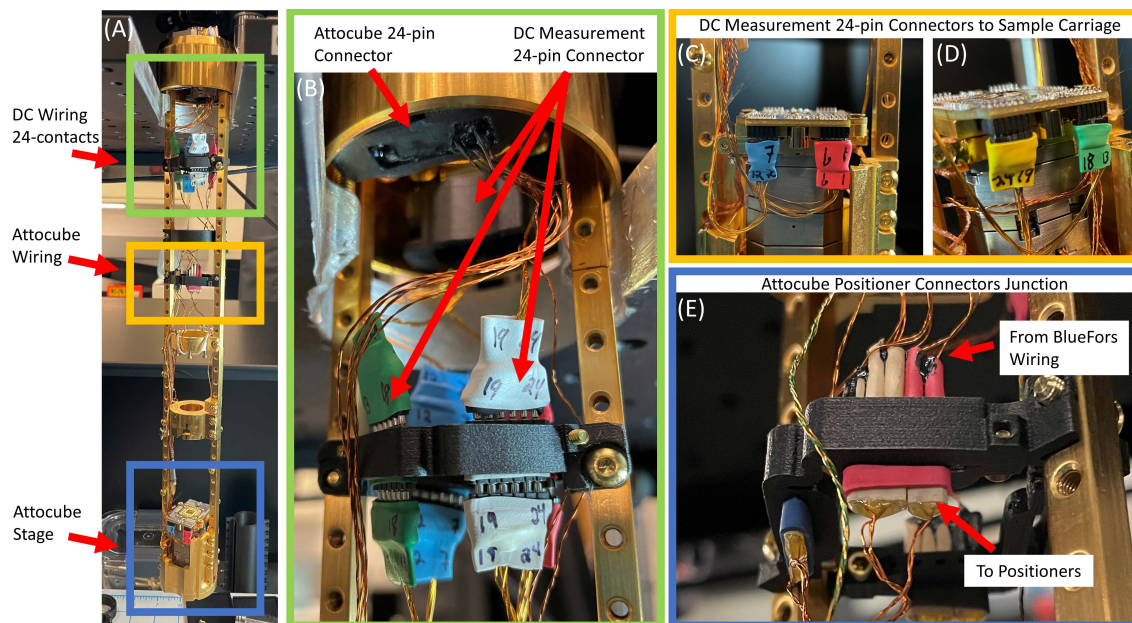


Figure B.4: (A) Full image of the probe. Important junction points for the DC and Attocube wiring are outlined. (B) Inside of the probe are two 25-pin Micro-D connectors. One of these connectors (labeled with an A) is for the Attocubes and the other is for the DC wiring used for gating or transport measurements of samples. These are shown as black nylon plugs. We 3D printed the black nylon adapters so that it was easy to insert and remove these connectors. The soldering inside the plugs are covered by Stycast epoxy to secure them and avoid damage. The Attocube connector currently only has 15-pin soldered. The DC measurement connector has all 24-pin soldered. The DC measurement wires break-out into four 6-pin connectors that attach to the probe junction shown here. (C) The Attocube wiring runs to another junction on the probe where the wiring connects to the wiring of the Attocube positioners. (D) The DC measurement wires run from the junction to the sample holder.

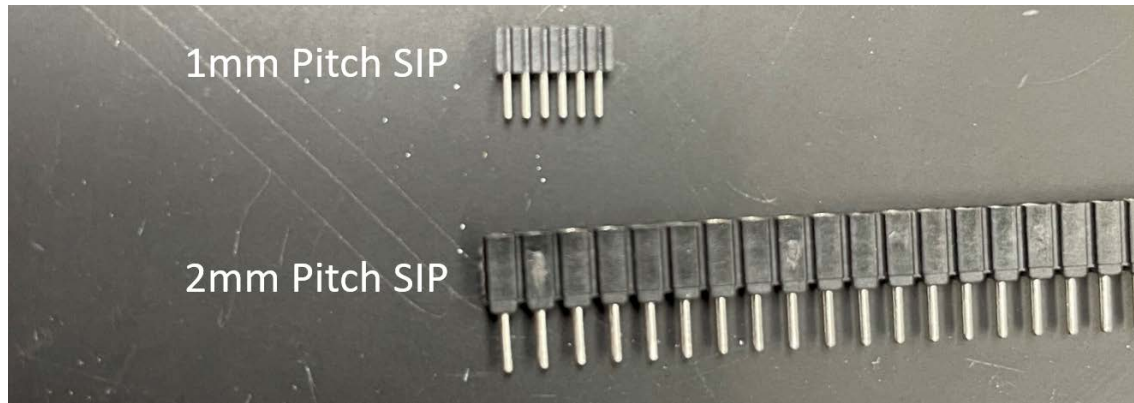


Figure B.5: The SIP connectors throughout the probe have a 2 mm pitch (bottom). The sample carriage required SIP connectors with a 1 mm pitch (top).

The D-sub connector for the DC wiring breaks out into four 6-pin 2mm pitch SIP connectors. These are shown in Fig. B.4(B). They plug into this 3D printed junction. On the other end of the junction is another wire that runs to the carriage board. Since the process of making a 25-pin micro D-sub connector is expensive and complicated, this intermediate wiring was used so that the top wiring doesn't have to be handled often. There are four intermediate cables with a 6-pin 2 mm pitch SIP connector on one end and 6-pin 1 mm pitch SIP connector on the other.

The SIP connectors on the carriage board are different from the other SIP connectors on the probe. The 6-pin SIP connectors on the carriage board have a 1 mm pitch, shown in Fig. B.5. This makes them smaller and more difficult to solder/handle. Be careful while inserting them into the carriage boards. Be sure to also pay careful attention to the numbering of the carriage board so that all of the contacts are connected to the corresponding wire bonding pads. 1 mm pitch SIP connectors can be purchased

as 50-pin connectors (part number: 861-87-050-10-001101) and then cut down to 6-pins connectors. Cutting these connectors can be tricky because of their small size. We had purchased 500 of the 6-pin 1 mm pitch SIP version (part number: 861-83-006-10-001101). Since these are pre-cut to 6-pins, they are much easier to work with. Unfortunately, they are not stocked by any company and must be custom ordered.

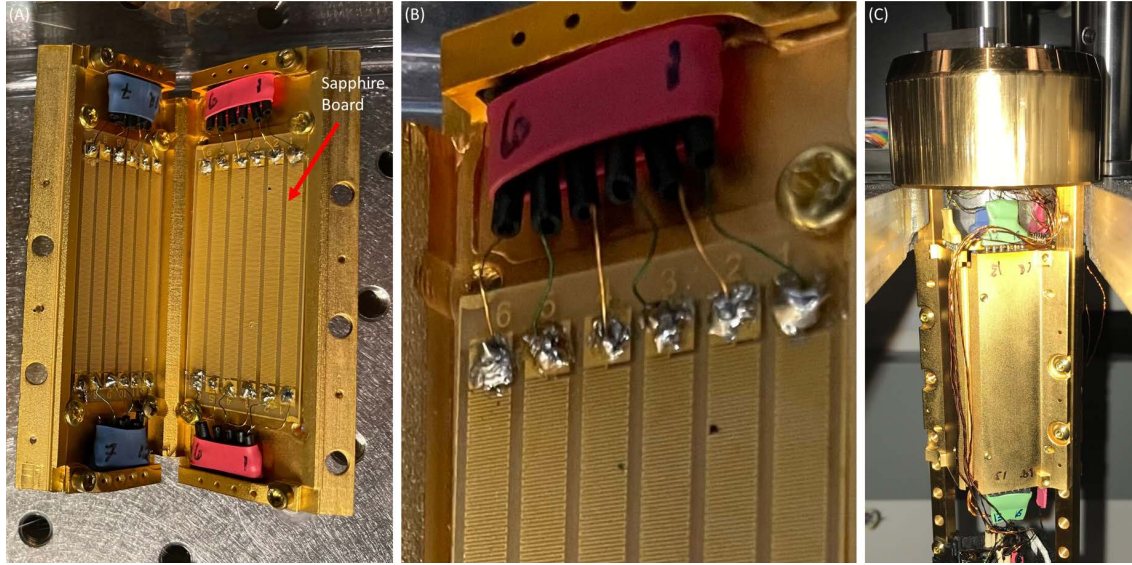


Figure B.6: (A) Image of the sapphire boards installed in their probe mount. There are a total of four sapphire boards with one meander line for each of the 24 contacts. The probe holder is gold-plated copper. 2 mm pitch SIP connectors are held on the top and bottom of the holder. Wires from the connectors are soldered using standard lead-solder to contact pads on the sapphire boards. (B) Close up view of the meander lines on the surface of the sapphire board as well as the soldered pads. (C) The sapphire board holder mounted on the probe.

### B.2.3 Sapphire Boards

In an effort to maximize the thermalization of the DC wiring in the probe, a set of sapphire boards were fabricated using photolithography and Ti/Au metal deposition, see Fig. B.6. These boards break out the DC wiring into a series of meander lines on the surface of a sapphire wafer. Sapphire is a unique material that has both a high electrical resistivity and high thermal conductivity. This makes it an ideal candidate as an insulating material at low temperatures. Since the wires provide a direct thermal link from 300 K to  $<100$  mK, without good thermalization of the wires, electrons injected into the sample

will have a higher energy than desired. In nearly all measurements conducted in this lab thus far, this is not a problem because we have thus far only used the wiring for gating or simple transport measurement. It only becomes critical for very sensitive materials, such as transport measurements of superconductors.

Although we fabricated these sapphire boards, we have never needed to use them, but they are available if there is ever a need for them in the future.



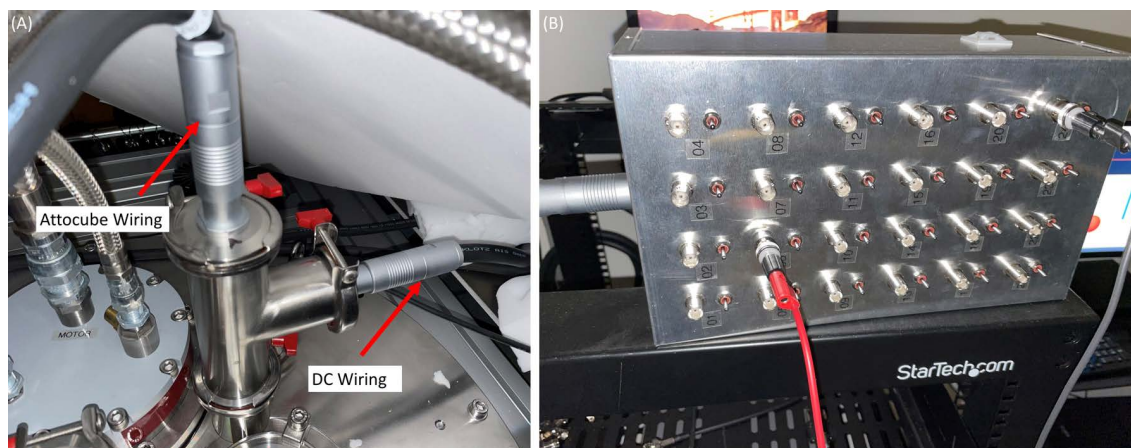


Figure B.7: (A) Exit flange for both sets of wiring in the BlueFors. The top Fischer connector is the wiring of the Attocube positioners and the side Fischer connector is the DC measurement wiring. (B) Break-out box from the Fischer connector to BNC connectors. Note the switches for each BNC connector. Pressed to the right (in this image) grounds the BNC contact. Setting the switch to the center position for measurements.

## B.2.4 Break-out DC wiring outside the BlueFors

There are two different kinds of connectors used for the wiring of the BlueFors. The connectors inside of the BlueFors and shown on the probe are Micro D-sub 25-pin socket connectors (part number: DCDM-25SSBN-LF). The connectors on the outside of the BlueFors, see Fig. B.7(A), are 24-pin Fischer connectors. These connectors can be difficult to solder and properly ground. Turn-key measurement cables with these connectors pre-installed can be ordered from CMR-direct (Product Code: 05-11-150). There are two 24-pin Fischer connectors on this system. One is for the Attocube positioners and the other is for DC measurements.

From the Fischer connectors, the DC measurement wiring must pass through a break-out box. An image of the current break-out box is shown in Fig. B.7(B). Using



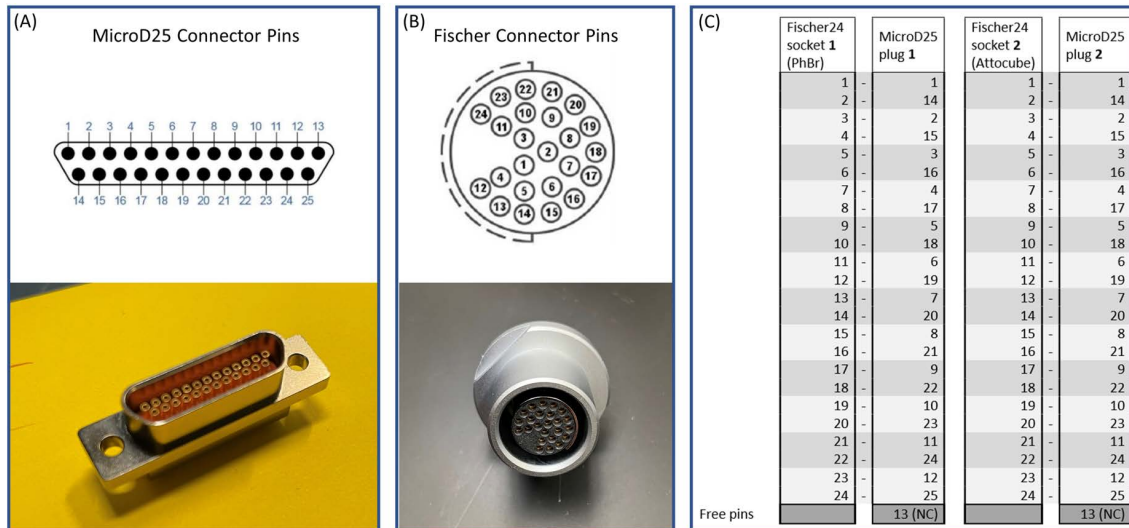


Figure B.8: (A) Pin numbering for the micro D-sub connector. (B) Pin numbering for the Fischer connector. (C) Wiring configuration of the two connectors in the BlueFors.

the pin layout in Fig. B.8, the wiring from the Fischer connector can be coded to the numbering of the micro D-sub connectors on the probe. The numbers on the break-out box correspond to the numbers written on the connectors seen in Fig. B.4.

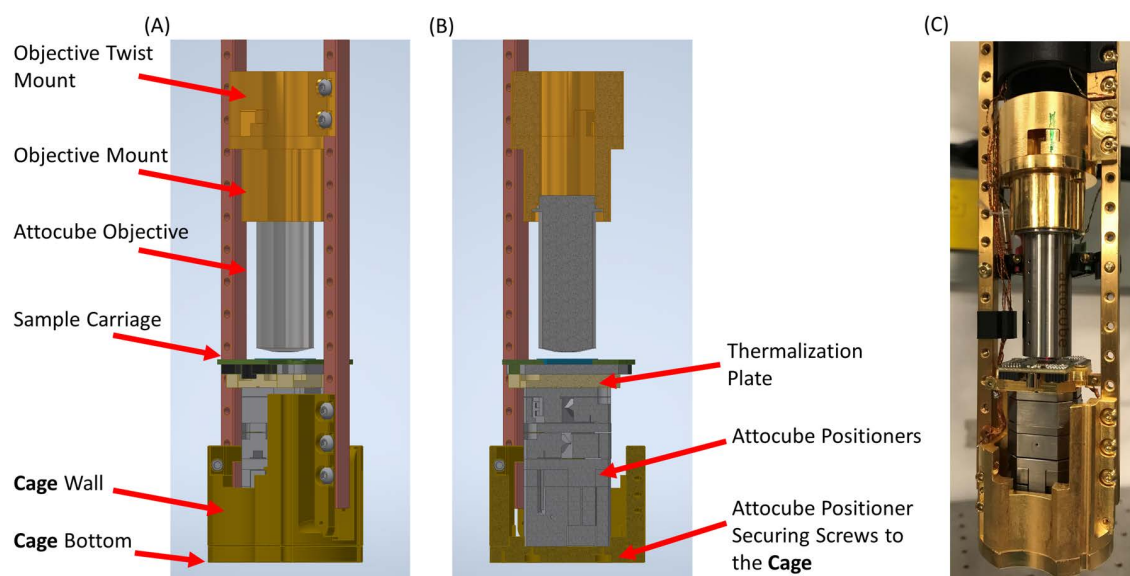


Figure B.9: (A,B) The custom 3D design of the holders for the Attocube and Objective. This is the most important part of the probe design. The sample is placed such that it is within 1 mm of the magnetic field center. The objective adapter that has two parts makes it easy to mount and dismount while also making sure it is always at the same position on the probe. (C) Image of the probe with the machined parts installed.

## B.3 Sample Positioning

### B.3.1 Cage Assembly

The first part of the probe that required designing was the sample holder and objective mounts. These are depicted in Fig. B.9. The assembly to hold the Attocube positioner, called the cage, is shown in Fig. B.9 extended 16.5 mm down from the end of the probe rods. The walls of the cage are secured to the probe rods. The bottom of the cage allows for the Attocube positioners to be secured in the center of the probe. This is illustrated in Fig. B.10(A).

On top of the Attocubes, we have installed a thermalization plate. This is similar to the design that is used by Montana on our Montana cryostat. The slip-stick design of the Attocube positioners makes them very poor thermal conductors. Therefore, to cool down the sample stage on top of the Attocube stack we needed a thermal link between the cage and the sample holder. The thermalization plate is designed with two extended clamps. Copper braids are connected on both sides of the thermalization plate and connect to the walls of the cage (there are three tapped holes on either side for this contact.) This assembly is shown in Fig. [B.10\(B\)](#).

Although this design has worked well enough in these measurements, this should be considered something to improve when trying to further optimize this system. The copper braids are not gold-plated nor soldered to their end points (as done by Montana or Attocube for their cryostats). If one would like to optimize thermal contact to the sample, consider contacting Attocube for a solution. They are the experts and have the tools necessary to make the parts for optimizing the thermal link.

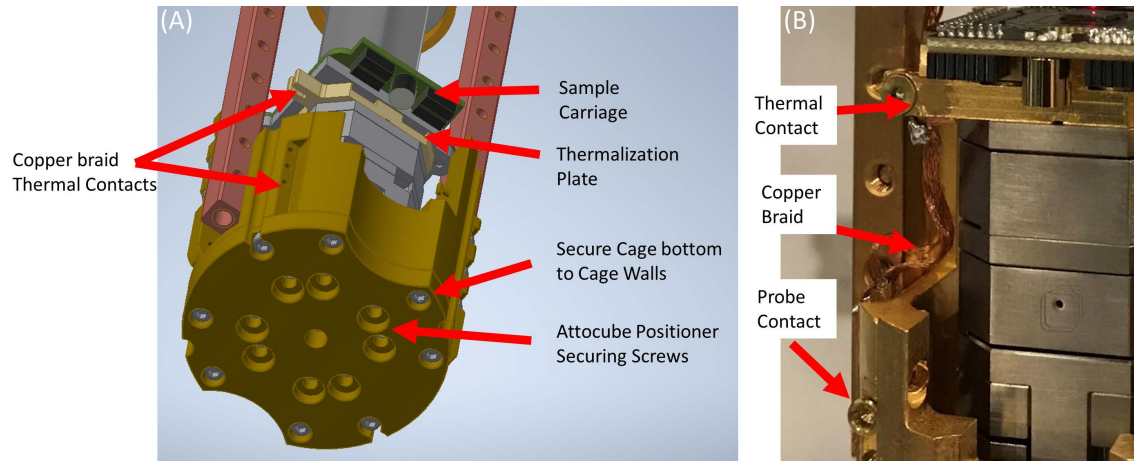


Figure B.10: (A) 3D CAD of the bottom cage assembly. There are 8 central counterbored holes for securing the bottom Attocube positioner. To allow for the positioner to be oriented in any direction, eight counterbored holes were made (only two are ever needed, but if for some reason the positioners need to be rotated 90 deg, this is possible). The other eight counterbored holes connect the bottom of the cage to the wall. (B) Copper braid thermal links are installed on either side of the thermalization plate. These copper braids are held in place through lead soldered joints and a set screw. The braids run to the walls of the cage and are held in place similarly.

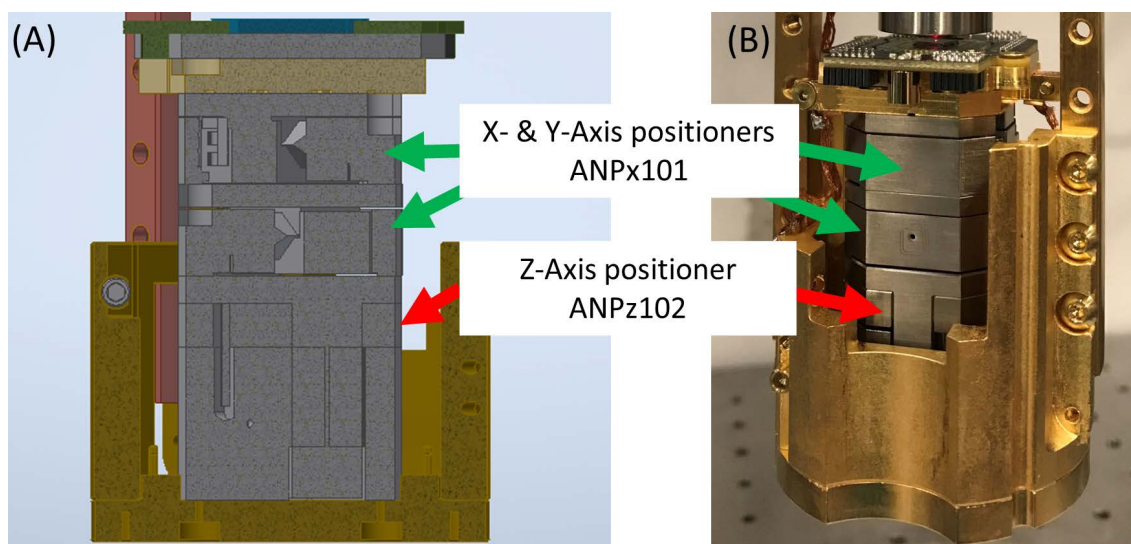


Figure B.11: (A) 3D CAD schematic of the Attocube positioners in the probe holder. Cross-sectional cut shown. (B) Image of the Attocube positioners installed in the probe holder. There are two ANPx101 to move the sample in the x-y directions (total motion 5mm x 5mm). There is one ANPz102 to move the sample in the z-direction for focusing.

### B.3.2 Attocube Positioners

The Attocube stack consists of two ANPx101/RES+/LT/HV and one ANPz102/RES+/LT/HV with a ANC350/3/RES/Vac Piezo Motion Controller. These allow for moving the sample while it is inside of the BlueFors dilution refrigerator. The current stack is shown in Fig. B.11 and allows for 5 mm X 5 mm motion in the x and y directions with micron steps as well as z-axis motion for focusing the sample and the objective.

The wiring inside of the probe, discussed in more detail later, is shown in Fig. B.4. The 25-pin micro D-Sub connector is plugged into the top of the probe, Fig. B.4(B). The wiring from this connector breaks out into three 2 mm pitch SIP connectors. There is a



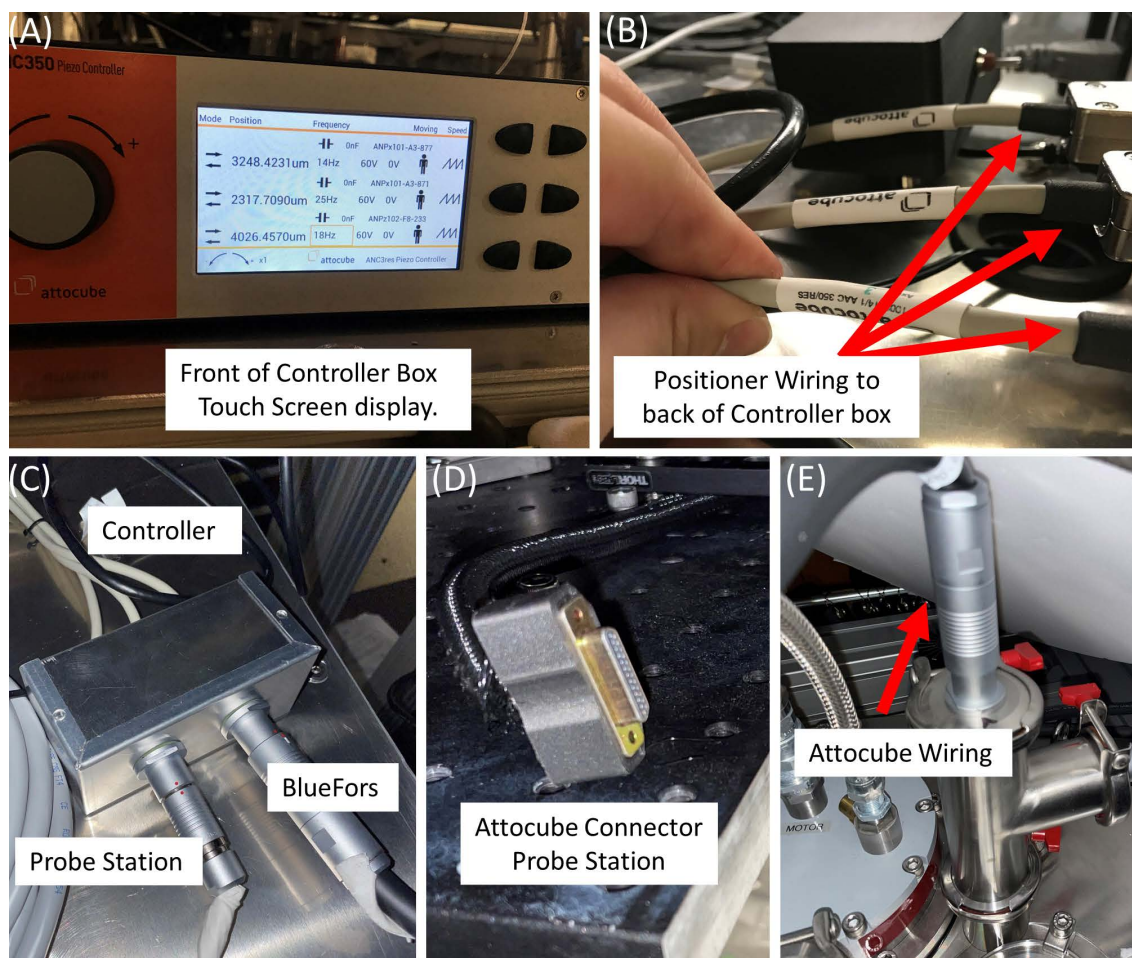


Figure B.12: (A) The ANC350 controller box with touch screen. The positioners can be moved and controlled using this box. The box can also be connected to a computer via the USB on its back. The controller box can be remote controlled by Attocube's Daisy software or VISA commands. (B) Wiring for each of the positioners connected into the back of the ANC350 controller box. Each wire should be numbered. Currently, we have 3 = z-axis. (C) Attocube wiring junction box. The BlueFors and Probe Station connectors are wired in parallel through this junction box to the controller box. Therefore, no wiring has to be changed when the Probe is moved from the BlueFors to the probe station. (D) 25-pin micro D-sub connector on the probe station. (E) 24-pin connector for the Attocube that enters through the top of the BlueFors.

SIP connector junction in the middle of the probe where the Attocube wiring connects to the break out wiring from the D-Sub connector, Fig. B.4(C).

The wiring outside of the cryostat is shown in Fig. B.12. The Attocube wiring exits the cryostat through the top 24-pin connector shown in Fig. B.12(E). This cable connects to the junction box shown in Fig. B.12(C) where the wiring breaks out to the 2 mm SIP connectors on the Attocube wiring provided for the controller box. There is one wire for each positioner and they connect to the back of the controller box, Fig. B.12(B). The controller box allows you to move the sample using the buttons the front panel, Fig. B.12(A). You can also use the Daisy software supplied by Attocube by connecting the ANC350 controller box to a computer via USB.

An important detail about the ANPx101/RES+/LT/HV and ANPz102/RES+/LT/HV Attocubes is that they have a feedback resistor installed that is always being read by the Attocube controller box. This will add a very large heat load to the probe if it is left to its normal operation. The default heat load by the feedback loop is so large that the probe will not be able to reach below 800 mK. This feature cannot be turned off. Even if the output is off, it is always sending a signal to the potentiometers on the Attocubes and heating the sample. One solution is unplug the wiring while a measurement is being made. This is very inconvenient and prevents any motion of the sample at lowest temperature. The other option is to change the sensor voltage used to read-out the potentiometers. This can be done on the Daisy software, Fig. B.13(B). The default voltage is 2 V. You can reduce this to a minimum of 100mV and lockin mode which will allow for base temperatures around 25 mK, but the accuracy of the positioners will be very low and noisy.



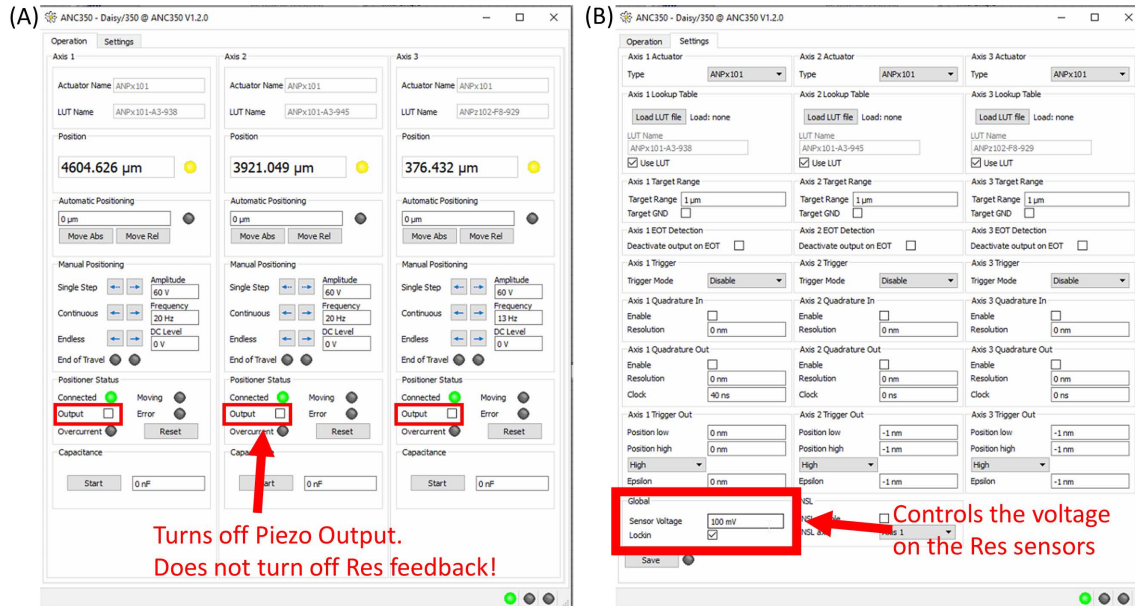


Figure B.13: (A) The positioners can be controlled using the Attocube Daisy software. Everything that can be done on the controller box can be done on the software. Note: Turning off the Output does not turn off the feedback voltage to the resistor in the positioners. (B) On the Settings tab, the sensor voltage can be changed. The most accurate is to use the maximum voltage of 2 V, which is the default. If this is used in the BlueFors, the sample will not get colder than 800 mK. Using a minimum sensor voltage of 100 mV and Lockin mode will allow the probe to reach  $\sim 25$  mK, but the accuracy of the feedback position will be very low (a few microns).

### B.3.3 Additional Attocube Stages

Adding additional Attocube positioning stages is possible. We currently have a x-y stepper, part number ANSxy100lr/LT/HV, that allows for very fine (nanometer) positioning. The system does not have feedback and I have been told it can drift, but it is far more precise than the slip-stick positioners. Since the objective can only be moved up in 10 mm steps because of how the probe is threaded, you will need to either make a new thermal plate to allow for the sample to be within range of the objective or get lucky that the additional stage is exactly 10 mm thick. In the case of the x-y steppers, this is the case. It is exactly 10 mm thick and the objective only needs to be moved up one step.

Installing the x-y steppers also requires changes to the wiring. First, you will need to solder a new 25-pin micro D-sub connector, Fig. B.4(B), since it is currently only soldered for the 15-pins of the 3 positioners. Second, you will need to modify the junction box in Fig. B.12(C). Both the BlueFors and probe station cables utilize all 24-pins, but the soldering inside the junction box needs to be soldered to account for the new stepper wiring. Finally, you will also potentially need to modify the copper braids that thermally connect the thermal contact under the sample to the probe stage depending on if it is long enough, Fig. B.10(B).

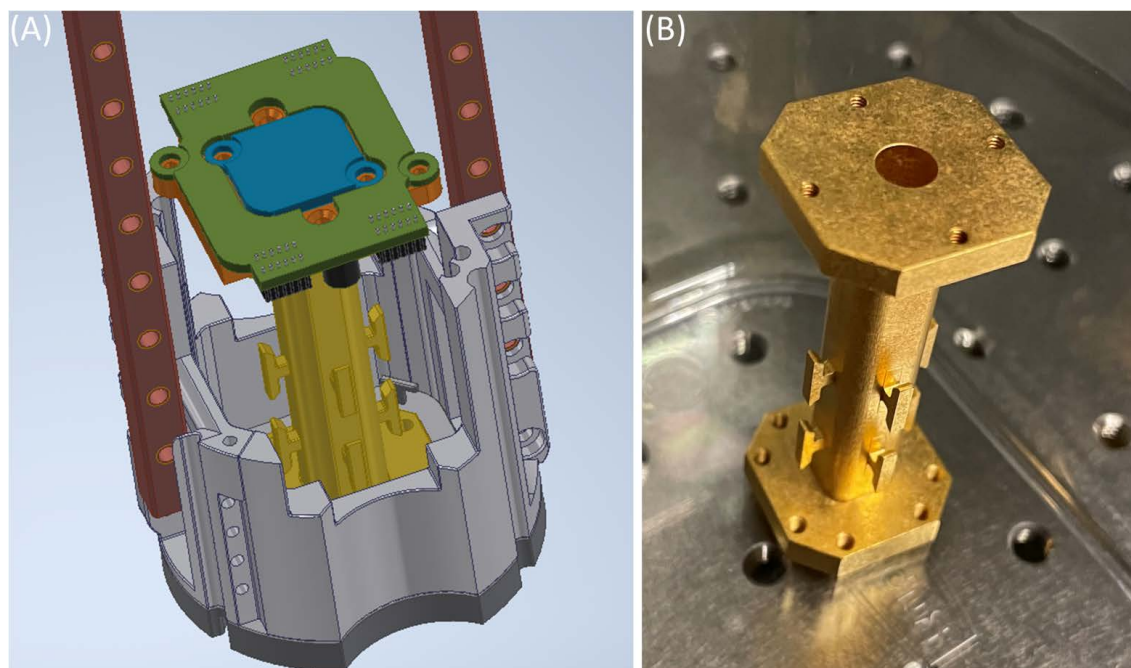


Figure B.14: (A) Blank Stage Mount 3D CAD presented in the cage assembly. (B) The blank stage mount machined out of copper and gold plated.

### B.3.4 Blank Stage Mount

In the event that some measurement did not require positioning (such as an electrical transport measurement), we also machined a blank holder, machined out of copper and gold plated, that can be placed in the probe cage assembly. This is the exact same height as the Attocube positioner stack so that the sample is at the magnetic center. The blank stage mount also has the same M2 tapped hole configuration as the Attocube positioners so the sample carriage can be secured to the top. 3D CAD of the holder in the probe cage assembly is shown in Fig. [B.14](#).

## B.4 Probe Optics

### B.4.1 Objective Mount Assembly

The objective was another component that required a lot of thought. Since the objective needs to be extremely close to the sample, we do not have much clearance to remove it. The z-axis Attocube positioner allows us to move the sample away from the objective, but we set the mount heights such that the sample would be in focus when the z-axis position was approximately in the middle of its full span, about 2.5 mm. Therefore, we can only move the sample down about 2.5 mm. This gives very little clearance for a human to remove the objective from the probe. It certainly could not be unscrewed from its RMS thread every time. Daniel Stone and I came up with the following solution to make sure that the objective never touches the sample and that it is always placed in the correct position when re-installed.

The probe objective mount is composed of two parts depicted in Fig. B.9 and Fig. B.15. The top attaches to the probe rods and is never removed. The bottom is the objective mount with an RMS threading. The Attocube objective can be screwed into this mount. It should not be removed often! Copper is a very soft metal and constantly unscrewing and screwing the objective will wear down the threads.

To remove the objective from the probe: **(1)** Lower the z-axis Attocube positioner to the lowest it will go. **(2)** Remove the three screws securing it to the top mount (shown in Fig. B.15(A)). **(3)** Twist the bottom mount and carefully remove it horizontally, depicted in Fig. B.15(B,C). Mounting the objective is the same procedure, only in reverse.

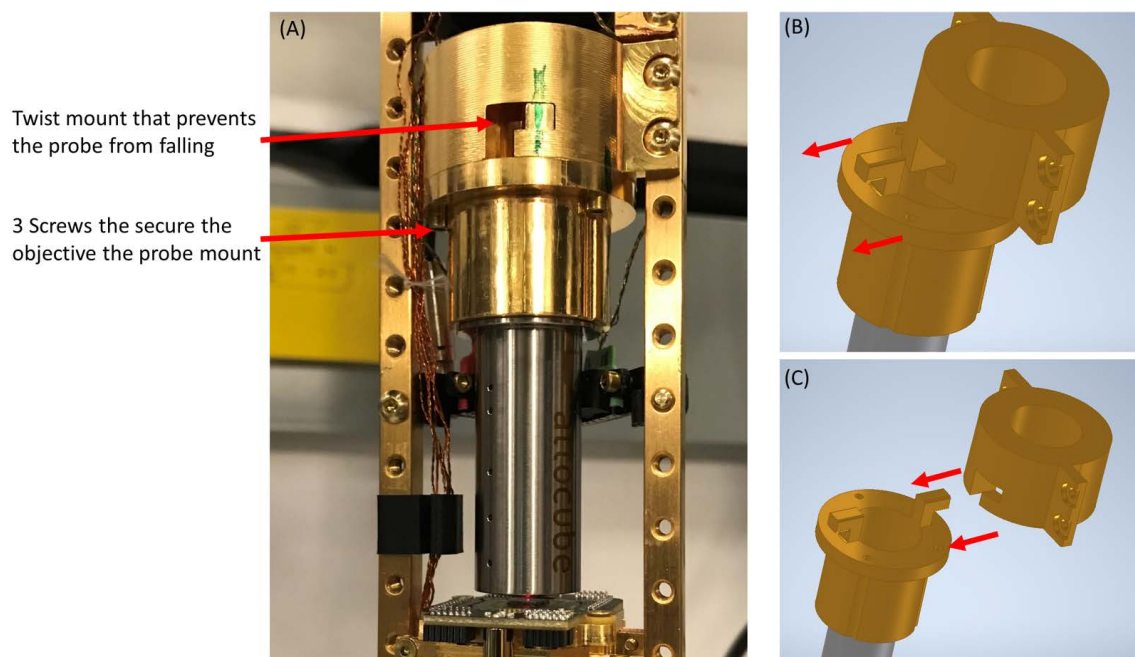


Figure B.15: (A) Image of the objective mount in the probe. There are three screws that secure the objective mount to the probe mount. When these three screws are removed, the probe will not fall because of the twist mount. (B,C) To remove the objective mount, twist the objective mount out of the  $\Gamma$ -shaped slot and slide it out of the probe mount. Be careful to not tilt the objective mount while removing it.

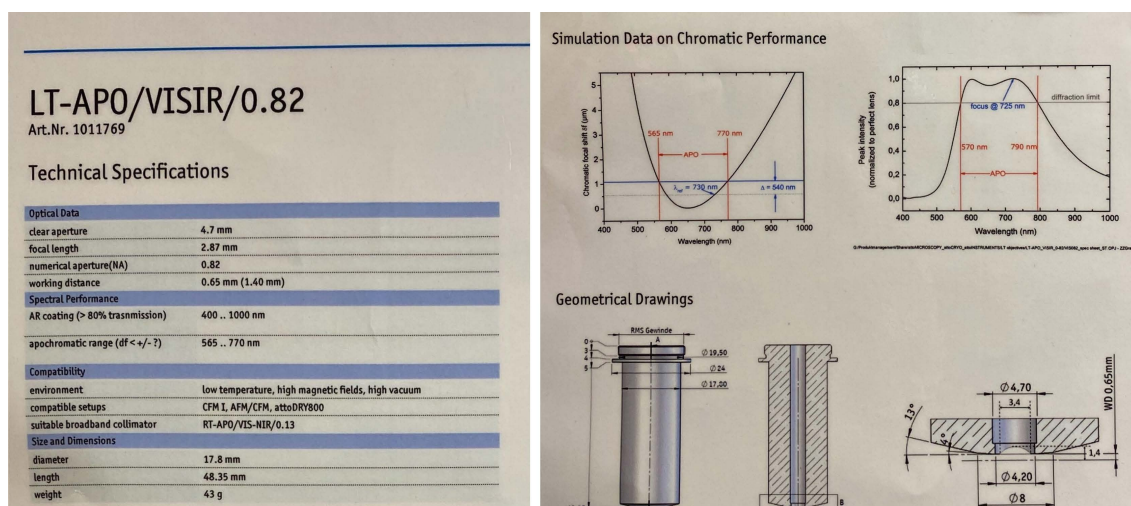


Figure B.16: Spec sheet supplied by Attocube for the objective used in the BlueFors Dilution refrigerator.

## B.4.2 Attocube Objective

The objective used on the probe is a specially made objective from Attocube that is capable of handling high magnetic fields, ultra-low temperatures, and high vacuum. Its specifications are listed in Fig. B.16. This objective is very expensive and must be handled with care which is why there was so much thought put into the mount design. The objective should remain screwed into the probe mount at all times to avoid damage to the RMS threading of the probe mount.

The objective has a working distance of 1.4 mm, but its design places a 0.75 mm lip at the bottom. This means that there is only 0.65 mm clearance between the bottom of the objective and the sample (which is the working distance listed on the spec sheet in Fig. B.16).



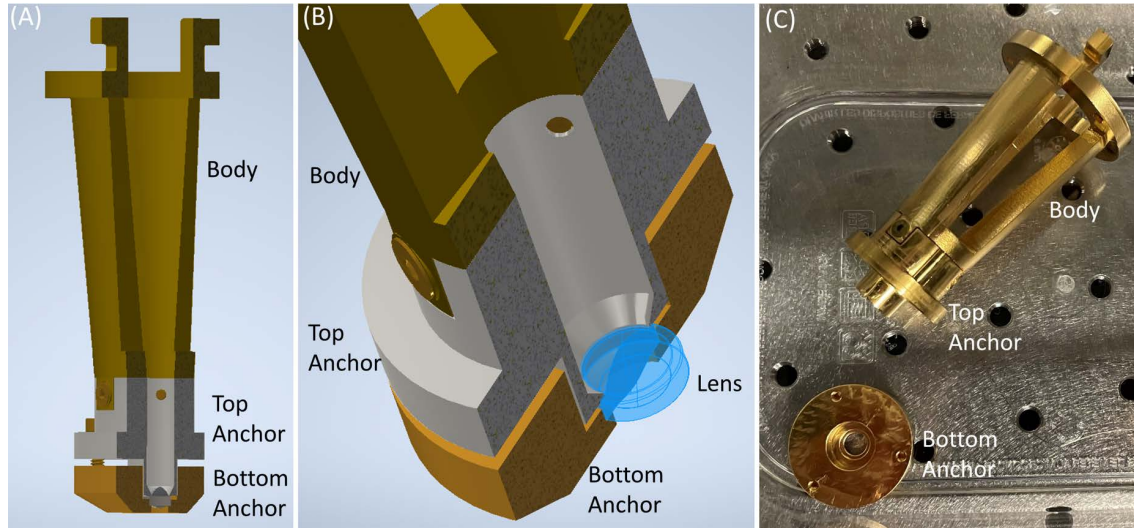


Figure B.17: Lens mount for 6.325 mm diameter and 1.556 mm edge thickness lenses. This fits into the same twist mount shown in Fig. B.15 and is machined to the exact length such that a 3.1 mm focal length lens will be at the same position as the working distance of the Attocube objective. Therefore, no changes are necessary to swap the lens and objective holders. (A) 3D CAD sectional visualization of the lens mount. There are three parts: body, top anchor, and bottom anchor. The design is intended to allow for different anchor systems to be used if different lenses were utilized. (B) Close up of the lens clamping anchors. (C) Image of the gold plated machined parts.

### B.4.3 Lens Mount Assembly

In addition to the objective mount, we machined an adapter for a lens that was used by Bin Cao in his Attocube cryostat measurements. The lens is an unmounted aspheric lens from Thorlabs, part number: 354330-B, with a focal length of 3.1 mm and NA of 0.7. It has a diameter of 6.325 mm and edge thickness of 1.556 mm. Therefore, we designed the mount, shown in Fig. B.17, such that the focal point would be the same for the lens mount as the working distance of the objective (i.e. the lens mount had to be shorter in length) so that they are easily swapped. We have never used this system, but it is available.

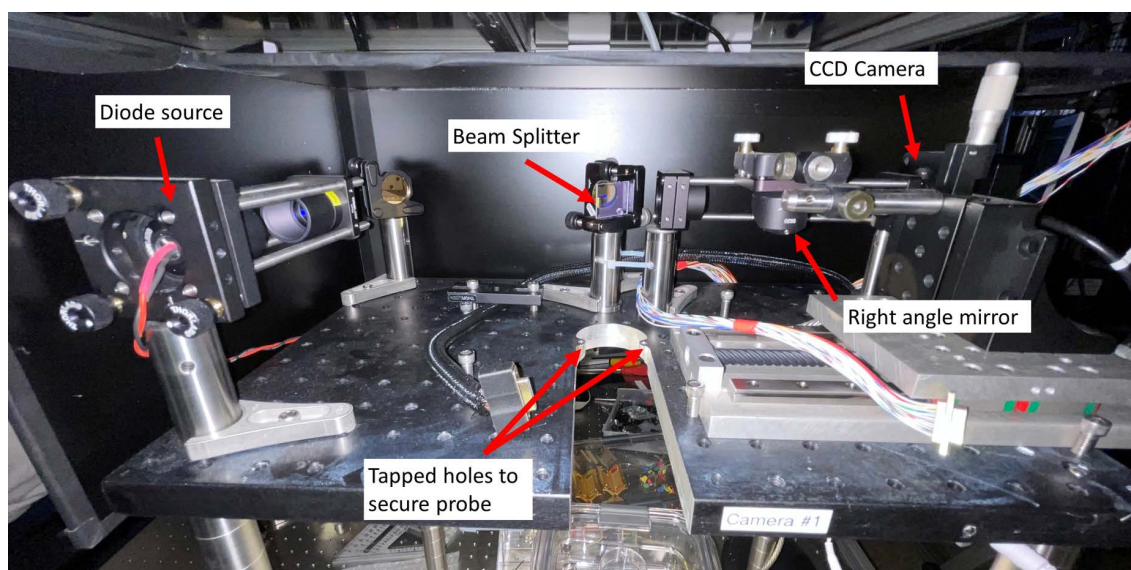


Figure B.18: This breadboard has been machined to allow the probe to be placed in the middle and secured via two tapped holes. Once the probe is in place, the right angle mirror can be moved above it and the diode source can be used to image the sample with the objective inside the probe. The image is collected on the CCD camera behind the right angle mirror's stage.

## B.5 Probe Testing Station

The easiest means of working on the BlueFors probe is to place it in the probe testing station that we had machined out of an optical breadboard, shown in Fig. B.18. The milled region is designed to allow for the probe to be secured at the center of the optical breadboard. This setup also allows for imaging of the sample via a diode source and CCD camera. Once the probe is placed in the optical breadboard (Fig. B.4(A)), the right angle mirror should be moved to its maximum position and the diode turned on. This will allow for imaging of the sample's surface if the objective is in place.

The Attocube positioners can be controlled to adjust the alignment and position

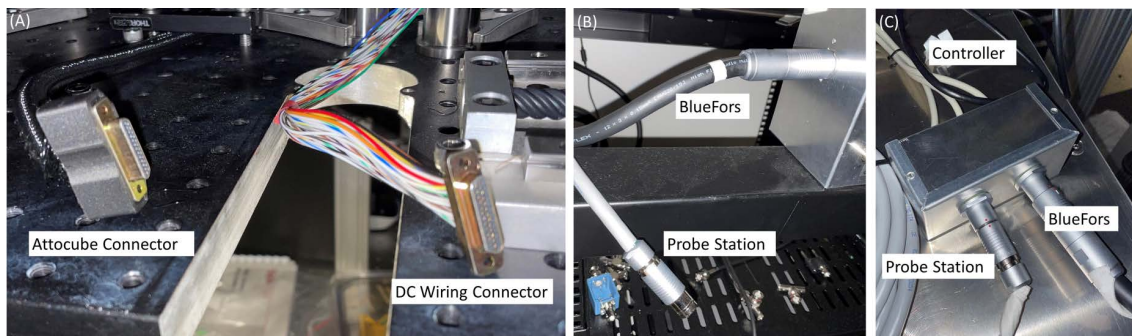


Figure B.19: (A) The probe can be tested in the probe testing station by connecting these micro D-sub 25-pin Plug connectors into the top socket connectors on the probe. **Do not mix them up.** If the Attocube controller box is connected to the DC measurement lines, it can damage your sample. The left, black connector is the Attocube wiring and should be connected to the socket connector labeled **A** on the probe. See Fig. B.2 for labeling. (B) To test the DC contacts to a sample on the probe, the Fischer connectors must be switched on the break-out box. (C) The Attocube's wiring for the BlueFors and Probe Station are soldered together. Nothing needs to be changed on this junction box.

of the sample by connecting the Attocube connector to the top D-sub connector on the probe head. Refer to Fig. B.2(B) and Fig. B.19(A). The micro D-sub 25-pin socket connector with **A** written next to it on the probe head corresponds to the Attocube wiring. Connect the micro D-sub 25-pin plug labeled "Attocube Connector" to this socket. Now the Attocube can be controlled with the controller box. The junction box in Fig. B.19(C) connects the controller box to the BlueFors wiring and the Probe station wiring. Therefore, the only connection that needs to be made is through the micro D-sub connectors.

To connect the DC wiring for device testing, first check the break-out box and make sure that the Probe Station connector is connected instead of the BlueFors connector, shown in Fig. B.19(B). If your device is sensitive to static charge, ground all of the

contacts on the break-out box before connecting the DC wiring Plug into the micro D-sub 25-pin socket on the probe. The correct socket on the probe is shown in Fig. [B.2\(B\)](#) with a "1" label. The sample can now be tested.

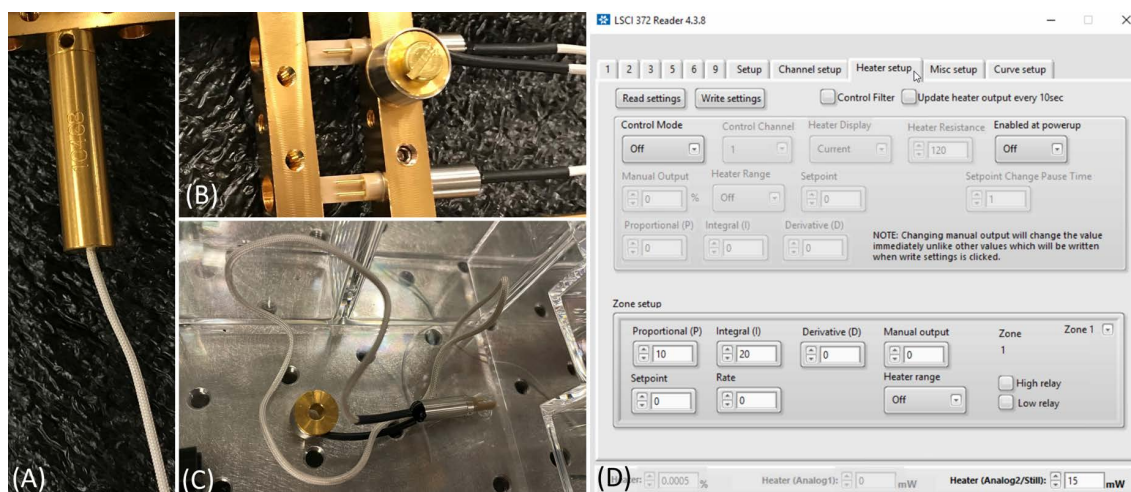


Figure B.20: (A) RuO<sub>2</sub> RX-102B Lakeshore thermometer calibrated and supplied by BlueFors to measure the temperature of the probe. Currently, the thermometer is attached next to the objective mount. (B,C) The heater supplied by BlueFors for the probe is a 120 Ohm resistive heater. I have not conducted any temperature dependent measurements and have not used this heater. It can be controlled by the PID software in (D), but I do not have any experience with this software.

## B.6 Thermometer and Heater

To measure the temperature of the probe, we use a RuO<sub>2</sub> thermometer manufactured by LakeShore, part number: RX-102B, and calibrated by BlueFors, Fig. B.20(A). It is connected to the LakeShore LS372 resistance bridge and readout via that module. Something important to know about these thermometers is that a current must be sent through the RuO<sub>2</sub> to measure its resistance. This will generate heat and making the measurements too often will cause the thermometer to become a heater. Therefore, the resistance bridge only measures the temperature every so often and not continuously.

There is also a 120 Ohm resistive heater that can be used with the probe,

Fig. B.20(B,C). I have personally never used the heater, but it also connects to the same LakeShore LS372 resistance bridge and can be controlled via the LSCI372 Reader software supplied by BlueFors, Fig. B.20(D). This software allows the user to set a temperature and use the PID loop to control the current through the heater to reach that set temperature. In addition to this program, one could directly connect to the LakeShore LS372 and control it using their own software.



## Appendix C: Sample Stage Design

### C.1 Outline of Chip Carrier and Carriage System

There are commercially available sample holders from companies like Spectrum Semiconductor Materials, Inc., but these packages tend to be bulky and we had very specific requirements for the BlueFors that needed to be met. Therefore, we decided to design our own sample stages to meet these constraints. We also wanted the design to be universally used in our other measurement systems (such as the Montana cryostat.)

The first problem that required a custom sample holder design was due to the Attocube objective requiring a very small working distance ( $WD = 0.65$  mm.) Nearly all commercially available packages have the sample placed within the holder with the gold-plated contact pads of the holder above the sample. This means that the wire bonds must be extended upward from the sample. Our objective will need to be placed dangerously close to the wires from the wire bonds to be able to focus on the sample. Our solution was to inverse this configuration with the sample placed at the top of the assembly and the wire bonds extending down. A diagram of this configuration is shown in Fig.C.1(A). Wire bonds require some loop radius, but with some practice this can be easily done.

The second problem was the relatively small space we had available from the bottom of the probe to the magnetic field center, refer to Fig. B.1. Note that the magnetic

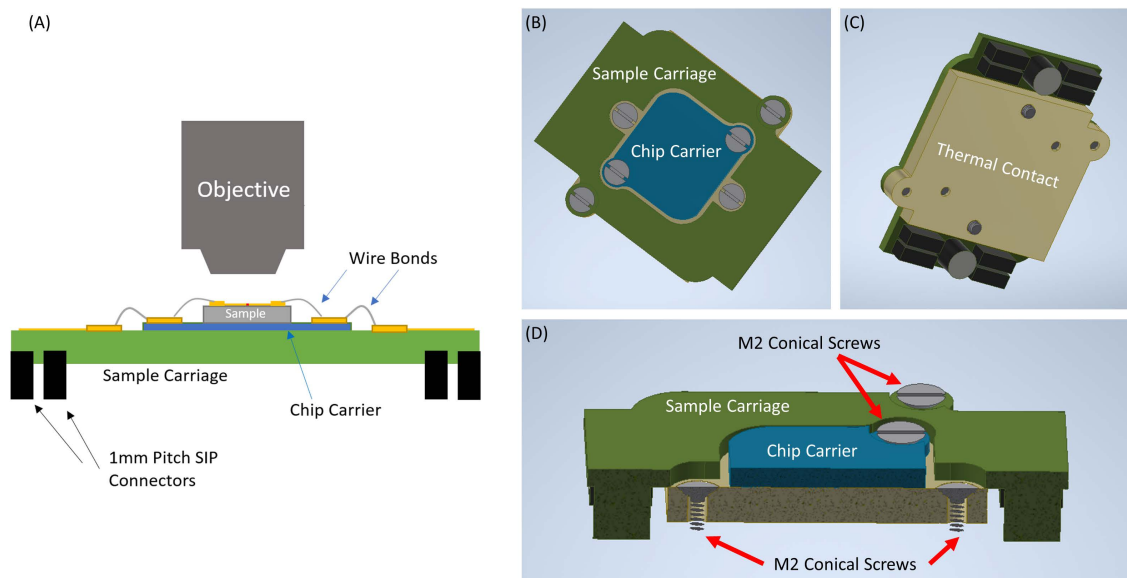


Figure C.1: (A) Cross-sectional profile schematic of the Sample Carriage and Chip Carrier with a wire bonded sample and the Attocube objective. (B) 3D CAD top view of the Chip Carrier and Sample Carriage screwed into the Thermal Contact. (C) 3D CAD bottom view of the Thermal Contact with the connectors extended on the side. (D) 3D CAD cross-sectional profile of the sample system. Conical M2 screws secure the Sample Carriage and Chip Carrier boards to the Thermal Contact. Two additional M2 conical screws are placed in the drilled holes of the Thermal Contact. These are positioned such that they can be screwed directly into the Attocubes or the Thermalization Plate in Fig. B.10. NOTE: All screws are shown as conical flat heads, but in practice we only use conical hex heads.

field center is not at the center of the probe. Therefore, all of the probe adapters, Attocube positioners, and the sample mount must be able to fit within the space below the magnetic field center. For the probe system to have the sample as close to the field center as possible, we needed to make the sample holder very thin. The total thickness of our design is less than 5 mm including the gold-plated copper thermal contact which the carriage and chip carrier sit upon. In comparison, DIP packages require at least 10 mm without including the wiring.

In addition to designing the sample holder to the requirements of the BlueFors, we also wanted the design to work with any of our cryostats (we only had the Montana cryostat at the time of the design, but most future cryostats can be designed to accommodate this sample holder.) This helps reduce the need for additional wire bonding of samples which tends to be a point of significant failure in sample fabrication (oxide punch-through, static discharge destroying samples, etc.). The best solution to this problem was to wire bond the samples only once. Therefore, we have designed a two stage sample contact system: (1) **chip carriers** and (2) **sample carriages**.

The idea for this system is to have the actual sample wire bonded to a chip carrier that is simpler and cheaper to manufacture. These are small and easy to store. There are numbered gold-plated bond pads on the chip carriers for wire bonding the sample. These pads do not connect to anything and are meant to be intermediate bond pads. This means that the sample can be bonded to these pads and never disconnected. Then all future wiring bonding is only between the bond pads on the chip carriers and the bond pads on the sample carriage. The sample does not need to ever be directly wire bonded again. In my experience, one of the most frustrating problems with wire bonding is oxide punch-

through. Repeated bonding to the same spot on the sample will increase the chances of punch-through. This solves that problem by eliminating the need for ever removing and re-bonding samples.

The chip carrier is then placed in the center of the sample carriage and secured to the thermal contact. The sample carriage is a larger electronic board that is assembled with 24 DC SIP connectors, 2 RF connectors, and 15 kHz low-pass filters on the DC lines. The numbered bond pads on the sample carriage are wire bonded to the corresponding numbered bond pads on the chip carrier. This will connect the sample to either the DC connectors or the RF connectors for measurements. The full sample stage can be placed on an Attocube positioner or the thermalization plate, Fig. [B.9](#), and the connectors on the sample carriage will extend over the edge to allow the user to connect wiring to the DC and/or RF connectors.

## C.2 Chip Carriers and Sample Carriages

### C.2.1 Manufacturing of the PCB Boards

Both the sample carriage and chip carrier PCB boards were manufactured by PCB Unlimited using FR4 Tg175 as the base material. The carriage boards are 1.5 mm thick and the chip carriers are 1.7 mm thick. The metal contacts are 1 oz thick copper that is plated with 30 microinches of soft gold without a nickel immersion layer.

The manufactured sample carriage board is shown in Fig. [C.2\(A,B\)](#). The sample carriage has 24 DC wire bonding pads connected to four 6-pin 1 mm pitch SIP connectors that extend out the bottom of the carriage board. These are the same 1 mm pitch

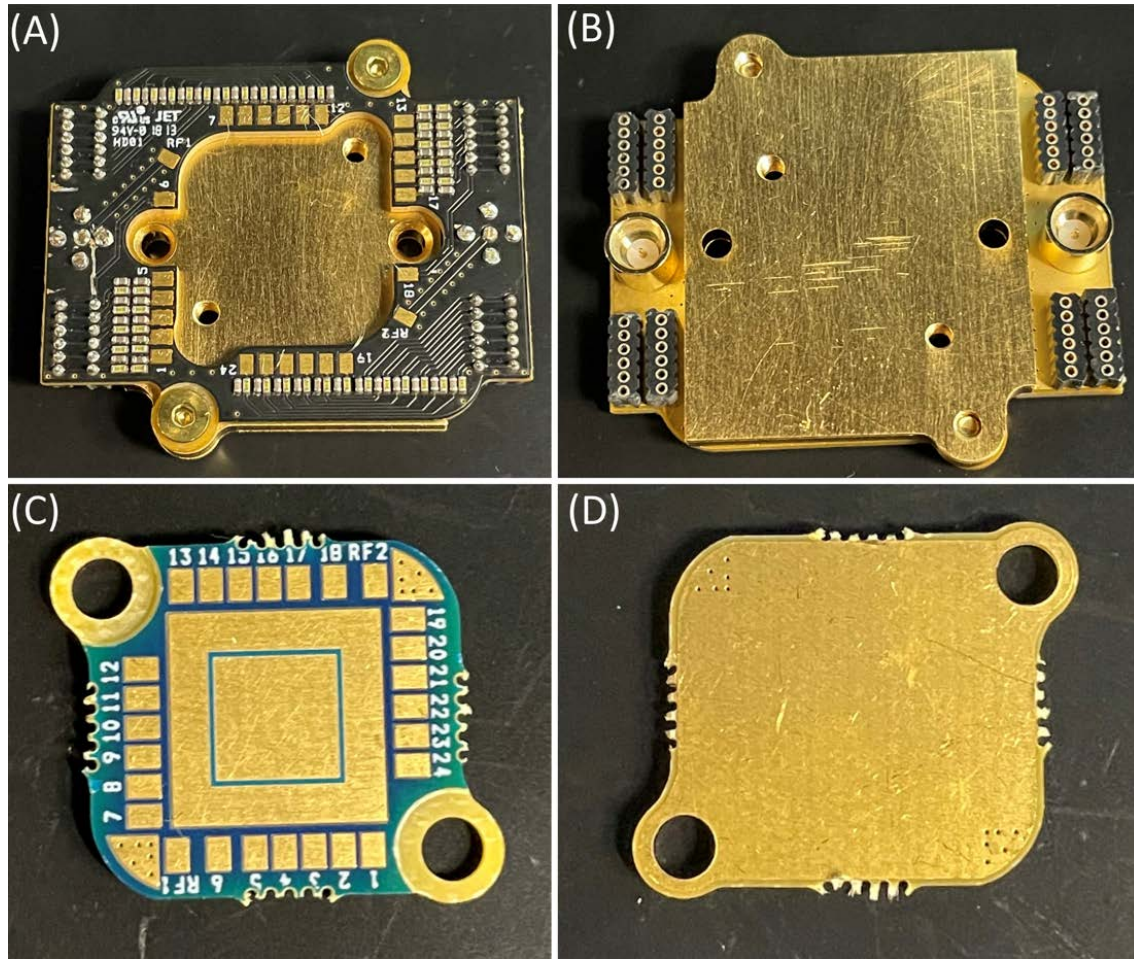


Figure C.2: The chip carriers and sample carriages were manufactured from the schematics illustrated in Fig. C.1. (A,B) Top and bottom of the carriage board installed on the thermal contact (gold-plated copper). On the back of the carriage, the 1 mm pitch SIP connectors are accessible as well as two SMP connectors for high frequency applications. (C,D) Top and bottom of the chip carrier. 5 mm x 5 mm soldermask outline in the center is only for guidance for where the Attocube positioners can move. It does not isolate the gold-plated copper in the center from the outside; i.e. silver pasted contacts to the center can be connected via wire bonds to the outer metal.

SIP connectors discussed in Fig. B.5. The selected low pass filters have a -3 dB cutoff at  $\sim 15$  kHz. They consist of a 5 kOhm resistor, Mouser part number: 754-RR0510P-4991D, and a 2.2 nF capacitor, Mouser part number: 80-C0402C222J3GACTU. The SMP connectors are rated up to 18 GHz, Pasternack part number: PE44348. The 1 mm pitch SIP connectors are from digikey with part number: 861-87-050-10-001101.

Note that there are a pair of SIP connectors for each pin Fig. C.2(B). These are connected to one another and both correspond to the same pins. The reasoning behind having a second set of connectors is to allow for grounding wiring from the probe while it is being loaded into the BlueFors. Without the grounding wire, the DC contacts are floating until the probe reaches the mixing chamber and connects to the internal D-Sub connectors in the BlueFors. Since this is done while the probe is hotter than the rest of the BlueFors wiring, there is some concern about static discharge when the contacts meet. The solution to this would be to have the carriage board grounded through a second set of wiring out the bottom of the probe that will disconnect whenever the probe is detached.

Ultimately, the grounding wiring was never used because we have not experienced any issues with devices being destroyed as the probe is loaded. This is possibly due to the nature of our devices and their durability. I have been told from BlueFors that it is of greater concern for superconducting devices that have high conductance which can be easily destroyed by small static discharges.

The manufactured chip carrier is shown in Fig. C.2(C,D). These are easier to have made because they do not require any additional assembly. There are currently 500 of them available. The idea is to have a sample wire bonded to a chip carrier once and never wire bonded again. This protects the device from oxide punch-through or static discharge.



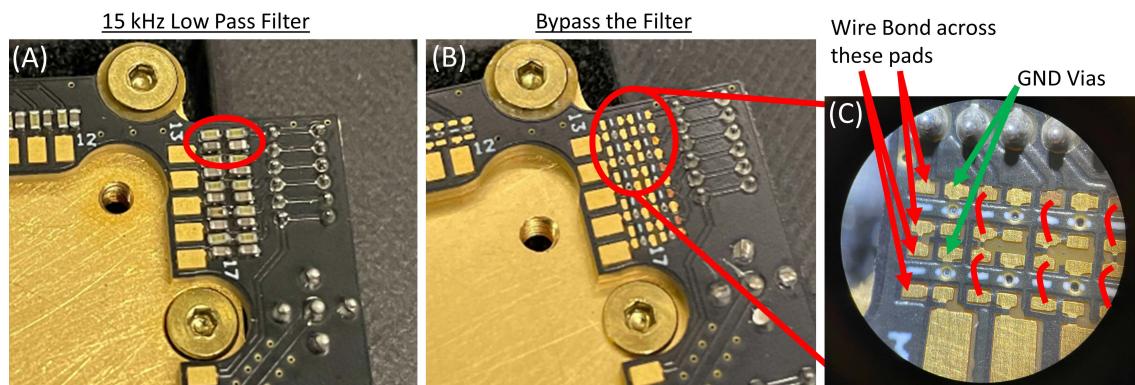


Figure C.3: There are two available types of sample carriages. I choose to leave five carriages without their low-pass filters being assembled. The other 12 have the two sets of 15 kHz RC low pass filters for each DC line except 6 and 18. (A) The carriage boards with the low pass filters will look identical to this board. There are two sets of the 15 kHz low pass filters in series. This increases the edge attenuation of the low-pass filter and further reduces high frequency thermal noise from reaching the sample. These components are only rated to 25 VDC and cannot be used for high voltage gating. DC lines 6 and 18 do not have filters so that they can be used for high voltage gating. (B) The other five carriages without filters are the same PCB board as in (A), but without the RC components soldered to the contacts. Therefore, you can wire bond across the resistor pads to bypass the gaps. The pads that must be wire bonded are in (C). Note that some of the pads are grounding and should be avoided.

## C.2.2 Two types of Carriage Boards

There are two available sample carriages that can be used when making measurements. 12 sample carriages have 15 kHz low-pass RC filters and 5 sample carriages that do not. The 5 that do not require wire bonding to connect the 1 mm SIP connectors to the numbered bond pads. Both options are shown in Fig. C.3. Since the RC components, Fig. C.3(A), in the 15 kHz lowpass filters are only rated to 25 VDC, they cannot be used for applications that require high gate voltages. There are two contacts on

all of the sample carriages that do not have RC components, 6 and 18. They can be used for gating if high voltage gates are necessary.

The RC low-pass filters are to reduce high frequency thermal noise or Nyquist noise. Since we have electrical contacts that connect 300 K to  $<100$  mK, there can be thermal noise from the higher temperature electronic components outside of the fridge that increase the electron temperature. Also, at dilution refrigerator temperatures, nearly all of the cooling of the sample comes through the wiring. Therefore, removing this thermal noise is helpful for reaching the lowest possible sample temperatures. This tends to be very important for superconducting samples [89].

If more gates are needed for a certain application, the 5 sample carriage boards that do not have the RC filters can be used, Fig. C.3(B). Since these sample carriages are not different from the ones with RC components, the only difference being that the filters are not installed, you will need to bridge the contacts where the resistors should be located to connect the SIP connector to the numbered bond pad. This can be done by wire bonding (many times) the labeled contacts in Fig. C.3(C). Note that the RC filters require a grounding contact for the capacitor to dump high frequency noise, so some of the exposed contacts are grounded and should be avoided.

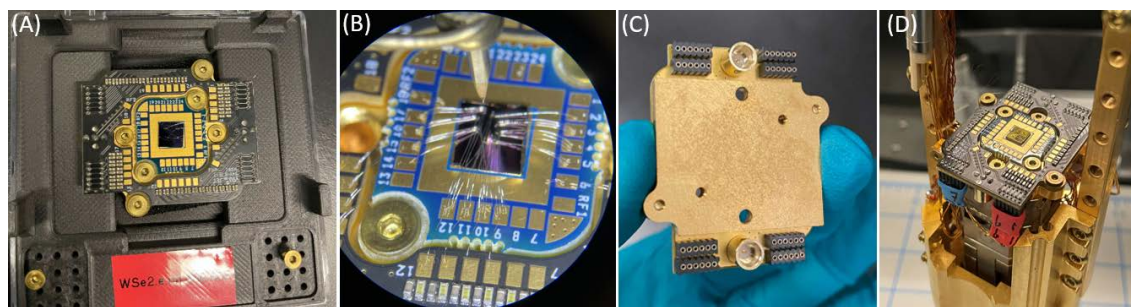


Figure C.4: (A) The chip carrier is placed on the copper holder in the middle of the sample carriage. Be sure that the numbering matches. (B) The sample can be wire bonded in this configuration. There are 1 mm connectors that allow for the carriage board pins to be grounded while wire bonding. Always bond from the carriage-to-chip carrier-to-device if you are concerned about static discharge. This will make sure that the wire will always be grounded before it reaches the sample bond pads. (C) The 1 mm connectors on the back of the carriage board will now be electronically connected to the sample. (D) Sample loaded into the BlueFors probe system.

### C.2.3 Sample Mounting

When mounting a sample to a chip carrier, it should be placed within the 5 mm x 5 mm box and look similar to Fig. C.4(A). This box represents the full motion of the Attocube positioners. Any part of the sample left outside this box will not be optically accessible. The box is made of a soldermask and sits on top of the gold-plated copper. Therefore, samples that require the use of their substrate as a backgate can be scribed and silver pasted to the gold-plated copper. Then contact can be made to backgate by wire bonding outside of the 5 mm x 5 mm box to a numbered bond pad (only use 6 and 18 for gating if you are using the filtered boards and require high gate voltages).

After the sample is installed in the chip carrier, the chip carrier should be secured to the copper holder in the middle of a sample carriage. Only use the 4 mm long brass

conical head screws with a 1.3 mm Hex key to secure the chip carrier to the thermal contact. These screws are purchased from McMaster, part number 97595A266. There are different lengths of these screws. If you use a longer screw, it will exit through the back of the thermal contact and it will not sit flat against the thermalization plate on the Attocube stack.

With the chip carrier installed on the thermal contact, it can be wire bonded. The safest way to wire bond a sample is to connect grounding 1 mm SIP wiring to the SIP connectors on the carriage prior to wire bonding. Then always bond from carriage-to-chip carrier-to-sample. This way the bonding wire is always grounded and any static discharge should be pulled through the wire instead of through your device. A wire bonded device to the chip carrier and sample carriage is shown in Fig. [C.4\(B\)](#).

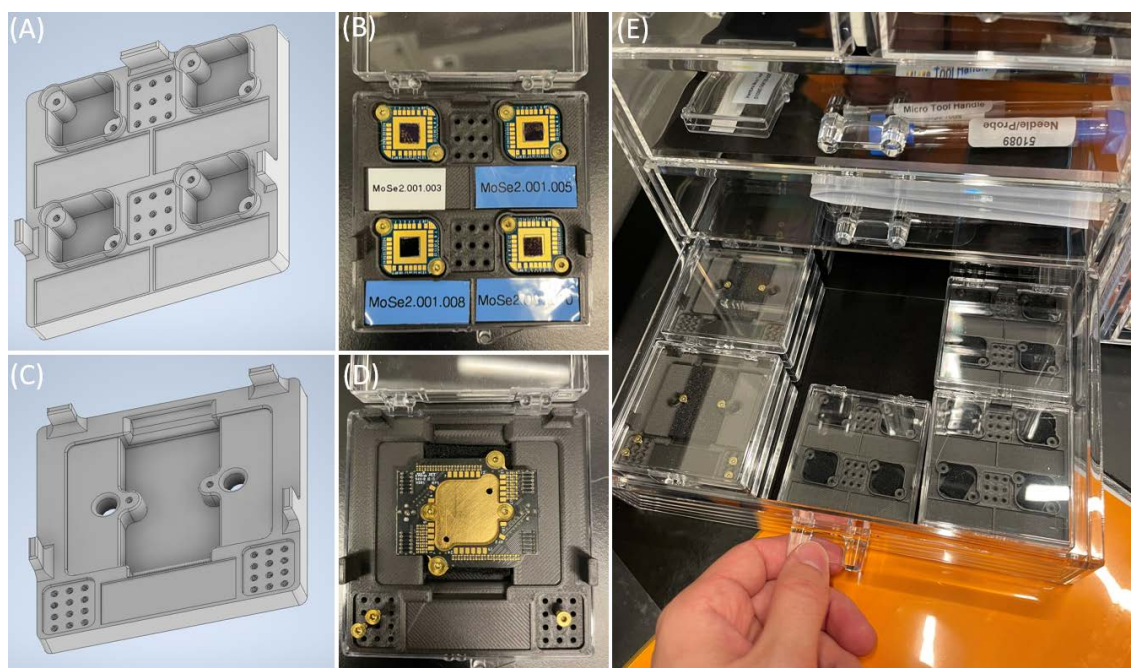


Figure C.5: (A) 3D CAD of the Chip Carrier holder. (B) Image of the 3D printed Chip Carrier holder; material: Onyx. It is placed in a clear plastic storage box from Newport. (C) 3D CAD of the Sample Carriage holder. (D) Image of the 3D printed Sample Carriage holder; material: Onyx. It is placed in a clear plastic storage box from Newport. (E) Spare holders can be easily stored away for future use. Holders with samples installed should be placed in one of the desiccator boxes in the lab.

## C.2.4 Chip Carrier and Sample Carriage Storage

To protect and store samples on the chip carriers or sample carriages, we 3D printed holder out of Onyx using the Markforged 3D printer. These holders are shown in Fig. C.5. The clear cases are purchased from Newport, product number: LAB-23. The holder is specifically designed to fit inside of these cases and have supports on the sides that touch the top of the case to prevent the 3D holder from moving if it is flipped upside-down. There is also a divot beneath the chip carriers and sample carriage to allow for ESD

conductive foam to be placed, Digi-Key part number: 16-1231-ND. This foam is 1/4" thick and can be cut to fit inside of the divot. The depth of the divot is designed to be less than a 1/4" so that the foam is always in contact with the chip carrier or sample carriage. The foam is made of carbon and dissipates any charge that may accumulate on the chip carriers, samples carriages, or in the atmosphere of the box.

These boxes are compact and allow for safe storage and shipping of the chip carriers or sample carriages. These boxes can also be safely vacuum sealed in plastic. When a device is installed on a chip carrier or sample carriage, the box should be stored in one of the desiccators in the labs. The only problem with this design is in the quality of the clear boxes supplied by Newport. The hinges are low quality and some of them easily break. In a future design, we may want to find better clear boxes, but these currently work well enough for continued use.



## Appendix D: BlueFors Measurement Optics

### D.1 Internal BlueFors Optics

There are two permanent optical elements inside of the BlueFors cryostat that must be considered while making measurements. The first are a set of optical windows on each of the radiation shields and vacuum can (4 windows total). BlueFors welded viewports onto each radiation shield and the vacuum can to allow for the windows to be installed. We ordered the specific windows with broadband anti-reflective coatings from UQGOptics. The second is a 45 deg mirror mount that is suspended above the mixing chamber plate on the cold plate. It redirects the side axis excitation path into the bore of the magnet and toward the probe. As of right now, both of these components are permanently installed in the cryostat. Depending on the requirements of future experiments, additional components can be added or these can be modified. Note that anything placed inside of the main cryostat of the BlueFors cannot be easily accessed or removed. A full warm-up and cool-down is necessary and can take about a week.

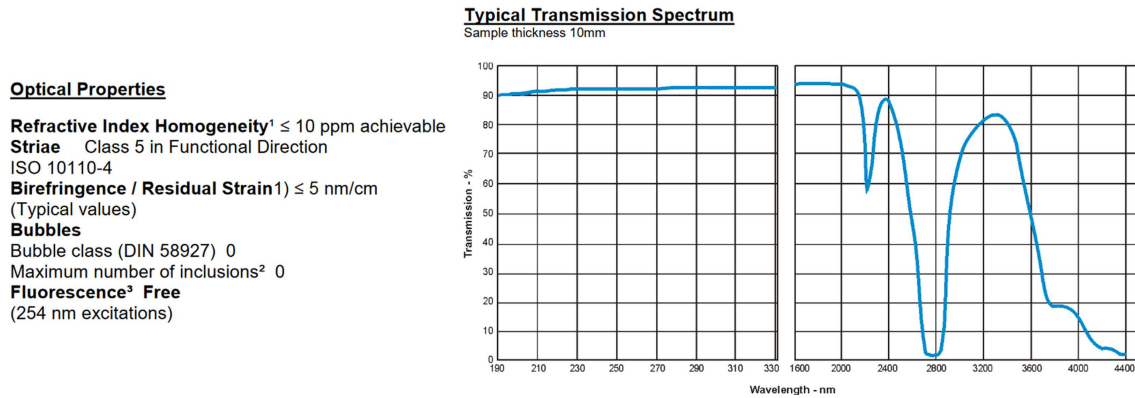


Figure D.1: Details for the Spectrosil 2000 UV Fused Silica windows purchased from UQGOptics. These are the windows of the BlueFors dilution refrigerator. They do not supply exact transmission details for the thickness of our optical windows and instead only give these standard parameters and transmission profiles.

### D.1.1 BlueFors Windows

BlueFors sells the system with only metallic pucks installed where the windows should be located on the radiation shields and vacuum can. We purchased Spectrosil 2000 UV fused silica windows from UQGOptics with an AR coating in the range of 500-1500 nm. The data sheet supplied by UQGOptics is provided in Fig. D.1. They provide this standard transmission plot for all of their Spectrosil 2000 optical windows.

There are four windows installed on the BlueFors, shown in Fig. D.2. A window is placed on each radiation shield to prevent thermal radiation from entering the inner radiation shield. UV fused silica's transmission quickly dies off for wavelengths greater than 4  $\mu\text{m}$ . The highest energy thermal spectral radiance is from the vacuum can at 300 K. Its blackbody emission primarily resides above 4  $\mu\text{m}$  and peaks around 10  $\mu\text{m}$ . Therefore, the UV fused silica windows are sufficient for blocking the thermal radiation inside of

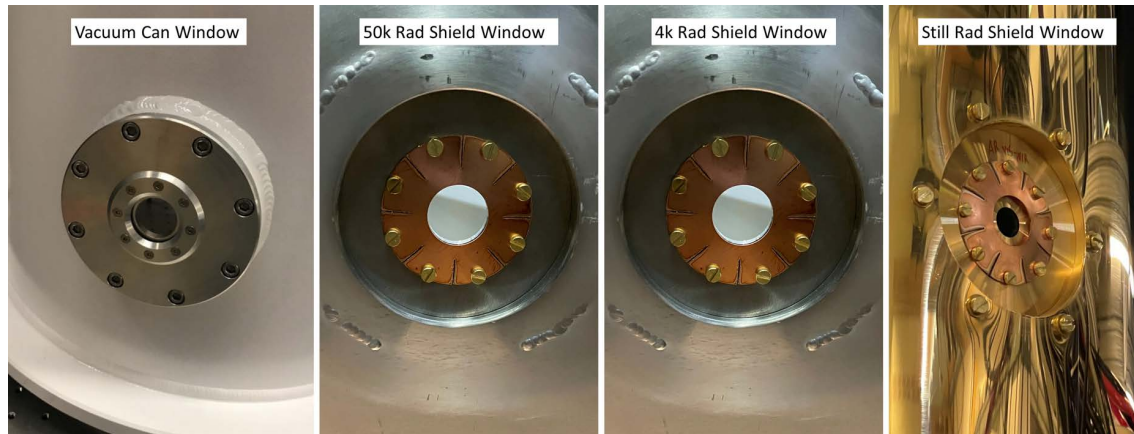


Figure D.2: Optical windows on each radiation shield of the BlueFors Dilution Refrigerator.

the cryostat. The vacuum can window is the thickest window because it has to handle the vacuum pressure. It has a diameter of 40 mm and a thickness of 3 mm. The other three inner windows have a diameter of 30 mm and thickness of 2 mm.

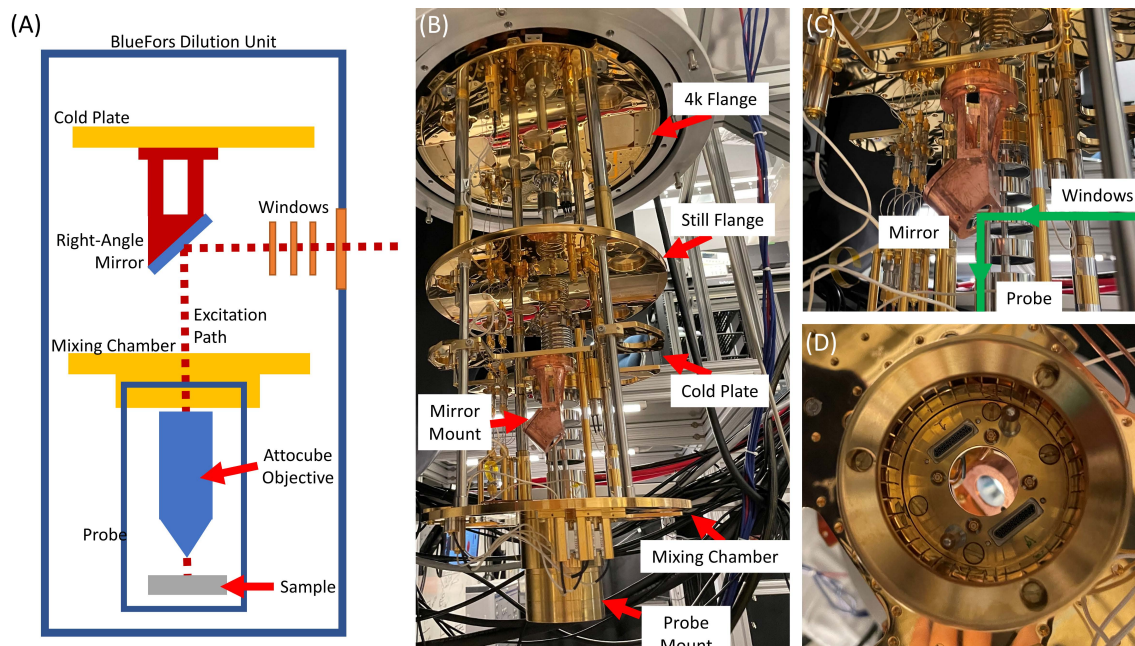


Figure D.3: (A) Schematic of the excitation path via the side axis of the BlueFors dilution refrigerator with the 45 deg mirror mount redirecting the path toward the probe. (B) Image of the opened BlueFors dilution refrigerator with the 45 deg mirror mount installed. (C) Close up image of the 45 deg mirror mount showing the excitation path. (D) View of the 45 deg mirror mount from the probe mount on the mixing chamber plate.

### D.1.2 BlueFors 45 Deg Cold Mirror Mount

To direct the light from the side axis to the vertical axis of the probe, a 45 deg mirror needed to be placed on the Cold Plate directly above the Mixing Chamber flange. Fig. D.3(A) is a schematic of this configuration. The Cold Plate has tapped holes around a central hole. The 45 deg mirror mount was designed to secure to these tapped holes with the mirror positioned at the exact height of the windows. Fig. D.3(B,C,D) are images of the BlueFors with the mirror mount installed on the Cold Plate. This 45 deg mirror mount is designed to work with a 1 inch mirror. The current mirror used is a precision broadband

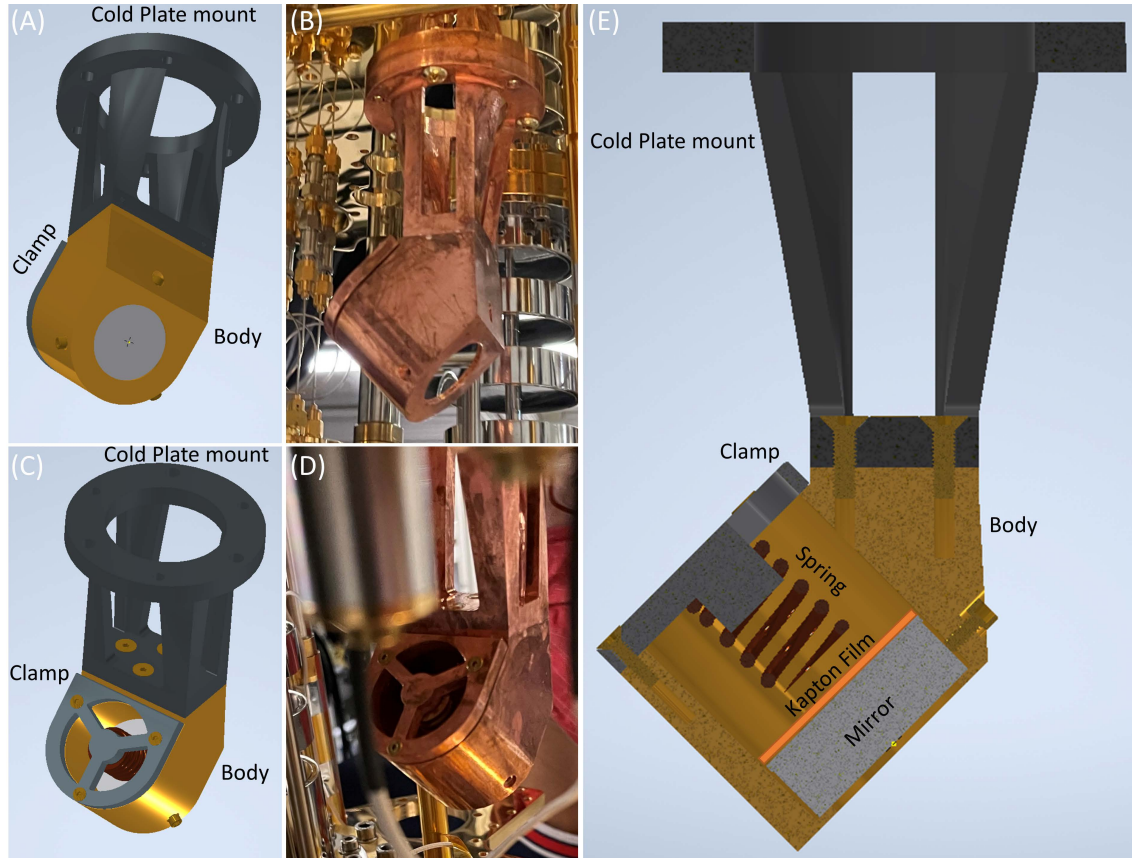


Figure D.4: (A) 3D CAD of the 45 deg mirror mount. (B) Image of the 45 deg mirror mount installed inside of the BlueFors on the Cold Plate. (C) 3D CAD of the back of the 45 deg mirror mount. There is a copper spring behind the mirror that holds it in place as well as to handle thermal compression and expansion of the mount due to cooling and warming the system. (D) Image of these components while the 45 deg mirror mount is installed in the BlueFors. (E) Half-sectional view of the 45 deg mirror mount. The internal spring system can be seen here. We have a spring that presses against the back of the 1” mirror with a 1” diameter Kapton film protecting the mirror from direct contact with the spring.

laser mirror from Edmund optics (Stock Number: 45-758).

The mount is machined in three parts. The first is the Cold Plate mount, depicted as the dark grey top part in Fig. D.4(A,B). This part secures to the Cold Plate and screws into the mirror mount assembly. The mirror mount assembly has two parts: the body and the clamp. In Fig. D.4(A,B), the body is depicted as the gold-colored piece while the clamp is depicted as the lighter grey part on the rear of the body.

The body has three tapped holes on the top that allow for the Cold Plate mount to be attached. The face of the body is machined to be 45deg with respect to the vertical and horizontal axis. There are three set screws on either side of the mirror opening that can be used to hold the mirror in place. They align the mirror to the center of the mirror opening, but should not be used to secure it. The concern is that if they are tightened they might cause the mirror to crack when the cryostat is warmed-up or cooled-down. The back of the body is hollow with three tapped holes for the clamp.

The clamp can be screwed into the rear of the body and has a central rod where a spring can be held, Fig. D.4(C,D). The internal spring presses against the rear of the mirror and holds it in place, Fig. D.4(E). As I designed this mirror mount, I was very concerned that if the holder was just a simple copper clamp around the mirror the thermal compression or expansion would cause the mirror to eventually break. To try to design around this problem, the only clamping mechanism of the mirror is a phosphor bronze spring, McMaster part number: 9657K255. The mirror is protected from direct contact with the metal spring by a thermally conductive kapton film, McMaster part number: 2271K24. The set screws on the body are only meant to keep the mirror from sliding while the clamp is installed and should be loosened afterwards.



So far, we have had no damage to the mirror after multiple years of use and many thermal cycles. This mirror mount design has proven to work.

Also, we have not gold-plated the mirror mount assembly due to time restrictions, but it should be eventually gold-plated to maximize cooling of the mirror.

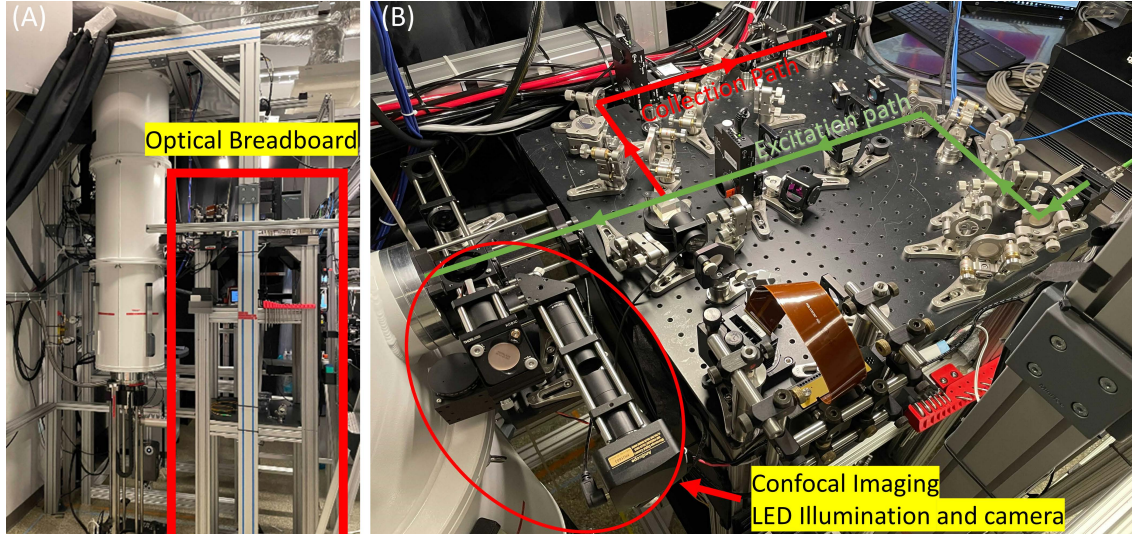


Figure D.5: (A) Image of the BlueFors dilution refrigerator and the optical breadboard assembly. The breadboard is mounted to the top of an aluminum t-slot structure that sits on the floor of the lab. (B) Image of the top of the optical breadboard and the optics used in the measurements. The green path indicates the laser excitation path and the red path indicates the collection path. The confocal imaging system used to image the surface of the sample consists of an LED and a CCD camera. There is a pellicle beamsplitter (currently removed) that can be placed in the holder just before the first BlueFors window. When the pellicle beamsplitter is in place, we can image the surface of the sample and see where the laser spot is focused.

## D.2 External BlueFors Optics

### D.2.1 Aluminum Breadboard Optical Assembly

Outside of the BlueFors dilution refrigerator, we installed an optical breadboard at the height of the windows, Fig. D.5(A). The optics on the breadboard are shown in Fig. D.5(B) and a schematic of the design is illustrated in Fig. D.6. We launch the excitation laser beam, depicted in green in Fig. D.6, from a broadband reflective collimator with a 4 mm beam diameter, Thorlabs part number: RC04APC-P01. It is

### BlueFors Optical Schematic

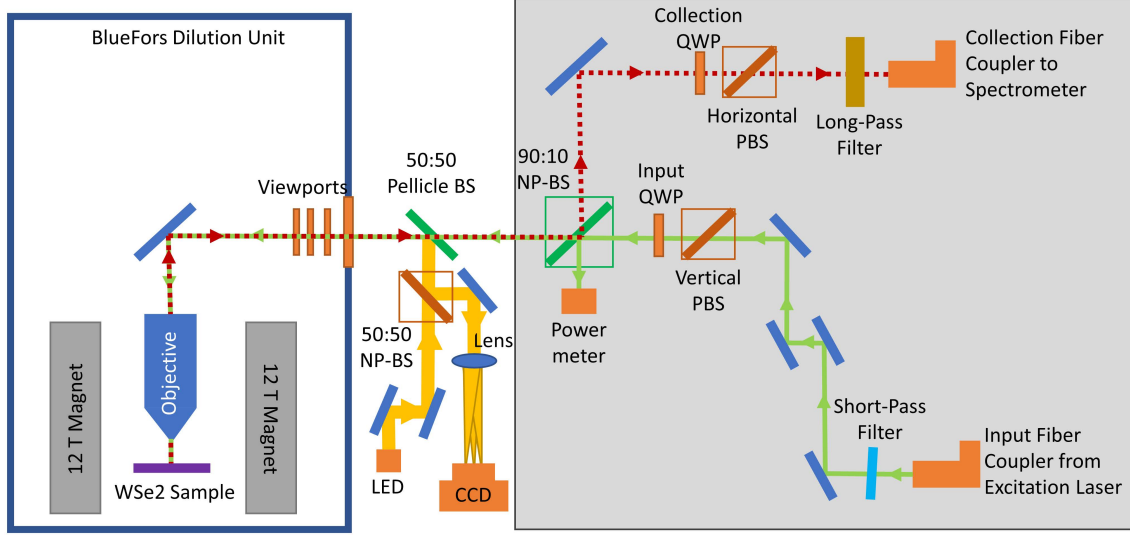


Figure D.6: Schematic of the free-space optics used in the BlueFors spectroscopy measurements. Laser light is launched from a reflective collimator denoted by the green path. The short-pass filter blocks any low energy side bands from the excitation laser. We have polarization selective optics that allow us to set the laser light to left or right circular polarization. The laser light enters the BlueFors and is focused on the surface of the sample by the objective. The reflected laser light and emission from the sample is redirected out of the Bluefors and directed along the red-dotted collection path by the 90:10 NP-BS. The collection light is also polarization resolved such that we can set the collection QWP to only allow either left or right polarized light to transmit through the horizontal PBS. The reflected laser light is blocked by a long-pass filter and the emission light from the sample is collected by a broadband reflective collimator into a fiber that is sent to a spectrometer for analysis.

then directed through polarization control optics to control the laser's polarization. For all experiments conducted in this dissertation, we needed the excitation beam to be either left or right circularly polarized. This involves the use of a linear polarizer, we used a polarizing beamsplitter (PBS), and then a quarter-wave plate (QWP). Setting the QWP's axis to  $\pm 45$  deg with respect to the linear polarization axis of the PBS changes the polarization of the excitation beam to either left or right circular polarization. The beam is then directed through a 90:10 non-polarizing beamsplitter (NP-BS). This is designed to reflect 90% of the light and transmit only 10%. The NP-BS used here is from Thorlabs, part number: BS029. The reflected 90% of the excitation beam is collected by a power meter to measure the excitation laser's power.

The laser continues through a pellicle BS coated for 50% reflectance and transmission. I will come back to this optical component later as it allows for imaging of the surface of the sample. The laser beam passes through the four windows in the BlueFors and is redirected by the 45 deg mirror mount toward the probe objective. The objective focuses the collimated laser light on the sample. Any response from the sample, as well as the reflected laser light, is collected by the objective and sent back along the path of the laser and out of the cryostat. This light passes through the 50:50 pellicle BS and 90% of its light is reflected by the 90:10 NP-BS in a different direction toward the collection optics. We have similar polarization selection optics (QWP and PBS) that allow us to select left or right circularly polarized light to transmit to the collection fiber. The long-pass filter is required to block the higher energy reflected excitation laser light. The lower energy light from the sample is then fiber coupled using another reflective collimator with 4 mm beam diameter. This light is sent to our spectrometer for analysis.

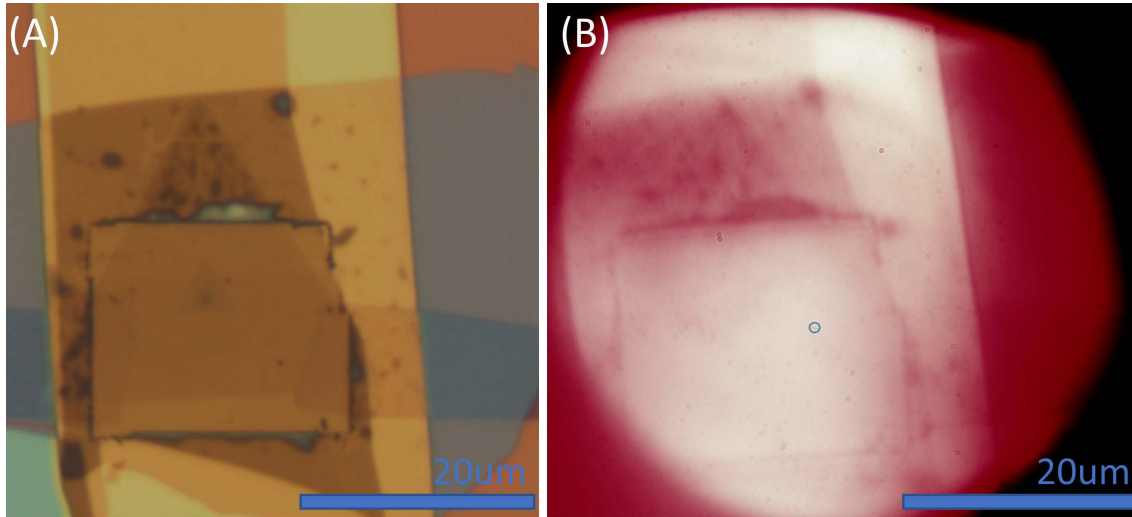


Figure D.7: (A) Optical image of our WSe<sub>2</sub> sample from a metallurgical microscope in our fabrication lab. (B) Optical image using the LED and CCD camera assembly in Fig. D.5(B) on the BlueFors.

### D.2.2 LED and CCD Imaging System

The pellicle is a thin film beamsplitter that eliminates internal reflections. It was purchased from Ealing, part number: 44-3960-000. It is great for imaging, but has concerning polarization and spectral responses and should be removed while making actual measurements. For it to be used in the rotation cage platform from Thorlabs, part number: B3CR, we 3D printed a mount holder out of Onyx, Fig. D.9. The rotation mount allows for the pellicle to be taken out while measurements are being conducted, Fig. D.8(A).

The pellicle BS allows for optical imaging of the sample using an LED. The light from the LED is focused on the back plane of the objective inside of the BlueFors probe to illuminate the entire field of view on the sample. The LED light reflects off the surface

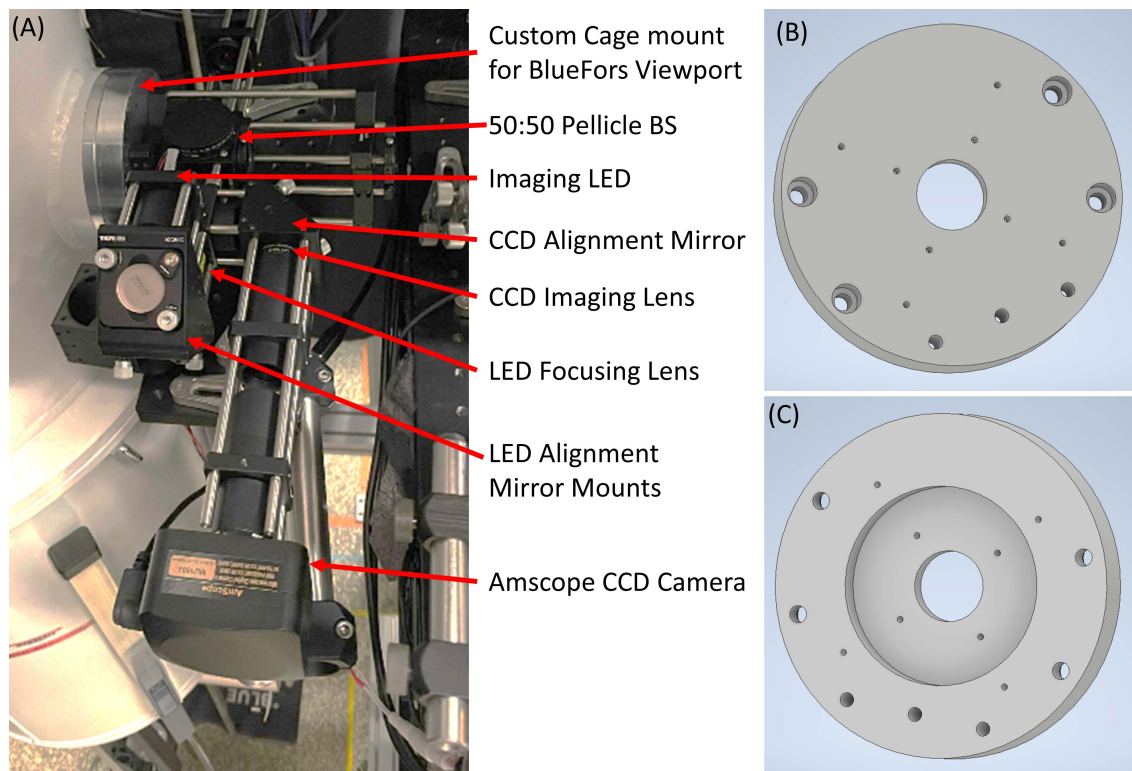


Figure D.8: (A) Optics attached to the side of the BlueFors vacuum can's viewport that allow for imaging of the sample. An illustration of assembly is depicted in Fig. D.6. (B,C) 3D CAD of the custom flange we machined out of aluminum to attach to the BlueFors viewport. We use 4 of the 8 screws that secure the window to the vacuum can's viewport to attach this additional flange. There are 8 total 4-40 tapped holes that form a 30 and 60 mm cage pattern. This is because all of Thorlab's cage systems use 30 and 60 mm dimensions. The bottom three holes are tapped with 1/4-20 threads to allow for a small aluminum breadboard to be attached. The cage optics also sit on this small aluminum breadboard to eliminate having all the optics hanging from the 4-40 cage taps.



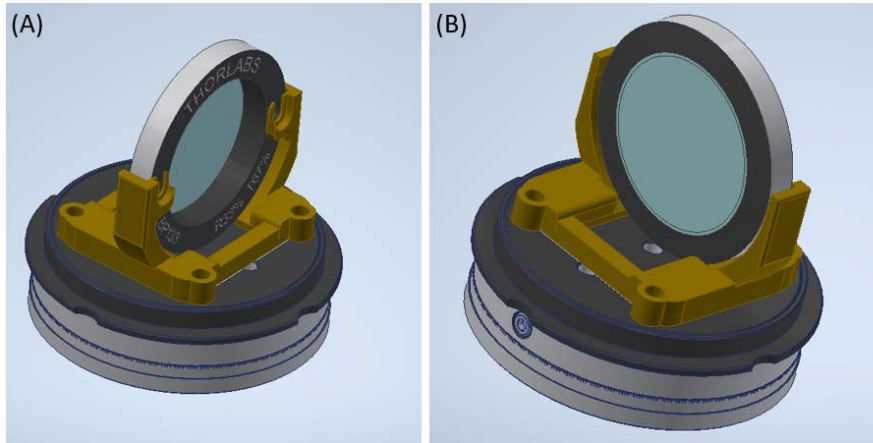


Figure D.9: The pellicle shown here is labeled with a Thorlab's part number, but it has the same design as the Ealing model we use in our system. (A) 3D CAD of the adapter we 3D printed to hold the pellicle beamsplitter on a B3CR rotation stage from Thorlabs. We 3D printed the part colored in gold.(B) Rear side of the holder.

of the sample and is redirected back to the pellicle BS. The image is recreated on a CCD camera, Amscope product number: MU1603. This is identical to how a standard metallurgical microscope works. We are able to image a region of  $\sim 40 \mu\text{m}^2$  using this configuration. Also, while the pellicle BS is in place, some of the reflected laser light is directed toward the CCD camera and tells us where our laser spot is on the surface of the sample. For this position to be accurate, the LED should have a wavelength similar to the laser's wavelength, Fig. B.16.

The imaging optics and the custom flange we machined to allow for the cage assembly to be mounted to the viewport of the BlueFors is shown in Fig. D.8. There are also two apertures for alignment of the excitation laser into the BlueFors on the cage assembly. As we discovered when we renovated the optical configurations a few times, as long as these apertures are attached to the viewport, alignment of the excitation path into

the BlueFors is fairly simple.

Alignment of the LED is more difficult and the best strategy is to first align the excitation laser and try to find the reflected laser spot from the sample on the camera image. This may require rotating the pellicle BS. Once the laser is focused to a small spot size, align the LED looking for the sample image, Fig. D.7(B). If the laser and LED are close in wavelength, the image should be close to in-focus and you only need to get the LED mirrors aligned. To make finding your sample easier in the BlueFors, the Attocube positioners should be moved to the sample location using the probe station prior to cooling down the probe, Fig. B.18. The main shift due to cooling is in the z-axis, i.e. the focus of the objective on the sample.

The LED has a spectral emission centered on 650 nm, Digikey part number: 1125-1053-ND. I used a 5 V power supply we had in the lab with a voltage divider to reduce the output voltage to the 2.2 V required for the LED. The LED's current cannot exceed 50 mA so the voltage divider resistors have to be selected according to the output current of the power supply. The voltage divider will get hot, but that is normal. I also soldered a switch on the power supply to allow for the LED to be turned on and off. The LED is mounted in a cage mirror assembly using an SM1 adapter from Thorlabs, part number: S1LM56. We use a convex lens to focus the LED light on to the backplane of the objective. The required focal length for the lens depends on how far away the objective is from the LED.

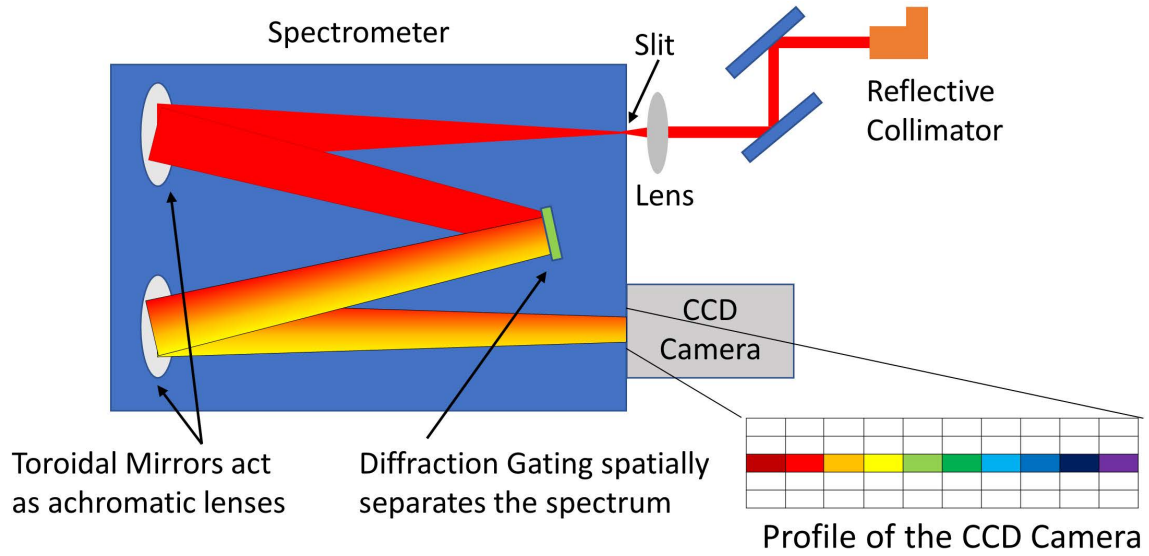


Figure D.10: Schematic of our spectrometer and CCD Camera assembly used to collect all of our measurements.

### D.2.3 Spectroscopy Optics

To conduct these spectroscopy measurements, we used a Princeton SP2750 equipped with an Andor Newton DU920P-BR-DD CCD camera on the output. A schematic of the optical spectroscopy assembly is presented in Fig. D.10. The light collected from the BlueFors or Montana cryostats is fiber coupled and brought to the spectrometer. It is then launched via a reflective collimator and aligned to a lens that focuses the light through a narrow slit. The beam then diverges inside of the spectrometer until the first toroidal mirror collimates the diverging beam towards a diffraction grating. The beam's reflection angle off of the diffraction grating depends on the wavelength of the incoming light. Therefore, the reflected light will be spectrally and spatially separated into collimated beams directed toward the second toroidal mirror. This mirror focuses

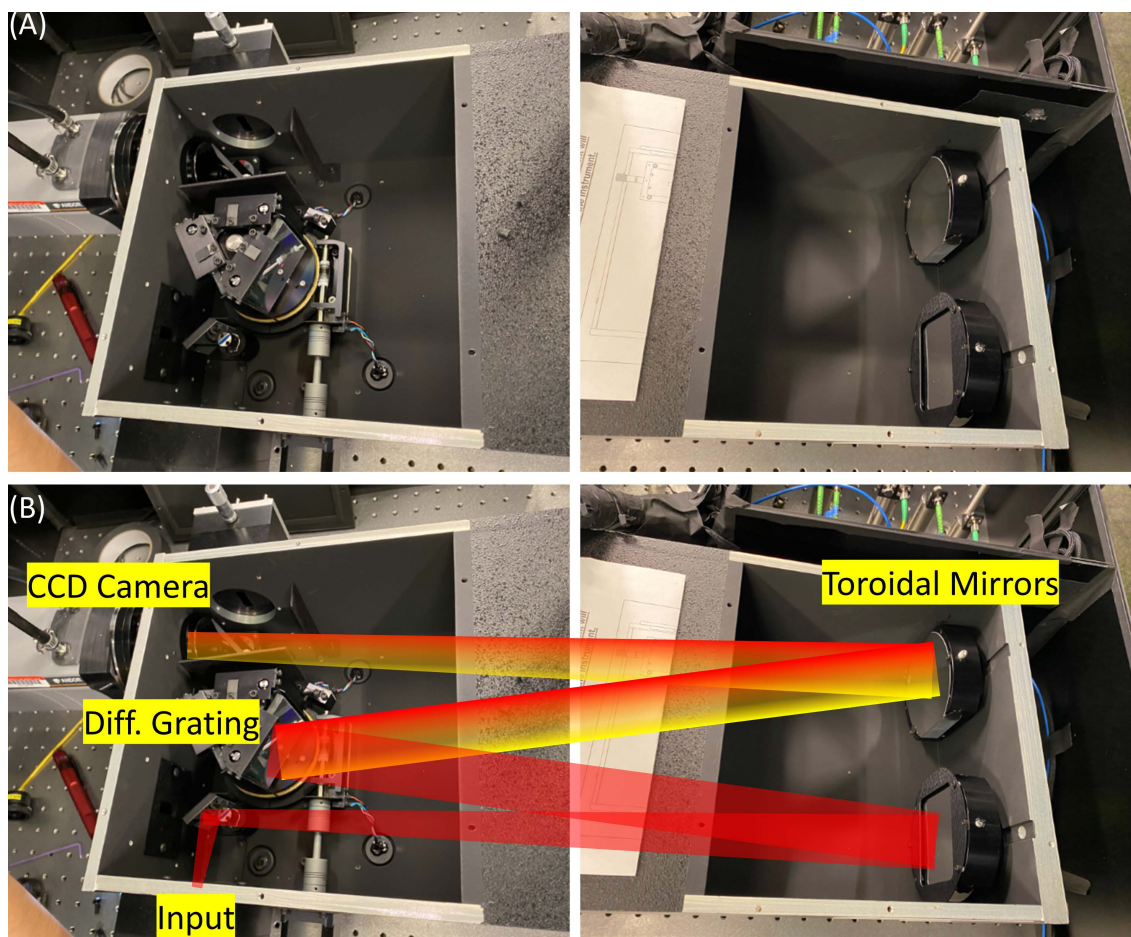


Figure D.11: (A) Images of the insides of the Princeton SP2750 spectrometer used in our measurements. The toroidal mirrors, diffraction gating, and CCD camera can all be seen. (B) Overlay with the light path.

each collimated beam onto a CCD camera. Since the light is spatially separated based on wavelength, each pixel on the CCD camera will correspond to a different wavelength of light. The distances from the input slit to the camera pixels are selected to be the same. Therefore, the spot size at the slit is the spot size on the CCD camera. For high precision spectroscopy measurements, the input spot size should be focused via the input lens to be as small as possible using the variable input slit. The inside of the Princeton SP2750 is shown in Fig. [D.11](#).

The external optics directing light into the spectrometer are shown in Fig. [D.12\(A\)](#). We used a broadband reflective collimator, Thorlabs part number: RC04APC-P01, to launch light from the measurement fiber into a 4 mm collimated beam. Two mirrors are used to align the beam through a 50 mm focal length lens. We need the beam's focal point to be at the center of the input slit of the spectrometer. Using the micrometer on the top of the input slit, you can change the slit width. Optimized alignment is when the slit can be set to a very narrow width and still nearly all of the laser power enters the spectrometer. This requires aligning the two mirrors and the input lens's distance from the input such that the focal point is exactly centered on the slit.

There are two important custom parts that we had machined for the spectrometer. The first is a Princeton-to-Andor adapter that allows us to install the Andor camera on the output of the Princeton spectrometer. This part was machined out of stainless steel because it is very thin and the entire weight of the camera hangs on it. The other part is an input adapter that allows us to place a 30 mm cage system from Thorlabs on the spectrometer's rectangular slit flange. We use the cage assembly to mount the input lens to the input flange of the spectrometer. This part is machined out of aluminum. The 3D

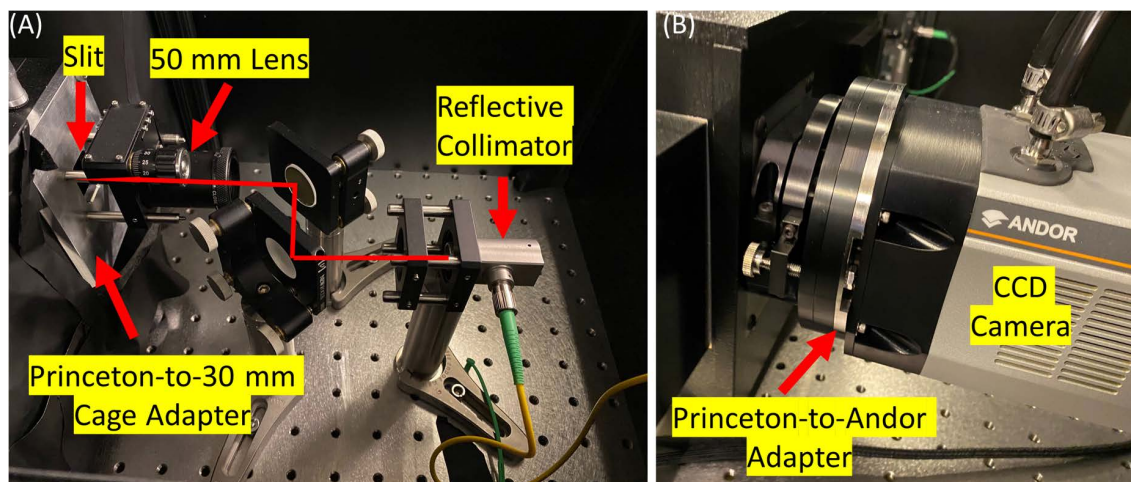


Figure D.12: (A) Reflective collimator directs measurement light toward the two alignment mirrors. These mirrors align the collimated light to a 50 mm focal length lens that focuses the light through a very narrow slit and into the spectrometer. We machined a custom adapter that mounts to the Princeton input that has four 4-40 tapped holes. These allow us to mount a 30 mm cage assembly to this flange. The 50 mm focal length lens is mounted on this cage assembly. (B) The Andor camera is mounted to the Princeton spectrometer. We needed to machine a custom adapter to mount the Andor to the Princeton. It is made out of stainless steel.

CAD illustrations for both parts are shown in Fig. [D.13](#) and images of each can be seen in Fig. [D.12](#).



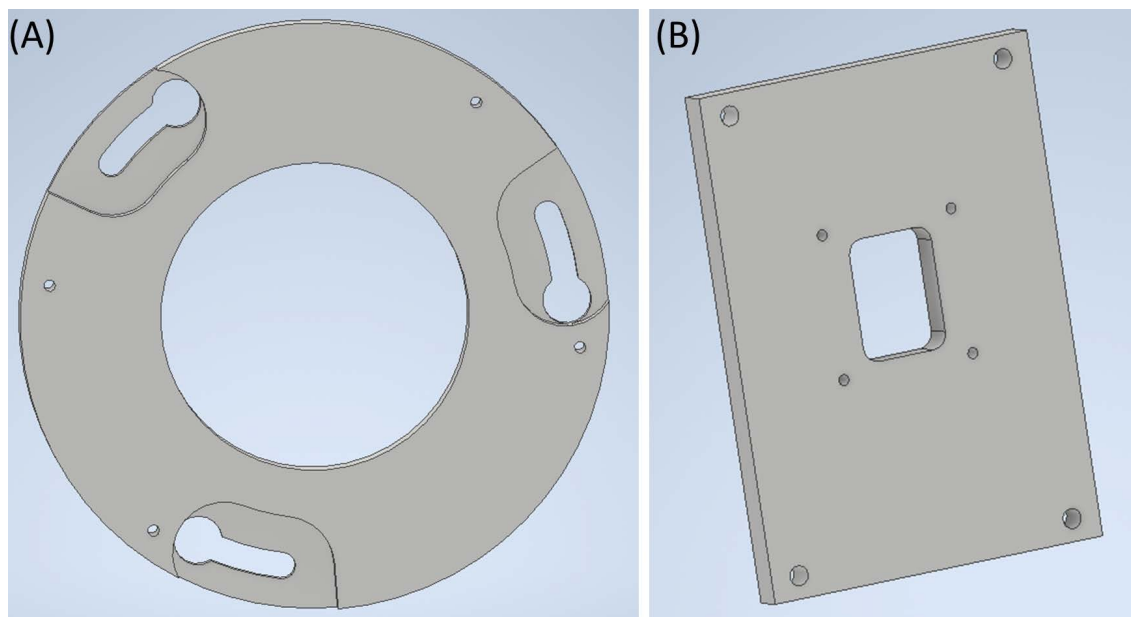


Figure D.13: (A) Princeton-to-Andor adapter that allows us to mount the Andor camera to the Princeton spectrometer. It is machined out of stainless steel. (B) 30 mm cage plate adapter for the rectangular slit mounts on the Princeton. These were machined out of aluminum and the four holes have 4-40 taps.

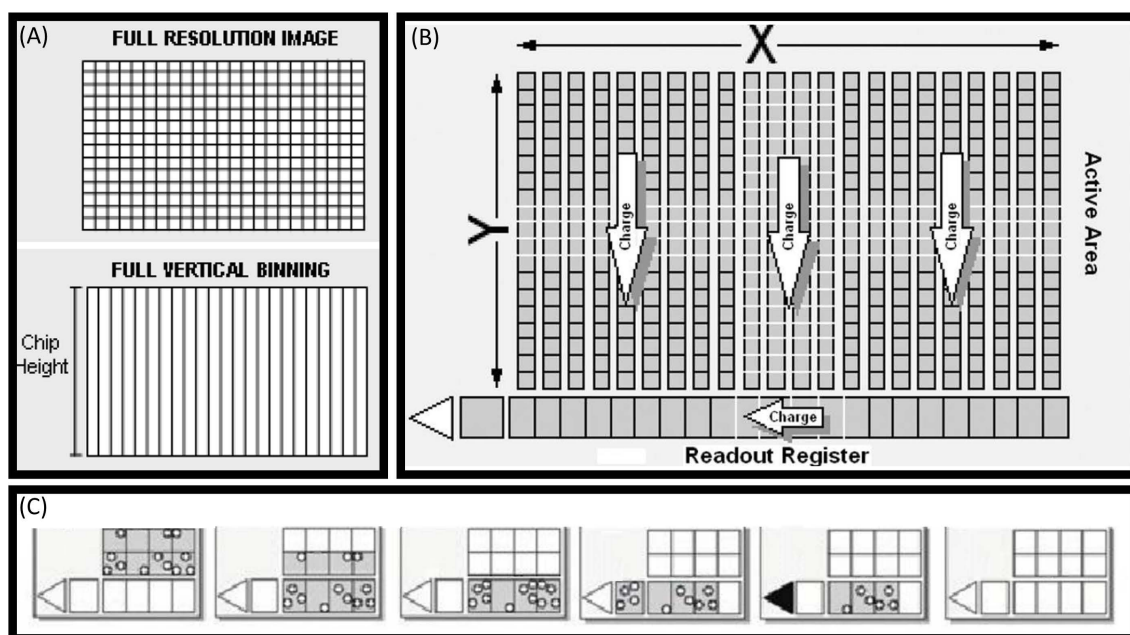


Figure D.14: These illustrations are from the Andor user manual [90]. (A) Illustration of the Image and Full-Vertical Binning (FVB) on the CCD Array. (B) Illustration of read-out from the CCD Array. (C) Illustration of FVB read-out with only two rows of pixels.

#### D.2.4 Andor Camera Readout

There are two possible read out modes from the Andor CCD camera. The first is the most obvious, which is image mode, Fig. D.14(A). In this mode, the number of counts for every pixel on the CCD is read-out and displayed to the user as an image. Measurements in this mode give both x- and y-axis resolution.

Read-out from the camera in image mode is illustrated in Fig. D.14(B). The active area is the CCD array and during the exposure time, if a photon hits a pixel, it will gain an electron at that site. Once the exposure time ends, each row of pixels is systematically shifted downward to a readout register. From this readout register, the

pixels are systematically shifted to the readout pixel on the left which can read-out the total charge for that pixel [90]. In image mode, this procedure has to be done for every single pixel.

For the spectroscopy measurements presented in this dissertation, we only have spectral resolution. This means that only the x-axis has information (which is the wavelength of the light). If we were to read-out the CCD in image mode, a white light signal would look like a few pixels wide horizontal line in the middle of the CCD array. Therefore, we don't have to use the full image read-out mode and can use the second mode known as Full Vertical Binning (FVB). In this mode, all of the y-axis counts for a column of pixels are collected together and read-out at the same time, Fig. D.14(A).

Read-out from the camera in FVB mode is different from image mode. All of the charge that has built up on every pixel in a column is brought to the readout register. Then each pixel in the readout register is read-out. This is different from the image mode because we only have to readout a single row of pixels; i.e. all of the y-axis counts are summed. FVB read-out is illustrated in Fig. D.14(C) for a CCD array with two rows of pixels. Since the largest source of noise from the Andor CCD camera is from electronic noise during read-out, FVB provides the highest signal-to-noise ratio [90]. Electronic noise is about 300 counts per read-out for short exposure times when the camera temperature is -100 C.

Something that can contaminate data collected in FVB read-out mode, especially for long exposure times, are cosmic events that spike the counts of a single pixel. Since we are summing all of the vertical counts, these are always included in our actual data. A solution to this problem is to align input light to the spectrometer such that the signal

(which is only a few rows wide) is aligned to the bottom of the CCD camera. This can be easily done if you input a weak white light source into the spectrometer and align the horizontal line to the bottom of the CCD array in image mode. You can set the FVB mode to measure only the bottom 10 rows instead of all 256 using the crop setting. This will greatly reduce the total number of cosmic events that appear in your data for long exposure times.

### D.3 Magnetic Field Dependent Motion of the Sample and/or Optics

This section is meant to illustrate a very important discovery of magnetic field dependent motion of the illumination spot on the sample (by either systematic movement of the sample or optics) in the BlueFors dilution refrigerator. One of the many challenges of making optical measurements inside a dry cryogenic system is that there is usually some motion of the sample from the pulsing helium pump that cools down the cold finger on which the sample is attached. This is extremely common in table top systems such as our Montana cryostat. Because of how those systems are designed, the sample will always be fluctuating at the frequency of the helium compressor and is a fairly well understood issue with those systems.

### D.3.1 BlueFors low drift and vibrations without magnetic field

Remarkably, the BlueFors exhibits very little drift or vibrations during our measurements and we do not see any vibrations of the sample while imaging with the LED/CCD camera assembly. In comparison, the vibrations are very visible for samples imaged by the Montana LED/CCD camera assembly. We attribute this to the design of the BlueFors (very well isolated flanges) and to the building. Our lab's corridor is on a different foundation from the lab itself and the vibrations from the floor are very minimal. Also, BlueFors must have done a very good job of isolating the mixing chamber flange from the vibrations of the PulseTube. We can measure the same spot with effectively zero drift for weeks (this was necessary to collect the PLE data reported in this dissertation).

We can further confirm that this is the case because of how sensitive our  $\text{WSe}_2$  sample's exciton emission energy is to changing spot position, Fig. D.15. The squeegee process induced strong strain in the sample which shifts the exciton emission energy [91]. We discovered that along the top squeegee indentation, there was a shift in the exciton's energy that was so systematic that changing the spot position even a few nanometers shifts the exciton's emission peak energy. Therefore, if we experience drift in the BlueFors while collecting PLE data over weeks, we would notice a shift in the energy of the exciton's emission energy (at  $B = 0\text{T}$ ). Since we do not see any such change, we know that the illumination spot is very exact throughout our measurements.

In the next few subsections, I will outline some of the issues we experienced as we set up the optics used to make these measurements in the BlueFors. Motion of the illumination spot while ramping the magnet was the biggest issue and it took a lot of



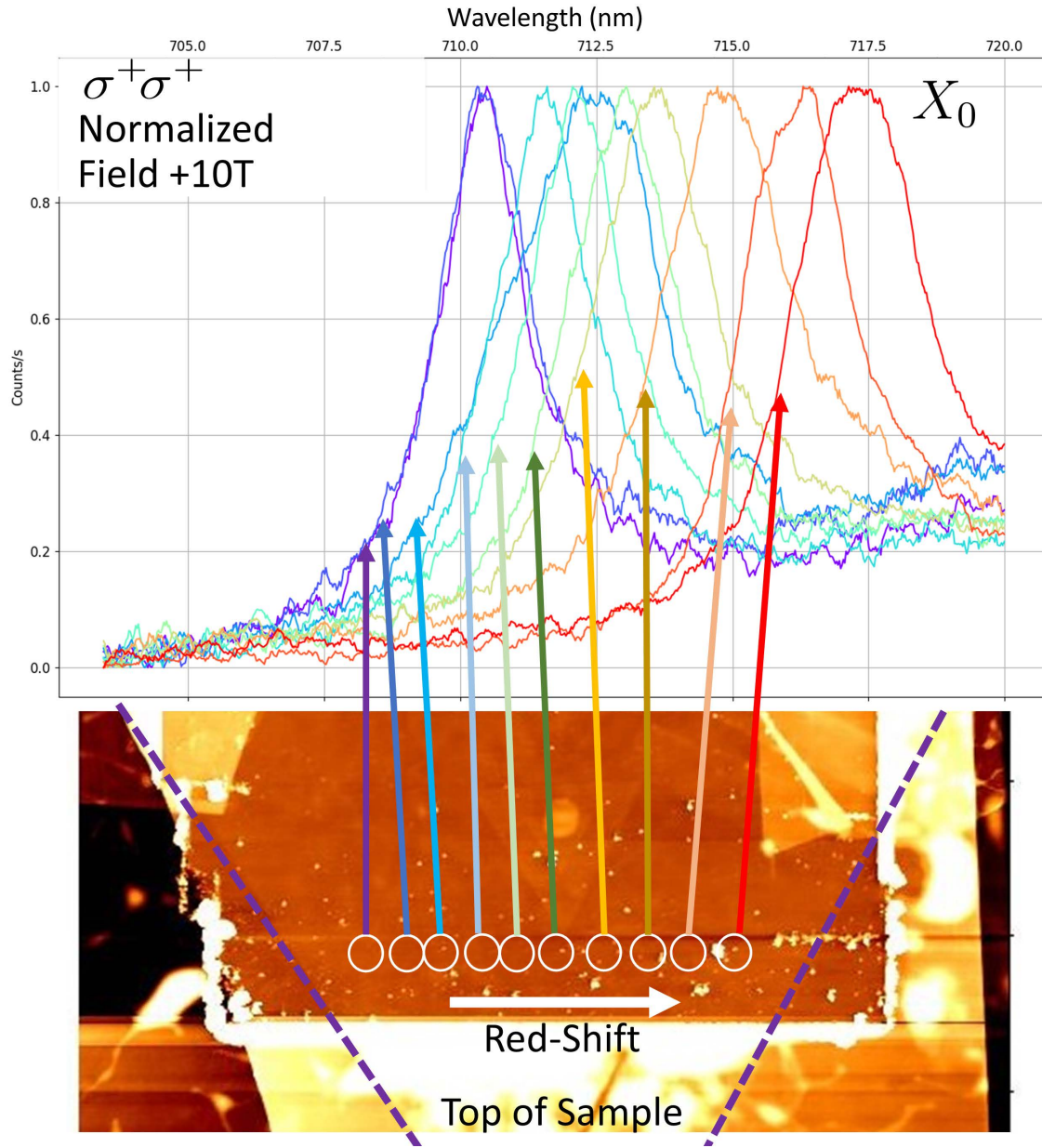


Figure D.15: AFM image of the WSe<sub>2</sub> sample used in this dissertation, WSe2.e.nrl.009.028. PL from illumination spots across the top of the sample show a systematic red shift in the  $X_0$ 's emission peak as the spot position is shifted from left to right.

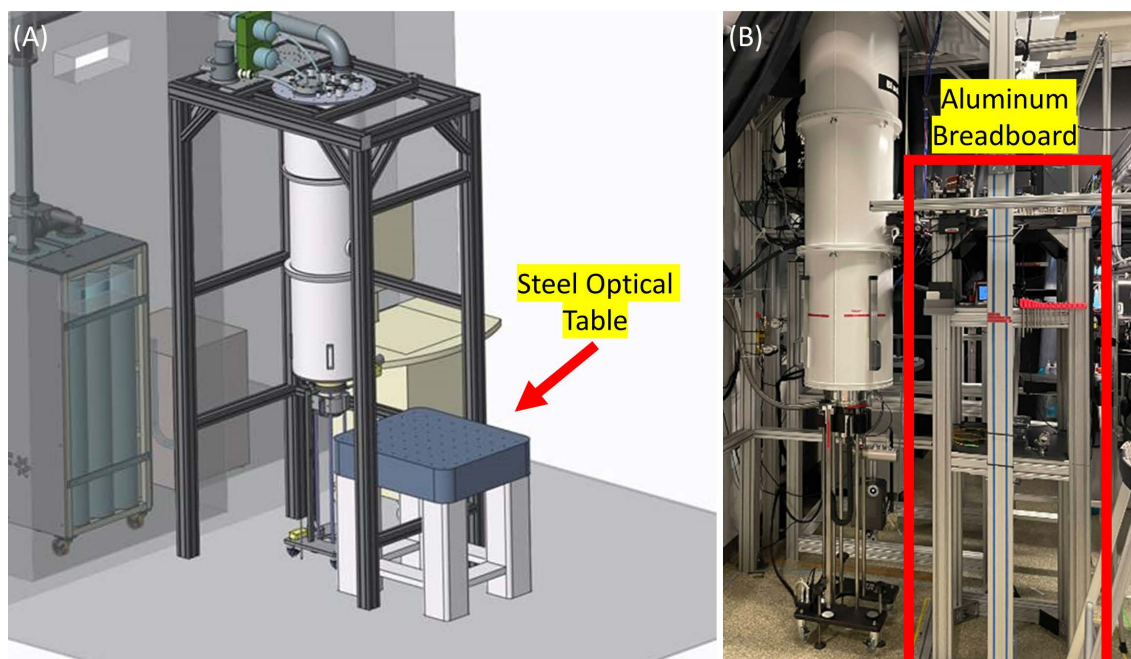


Figure D.16: (A) The initial design was to place a small optical table next to the BlueFors and build a structure above it to hold an optical breadboard near the viewport. This ended up not working very well because the stray field from the magnet would apply a strong force to the optical table and would move all of the optics. (B) We replaced the optical table with an aluminum t-slot structure and aluminum breadboard. This drastically reduced magnetic dependent motion in comparison to the small optical table.

effort to make sure that the optics were not affected by the stray magnetic field due to how many possible sources can contribute to such small shifts in spot position. I will outline the major ones we dealt with in the design.

### D.3.2 BlueFors Optical Table and Breadboard Designs

The first source of magnetic field dependent optical shift was from the first optical table/breadboard design that placed a steel optical table too close to the magnet, Fig. D.16(A). BlueFors suggests keeping any steel structures at least 6ft away from the

magnet. We initially did not follow this guidance and tried to place a smaller steel optical table right next to the BlueFors so that we could build an optical breadboard above it. The magnet's pull on the optical table caused substantial motion of all of the optics and shifted the spot's position on the sample. Due to the large change in spot position as a result of the optical table moving, this problem was fairly easy to diagnose. The solution was to remove the optical table and build a t-slot aluminum structure in its place, , Fig. D.16(B). An aluminum optical breadboard, Thorlabs part number: PBG12105, was placed on the top of the aluminum t-slot structure and all of the optics were placed upon it.

We tried to exclusively use non-magnetic mirror mounts and optics, and placed a special order from Newport for non-magnetic mirror mounts. They still had some magnetic components inside of them and had roughly the same magnetic response of the Polaris mirror mounts from Thorlabs. Therefore, we exclusively used Polaris mirror mounts for optics on the breadboard and tested every component with a powerful magnet before installing it.

### D.3.3 Additional Magnetic Dependent Spot Motion (X-K Zeeman Data)

The t-slot structure proved to work very nicely for all measurements reported in this dissertation, but more precise measurements that require the illumination spot to remain exact while the magnetic field is swept may experience issues. We experienced this problem in the high stress regions of our WSe<sub>2</sub> sample.

We are able to detect very small magnetic field shifts in the spot position by making very precise PL vs. magnetic field measurements on our WSe<sub>2</sub> sample. Due

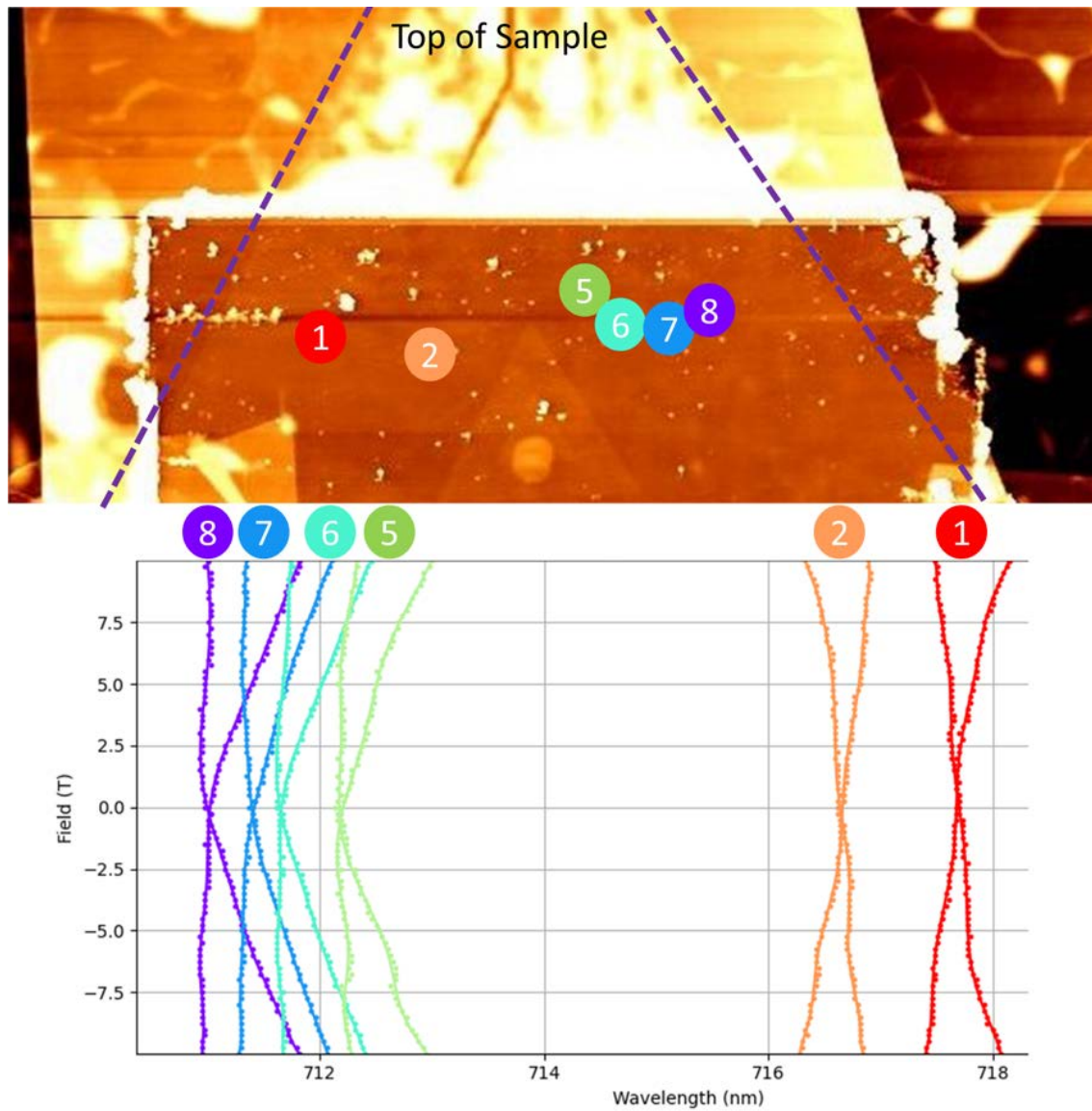


Figure D.17: We noticed a shift from near X-shaped valley Zeeman splitting to K-shaped valley Zeeman splitting depending on the laser's spot position on the sample.

to the strain induced by the squeegee method used on the sample, there was a very well-defined spectral shift in the exciton lines vs. spatial position toward the top of the sample, Fig. D.15. Since the emission energy shift was continuous across the roof of the WSe<sub>2</sub> sample, it is imperative that the laser excitation and collection spots do not move while the magnetic field was swept. If spot did shift with applied magnetic field, the data would include both an energy shift in the exciton's emission from the valley Zeeman splitting and from the spot moving across the strained region of the WSe<sub>2</sub> sample.

This led to an unusual set of data that we often referred to as X-K data, Fig. D.17. Some of the data collected showed a good Zeeman shift, which is X shaped, while the other showed this strange K shape. We believed this had something to do with the strain on the sample. It was later discovered that it was caused by the magnet moving the optics or the sample a very small amount such that it countered the Zeeman splitting in one direction, Fig. D.18(A).

This was discovered by flipping the sample 180 deg and measuring the PL vs. magnetic field again. If the K-shape flips from red-shifting to blue-shifting, i.e. K-shaped to  $\aleph$ -shape, then this unexpected magneto-optical result is not from some physical phenomenon, but instead caused by the optics or sample moving. This turned out to be the case, as shown in Fig. D.18. The reasoning behind this flip from K to  $\aleph$  is because the magnetic field motion is always in the same direction and doesn't depend on the sign of the field. Hence, the spectral shift in the exciton caused by the magnetic field is then either  $<$  or  $>$  shaped depending on if it is causing the spot to move in the red- or blue-shifting direction. It just so happens that the valley Zeeman splitting and the magnetic field spot shift are comparable in energy when the laser is in good alignment. Therefore, the sum

of the valley Zeeman splitting (X-shaped) and the field motion (< or > shaped) generates the K- or X-shape. If the alignment of the laser is bad, then the spot movement due to the applied field is larger and dominates over the valley Zeeman splitting, Fig. D.19.

This is a very difficult problem to solve and I don't think it is one that we can solve. Even if we used a galvo to adjust the optics, there is no feedback that could be used to guarantee that the beam was on the same spot of the sample. It is also not known whether the heating from the magnet as it is ramped is moving the sample or if the stray field is moving the optical beam path. Since the spot position shift is so small, we currently cannot say which is the case. This is likely a problem that we have to live with, but luckily, it is only a problem if we need exact field data at a local point on the sample. In many measurements, this is not the case and movement of the spot position by a few nanometers does not affect the data. We have a unique situation in our WSe<sub>2</sub> sample that there is a very systematic and large shift in the emission energy of the excitons across the top of the squeezed region. Even very small shifts in the spot position results in comparable exciton energy shifts to the valley Zeeman splitting.

All of the magnetic dependent data collected in the main text of this dissertation was from a spot near the middle of the sample that does not have this systematic stress and the exciton emission energy does not change with small changes in the spot position.



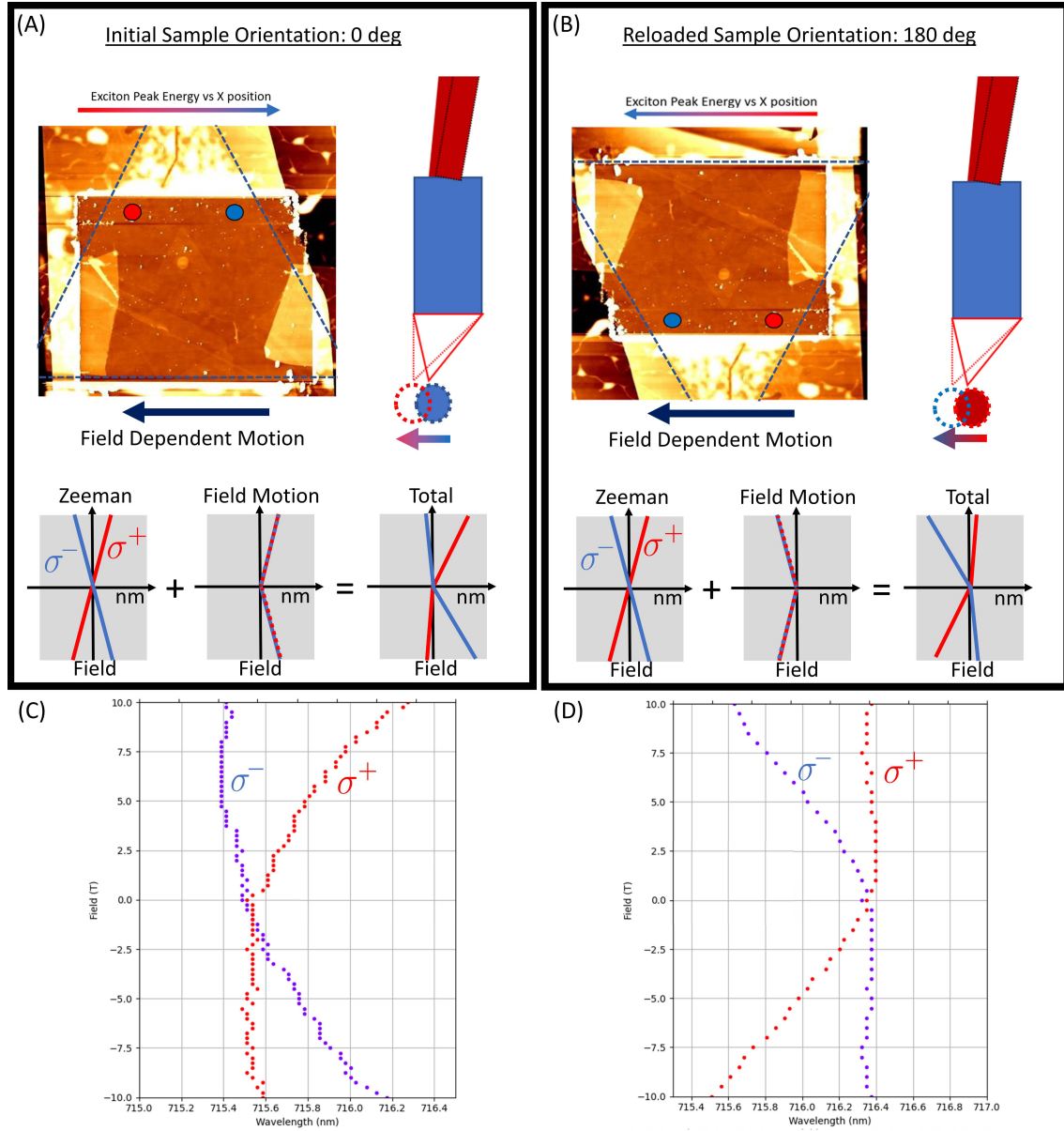


Figure D.18: (A, C) The initial orientation of the sample; i.e. 0 deg. An AFM image of the sample is notated with the change of the exciton's emission energy vs. illumination spot position due to strain (left is more red and right is more blue). If the illumination spot is always systematically shifting to the left due to an applied magnetic field, we expect the exciton peak to red-shift due to the changing position. This field dependent shift added to the valley Zeeman splitting gives a K-shaped magneto-photo response from the sample (x-axis = wavelength.) (B,D) If we rotate the sample 180 deg inside the probe, the magnetic field dependent shifts will now blue-shift the exciton emission energy. Therefore, the new field dependent shift added to the valley Zeeman splitting gives a X-shaped magneto-photo response from the sample (x-axis = wavelength).



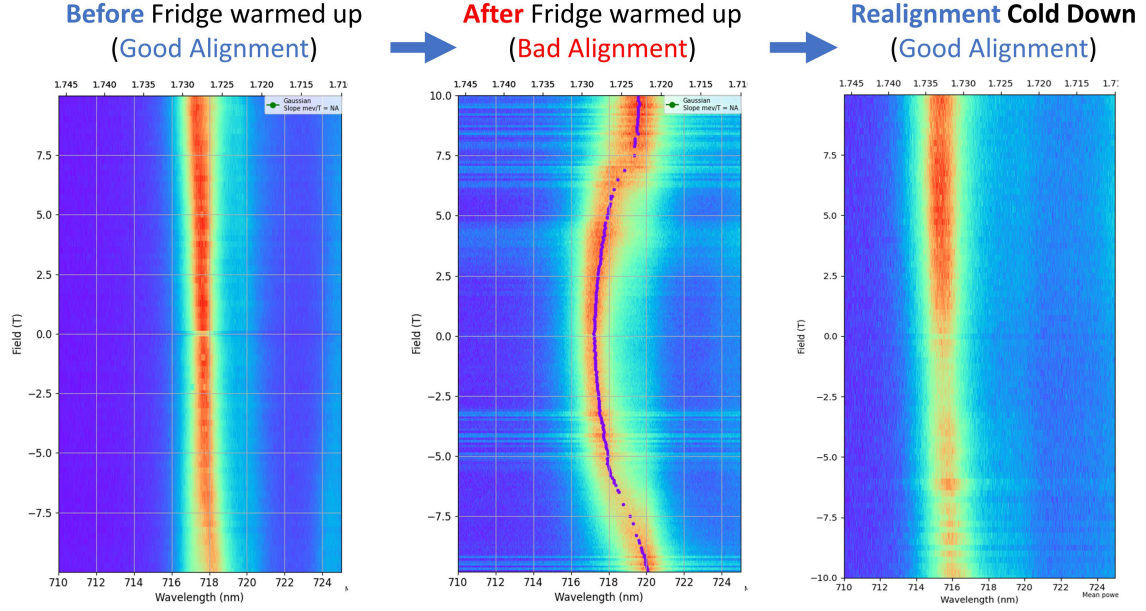


Figure D.19: (A) The optics are in good alignment on the sample. We see a linear magnetic dependent shift in the exciton emission energy of  $\sim 0.1$  meV per 10 T, which corresponds to the expected valley Zeeman splitting. (B) After a quench event, the sample was cold down, but the optics were not re-aligned. The beam path was very misaligned when this data was collected. We see a magnetic dependent shift in the exciton emission energy that independent of the sign of the magnetic field. Also, the energy shift is  $\sim 7$  meV per 10 T, which is much higher than the expected valley Zeeman splitting. (C) Re-aligning the optics brings us back into good alignment and we get data similar to that in (A).

## Appendix E: BlueFors Magnet

### E.1 Summary

The current BlueFors dilution refrigerator's magnet is a  $\pm 12$  T superconducting magnet from American Magnetics, Inc. It is attached to the middle 4K radiation shield, Fig. E.1, and the still radiation shield sits within its bore. The probe system is designed to load inside of the still radiation shield and reside inside the bore of the magnet. The specifications of the magnet are listed in Fig. E.1. Some of these values must be entered into the magnet controller prior to its use to calibrate the output current to the magnetic field in the bore. Additional details regarding the magnet installation can be found in the BlueFors documentation.



## MAGNET SPECIFICATIONS

AMI Magnet Number: 14850/14851  
 Type: Cryogen-Free Compensated Solenoid  
 For: BlueFors Cryogenics Oy Ltd  
 Test Date: 28 March 2018

|  |                             |
|--|-----------------------------|
| Rated Central Field @ 4.2K <sup>1</sup> .....          | 120 kG                      |
| Rated Operating Current.....                           | 94.13 Amperes               |
| <u>Field to Current Ratio.....</u>                     | <u>1.275 kG/Ampere</u>      |
| Charging Voltage (varies).....                         | 1.0 V                       |
| Ramp Rate (0 to 120 kG) .....                          | 0.019 Amp/Sec               |
| Homogeneity over 1 cm DSV.....                         | +/-0.1%                     |
| Inductance.....  | 52.6 Henrys                 |
| Clear Bore.....  | 3.0 inches [76 mm]          |
| Overall Length.....                                    | 17.7 inches [450 mm]        |
| Maximum Outside Diameter.....                          | 13.86 inches [352 mm]       |
| Magnet flange to center field.....                     | 11.96 inches [304 mm]       |
| Field Compensated from center field ..                 | <1000g at Z=14.0" [356 mm]> |
| Persistent Switch Heater Current.....                  | 18 mA                       |
| Persistent Switch Heater Resistance <sup>2</sup> ..... | .82 Ohms                    |
| Total Magnet and Switch Resistance <sup>2</sup> .....  | .38 Ohms                    |
| Magnet Weight.....                                     | 121 pounds [55 kg]          |

Figure E.1: Image of the magnet attached to the 4k middle radiation shield. Spec sheet supplied by American Magnetics. The most important value is the Field to Current Ratio which must be entered into the controller unit to calibrate the field values.

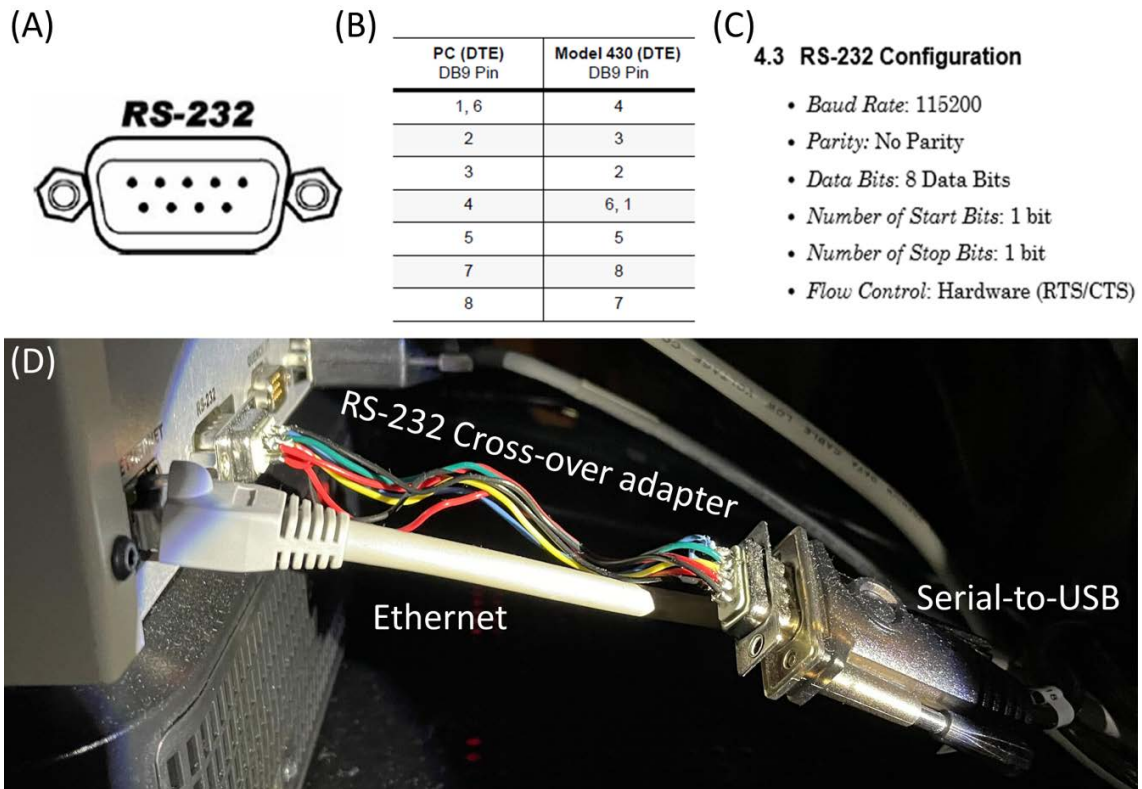


Figure E.2: All schematics and tables are from the American Magnetics manual [92]. (A) The RS-232 9-pin connector that is used to communicate with the magnetic controller over serial commands. (B) The cross-over pin configuration necessary for a 9-pin serial-to-serial adapter. (C) Serial protocols used to communicate with the magnet controller box. (D) Image of the cross-over cable that I soldered to allow for a USB-to-Serial adapter to work with the magnetic controller.

## E.2 Computer Control

The most direct means of connecting the magnet controller to a computer is via a Serial port on the back of the controller box. This is a 9-pin RS-232 connector and a cross-over adapter is required to connect it to a USB-to-Serial adapter. Such an adapter can be soldered together, as I did in Fig. E.2(D), using the table in Fig. E.2(B). The serial protocols for communicating with the magnet controller using serial commands are

standard and you will likely need to change the baud rate to establish a connection.

In addition to the serial port, the magnet can be controlled over Ethernet on a local network. Also, the software supplied by American Magnetics, Inc. connects to the magnet controller over a local network. This is better than serial because it means any computer can connect to the magnet controller without disconnecting USB cables. The IP Address and System Name are required inputs for the software to establish a network connection to the controller box. These are shown in Fig. [E.3](#). If your local network router does not have a defined static IP for the magnet controller, the IP Address will change any time it disconnects from the network.

I have used both Ethernet and Serial to communicate with the magnet controller box and have the controller box currently set up to use Serial for measurement controls and Ethernet for monitoring the field values on the BlueFors Controller laptop. Exclusively using Ethernet for data measurements is more risky than serial because you may have network interruptions that can cause the software to stop working if you don't have built in redundancies.

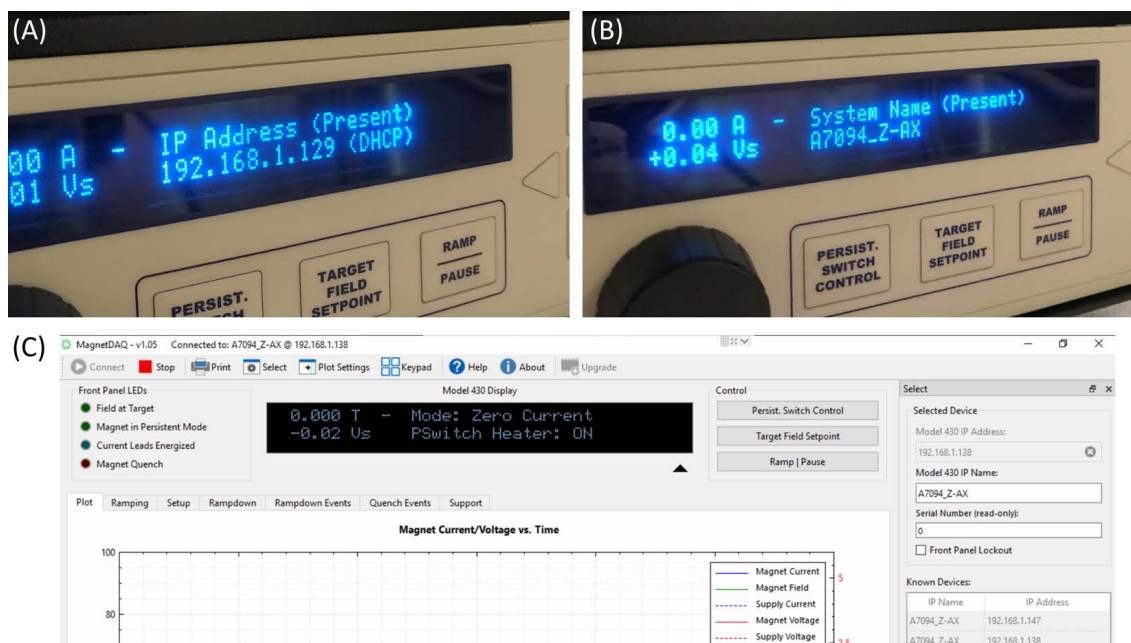


Figure E.3: (A, B) The IP Address and System Name can be found on the magnet controller. The IP Address will likely change if the controller box is turned off. (C) The software provided by American Magnetics to monitor and control the magnetic controller over Ethernet. You will need to enter the IP address and system name on the right hand side and click Connect (top right). All of the commands on the magnet controller can be accessed on this software.



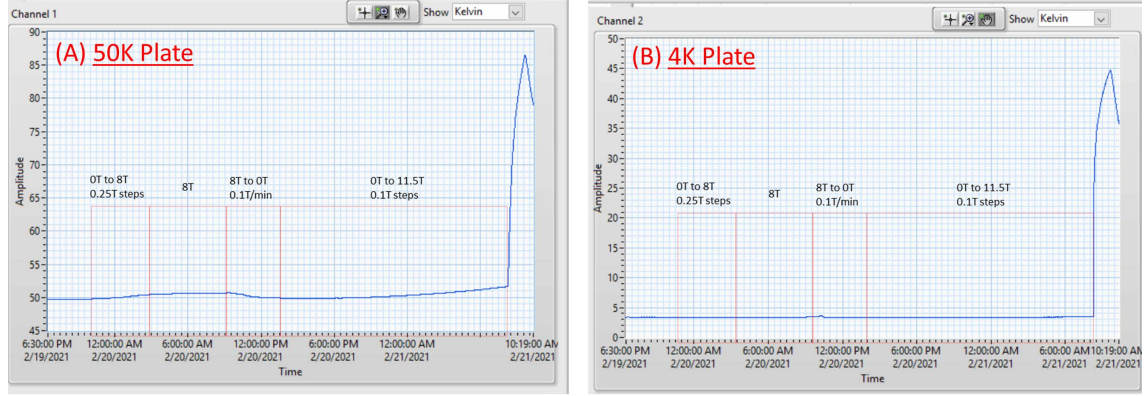


Figure E.4: (A, B) 50K and 4K plate temperatures in the BlueFors dilution refrigerator after a quench event.

### E.3 Quench Event

The biggest danger with the magnet is the possibility of a quench event where the coils stop superconducting and all of the current rapidly heats up the cryostat. This has happened a few times in our lab. The biggest cause was from poor power stability from the building's 240 V lines. One of the two phases will drop too low in voltage and the magnet power supply will stop working. We solved this problem by installing an in-line 240 V UPS and have never had any problems with the magnet since.

The other possible reason for a quench is if the temperature of the cryostat goes above the critical temperature of the coils. This has happened to us a few times when the building power shut off the Cryomech compressor. The temperature of the cryostat rose overnight until the magnet stopped superconducting. We have since updated the firmware of the cryomech compressor and it is far less responsive to the voltage fluctuations on the 480 V lines.



Quenches can be dangerous to the magnet, especially to the magnet power supply. The last quench event was caused by the Cryomech compressor shutting off and the fridge heating up. This caused the magnet to dump all of its current into the power supply and burned out the electronics. We had to send the power supply back for repairs.

If you experience a quench event, the temperature of all the cryostat's flanges will rapidly increase in temperature, as shown in Fig. E.4 for the 50K and 4K plates. The magnet controller will report a quench event that will need to be manually cleared before it can be used again, Fig. E.5(A,B), and the magnet power supply will register a fault, Fig. E.5(C,D). If the dilution unit is condensing helium mixture, all of the helium mixture will rapidly expand and likely cause the Turbo 1 to shutdown. You should immediately open V13 to alleviate the increased pressure in the gas handling system (there is a blow-out valve that will bypass V13 if the pressure grows too large). After a quench event, the only thing you can do is wait for the cryostat to return to base temperature and check that the magnet still works.



Figure E.5: (A) The magnet controller operating correctly at a target field of -6T. (B) The magnet controller reporting a quench event that must be reset. (C) Magnet power supply operating correctly. (D) Magnet power supply experiencing a fault event.

## Appendix F: Sirah Matisse DR Dye Laser

### F.1 Introduction

To be able to make the PLE measurements reported in this dissertation, a Continuous Wave (CW) laser in the energy regime of the  $2s$  Rydberg series of  $\text{WSe}_2$  was required. Unfortunately, this energy range is quite difficult to access with solid-state laser systems. Our M-Squared Ti:Sapphire CW laser only allowed access to energies from 1.24 eV to a maximum of 1.78 eV, well below the energy range of 1.8 eV to 1.9 eV required for our measurements.

Instead, we had to move to an older technology in the use of a dye laser. We tried three different generations of dye lasers and eventually managed to get an older Sirah Matisse DR that could be computer automated and reliably tuned. Sirah is one of the only companies that still sells dye lasers. This system was heavily modified prior to us receiving it from NIST because it can also be set up as a Ti:Sapphire laser, which was the partial configuration of the laser when we received it. Therefore, we needed to re-install the dye laser optics and align the Matisse from scratch to get it operational.

Dye lasers allow for a broad range of different energy spectrums to be utilized by changing the dye and the mirrors in the cavity. Energy ranges from  $<1.65$  eV to  $>2.25$  eV are accessible depending on the dye and cavity mirrors. The possible energy ranges

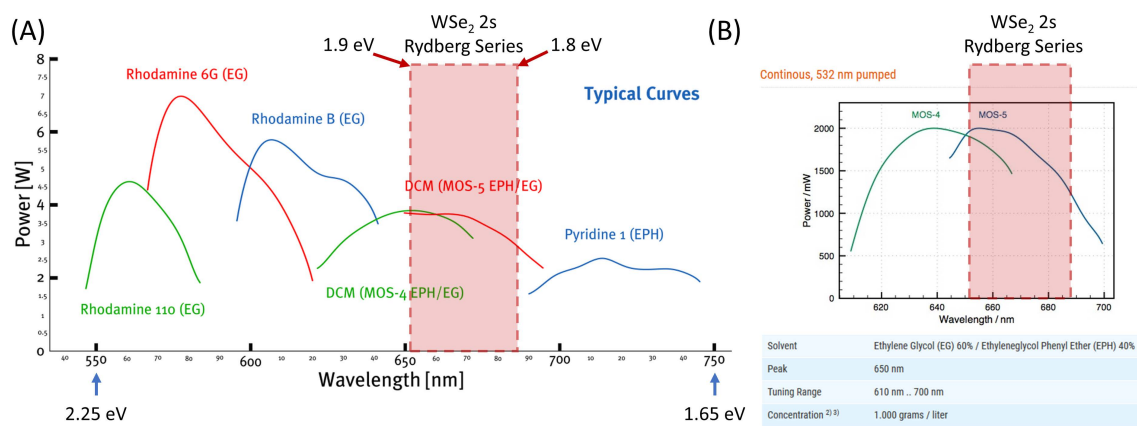


Figure F.1: These figures are from Sirah's website [93] advertising the laser energy ranges accessible with various dyes in their Matisse DR dye laser. (A) The output power vs wavelength of the Sirah Matisse DR for all available dyes. The energy range of the  $2s$  states probed in our PLE measurements is labeled and accessible via DCM dye MOS-5 mirrors. (B) There are two possible mirror configurations for DCM dye. All of our measurements fall within the MOS-5 wavelength range. The suggested dye mixture concentration by Sirah is listed below.

vary across the energies shown in Fig. F.1(A). The energy range we require for the PLE measurements of the  $2s$  Rydberg excitons in  $\text{WSe}_2$  is also shown on Fig. F.1(A). We are lucky that we only require one dye and one mirror configuration (DCM and MOS-5) to access the entire energy range required for our PLE data. Although dye lasers allow for a very broad range of laser energies, changing dye and/or cavity mirrors is a manual process that can be very time consuming.

## F.2 Mixing of DCM Dye

Fig. F.1(B) is a more detailed analysis of the energy range accessible with DCM dye. This dye can be ordered from the company Luxottica and you can request that they send the dye in pre-measured vials. This makes mixing the dye much simpler because measuring the dye powder is a messy business. The concentrations suggested for optimal output power are also listed in Fig. F.1(B). The 60% Ethylene Glycol (EG) and 40% Ethyleneglycol Phenyl Ether (EPH) mixture should be combined prior to adding the dye. DCM is a difficult dye to dissolve and it is suggested to mix it with a magnetic spinner in a 3L jug for 3 days to get nearly all of the DCM powder to dissolve. This is shown in Fig. F.2. Be sure that the dye mixture has been fully dissolved before using it or the remaining dye will settle in the pump and can/will cause it to clog.

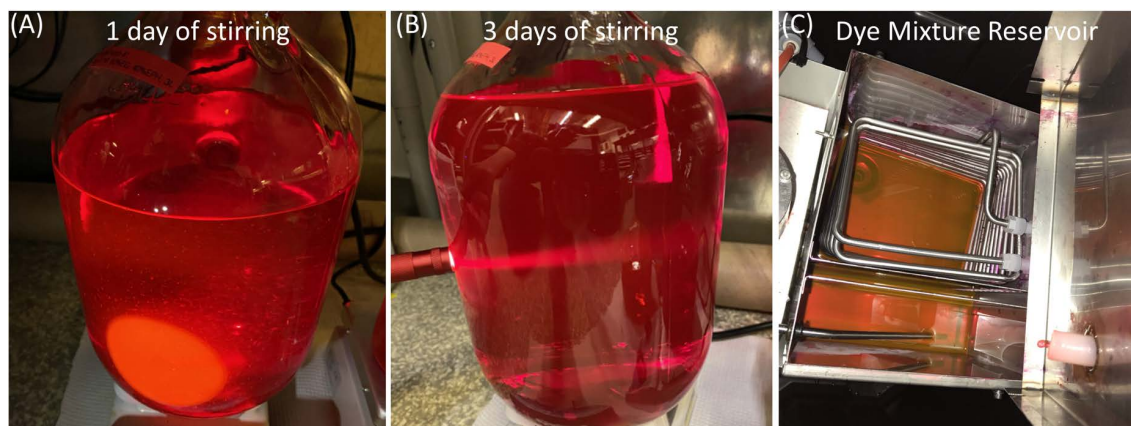


Figure F.2: Mixing of DCM dye using a magnetic stirrer. 3 grams of DCM powder is mixed in a 1.8 L Ethylene Glycol (EG) and 1.2 L Ethyleneglycol Phenyl Ether (EPH) solution. Mixing was conducted at room temperature. (A) After 1 day of stirring there is still a large number of undissolved dye in the solution that can be easily seen by shining a flashlight through the mixture. (B) After 3 days of stirring, nearly all of the dye had been dissolved into the solution. This DCM dye mixture was used for the dye laser. (C) The entire dye mixture should be poured into the circulator's reservoir. The laser should not be used unless a sufficient amount of dye is available. There must be enough dye mixture to be cooled via cooling water while running or it may get too hot and damage the dye jet.



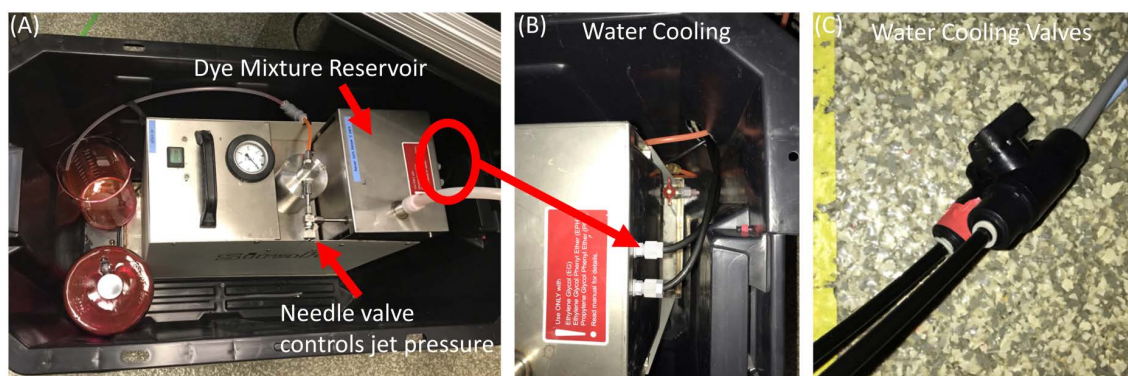


Figure F.3: (A) Dye circulator from Sirah. We have it placed within a heavy plastic box to avoid dye mixture spilling on the floor of the lab. There is a needle valve on the top of the unit that controls the dye mixture's pressure through the dye jet. The output tubing has since been changed, but the main unit is the same. The cooling lines come in through the back of the dye laser. (B) Close up of the water lines as they enter the dye mixture reservoir. (C) Water cooling valve on the floor next to the circulator. These must be opened before running the circulator.

### F.3 Dye Mixture Circulator

Once the dye is mixed it must be poured into the dye circulator, Fig F.3(A). This unit can store between 3-4 L of dye mixture in the reservoir, Fig. F.2(C). The circulator pumps the dye mixture at a pressure between 10-20 bar through the dye jet that is located inside of the laser unit. There is a needle valve on the top of the circulator that changes this pressure, Fig. F.3(A). This high pressure is required to generate a steady laminar flow of the dye mixture. A laminar flow is required for the laser to work because any flickers in the dye jet will cause the laser's power to fluctuate or cause that laser to stop working.

Before the circulator can be used, that water cooling system must be run to avoid overheating of the dye mixture. If the dye mixture gets too hot, it can cause damage to

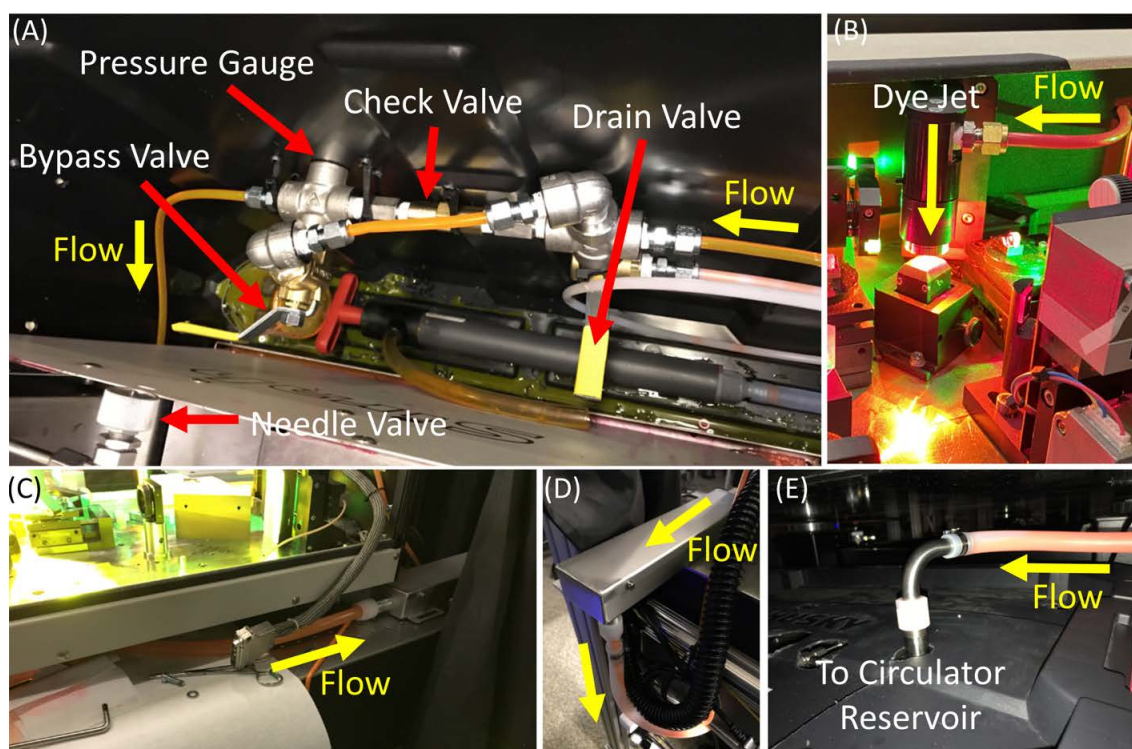


Figure F.4: (A) This is the high pressure tubing on the output line from the Sirah circulator. The dye mixture enters from the right and its pressure is controlled by the needle valve on the top of the circulator. There are three valves that determine the flow of the dye mixture. The first is the drain valve. This should always be closed unless you are draining the dye mixture from the dye jet. The second is the check valve. A check valve only allows liquid to flow in one direction; i.e. it prevents air from entering the tubing through the dye jet (which is open) when the circulator is off. The third valve is a bypass valve for the check valve. This valve should also be closed while the circulator is on. This valve is only used when draining the dye mixture from the dye jet. There is also a pressure gauge (not pictured here) that extends out of the plastic enclosure to allow users to read the mixture pressure without opening the enclosure. (B) After the dye mixture passes through the valve assembly, it enters the laser and exits through the dye jet. The mixture is projected out of the dye jet at a high enough pressure to form a laminar flow and then it is collected by the dye catch below the laser. (C) The dye catch directs the used dye mixture into the pan. (D) The pan is design to eliminate air bubbles that may form in the mixture as it exits the dye jet and collects in the catch. This is done by allowing the dye mixture a large surface area to settle and drain. (E) The dye mixture is then directed back into the reservoir where the mixture is cold via the water lines.

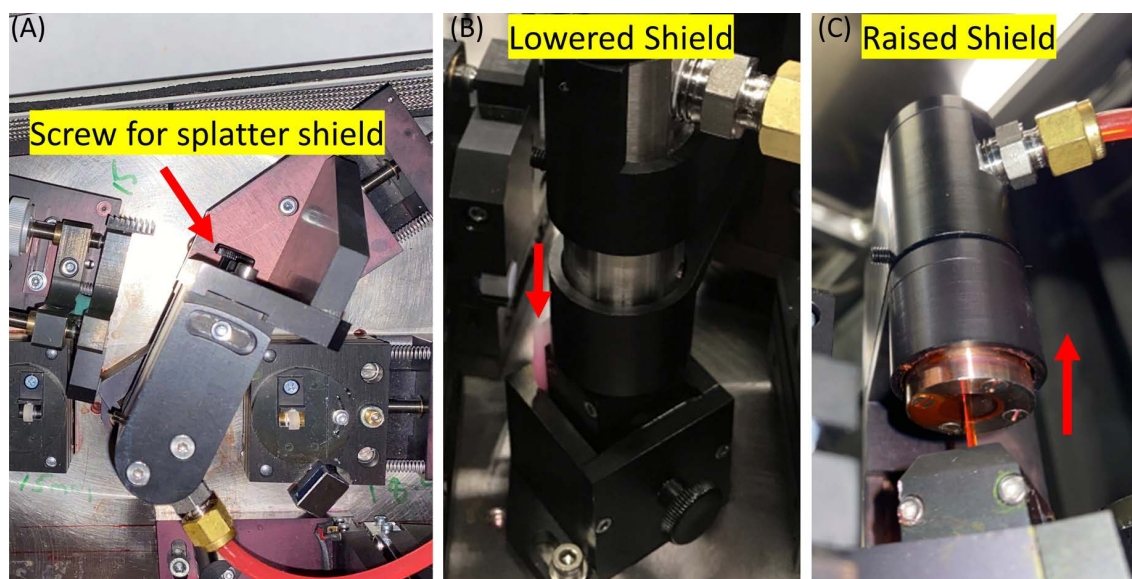


Figure F.5: (A) The hand screw on the back of the dye jet assembly allows for the splatter shield to move up and down. (B) When the dye jet is first turned on, the splatter shield should be lowered to the position shown here. If there are any air bubbles that disrupt the dye jet's stream, when the dye mixture splatters, it will not reach the optics. (C) After the dye jet has stabilized, the splatter shield can be raised out of the way and the laser is ready for use.

the dye jet. The water lines enter through the back of the circulator, Fig. F.3(B) and cool down the dye mixture in the reservoir, Fig. F.2(C). There are two push-to-connect valves for the water lines on the floor outside of the circulator that can be used to turn the water on or off, Fig. F.3(C). Be sure that these are open and the water is flowing before running the circulator.

To start the dye circulator, be sure that the drain valve and bypass valve are closed, Fig. F.4(A). When the circulator is started, there is some chance that dye will splatter on the surrounding optics while the pressure stabilizes in the first few minutes. This is due to air bubbles in the tubing being forced out of the dye jet at very high pressures and breaking the laminar flow of the dye mixture. The check valve, Fig. F.4(A), is in place to avoid the formation of air bubbles in the tubing, but there is still a chance that there are some small pockets that form while the circulator is off.

To avoid dye getting on the optics, lower the splatter shield around the dye jet, Fig. F.5(A,B). The screw on the back of the dye jet mount allows for the shield to be lowered around the exposed dye jet, Fig. F.5(B). Once the dye jet has stabilized after a few minutes, the shield can be raised, Fig. F.5(C). This will prevent any of the dye mixture from splattering on the optics. If dye does get on the optics, you can clean them using methanol or IPA and optical tissues. After a few minutes, the spatter shield can be raised and the pump laser can be turned on.

A problem that can occur with the circulator is if it has not been used for a while, the dye will settle to the lowest point which is where the pump is located. This will prevent the circulator from being able to turn on. If this happens, you will hear a light humming from the dye circulator, but it will not be running. There is an easy fix to this problem, but



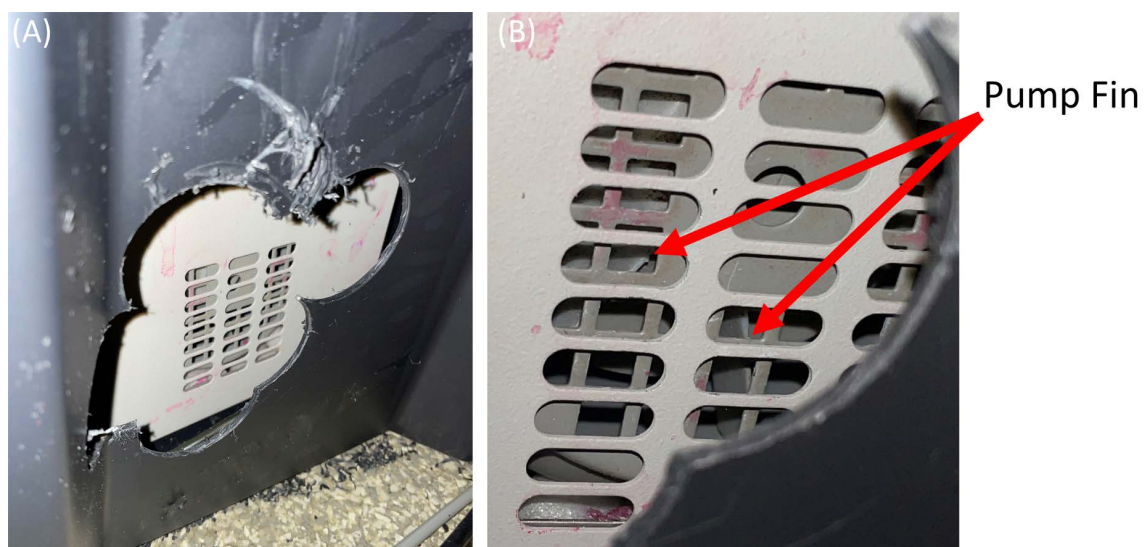


Figure F.6: (A) A hole is cut out of the back of the plastic enclosure that stores the Sirah circulator. This allows access to the fins of the pump. (B) If the pump is clogged with sediment from the dye mixture, you will need to rotate the fins manually while the circulator is on to get it started. You must use something small and strong (I used dental tools) to manually rotate the fins through this small slit until the pump starts working.

requires you to manually rotate the pump fins. They are unfortunately difficult to access. You can try to access them through a hole cut out of the back of the plastic enclosure that houses the circulator, Fig. [F.6\(A\)](#). Through the small grating on the circulator, the pump fins can be seen and rotated with a small instrument such as a dental tool or small screwdriver. After a few rotations of the fins, the pump should start working again.

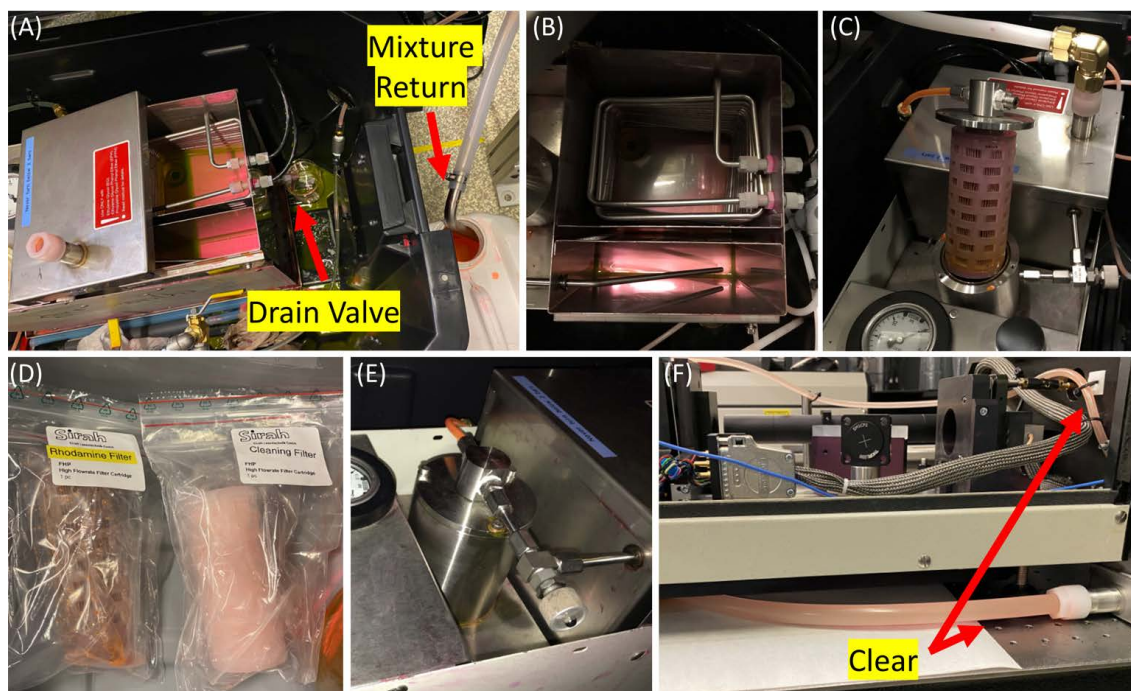


Figure F.7: (A) Image of the drain valve and the dye mixture reservoir with the top open. The dye mixture in the reservoir can be drained through this valve. The mixture return is placed inside of a container to collect dye mixture. (B) The dye mixture reservoir after it has been drained and flushed with pure EG. (C) Removing the filter for the current dye mixture. (D) Place the old dye filter in multiple plastic bags and label it. (E) Once the new filter is installed, re-connect the filter assembly. (F) Flush out the circulator lines with a few liters of pure EG. Once the lines are mostly clear, the remaining pure EG can be drained and the new dye mixture can be used.

## F.4 Changing Dye

Whenever the dye in the circulator needs to be changed, the entire system needs to be drained and flushed with EG. This is a dirty process that takes a lot of EG to complete. You will also need to change the dye filter to the one previously used with the new dye (or a new one). The details are also explained in the Sirah Matisse manual [94], but I will explain the procedure we used to switch from Rhodamine 6g to DCM. The procedure is



as follows:

(1) Open the bypass valve and the drain valve on the high-pressure tubing in Fig. F.4(A). Be sure that the tube from the drain is going into a bottle or glass beaker to collect the dye that will drain. This will drain the dye from the dye jet. Disconnect the mixture return from the top of the circulator reservoir and place it inside of a large jug (volume  $\geq 4\text{L}$ ), Fig. F.7(A).

(2) Place a glass beaker (has to be small to fit) underneath the drain nozzle at the bottom of the circulator, Fig. F.7(A). Open the nozzle and fill up the beaker. This will need to be done many times until all of the dye mixture in the reservoir has been drained out of the circulator.

(3) Once the dye has been drained, flush the circulator with 1-2 L of pure EG. This is done by closing the drain valve, pouring the EG into the reservoir, and running the circulator. BE SURE THAT THE SPATTER SHIELD IS DOWN AROUND THE DYE JET, Fig. F.5(B)! There is a lot of air in the lines now and the jet will splatter a lot. Watch carefully as the EG is pumped out of the reservoir! Never run the pump when there is no EG in the reservoir. This will clean out some of the remaining dye mixture in the reservoir, tubing, and filter. The reservoir should look similar to Fig. F.7(B) after the EG flush.

(4) The dye filter that catches small particles in the dye mixture must be changed to either a new filter or to a filter that was previously used with the new dye. The filter hub is connected to the needle valve that controls the pump pressure, Fig. F.7(C). Disconnect the needle valve and unscrew the three screws on the top of this hub. Lift the top of the assembly and the filter will come out of the unit. The filter can be pulled off and replaced

with the new filter, Fig. F.7(D). Clean out the hub with fresh EG and cleanroom wipes and then re-secure the top. Be careful with this step. If the O-ring is not secure, the unit will quickly leak because of the high pressures of the dye mixture.

(5) Flush the system with 3-4 L of EG until the tubing lines become as clear as shown in Fig. F.7(F). Now the circulator is ready for the new dye mixture. Drain any remaining EG that may be in the reservoir through the drain valve, Fig. F.7(A), and any that may remain in the dye jet, Fig. F.4(A). Be sure that all of the valves are closed and then pour the new dye mixture into the circulator's reservoir. Place the mixture return tube back on top of the reservoir. The system is now ready to start circulating the dye mixture.

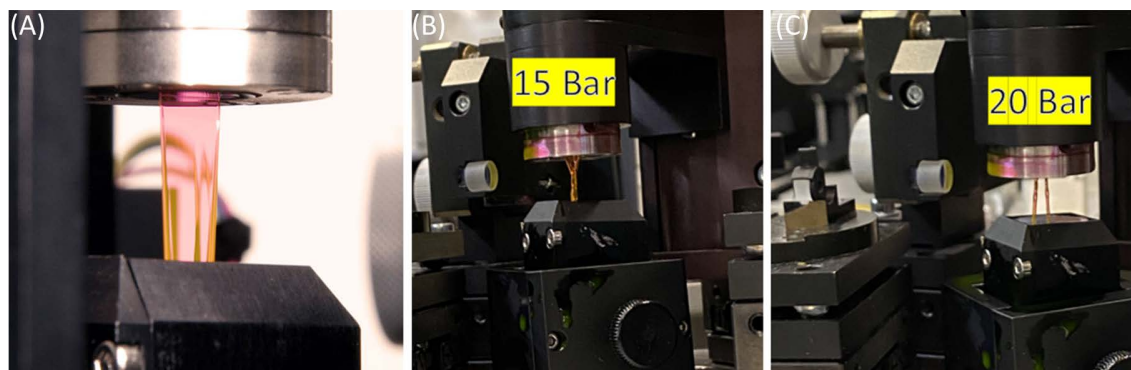


Figure F.8: (A) This is what the dye jet should look like while operating. The laminar flow should be very thin, uniform, and spread the width of the dye jet [93]. When we had dirt clogged in the dye jet, these were the two signs. (B) The dye mixture's flow was very narrow and non-uniform. (C) the flow breaks into two different streams at higher pressures.

## F.5 Dye Jet Problems

The dye jet's stream should be very thin and very uniform. If the jet looks different than shown in Fig. F.8(A), there are a number of potential issues that can cause this. The most common would be a particle (dirt or dried dye clump) stuck in the dye jet that is blocking the exit. If this is the case, the jet will most likely look something like that shown in Fig. F.8(B,C) when the dye stream breaks very rapidly or splits into two different jets at higher pressures. The jet can be cleaned by turning off the circulator and draining the dye jet of any remaining mixture. You can try to clear the clog by blowing an air gun through the jet exit. Then use a spray bottle of Ethylene Glycol to spray EG through the dye jet's exit. Do not use Acetone! Acetone may degrade the epoxy holding the dye jet together and permanently damage the assembly. EG will prevent damage to the dye jet (most of the dye mixture is EG) and may dislodge the obstruction.

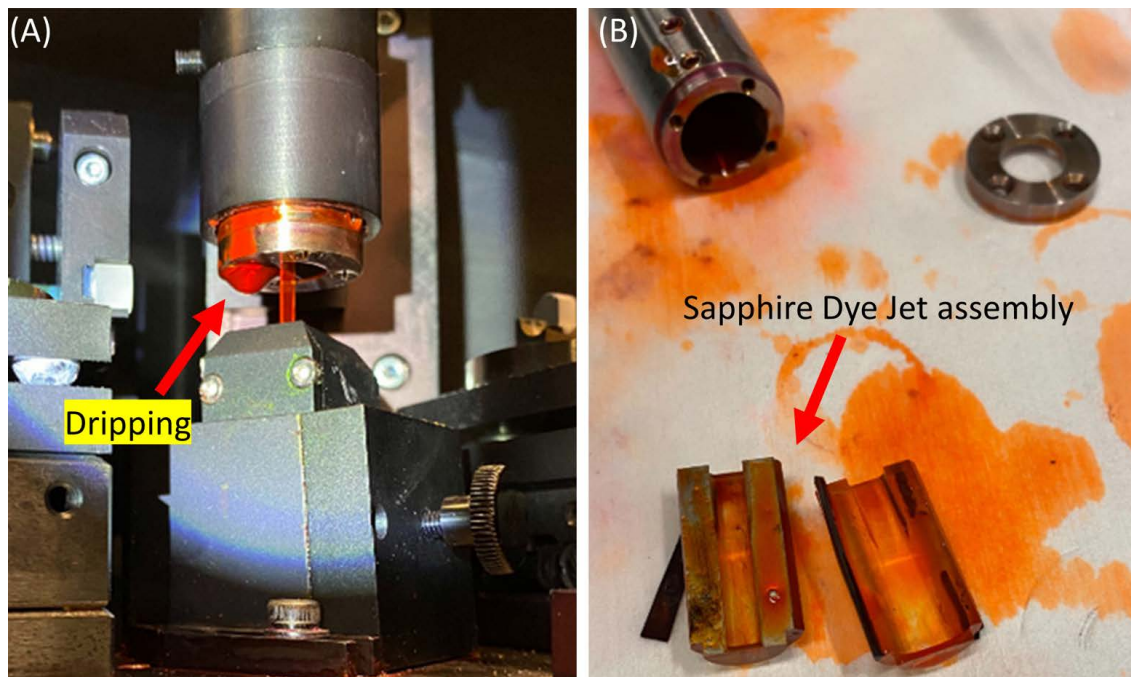


Figure F.9: (A) Notice the dripping from one of the screws on the dye jet. This is not supposed to happen and when it grew large enough, it would block the pump laser while the dye laser was running. This would cause the laser to stop working and would vaporize the dye drip. (B) Opening the dye jet assembly revealed that the epoxy holding the sapphire jet together had melted and the two pieces came apart. We attempted to epoxy the jet back together, but were unable to make it leak proof. Ultimately, we purchased a new dye jet assembly from Sirah.

We also experienced a bigger issue with the dye jet when the cooling water shut down unexpectedly one day. The dye jet composed of two pieces of sapphire epoxied together to form the narrow slit at the end of the jet assembly. As the dye's temperature continued to rise while the laser was running, it eventually caused the epoxy to melt and the two sapphire pieces came apart. Once the epoxy fully melted, we could not increase the pressure of the jet past 5 bar and there was a dripping from the screw on the bottom of the jet assembly, Fig. F.9(A). When we took the dye jet assembly apart, the two pieces of the sapphire jet (that are supposed to be epoxied together, fell apart, Fig. F.9(B)). We tried to epoxy the jet together ourselves, but were ultimately unsuccessful and had to order a new dye jet assembly from Sirah. (They noted that this could happen because our Matisse was one of their first models and they have since started using new epoxy that would not melt.)

If you experience any issues with the dye jet, contact Sirah's support. They are very responsive and helpful in solving these issues.

## F.6 Replacing Mirrors

To access a new energy range with the dye laser, you will need to swap out the cavity mirrors to match the dye and/or energy range required. The process isn't very complicated, but can be tricky the first time. All of the mirrors are screwed into their mounts in the laser and use the same assembly (except for the focusing mirrors FM1 and FM2 which are never changed). Mirror M2 is shown in Fig. [F.10\(A\)](#), but all other mirrors in the cavity look similar. The most important part of switching mirrors is making sure that the correct mirrors are used. Each one of the mirrors has details pertaining to that particular mirror written on the side as well as an arrow indicating the side with the coating. The best strategy is to swap one mirror at a time and make sure to match the details on the out-going mirror with the details on the in-going mirror.

Note that if the dye and mirrors have been changed, the BRF must also be changed. There is usually a pencil mark or line on the BRF that must be aligned to the BRF's set screw. The details regarding the BRFs and their installation is covered in the Sirah manual.

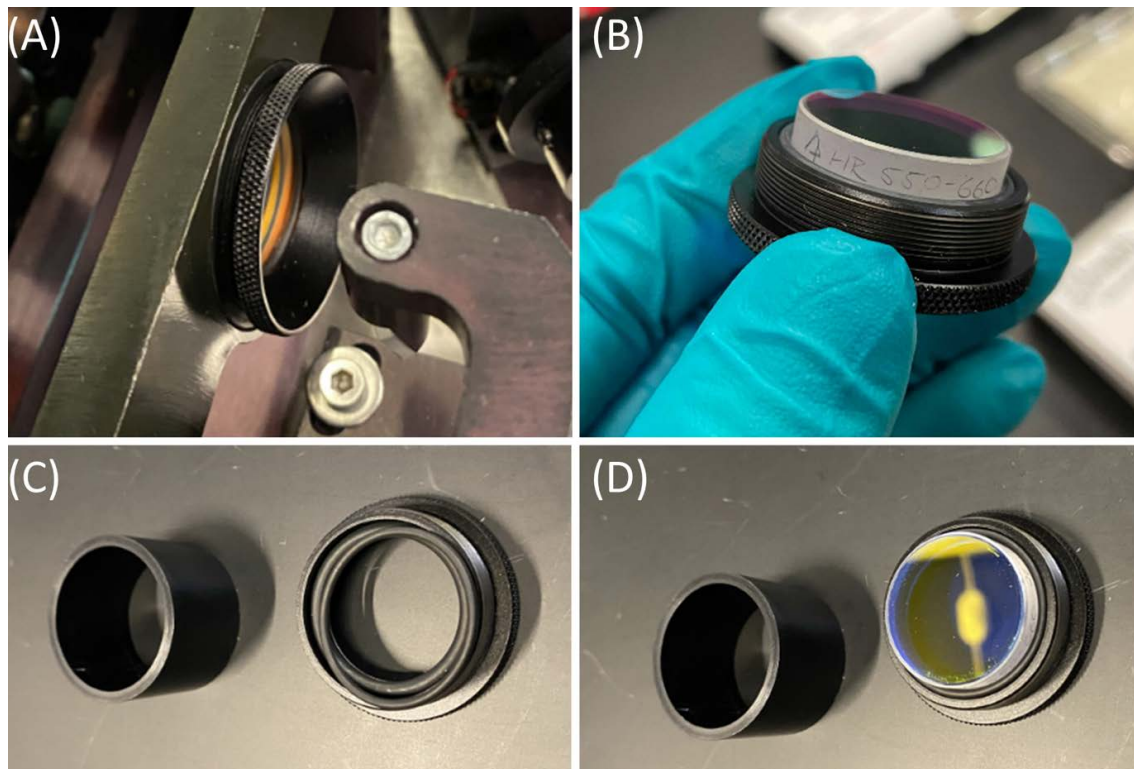


Figure F.10: (A) Image of the M2 mirror installed in the Sirah Matisse dye laser. All of the other mirrors that need to be replaced in the cavity look similar to this configuration. (B) The mirror was removed from the laser. Note the labeling written on the side. The wavelength range, angle, and reflection percentages are written here. (C) There are two different sized o-rings inside the thread assembly that hold the mirror in place. The bottom (and thicker) o-ring is placed inside of the thread assembly first. The top o-ring is thinner and holds the mirror in place. (D) Using the black tube shown here, press the o-ring and mirror into the thread assembly. This must be done uniformly so that the mirror is held in place and the mirror/o-ring looks the same as (B).



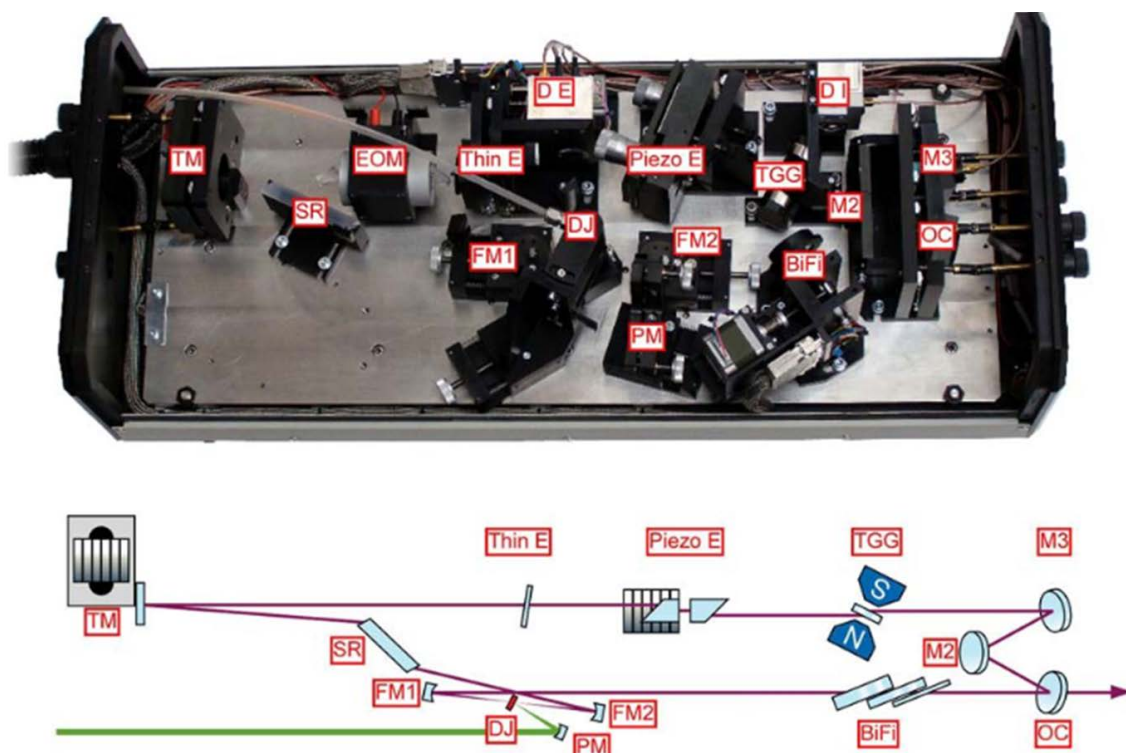


Figure F.11: Schematic and labeling taken from the Sirah Matisse DR dye laser manual [94]. This outlines the labeling of each mirror and the various components involved in the ring cavity.

## F.7 Alignment

If the cavity is completely misaligned (i.e. if the system is in a Ti:Sapphire configuration and is being switched to a dye laser), aligning the mirrors can be a challenging task and will likely take a few days. I will walk through our procedure for aligning the laser in this section.

Currently, the laser is in pretty good alignment and should only need to be slightly re-aligned on a weekly basis to maximize its output power. If the laser is not lasing within small adjustments, check that the BRF position is correct. If the BRF is set to a position

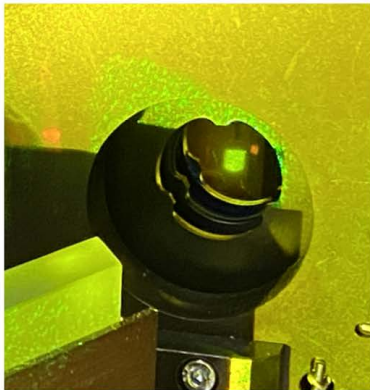
outside of the wavelength range of the dye or mirrors, the laser will not be able to lase. If this doesn't work, check that the dye stream is forming a proper laminar flow as shown in Fig. F.8(A).

For a full re-alignment of the dye laser, the first step is to remove the BRF filter and the thin etalon. Both of these optical components select a narrow bandwidth of light allowed to propagate in the cavity which makes it more difficult to align. This is especially true if the BRF is in the wrong position. The laser will be unable to lase. With them removed, all of the light will circulate in the cavity and when properly aligned, the power-maximum wavelength will lase. There is a procedure in the Sirah manual [94] for alignment, but I will walk through some of our procedure.

Fig. F.11 is a schematic of the Sirah Matisse DR dye laser's ring cavity. There are three mirrors around the dye jet (DJ). The first is the pump mirror (PM). It focuses a 532 nm pump laser on to the laminar flow of dye mixture formed by the dye jet. The pump's high energy laser light is absorbed by the dye which then fluoresces a broadband spectrum at lower energy. This light is collected by two spherical mirrors (FM1 and FM2) that are focused on the pump spot in the dye stream. The light from the dye is collimated by these two mirrors and begins to navigate around the ring cavity.

Because there are two possible paths around the cavity, a component labeled TGG, which is a Faraday-rotator, is in the cavity path. This acts as an optical diode and allows the light to travel in only one direction around the cavity. This direction is counterclockwise around the cavity in Fig. F.11. Therefore, collimated light from FM1 is directed through the BRF, which can be tuned to select a  $\sim 1$  nm spectral width of the dye's emission spectrum. This light reaches the output coupler (OC). It is a beamsplitter that

(A) Blocked M3 Mirror



(B) Blocked FM2 Mirror



(C) Spots overlap

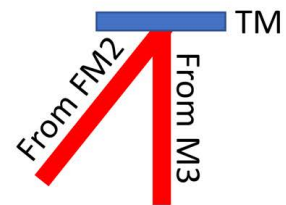
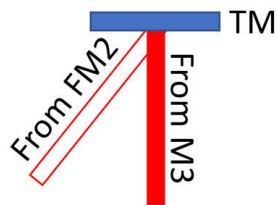
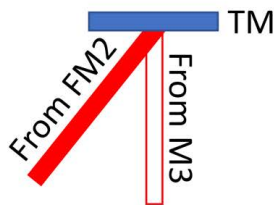
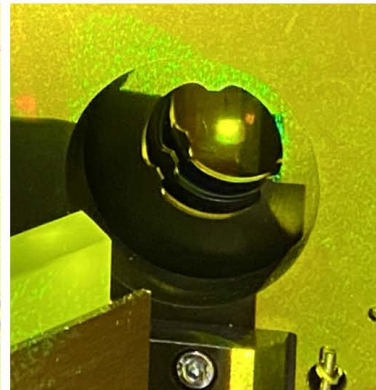


Figure F.12: (A) The light spot on the TM mirror from only the FM2 mirror. (B) The light spot on the TM mirror from only the M3 mirror. (C) Both spots from the FM2 and M3 mirrors overlap on the TM mirror. Note: the laser is at a lower pump power and is not currently lasing.

allows some of the light to exit the cavity (this is the laser light used in our experiment). The rest of the light reflects off the OC and proceeds around the cavity. It is reflected off of M2 and M3 where it passes through the etalons. We do not use the Piezo etalon (Piezo E). It is the finest spectral selective component in the ring laser and our experiment did not require such a narrow line width. We do use the thin etalon (Thin E). When utilized with the BRF, the thin etalon acts as a narrow band pass filter with a bandwidth of  $\sim 20$  pm if not less. The laser continues to the TM mirror (it can be piezo controlled, but we do not use this feature) where the beam path is redirected through SR to reach FM2. The collimated cavity light is focused back on the dye (which is the gain medium) and starts its journey around the cavity again.

The easiest way we found to align the laser was to look at the light reflected off of the TM mirror. We can see light from the FM2 and M3 on the TM mirror, and their overlap is a good way to determine alignment of the cavity. The first step is to make sure the light from M3 is at the correct height and not changing. Place two apertures at the exact height of 60 mm in the path between M3 and TM (the etalons can be removed until the laser is aligned, but leave the dummy piezo etalon in place). Align mirrors M2 and M3 until the height of the beam is correct. You should only need to change the horizontal position of the light to complete the alignment. Fig. [F.12](#) shows what the light should look like on the TM mirror when either FM2 or M3 are blocked and when they overlap.

The measured distances of the actuators for our alignment were:

$$\text{FM1 position} = 18.5\text{mm} \qquad \text{FM2 position} = 15.0\text{mm} \qquad (\text{F.1})$$

$$\text{Jet position} = 16.5\text{mm} \qquad \text{Pump position} = 15.0\text{mm} \qquad (\text{F.2})$$

These are only approximate and differ slightly from what Sirah suggests. The best alignment is likely close to these, but they are good numbers to start with.

Once this alignment is complete, increase the pump power. With DCM dye, the laser should start to lase for a pump power of  $\sim 8$  Watts. If it doesn't, monitor the output power of the laser and try to only manipulate the horizontal actuators for the M2, M3, and TM mirrors. The power should slowly increase and then jump as the laser starts lasing. When the laser begins lasing, the optics will look similar to the images in Fig. [F.13](#).

If you are unable to get the laser lasing at this stage, reference the Sirah Matisse DR manual for additional instructions and suggestions on how to get the laser aligned. Their support is also very helpful and quick to respond.

Once the laser is lasing, try to maximize the output power by optimizing the alignment. You can use the graphs in Fig. [F.1](#) as reference for the maximum output power. We have never fully realized this high of an output power with our laser and Sirah said that is likely due to the age of our system. If you are able to get  $>300$  mW of power using DCM dye with a pump power of  $\sim 10$ W, that is pretty good alignment and more than enough laser power for all of the measurements conducted in this dissertation.

The BRF and thin etalon can now be installed in the laser and calibrated. To understand how the wavelength filtering works, refer to Fig. [F.14](#). The dye is excited

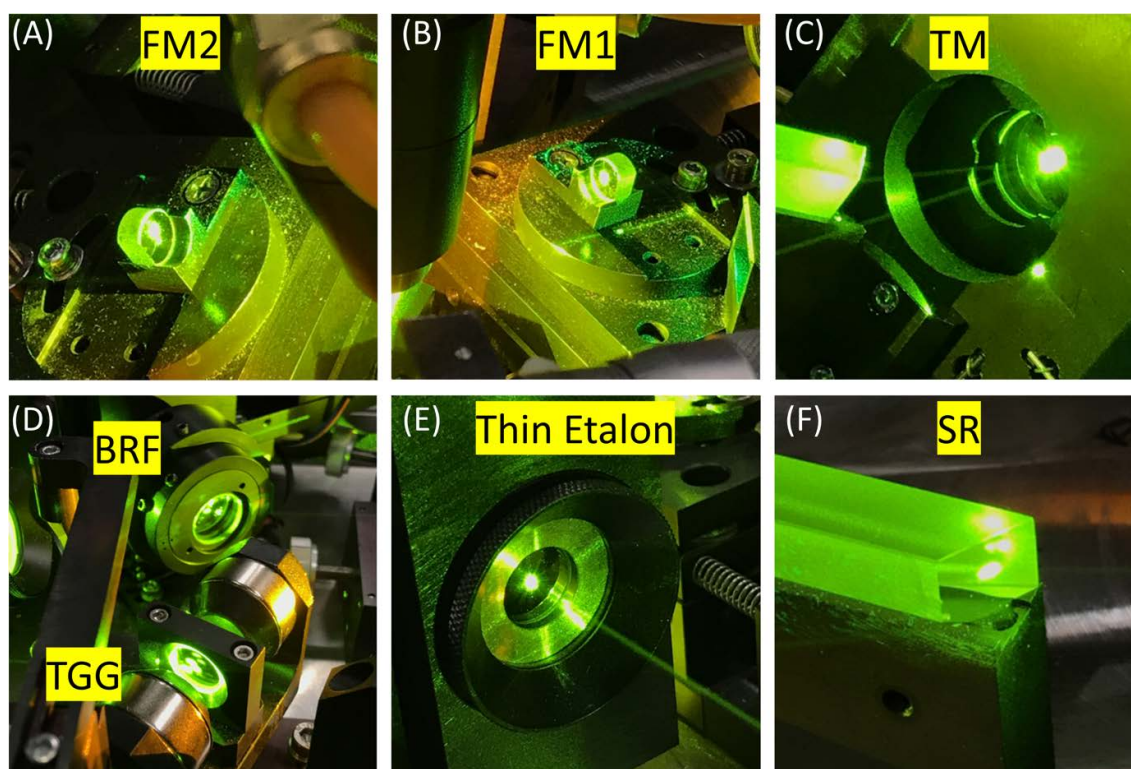


Figure F.13: The dye laser optics while it is lasing. The dye was Rhodamine 6g when these photos were taken, but it looks identical to DCM dye with just a different wavelength.

through the high power 532 nm pump laser. This causes the spot on the dye stream to fluoresce a broad spectrum (similar to the fluorescent spectrum of the Ti:Sapphire crystal in Fig. F.14). The mirrors of the cavity are coated to only have high reflectivity for some wavelength range. Therefore, wavelengths outside of the range of mirrors will quickly lose power and be unable to lase. Next, the BRF acts as a narrow band-pass filter with a spectral width of 1 nm. The BRF is designed such that this spectral range changes as it is rotated and allows us to sweep the allowed wavelength band across the spectral range of the mirrors. The final spectral filter we utilize is the thin etalon which also acts as a band-pass filter, but allows us to select an even narrower spectral width. We measured the spectral width to be about  $\sim 20$  pm. It is possible to select a single emission mode using the thick etalon (or piezo etalon), but such fine tuning was unnecessary for our measurements and we did not use this component.

The calibration of the BRF through the Sirah software will be explained in the next section, but pay close attention to the labeling on the BRF filter. You must use the correct one and place it in the correct position. Refer to the Sirah manual for details on which BRF to use with the dye and mirror configuration of the laser.



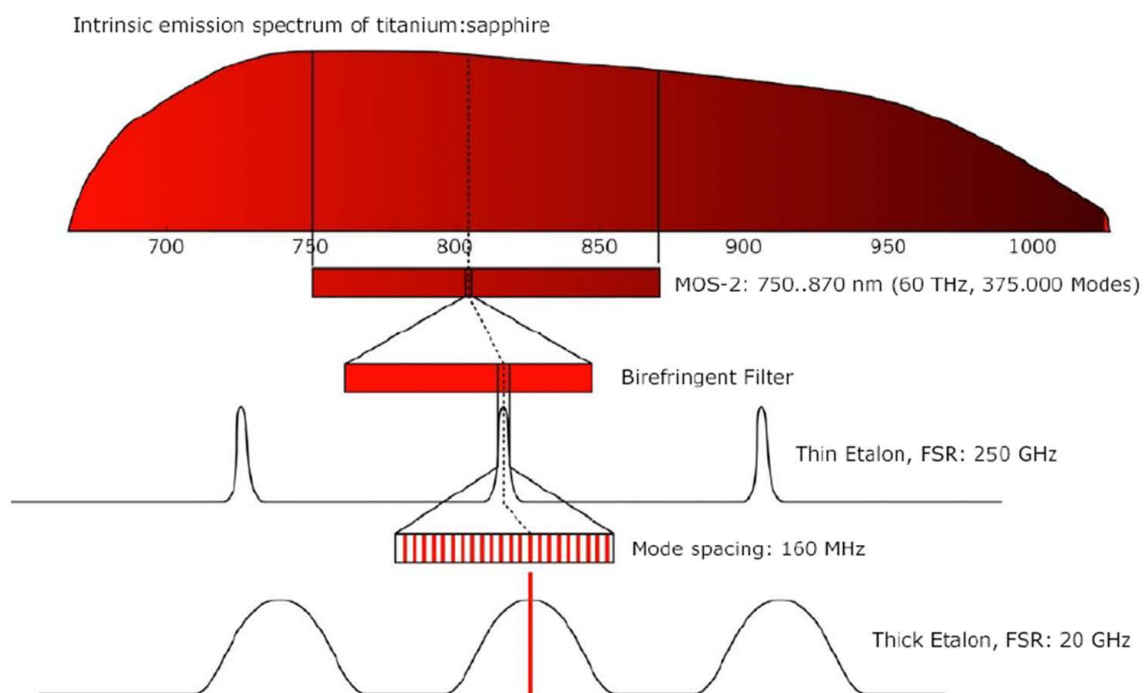


Figure F.14: Illustration from the Sirah Matisse User Manual [94] of how the wavelength of the laser is selected with the BRF and the etalons. This is for a Ti:Sapphire crystal's emission and MOS2 mirrors, but it's the same principle for the fluorescent spectrum of a dye.

## F.8 Sirah Matisse Commander Software, Homing, and Calibration

The dye laser has an electronic controller box that can send and receive VISA commands to and from a computer for automation of the dye laser. The controller box is shown in Fig. [F.15](#). This unit controls all of the motors in the dye laser and a lot of additional optical components that we do not utilize (such as monitoring the photodiodes inside the cavity, controlling the piezo mirrors, etc.). We exclusively use it to control the BRF and thin etalon motors.

Sirah supplies a software package for controlling the laser written in LabView called Matisse Commander. Unfortunately, the software is updated to work with the Sirah Matisse 2 dye laser and some of the software does not work with our earlier model. The most notable issue is with the homing of the BRF and thin etalon motors. These are the two optical components that we use to select and narrow the laser's linewidth (we do not use the piezo etalon). Each of these components has a stepper motor that controls its position which changes the laser's wavelength.

The Matisse software needs to home these motor positions to know where the zero is located. This is because the software (and firmware) does not allow for negative motor positions. Therefore, the motors must be homed to allow for the full range of the motors to be accessible. If they are not properly homed, the motor may only be able access a small range of its possible motion. They have changed the homing procedure on the new Matisse lasers and it is incompatible with the old sensors. Therefore, you cannot use the home commands to zero these motors. The only way to use the home functions is to manually press the white-sensors on these stages while the home procedure is running.

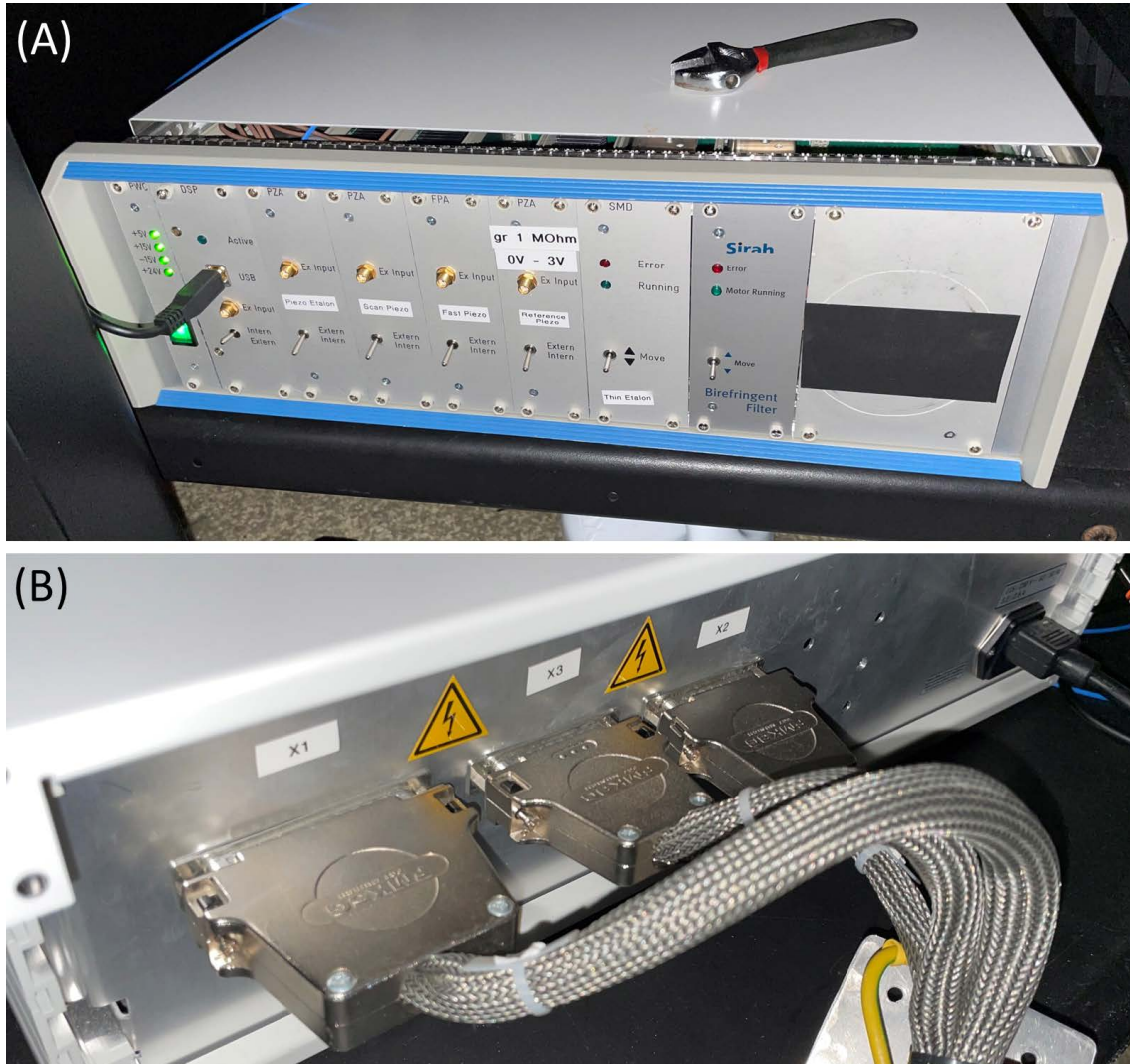


Figure F.15: (A) The front of the controller box. There are various LED indicators that warn the user if something is happening with the various motors. There is a USB input for computer automation. (B) Rear of the controller box. There are three sets of connectors that need to be connected from the dye laser to the controller box.

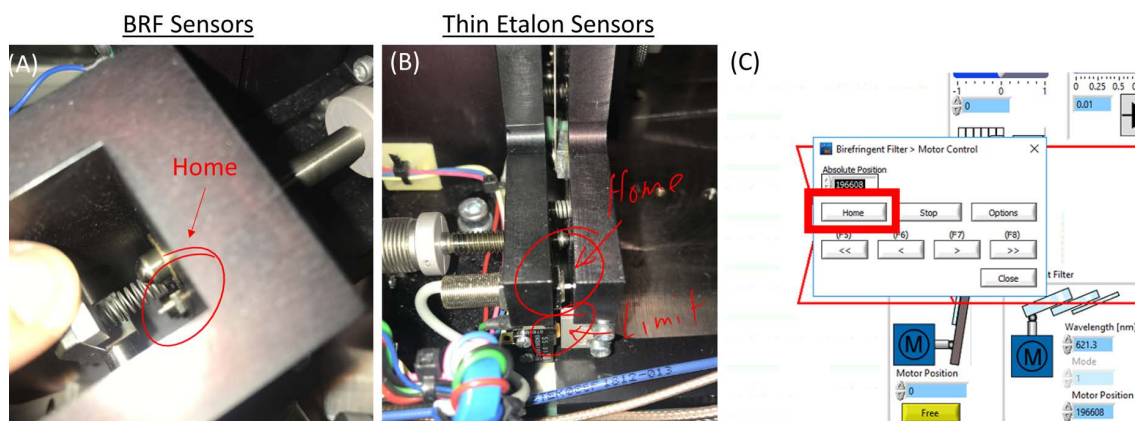


Figure F.16: (A) The homing button sensor for the BRF is below the lever arm underneath the stepper motor. (B) The thin etalon's homing button sensor is to the right of the stepper motor. There are also two limit switches, one on each end of the tilt stage. (C) To start the homing procedure, open up the motor controller for the specific motor and press Home. This will start the homing procedure, but since our system has different sensors than the newer models, you have to manually press the homing button sensors or the motors may break.

This is unfortunately quite crude. You have to press the Home button on the software and then press the sensor when you feel that it has reached the min/max, Fig. F.16. If you do not, you risk the motor not stopping and jamming the actuators. It may take a few tries to get a good motor range.

I had to previously run the Homing command a lot because the motors would slip and/or jump beyond their allowed values, causing a lot of errors on the software. This was eventually fixed by adding grease to all of the threads on the motor actuators and now it seems to run without much issue.

If you get the homing to work, you can now calibrate the BRF. This is done on the Matisse Commander software and is the only feature I've used from the software. This is because it programs the hardware of the Matisse controller with this calibration

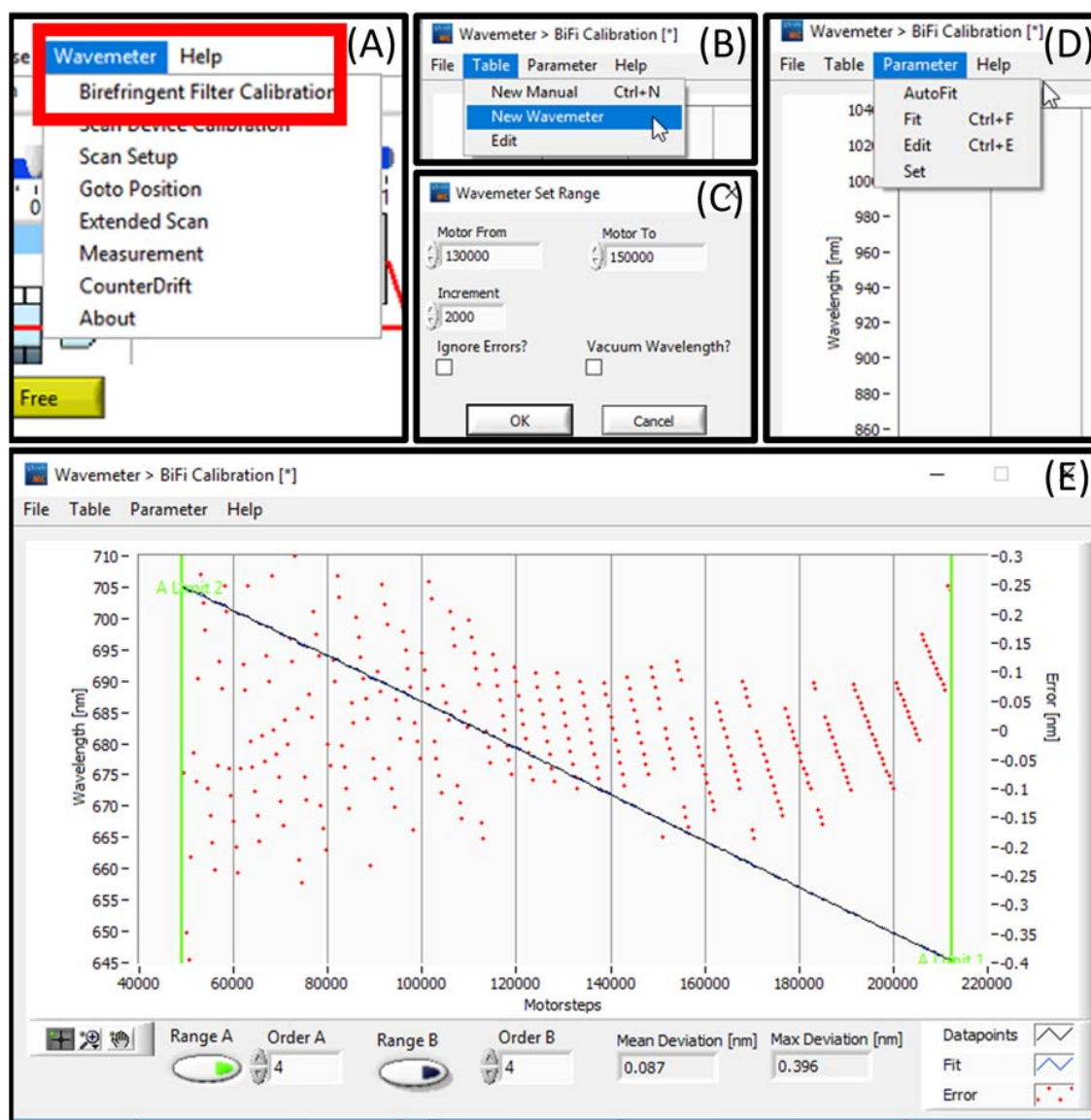


Figure F.17: BRF motor calibration. (A) In the Matisse Commander software select **Birefringent Filter Calibration** under the **Wavemeter** tab. This will open up the BRF calibration window. (B) On this window, select **New Wavemeter** to start a new calibration of the motor. (C) A new window will ask for start and end motor position as well as an increment step. These values should be determined by either running a very broad calibration first. Also, make sure you check the box **Ignore Errors**. This box will ignore errors when the wavemeter is unable to read a value because the laser stopped lasing as the BRF goes out of range. (D) Once the calibration data is collected, select **AutoFit** to linearly fit the calibration data. (E) Once you have a good calibration and fit, select **Set** shown in (D) to program the hardware in the dye laser controller.

curve, fitted data shown in Fig. F.17(D). Therefore, you no longer need to use the Matisse Commander software and any VISA commands sent to the Matisse using Python, Matlab, Labview, NI-MAX, etc. can access this calibration curve by telling the BRF motor to move to a certain wavelength.

The procedure for calibrating the BRF motor is pretty simple. First, open the Matisse Commander software supplied by Sirah. Under the **Wavemeter** tab, select **Birefringent Filter Calibration**, Fig. F.17(A). This will open a new window that runs the calibration program. In this new window, under the **Table** tab, select **New Wavemeter**. This tells the program that you are going to calibrate the BRF motor positions using the wavemeter, Fig. F.17(B). In the new window that opens, you need to enter start, end, and step motor positions as shown in Fig. F.17(C). You need to have some idea of which BRF motor positions lase and which don't. The easiest means of doing this is to run a calibration with large increments first and then run the calibration again with a narrow position range and smaller increments. Once the calibration data is collected, the program needs to fit it. Under the **Parameter** tab, select **AutoFit**, Fig. F.17(D). The final calibration data with the fit will appear similarly to Fig. F.17(E). To program the Matisse's controller box with this calibration for the BRF motor, select **Set** under the **Parameter** tab, Fig. F.17(D).

We do not calibrate the thin etalon because its motor positions are dependent on the BRF's position. This would require mapping the motor positions of the thin etalon for all BRF positions which would be difficult. Instead, I tune the thin etalon via my Python script after the BRF is set close to the desired output wavelength. The script sweeps the full range of the thin etalon motor and monitors the output wavelength on the wavemeter.



When the wavelength falls within the user defined threshold, the script ends.

The Python script for controlling the Matisse dye laser can be found in the directory: `G:\Shared drives\2DM\06 Python Data Programs\01b Instruments\Sirah.py`.



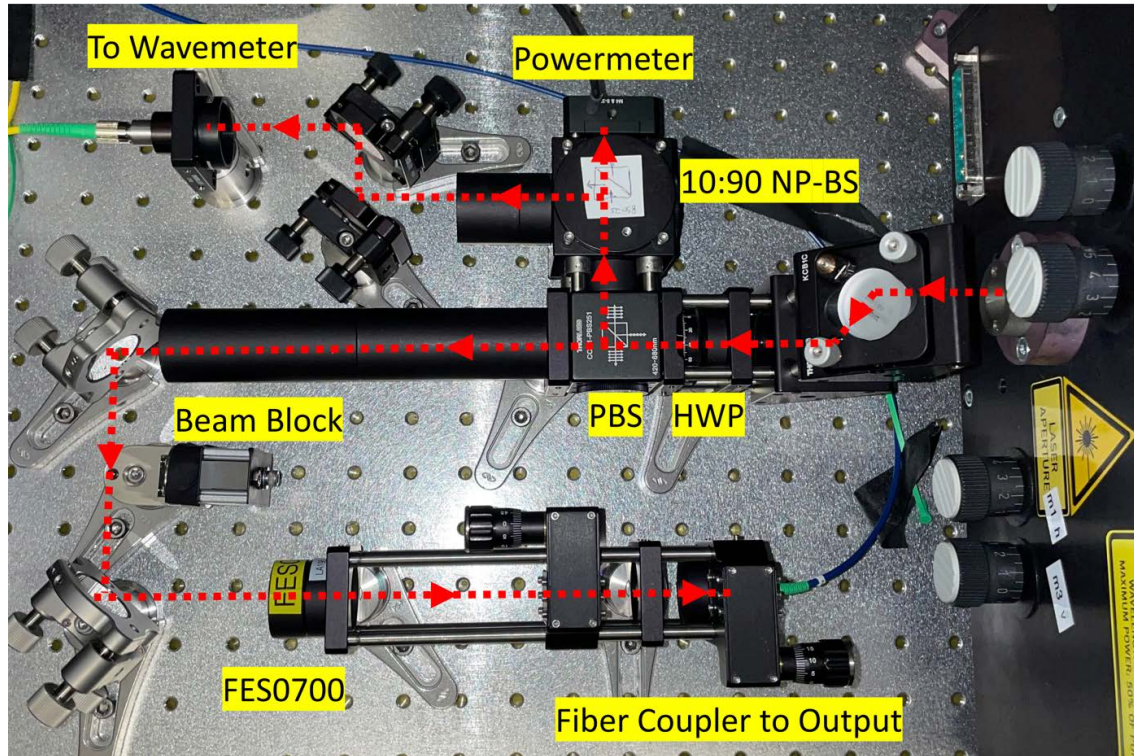


Figure F.18: Image and schematic of the output optics of the dye laser. The HWP on the output controls how much power passes through the PBS to the output fiber and how much is redirected to the power meter and wavemeter.

## F.9 Output Optics

The output optics of the dye laser are shown in Fig. F.18. We change the output height of the beam using a periscope and direct the laser through a half-wave plate (HWP) and polarization beamsplitter (PBS). The HWP allows us to change the polarization of the output laser beam which determines how much power transmits through the PBS. The reflected light from the PBS is directed through a non-polarizing beamsplitter (NP-BS) with a 10:90 reflection:transmission ratio. The transmitted light is collected by a thermal power meter. The reflected light is fiber coupled and sent to the wavemeter to measure

the output wavelength. The transmitted light from the PBS continues through a short-pass filter and is fiber coupled into the output fiber used in the experiment.

## F.10 Filtering Side Bands

The BRF and thin etalon allow for the dye laser to have a very narrow linewidth, but there are also low energy side bands that also exist in the cavity. These side bands, although very low intensity in comparison to the laser line, will contaminate the excitation light unless filtered out. To give an idea of the level of contamination from the laser side bands, refer to Fig. F.19. The characterization is done by shining the dye laser light on an hBN flake in the BlueFors dilution refrigerator. The light reflected off the substrate and the flake is collected, filtered with a 700 nm long-pass filter, and analyzed on our spectrometer. The experiment is a PLE measurement of the hBN flake and monitors the same energy range as the  $X_0$  exciton for  $\text{WSe}_2$ . hBN is transparent in this energy range and there should be no photo-response in this data. These two plots show the difference between illuminating the sample with raw laser light from the dye laser, Fig. F.19(A), and laser light that passes through a short-pass filter, Fig. F.19(C).

In Fig. F.19(A), the raw laser light from the dye laser is illuminated on an hBN flake. The 45 deg linear features that appear in the PLE data exhibit a 1:1 shift in wavelength as the wavelength of the laser is changed (y-axis). This could be a Raman mode from the substrate, but because of the abundance of these features, we believed it to be most likely due to the side bands of the dye laser.

In Fig. F.19(C), we placed a rotated 700 nm short-pass filter on the output of the dye laser before it reaches the flake. By rotating the short-pass filter, we are able to blue-shift its edge. This procedure is shown and explained in Fig. F.20. It is important that the short-pass filter has an edge that is less than the 700 nm long-pass filter so that any

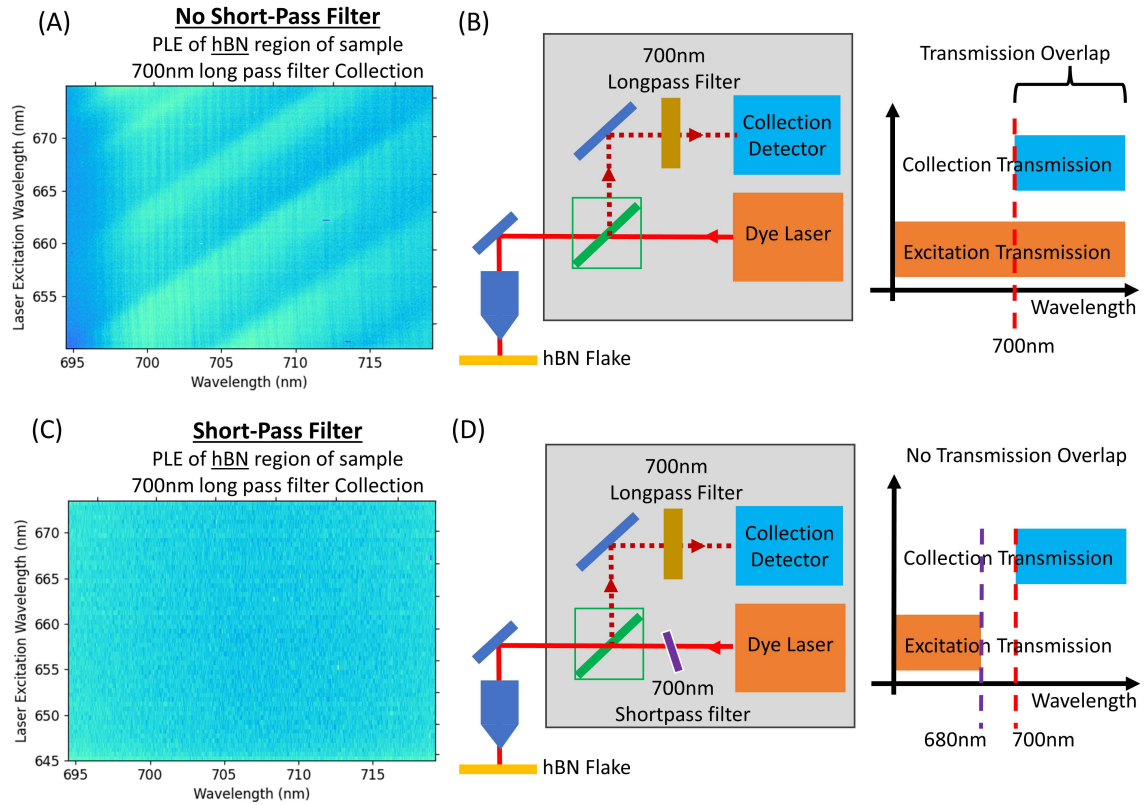


Figure F.19: Laser light from the Sirah Matisse dye laser is illuminate on an hBN flake. The laser light is collected, filter with a 700 nm short-pass filter, and sent to our spectrometer. This is the same PLE measurement conducted on WSe<sub>2</sub> while monitoring the X<sub>0</sub> emission except this data was from an hBN flake which should have no PL response in this energy range. (A) Without a short-pass filter at the output of the dye laser, illustrated in (B), the laser's side bands reflect off the surface of the sample and are detected in our spectroscopy. These are the 45 deg linear features detected in the PLE data. In this scenario, any light above 700 nm from the laser will be collected by the detector (as shown in the transmission overlap illustration). (C) When a short-pass filter is placed at the output of the dye laser and rotated to block light below 680 nm, illustrated in (D), all of the laser side bands are blocked by the short-pass filter and no longer show up in the PLE data. In this scenario, there is no transmission overlap between the excitation laser's transmission and the collection transmission.



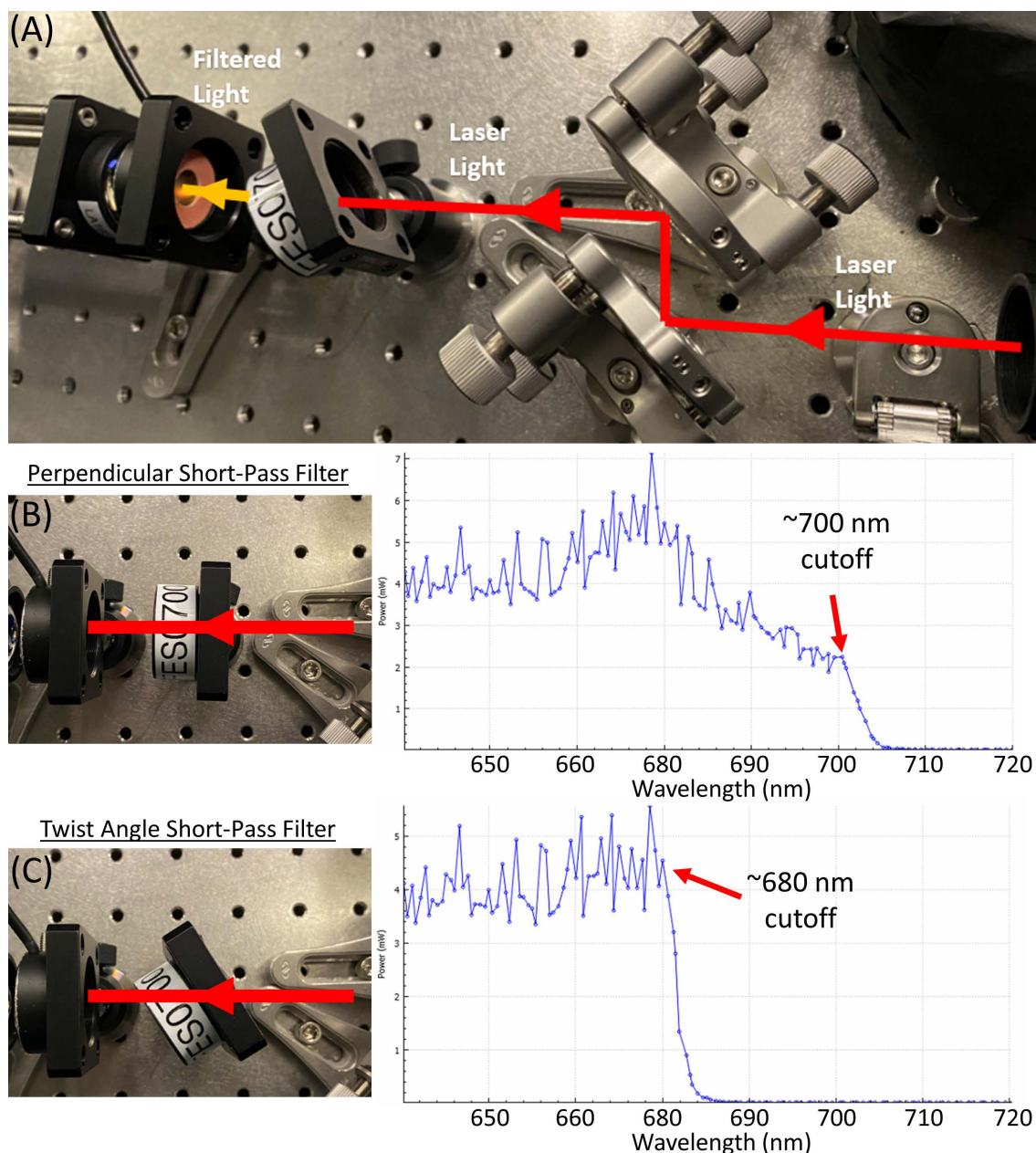


Figure F.20: A very useful feature about edge-pass filters (long-pass and short-pass) is that the edge cutoff can be blue-shifted by rotating the filter. This makes these filters variable and gives one the ability to select a more precise edge. This is mentioned on the Thorlabs website, but a clearer depiction is given by Semrock in Ref. [95]. (A) Image of laser light from the dye laser being directed through a rotated short-pass filter (FES0700 from Thorlabs). As the output wavelength of the dye laser is swept, the power for each wavelength is collected by a power meter. (B) When the short-pass filter is not rotated, we see an edge cutoff at  $\sim 700$  nm. (C) By rotating the short-pass filter, we are able to move the edge cutoff to  $\sim 680$  nm. Thorlabs notes that rotating their filters between 0-45 deg can produce a shift of about 10% in the edge cutoff wavelength.

side band light is completely filtered before it reaches the detector. In Fig. F.19(C), the filter was set to the same position shown in Fig. F.20(C) to give a band edge of  $\sim 680$  nm. Therefore, only wavelengths less than 680 nm reach the sample and only wavelengths greater than 700 nm reach the detector, as illustrated in Fig. F.19(D).

Since the addition of a short-pass filter removed these 45 deg features in the emission, we know they originated from the dye laser. In all measurements with the dye laser, we must have a short-pass to block these side bands that will otherwise contaminate our data. Short-pass filters can be selected and/or rotated such that their edge overlaps with whatever long-pass filter we use for collection. This is outlined in Fig. F.20.

## F.11 Power Stabilization

As the dye laser's wavelength is swept, the laser's power fluctuates dramatically, Fig. F.21(A). The PLE measurement would be very difficult unless we had an active component that stabilized the laser power as the wavelength is swept. In this section, I will go over the use of an electronically controlled fiber attenuator we used to stabilize the dye laser's power as the wavelength is swept.

Power fluctuations as a laser's wavelength is swept is a fairly common problem in optical measurements and Bin Cao had already written a PID loop Labview program to stabilize his laser's power. Bin's optical setup utilized a liquid-crystal and a polarizing beamsplitter in free-space to electronically control the laser's power. Since the dye laser is coupled into a fiber, we are able to use a simpler to implement a component called an Electronic Variable Optical Attenuator from Thorlabs. The exact part number is V600PA and is a polarization maintaining fiber attenuator over the wavelength range of 620 to 850 nm. The device is very simple to use. A DC voltage between 0 and 5 V can be applied to the optical attenuator which correlates to the attenuation of the light through the fiber.

It was fairly easy to modify Bin's labview program to work with the fiber attenuator and the VI can be found in the directory: G:\Shared drives\2DM\06 Python Data Programs\05 PID Laser Power LabView\01 PID, TCPIP, MEMS, Thorlabs SMA\LaserPower\_PID\_Fiber\_MEMS\_TCPIP.vi The main screen of the program is shown in Fig. F.21(B). I also added a feature that broadcasts over TCP/IP whether or not the laser's power has stabilized to the parameters set by the user. This part of the VI is shown in Fig. F.21(C). My Python script monitors



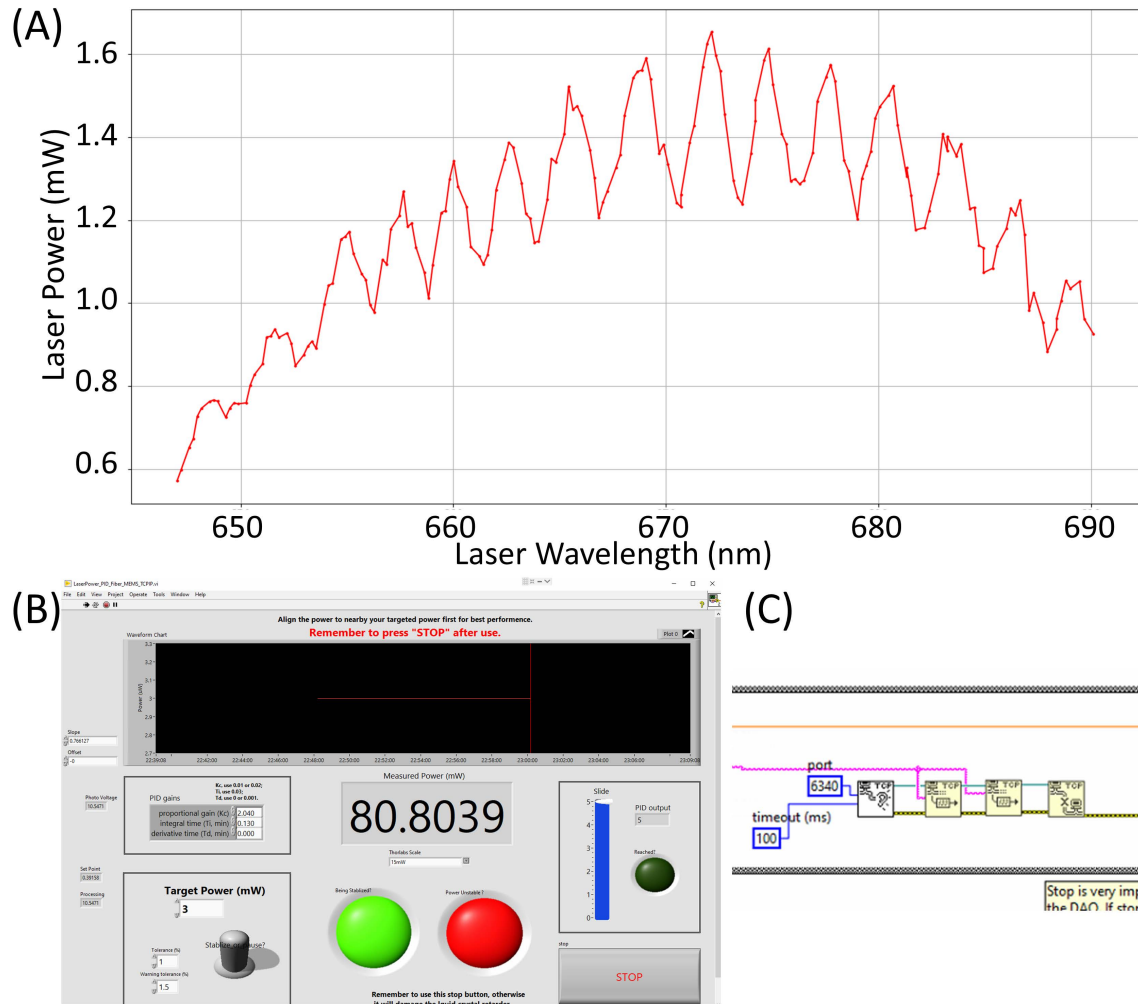


Figure F.21: (A) Power fluctuations as the wavelength of the dye laser is swept. (B) Power stabilization interface of the PID loop Labview program written by Bin Cao and adapted for the dye laser and fiber attenuator. (C) TCP/IP protocol that broadcasts whether or not the laser power has stabilized.

this signal and waits until the Labview program stabilizes before collecting the next PLE wavelength's data.

The hardware necessary for the laser power stabilization using the fiber attenuator is outlined in Fig. F.22(A). The dye laser is fiber coupled and directed through the fiber attenuator. The laser is then coupled into free-space and directed through a beamsplitter. Some of the light is sent to a power meter and the rest of the light is directed to the experiment. The power meter sends a reading to a DAQmx card connected to a computer. The Labview program on the computer is a PID loop that determines what output voltage must be applied to the fiber attenuator such that the power meter's reading matches the set value. This voltage is applied by the DAQmx card to the fiber attenuator. This is active stabilization of the laser power, so the Labview program is always receiving feedback from the power meter and adjusting the voltage on the fiber attenuator to compensate. Each of these components are shown in Fig. F.22(B,C,D).

This power stabilization method works quite well and allows for very stable PLE measurements over long periods of time. We are able to keep power fluctuations to around a few percent.

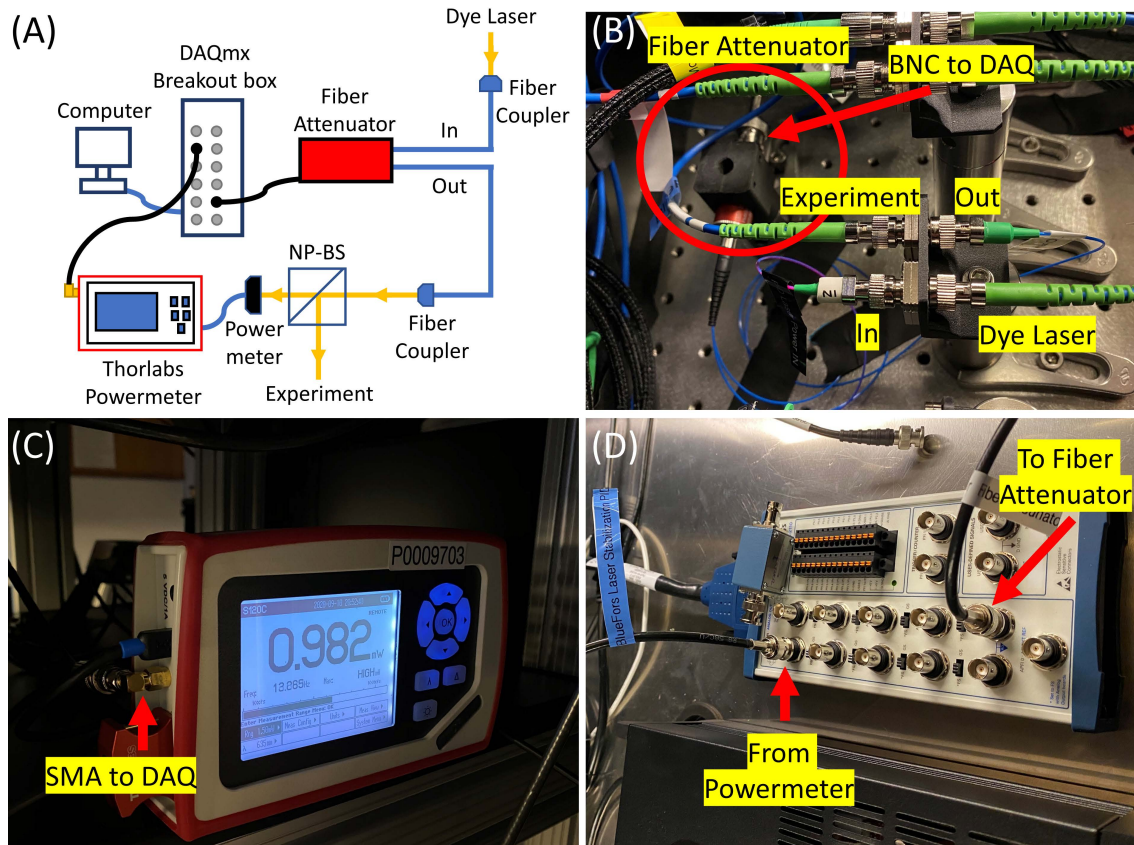


Figure F.22: (A) Schematic of the fiber attenuation feedback loop utilized in the power stabilization program. (B) The fiber attenuator and its input and output fibers. (C) Thorlabs power meter. Its detector measures the power reflected from the 90:10 NP-BS used in the BlueFors optics. (D) DAQmx breakout box that connects to the DAQmx card in the computer that runs the PID laser power stabilization program. The Thorlabs power meter is read by the DAQmx card and an output voltage is generated by the DAQmx card to change the optical attenuation.

## Appendix G: Additional Lab Equipment

### G.1 Montana Cryostat

I will briefly discuss the table top Montana cryostat that can be used to make 4 K optical measurements, Fig. [G.1](#). It does not possess a magnet, but can be used for any low temperature spectroscopy that does not require a magnetic field. Also, the Montana cryostat has significantly more vibrations than the BlueFors system. The vibrations are visible on the Montana's imaging system as the image of the sample's surface going in and out of focus. These vibrations are a result of the dry helium pump's motor and are a fairly well-understood issue with this table top cryostat.

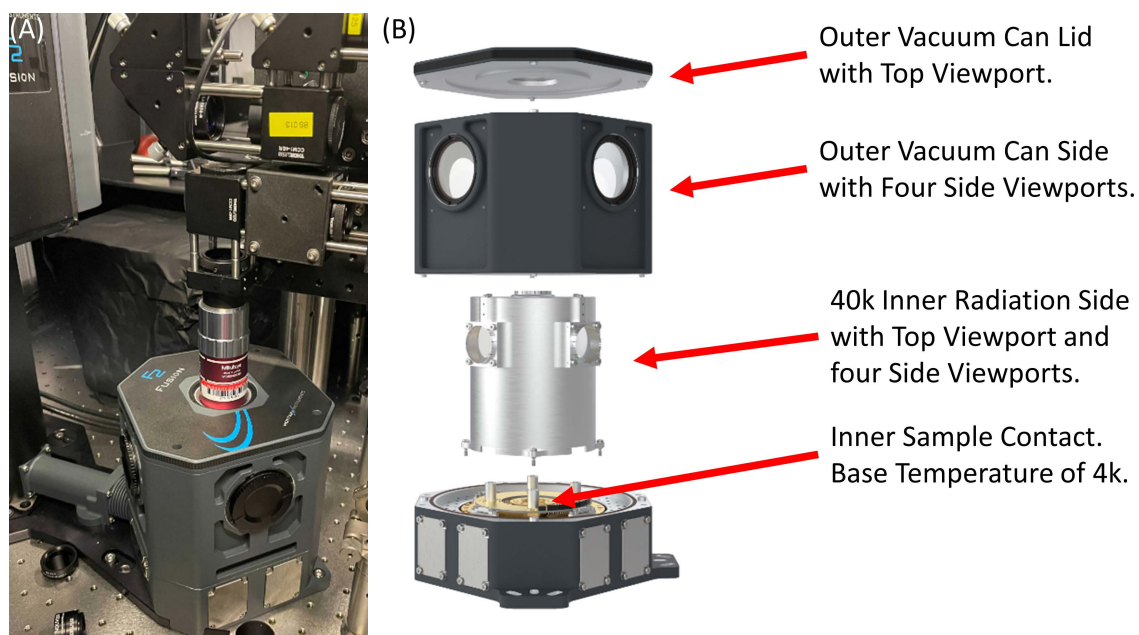


Figure G.1: (A) Image of our table top Fusion Montana cryostat. (B) Diagram of the inner construction of the Montana cryostat from their website. Disclaimer: This diagram is from Montana's website, but because Montana no longer sells this cryostat, the website is no longer accessible to cite.

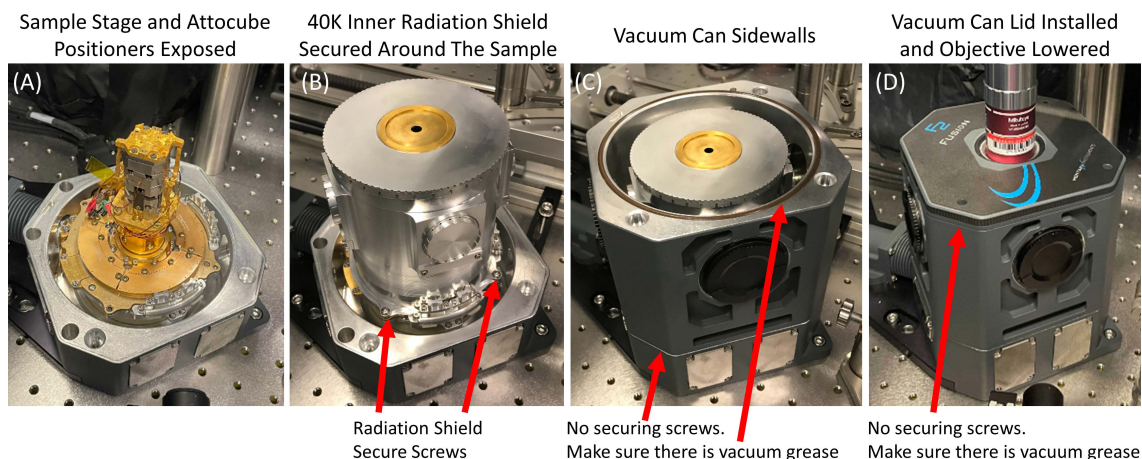


Figure G.2: (A) The full open Montana Cryostat. The Attocube positioners and sample stage can be seen in the middle of the cryostat. (B) Place the 40 K radiation shield in place and secure it to the 40 K plate via the four screws. (C) Place the vacuum can wall in place. Be sure to clean the surface and o-rings to avoid a leak. (D) Place the vacuum can lid on top of the wall. Also be sure to clean the surface and o-rings to avoid a leak. There are no screws that secure the vacuum can in place. It is held entirely by vacuum. You can start pumping out the system and the optics can be lowered into place.

### G.1.1 Table Top Cryostat Details

The Montana cryostat can be assembled following the procedure in Fig. G.2, or disassembled by following the reverse order. The sample stage is very similar to the stage in the BlueFors. The central plate in the middle of the cryostat is the cold head and reaches temperatures  $<4$  K. Attached to this plate are spacers, three Attocube positioners (x,y,z), and a thermal contact. The thermal contact has two thermal bridges that connect the plate above the Attocube stack to the cold head and is required for the sample to reach minimum temperature (Attocube positioners are very poor thermal conductors.) We used the thermal contact design from the Montana as reference for the design of the thermal



Sample stage and Attocube positioners exposed

Secure the sample carriage on the sample mount

Plug the SIP connectors into the carriage, if needed

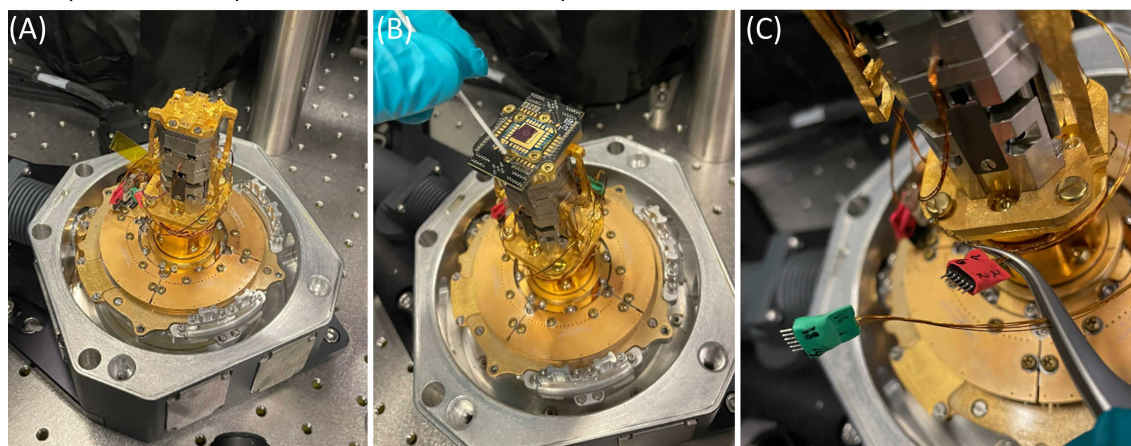


Figure G.3: (A) Sample stage without any sample installed. (B) Sample carriage placed on the sample stage and the two M2 screws secure it to the thermal contact. (C) If electrical contacts are required, plug the 1 mm pitch SIP connectors into the carriage board. Since we only have 10 DC cables available, only connectors 2-6 and 13-18 are used, specifically because 6 and 18 are gate contacts on the filtered boards. Be sure to only use these wire bonds pads on the carriage board if you intend to make electrical measurements on the Montana cryostat.

contact used in the BlueFors probe.

Installation of the sample carriage to the thermal contact above the attocube stacks is shown in Fig. G.3. The sample carriage is placed on top of the thermal contact and using two brass M2 screws, secured in place. If electrical contacts are required, the 1 mm SIP connectors can be connected to the carriage board. Since we only have 10 DC contacts, only pins 2-6 and 14-18 can be used in the Montana. Refer to the subsection that covers electrical contacts for more details.



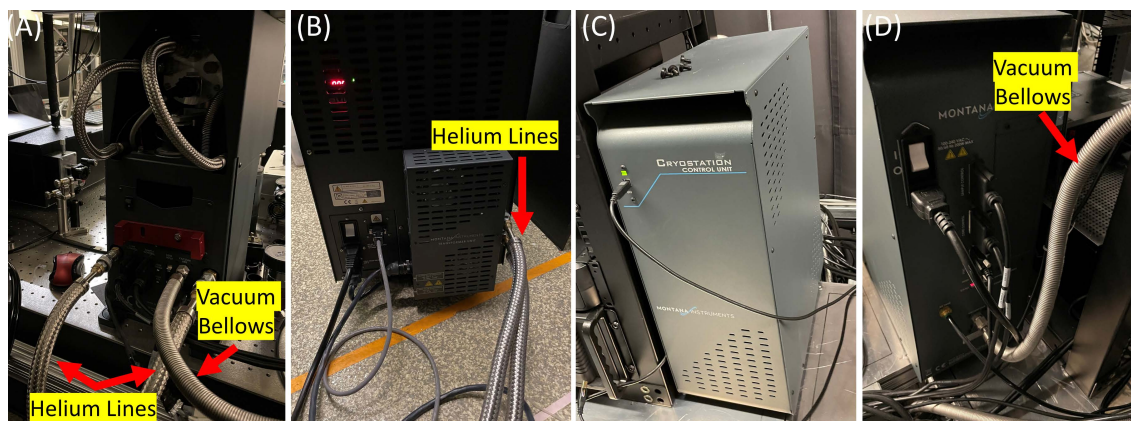


Figure G.4: (A) Rear of the table top cryostat. The helium pump lines from the compressor in (B) connect to this unit. The pulse tube motor is on the top of the table top unit. There is also a vacuum bellows that connects to the pump box in (C,D).

### G.1.2 Montana Pumps

There are three parts to the Montana cryostat, Fig. G.4. The first is the table top cryostat itself which should be secured to an optical table. The helium lines from the compressor unit and the vacuum bellows from the vacuum pump connect to the rear of this unit. This unit also contains all of the electronics for controlling the cooling and warming of the cryostat. It must be connected to a computer, and Montana supplies their own software package. Sometimes this software has trouble connecting to the control unit. If this happens, the best solution is to restart the software and unplug the USB cable from the control unit. Then plug the USB back into the control unit and start the software again.

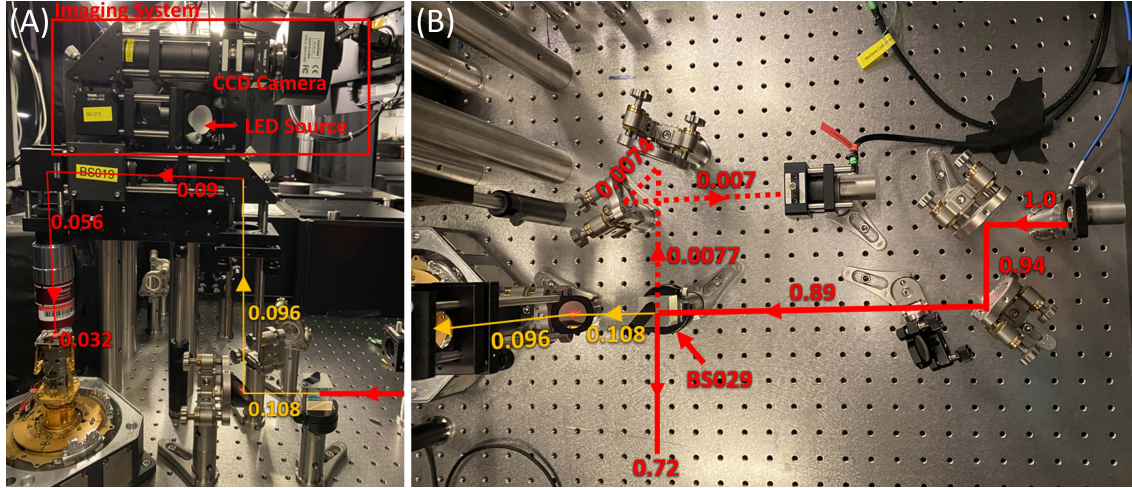


Figure G.5: (A) The cage system used to direct light to and from the optical table through the top window of the Montana cryostat. The top optics are for imaging the surface of the sample using an illumination LED and CCD camera. This is a very similar optical configuration as used for the BlueFors, Fig. D.8, except we only used cube beamsplitters instead of a pellicle. This added a lot of back reflection from the LED and blurred our image some. The bottom optics are exclusively for the excitation and collection path. (B) Optics on the optical table that direct the laser to the sample and the light from the sample to the collection fiber coupler. Note: Power losses are labeled at each stage of the optical assembly. With the optics utilized here, about 3.2% of our laser light reaches the sample. The numbers labeled at different stages correspond to the percentage of laser power starting with 1.0 as the output by the fiber.

### G.1.3 Optical Excitation

The optics involved in the excitation path from above the Montana are attached to an aluminum breadboard on a 3-axis stage. The Mitutoyo 100x M Plan APO NIR High Resolution Objective, part number: 378-864-5, used in our high magnification measurements has a small working distance of 10 mm. This means the objective has to be lowered into a viewport that resides beneath the vacuum can lid to get that close to the sample. Hence, we must be able to move the entire optical assembly, shown in

Fig. G.5(A), up and down to allow for the objective to be removed or installed.

The measurement configuration we utilized was to launch the laser from a reflective collimator and through a 90:10 NP-BS, Fig. G.5(B). The excitation path was directed up to the optics on the 3-axis stage. These optics re-direct the excitation laser toward the objective that focuses it on the sample. The collection path is redirected at the 90:10 NP-BS toward another reflective collimator. The collection fiber takes the light to our spectrometer for analysis.

There is also a LED and CCD camera imaging system as part of the Montana optical system attached to the breadboard on the 3-axis stage. This allows us to image the surface of the sample. Unlike the BlueFors optical assembly, we used cube beamsplitters instead of pellicle beamsplitters. This results in a lot of back reflection from the LED on the CCD camera and makes the image blurry. In the future, these cube beamsplitters should be exchanged with pellicle beamsplitters.

#### G.1.4 DC Wiring

The Montana is currently equipped with 25 DC cables that allow for electronic control of instruments or devices inside of the cryostat. A detailed outline of the wiring is shown in Fig. G.6. 15 of the wires are used for the closed loop feedback Attocube positioners that make up the sample stage and allow for movement of the sample in x, y, and z. The remaining 10 DC contacts can be used for measurements of devices whether through transport or gating.

The internal connectors of the Montana are 2 mm SIP and the we have soldered and epoxied 32 AWG wires from Lakeshore to 1 mm SIP connectors used by our sample carriage. Since we only have 10 DC lines to use, and our carriage system is designed such that only pins 6 and 18 can be used for high voltage gating above 25 VDC, we made the wiring only for 2-6 and 14-18. Pin 1 and 13 are **NOT** used. Therefore, if you want to make electrical measurements in the Montana, make sure to only use bond pads: 2-6 and 14-18.

The 10 DC wires are broken out into a BNC breakout box with grounding switches. Therefore, the wires can be grounded prior to plugging in the SIP connectors to the carriage board. The 15 other lines connect to the Attocube wiring that goes to the Attocube controller box.



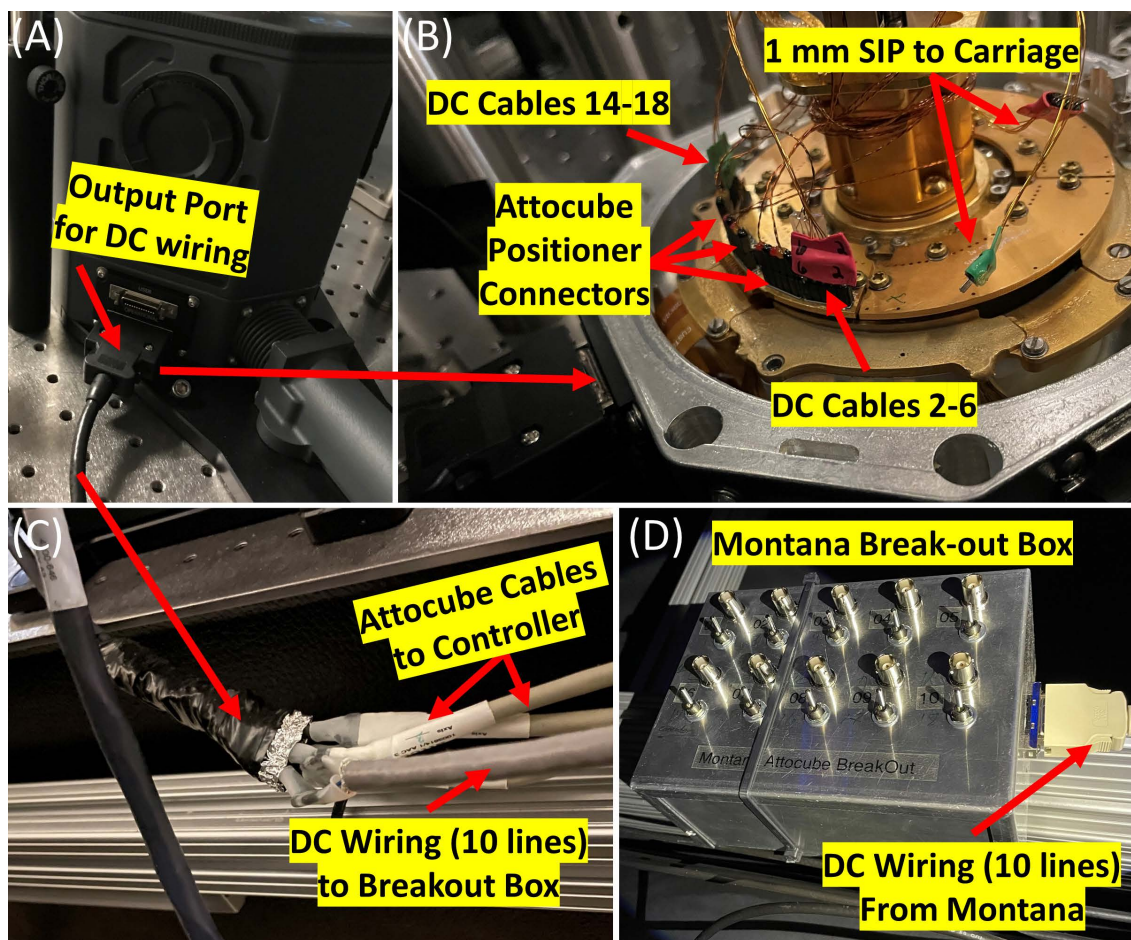


Figure G.6: (A) On the back side of the Montana cryostat, there is a 25-pin D-sub connector that connects to the internal DC wiring of the Montana. (B) These 2 mm pitch SIP connectors breakout the wiring from the external 25-pin D-sub connector. 15 of these wires are used for the closed-loop feedback and control of the Attocube positioners. The remaining 10 can be used for DC wiring to devices. We currently have two soldered wires that connect the 10 DC SIP to our 1 mm pitch SIP connectors on the sample carriage. Since there are only 10, we have cables labeled for pins 2-6 and 14-18. (C) From the 25-pin D-sub connector, the wiring breaks out into these 4 cables. 3 of the cables go to the Attocube controller box while the fourth cable goes to the BNC breakout box shown in (D). All 10 DC lines are broken out and soldered to their individual BNC port with switches that allow for grounding of the wiring.

## G.2 Continuous Wave Laser Systems

### G.2.1 Summary

I have already discussed the dye laser in extensive detail, but would also like to acknowledge a few other CW laser systems we have in the lab that were used in some of our PL measurements. These include a M-Squared Ti:Sapphire laser with an optical range between 698-1100 nm, a HeNe laser with fixed wavelength at 633nm, and a diode laser with fixed wavelength at 532nm. Only the HeNe and diode laser were used in data presented in this dissertation, but the Ti:Sapphire laser is being utilized for measurements of other systems that have exciton energies below 750 nm.



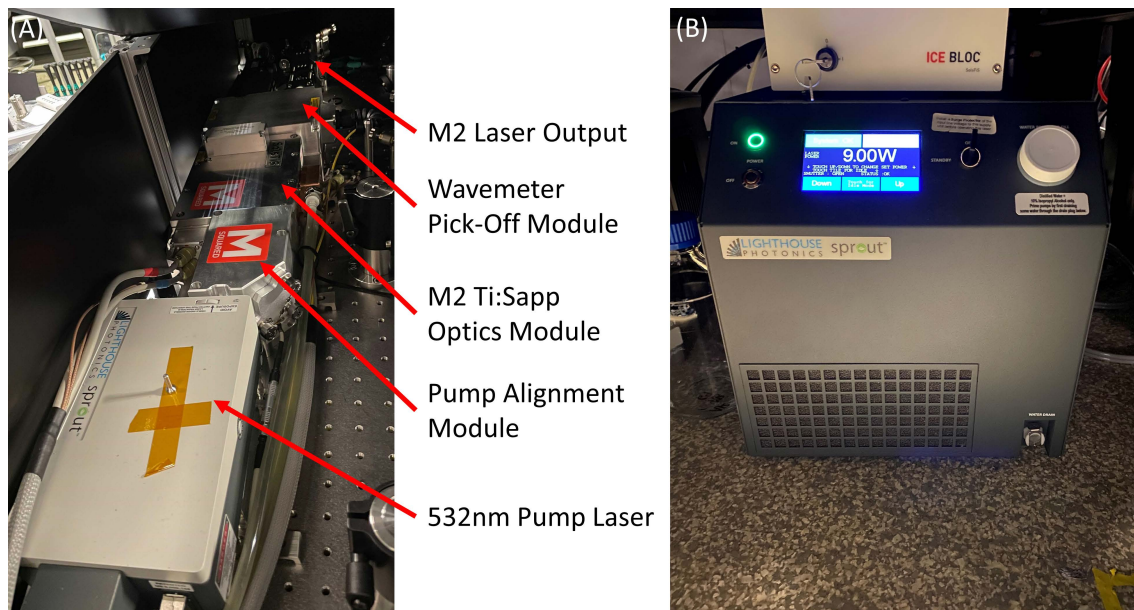


Figure G.7: (A) The M-Squared laser system aligned on the optical table. (B) Lighthouse control unit and IceBloc for controller the M-Squared laser.

### G.2.2 M-Squared Laser

The M-Squared laser is a Ti:Sapphire CW laser system. It has a continuous wavelength range between 698 - 1100 nm (if the pump is well aligned) and is very easy to control via its browser portal (see M-Squared laser manual.) We do not use the M-Squared laser in any of the measurements conducted in this dissertation because its energy range is outside of that required for the TMDs. It is a good laser system for solid-state systems with exciton energies below 750 nm (such as GaAs quantum wells.)

This sub-section outlines the various details of the M-Square Ti:Sapphire laser in Figures G.7, G.8, G.9. The most important detail when aligning the M-Squared is to make sure the 532 nm pump laser is aligned properly. You will be able to get the M-Squared to lase pretty quickly for wavelengths between 715-1000 nm, but accessing wavelengths

<710 nm requires the pump to be very well aligned. This is tricky because there is only one aperture visible to the user, Fig. G.8, while the other one is inside of the secured module. You are not supposed to open the Ti:Sapphire module because it will expose the optics to humid air, but if you do, be sure to quickly pump nitrogen through the side ports of the module and that the desiccant is attached on the top.

Once the laser module is lasing, you will need to align the fiber pick-off. This unit reflects a small amount of laser light off of a piece of glass to a fiber coupler which brings the light to a wavemeter that measures the output wavelength. The fiber coupler module is shown in Fig. G.9(B) and the wavemeter is shown in Fig. G.10(B). The wavemeter has its own software that must be running for the closed loop feedback loop of the M-Square that monitors and stabilizes the wavelength. All of these details are covered in the M-Squared laser's manual.

We direct the output beam of the M-Squared through a HWP/PBS to manually control the output power, Fig. G.10(A). We have a second HWP before the fiber coupler to rotate the polarization of the laser to match the fast-axis of our polarization-maintaining fiber.

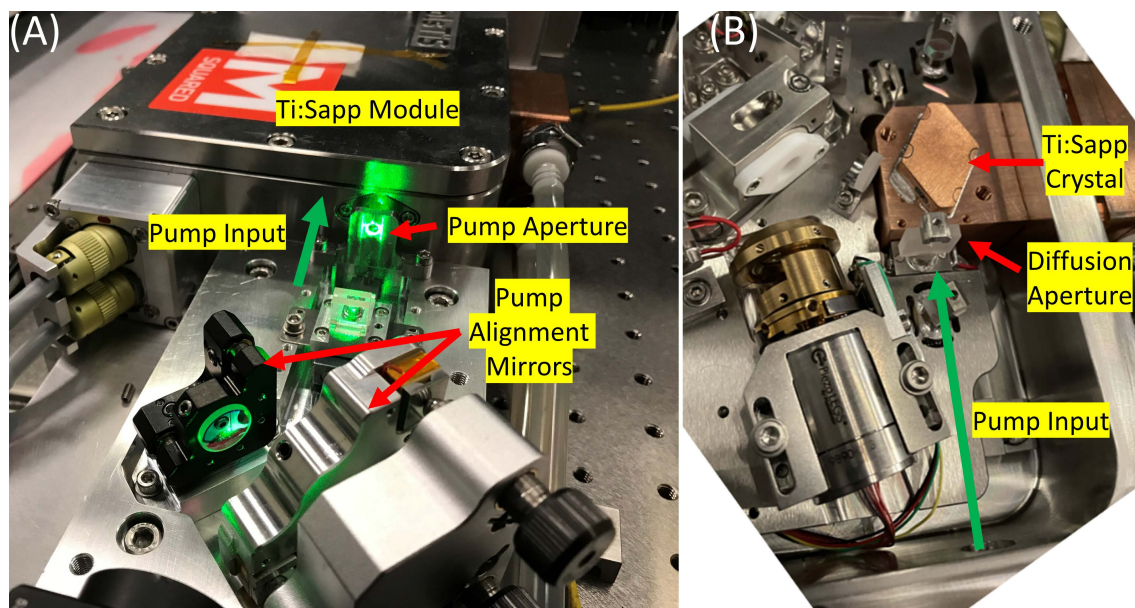


Figure G.8: (A) The 532 nm pump laser is directed into the M-Square via the two mirrors shown here. The design of the M-Squared makes it difficult to quickly align the pump laser because there is only one aperture outside of the module. The other alignment aperture is inside of the Ti:Sapphire module, shown in (B), and is made of a diffusion glass. You are supposed to do the pump alignment without opening the Ti:Sapphire module.



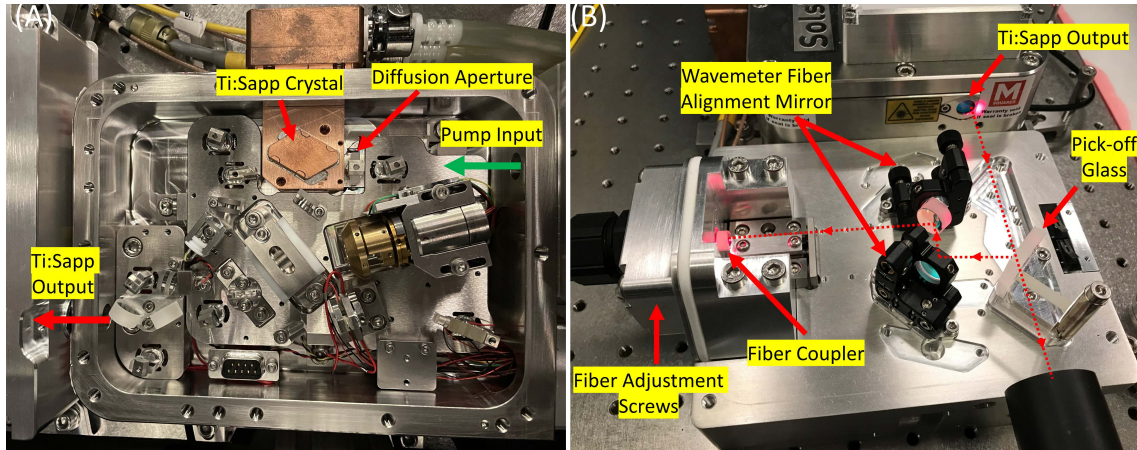


Figure G.9: (A) Once the pump is aligned, the Ti:Sapphire crystal emits a broadband fluoresce that is locked to the cavity module of the M-Squared module. The laser tunes the optics to allow only a very narrow linewidth to propagate in the cavity. (B) A small percentage of the output laser is picked-off by the glass plates and directed to the fiber coupler. This fiber connects to the wavemeter in Fig. G.10(B) which reads that wavelength of the output laser light.

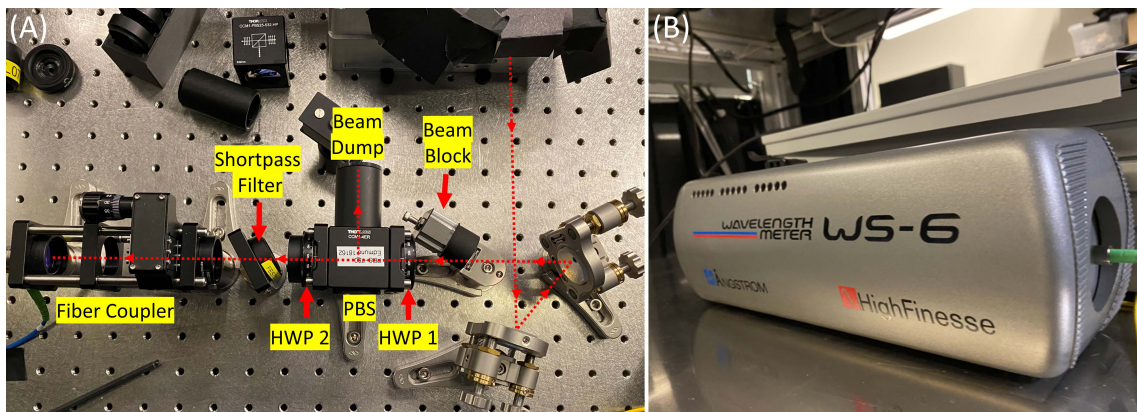


Figure G.10: (A) The laser light output from the M-Squared laser is directed through a HWP and PBS. This allows us to control the power transmitted through the PBS by changing the polarization of the laser light using the HWP. The reflected light of the PBS is dumped. The second HWP allows us to rotate the laser's polarization to match the polarization maintaining fiber. We can also use a shortpass filter to block any low energy side bands that may be detected on our spectroscopy measurement. (B) Wavemeter reads the exact wavelength of the light being emitted by the M-Squared.

### G.2.3 HeNe and 532 nm Diode Lasers

The PL measurements reported in this dissertation were collected with the use of a 633 nm (1.958 eV) HeNe laser, Fig. G.11(A), and a 532 nm (2.33 eV) diode laser, Fig. G.11(B). The HeNe is from Lumentum, purchased through Edmund Optics part number: 62-732, and has an output power of 21 mW. It is fiber coupled for use on either the BlueFors or Montana. The 532 nm diode laser is from Edmund Optics, part number: 35-072, and has a maximum output power of 50 mW (its power is variable from the control unit). The diode laser is sold by Edmund Optics, but its actual model number is MGL-III-532nm-50mW-M2 1.2-20011115 from a company called CNI Optoelectronics Technology Co. We also fiber couple this laser for use on either the BlueFors or Montana.

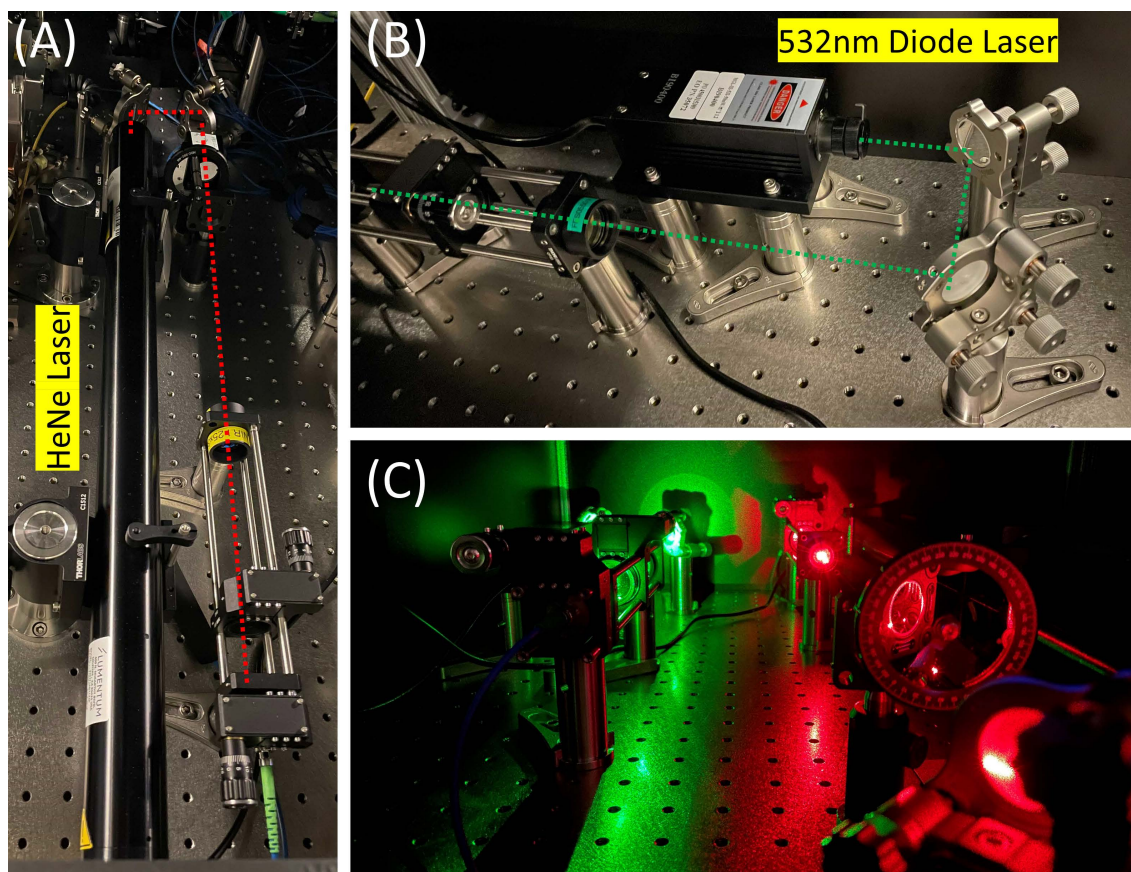


Figure G.11: (A) The HeNe laser is a large gas tube and takes up a lot of table space. We aligned it to a fiber coupler for use on both cryostats. (B) The 532 nm diode laser is a much smaller package and also aligned to a fiber coupler for use on both cryostats. (C) Both lasers while in operation.



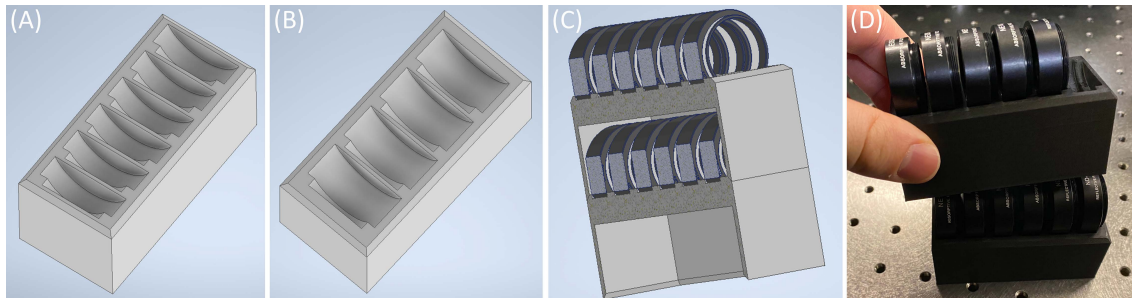


Figure G.12: (A) 3D CAD of the SM1L03 tube holder. (B) 3D CAD of the SM1L05 tube holder. (C) Sectional view of the 3D CAD depicting the stackability of the SM1 tube holders. (D) Image of the actual 3D printed SM1 tube holders; material: Onyx.

### G.3 3D Printed SM1 Tube Holders

We use a lot of SM1L03 and SM1L05 tubes from Thorlabs to hold optical components. The most common components are ND filters placed within the SM1L03 tubes. The SM1L05 tubes are good for edge-pass filters or lenses. We always had the problem that these optics would be left on the optical table when not in use and either get dust on them or scratched. I designed these holders to store the optical components in these tubes vertically on the optical table, Fig. G.12. I've currently only designed holders for SM1L03, Fig. G.12(A), and SM1L05, Fig. G.12(B), tubes, but they could be modified to fit any SM1 tube size. The design also allows for them to be stacked on top of each other to reduce table space, Fig. G.12(C, D).

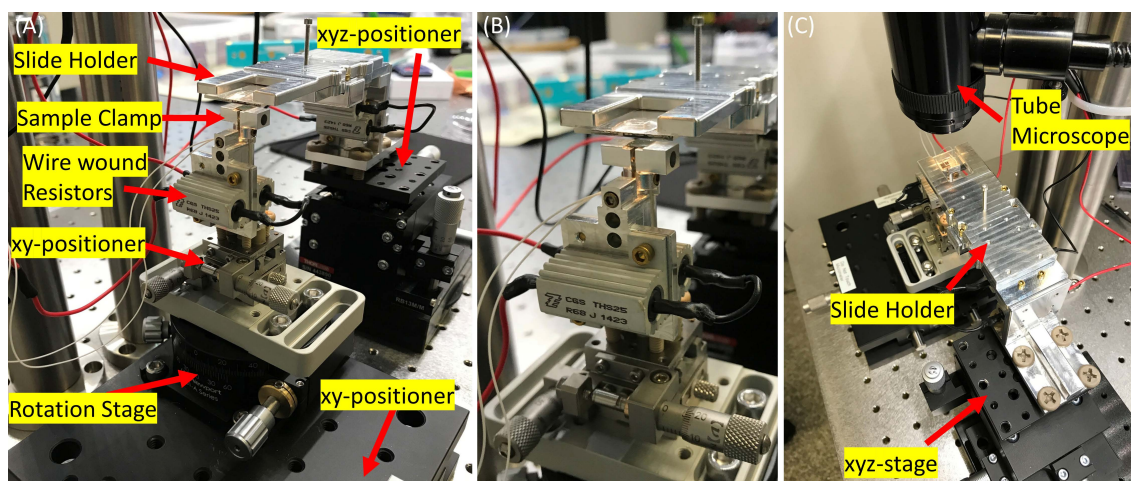


Figure G.13: (A) There are two parts to this version of the encapsulation system. The first is the substrate mount that has a clamping mechanism that holds the substrate in place as the PDMS stamp on the glass slide is applied to the substrate to pick up or drop 2D monolayers. The substrate mount has two wire wound resistors for heating the sample to the required temperatures. There is also a thermometer attached to this stage. The substrate mount is thermally isolated from the positioning stages by PEEK rods. The first xy positioning stage is used to move the sample under the microscope and align it with the slide. The stage underneath that is for rotation of the substrate. The final stage that all of the assembly sits upon is a larger xy positioning stage. This last stage is only for aligning the center of the rotation stage with the microscope. (B) A close up image of the clamping mechanism and the slide holder positioned above it. (C) Image of the slide holder and the tube microscope. The slide holder is on an xyz positioning stage to align the slide and lower/raise it from the substrate.

## G.4 Encapsulation System

We also designed an encapsulation system to assemble these 2D devices ourselves. There are now commercially available systems and I strongly suggest purchasing one of these turn-key units instead of trying to design one yourself. The design isn't too complicated, but there are issues that you can run into and it is just better to buy one that works.

I will walk through a quick summary of the requirements for an encapsulation system and how it is used. A substrate with mechanically exfoliated or grown 2D material must be held underneath a microscope while another stage holds a glass slide with a PDMS stamp above the sample. The PDMS stamp is coated with the polymer propylene carbonate (PC) or polypropylene carbonate (PPC) which is used to adhere to the 2D flake and lift them off the substrate [96–98]. The temperature of the substrate determines whether or not the PC or PPC will pick up the flakes. The glass slide and 2D material on the substrate have to be aligned under the microscope before they are brought in contact and the substrate has to be heated so that the 2D material will stick to the PC or PPC when the glass slide is lifted back up. Finally, when the 2D device has been assembled, the PC or PPC is melted off the PDMS stamp and dropped on the substrate. (This is done by heating the substrate to a high enough temperature). The PC or PPC is dissolved in a bath of chloroform and the 2D stack is left behind on the substrate's surface.

The first design (not shown here) was machined to hold the sample using vacuum, but never worked very well. We ended up having to use double-sided kapton tape to keep the substrate from sticking to the PDMS stamp and lifting off the vacuum stage. Therefore, I moved to a clamping design, Fig. G.13. This worked quite well. Since it did not rely on vacuum, we didn't have to worry about having a vacuum pump and tubing where ever the stage was placed. The CAD for the newest version of the clamping mechanism is shown in Fig. G.14(A).

The only issue with this design was that I tried to save money by having the clamping mechanism machined out of aluminum. If I were to redo this design I would have it machined out of stainless steel or titanium. The problem with aluminum is that it

is a very soft metal and expands with increased temperature. This would often cause the stainless steel screws to jam in the aluminum threads because the aluminum expanded. If the stage is hot and expands, and you try to tighten or loosen the screws, the screws will get jammed in the threads. The only solution was to make sure that the screws are not tightened or loosened while the clamping mechanism is hot.

The slide mount design works really well and is still being used in the current encapsulation system. There are two components that secure the glass slide in the holder assembly, Fig. G.14(B,C). The bottom part can be attached to any stage and has a small groove machined for the glass slide. The top part sits on top of the bottom part and also has a small groove for the glass slide. The top extends out to cover the entire glass slide and to apply uniform force on the glass slide as it is lowered to make contact with the substrate. The machined out middle region allows for imaging of the PDMS stamp and the substrate below it with the tube microscope that hangs above the substrate.

Ultimately, the clamping mechanism was abandoned when we discovered that the company that makes our wire bonder, West Bond, sells a heated, vacuum stage (product number: -45.033 with controller uni: K 1200-D). This is shown in Fig. G.15(A). We also redesigned the layout of the stages to incorporate the new vacuum mount and changed the stages for the slide holder (using the same glass slide holder as shown in Fig. G.14(B,C)) to include a sliding track that allows for the entire glass slide assembly to be slid in and out. The final (and current at the time of this dissertation) encapsulation system is shown in Fig. G.15.

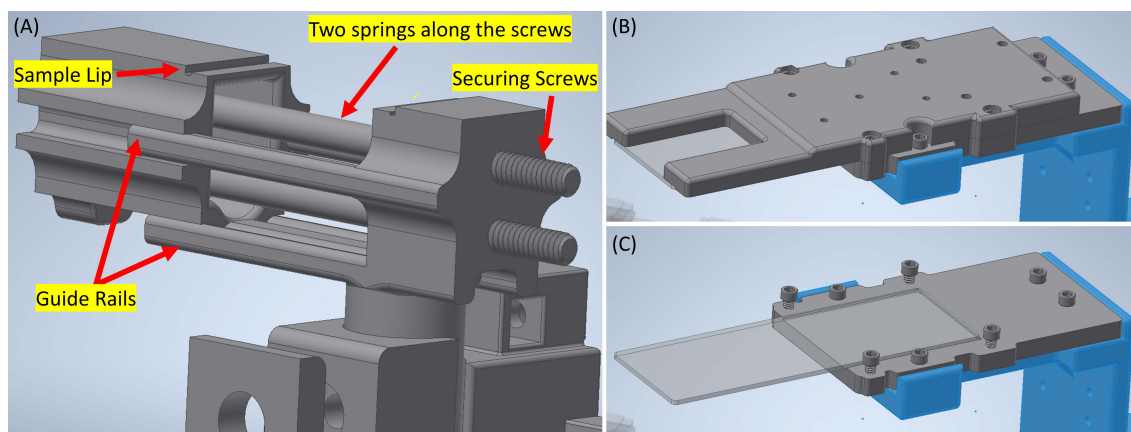


Figure G.14: (A) The CAD of the final version of the clamping mechanism. We had this part machined and it worked quite well. Unlike the one shown in Fig. G.13(A,B), it allows for larger samples (up to 1 cm) to be clamped. The first version, in Fig. G.13(A,B), only worked with 5 mm long samples. The idea is to have two long screws connect the clamping mechanism together with a spring along each screw (not shown in CAD). The spring and screw combination keeps the two clamping mechanisms aligned and in tension. The screws are also fully threaded so the clamping mechanism can be brought all the way together or extended until the guide rails stop. Note: a spring with this compression/extension ratio must be selected to access this full range. (B) Top of the slide holder that secures the glass slide in place. (C) Bottom of the slide holder that secures the glass slide in place. Both the top and bottom are machined to have a groove for the glass slide to prevent it from moving.

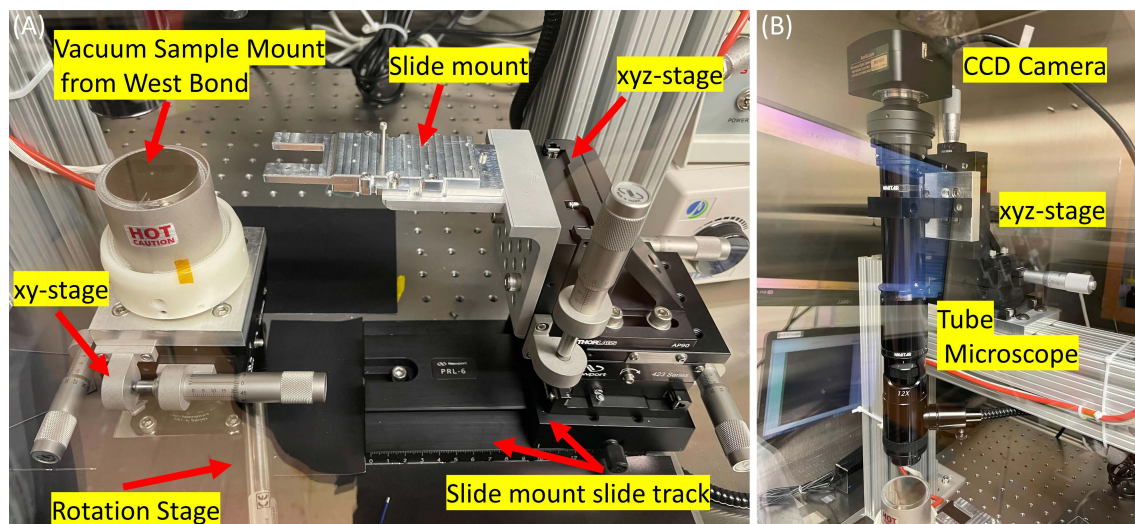


Figure G.15: (A) We redesigned the encapsulation system to utilize a heated and vacuum mount that West Bond sells for use with their wire bonders. The mount has a vacuum hole in the center for the substrate to be placed and held. We placed this mount on two linear stages that sit on a rotation stage. The slide mount is the same as the previous design (it works really nicely to keep the slides from moving), but the mount and stages are different. We machined a simple 90 deg aluminum mount that attaches to an xyz-stage. This stage sits on a slide track so that the entire slide assembly can be easily moved in or out. (B) The tube microscope is attached to an xyz stage that sits on a t-slot bracket. This suspends the tube microscope above the vacuum stage.



## Bibliography

- [1] Andre K Geim and Irina V Grigorieva. Van der Waals heterostructures. *Nature*, 499(7459):419–425, 2013.
- [2] Keliang He, Nardeep Kumar, Liang Zhao, Zefang Wang, Kin Fai Mak, Hui Zhao, and Jie Shan. Tightly bound excitons in monolayer WSe<sub>2</sub>. *Physical review letters*, 113(2):026803, 2014.
- [3] Gang Wang, Alexey Chernikov, Mikhail M Glazov, Tony F Heinz, Xavier Marie, Thierry Amand, and Bernhard Urbaszek. Colloquium: Excitons in atomically thin transition metal dichalcogenides. *Reviews of Modern Physics*, 90(2):021001, 2018.
- [4] Heather M Hill, Albert F Rigosi, Cyrielle Roquelet, Alexey Chernikov, Timothy C Berkelbach, David R Reichman, Mark S Hybertsen, Louis E Brus, and Tony F Heinz. Observation of excitonic Rydberg states in monolayer MoS<sub>2</sub> and WS<sub>2</sub> by photoluminescence excitation spectroscopy. *Nano letters*, 15(5):2992–2997, 2015.
- [5] Shao-Yu Chen, Zhengguang Lu, Thomas Goldstein, Jiayue Tong, Andrey Chaves, Jens Kunstmann, LSR Cavalcante, Tomasz Wozniak, Gotthard Seifert, DR Reichman, et al. Luminescent emission of excited Rydberg excitons from monolayer WSe<sub>2</sub>. *Nano letters*, 19(4):2464–2471, 2019.
- [6] Erfu Liu, Jeremiah van Baren, Takashi Taniguchi, Kenji Watanabe, Yia-Chung Chang, and Chun Hung Lui. Magnetophotoluminescence of exciton Rydberg states in monolayer WS<sub>e</sub> 2. *Physical Review B*, 99(20):205420, 2019.
- [7] Tianmeng Wang, Zhipeng Li, Yunmei Li, Zhengguang Lu, Shengnan Miao, Zhen Lian, Yuze Meng, Mark Blei, Takashi Taniguchi, Kenji Watanabe, et al. Giant valley-polarized Rydberg excitons in monolayer WSe<sub>2</sub> revealed by magneto-photocurrent spectroscopy. *Nano Letters*, 20(10):7635–7641, 2020.
- [8] Gang Wang, Xavier Marie, I Gerber, Thierry Amand, Delphine Lagarde, Louis Bouet, M Vidal, Andrea Balocchi, and Bernhard Urbaszek. Giant enhancement of the optical second-harmonic emission of WSe<sub>2</sub> monolayers by laser excitation at exciton resonances. *Physical review letters*, 114(9):097403, 2015.

- [9] Robert Nyden Hill. Proof that the H<sup>-</sup> ion has only one bound state. *Physical Review Letters*, 38(12):643, 1977.
- [10] Shiue-Yuan Shiau, Monique Combescot, and Yia-Chung Chang. Trion ground state, excited states, and absorption spectrum using electron-exciton basis. *Physical Review B*, 86(11):115210, 2012.
- [11] Koloman Wagner, Edith Wietek, Jonas D Ziegler, Marina A Semina, Takashi Taniguchi, Kenji Watanabe, Jonas Zipfel, Mikhail M Glazov, and Alexey Chernikov. Autoionization and Dressing of Excited Excitons by Free Carriers in Monolayer WSe<sub>2</sub>. *Physical Review Letters*, 125(26):267401, 2020.
- [12] Ashish Arora, Thorsten Deilmann, Till Reichenauer, Johannes Kern, Steffen Michaelis de Vasconcellos, Michael Rohlfing, and Rudolf Bratschitsch. Excited-state trions in monolayer WS<sub>2</sub>. *Physical review letters*, 123(16):167401, 2019.
- [13] Erfu Liu, Jeremiah van Baren, Zhengguang Lu, Takashi Taniguchi, Kenji Watanabe, Dmitry Smirnov, Yia-Chung Chang, and Chun Hung Lui. Exciton-polaron Rydberg states in monolayer MoSe<sub>2</sub> and WSe<sub>2</sub>. *Nature Communications*, 12(1):1–8, 2021.
- [14] Thomas Goldstein, Yueh-Chun Wu, Shao-Yu Chen, Takashi Taniguchi, Kenji Watanabe, Kalman Varga, and Jun Yan. Ground and excited state exciton polarons in monolayer MoSe<sub>2</sub>. *The Journal of Chemical Physics*, 153(7):071101, 2020.
- [15] Characterization of electronic transitions in complex molecules, author=Kasha, Michael. *Discussions of the Faraday society*, 9:14–19, 1950.
- [16] Samuel Brem, Malte Selig, Gunnar Berghaeuser, and Ermin Malic. Exciton relaxation cascade in two-dimensional transition metal dichalcogenides. *Scientific reports*, 8(1):1–8, 2018.
- [17] Shao-Yu Chen, Thomas Goldstein, Jiayue Tong, Takashi Taniguchi, Kenji Watanabe, and Jun Yan. Superior valley polarization and coherence of 2 s excitons in monolayer wse<sub>2</sub>. *Physical review letters*, 120(4):046402, 2018.
- [18] JC Sell\*, JR Vannucci\*, DG Suarez-Forero, B Cao, DW Session, H-J Chuang, K McCreary, M Rosenberger, B Jonker, S Mittal, et al. Magneto-Optical Measurements of the Negatively Charged 2s Exciton in WSe<sub>2</sub>. *arXiv preprint arXiv:2202.06415*, 2022. \*Both authors contributed equally to this work.
- [19] Marta Skoda, Ilona Dudek, Anna Jarosz, and Dariusz Szukiewicz. Graphene: one material, many possibilities—application difficulties in biological systems. *Journal of Nanomaterials*, 2014, 2014.
- [20] Richard Van Noorden. Production: Beyond sticky tape. *Nature*, 483(7389):S32–S33, 2012.

- [21] Kostya S Novoselov, Andre K Geim, Sergei V Morozov, De-eng Jiang, Yanshui Zhang, Sergey V Dubonos, Irina V Grigorieva, and Alexandr A Firsov. Electric field effect in atomically thin carbon films. *science*, 306(5696):666–669, 2004.
- [22] Andre Konstantin Geim. Graphene: status and prospects. *science*, 324(5934):1530–1534, 2009.
- [23] KS Novoselov, o A Mishchenko, o A Carvalho, and AH Castro Neto. 2D materials and van der Waals heterostructures. *Science*, 353(6298):aac9439, 2016.
- [24] Seongjoon Ahn, Gwangwoo Kim, Pramoda K Nayak, Seong In Yoon, Hyunseob Lim, Hyun-Joon Shin, and Hyeon Suk Shin. Prevention of transition metal dichalcogenide photodegradation by encapsulation with h-BN layers. *ACS nano*, 10(9):8973–8979, 2016.
- [25] Michele Cotrufo, Liuyang Sun, Junho Choi, Andrea Alù, and Xiaoqin Li. Enhancing functionalities of atomically thin semiconductors with plasmonic nanostructures. *Nanophotonics*, 8(4):577–598, 2019.
- [26] Andrea Splendiani, Liang Sun, Yuanbo Zhang, Tianshu Li, Jonghwan Kim, Chi-Yung Chim, Giulia Galli, and Feng Wang. Emerging photoluminescence in monolayer MoS<sub>2</sub>. *Nano letters*, 10(4):1271–1275, 2010.
- [27] Maciej Koperski, Maciej R Molas, Ashish Arora, Karol Nogajewski, Artur O Slobodeniuk, Clement Faugeras, and Marek Potemski. Optical properties of atomically thin transition metal dichalcogenides: observations and puzzles. *Nanophotonics*, 6(6):1289–1308, 2017.
- [28] Zhiyong Y Zhu, Yingchun C Cheng, and Udo Schwingenschlögl. Giant spin-orbit-induced spin splitting in two-dimensional transition-metal dichalcogenide semiconductors. *Physical Review B*, 84(15):153402, 2011.
- [29] Benjamin T Zhou, Katsuhisa Taguchi, Yuki Kawaguchi, Yukio Tanaka, and Kam Tuen Law. Spin-orbit coupling induced valley Hall effects in transition-metal dichalcogenides. *Communications Physics*, 2(1):1–7, 2019.
- [30] Ajit Srivastava, Meinrad Sidler, Adrien V Allain, Dominik S Lembke, Andras Kis, and A Imamoglu. Valley Zeeman effect in elementary optical excitations of monolayer WSe<sub>2</sub>. *Nature Physics*, 11(2):141–147, 2015.
- [31] Di Xiao, Gui-Bin Liu, Wanxiang Feng, Xiaodong Xu, and Wang Yao. Coupled spin and valley physics in monolayers of MoS<sub>2</sub> and other group-VI dichalcogenides. *Physical review letters*, 108(19):196802, 2012.
- [32] Ashwin Ramasubramaniam. Large excitonic effects in monolayers of molybdenum and tungsten dichalcogenides. *Physical Review B*, 86(11):115409, 2012.
- [33] Bairen Zhu, Xi Chen, and Xiaodong Cui. Exciton binding energy of monolayer WS<sub>2</sub>. *Scientific reports*, 5(1):1–5, 2015.

- [34] Alexey Chernikov, Timothy C Berkelbach, Heather M Hill, Albert Rigosi, Yilei Li, Ozgur Burak Aslan, David R Reichman, Mark S Hybertsen, and Tony F Heinz. Exciton binding energy and nonhydrogenic Rydberg series in monolayer WS<sub>2</sub>. *Physical review letters*, 113(7):076802, 2014.
- [35] Maciej Koperski, Maciej R Molas, Ashish Arora, Karol Nogajewski, Miroslav Bartos, Jan Wyzula, Diana Vaclavkova, Piotr Kossacki, and Marek Potemski. Orbital, spin and valley contributions to Zeeman splitting of excitonic resonances in MoSe<sub>2</sub>, WSe<sub>2</sub> and WS<sub>2</sub> Monolayers. *2D Materials*, 6(1):015001, 2018.
- [36] Humberto R Gutiérrez, Nestor Perea-López, Ana Laura Elías, Ayse Berkdemir, Bei Wang, Ruitao Lv, Florentino López-Urías, Vincent H Crespi, Humberto Terrones, and Mauricio Terrones. Extraordinary room-temperature photoluminescence in triangular WS<sub>2</sub> monolayers. *Nano letters*, 13(8):3447–3454, 2013.
- [37] Jiani Huang, Thang B Hoang, and Maiken H Mikkelsen. Probing the origin of excitonic states in monolayer WSe<sub>2</sub>. *Scientific reports*, 6(1):1–7, 2016.
- [38] Pramoda K Nayak, Fan-Cheng Lin, Chao-Hui Yeh, Jer-Shing Huang, and Po-Wen Chiu. Robust room temperature valley polarization in monolayer and bilayer WS<sub>2</sub>. *Nanoscale*, 8(11):6035–6042, 2016.
- [39] Matthew R Rosenberger, Hsun-Jen Chuang, Kathleen M McCreary, Aubrey T Hanbicki, Saujan V Sivaram, and Berend T Jonker. Nano-“squeegee” for the creation of clean 2D material interfaces. *ACS applied materials & interfaces*, 10(12):10379–10387, 2018.
- [40] Matthew R Rosenberger, Chandriker Kavir Dass, Hsun-Jen Chuang, Saujan V Sivaram, Kathleen M McCreary, Joshua R Hendrickson, and Berend T Jonker. Quantum calligraphy: writing single-photon emitters in a two-dimensional materials platform. *ACS nano*, 13(1):904–912, 2019.
- [41] F Dybała, MP Polak, J Kopaczek, P Scharoch, Kedi Wu, Sefaattin Tongay, and R Kudrawiec. Pressure coefficients for direct optical transitions in MoS<sub>2</sub>, MoSe<sub>2</sub>, WS<sub>2</sub>, and WSe<sub>2</sub> crystals and semiconductor to metal transitions. *Scientific reports*, 6(1):1–12, 2016.
- [42] Claus F Klingshirn. *Semiconductor optics*. Springer Science & Business Media, 2012.
- [43] Jinying Wang, Shibin Deng, Zhongfan Liu, and Zhirong Liu. The rare two-dimensional materials with Dirac cones. *National Science Review*, 2(1):22–39, 2015.
- [44] Gui-Bin Liu, Wen-Yu Shan, Yugui Yao, Wang Yao, and Di Xiao. Three-band tight-binding model for monolayers of group-VIB transition metal dichalcogenides. *Physical Review B*, 88(8):085433, 2013.

- [45] Yohta Sata, Rai Moriya, Satoru Masubuchi, Kenji Watanabe, Takashi Taniguchi, and Tomoki Machida. N-and p-type carrier injections into WSe<sub>2</sub> with van der Waals contacts of two-dimensional materials. *Japanese Journal of Applied Physics*, 56(4S):04CK09, 2017.
- [46] Hao-Ling Tang, Ming-Hui Chiu, Chien-Chih Tseng, Shih-Hsien Yang, Kuan-Jhih Hou, Sung-Yen Wei, Jing-Kai Huang, Yen-Fu Lin, Chen-Hsin Lien, and Lain-Jong Li. Multilayer graphene–WSe<sub>2</sub> heterostructures for WSe<sub>2</sub> transistors. *ACS nano*, 11(12):12817–12823, 2017.
- [47] Zefang Wang, Liang Zhao, Kin Fai Mak, and Jie Shan. Probing the spin-polarized electronic band structure in monolayer transition metal dichalcogenides by optical spectroscopy. *Nano letters*, 17(2):740–746, 2017.
- [48] Shivangi Shree, M Semina, Cédric Robert, B Han, Thierry Amand, Andrea Balocchi, Marco Manca, Emmanuel Courtade, X Marie, T Taniguchi, et al. Observation of exciton-phonon coupling in MoSe<sub>2</sub> monolayers. *Physical Review B*, 98(3):035302, 2018.
- [49] Karen J Moore, Geoffrey Duggan, Karl Woodbridge, and Christine Roberts. Observations and calculations of the exciton binding energy in (In, Ga) As/GaAs strained-quantum-well heterostructures. *Physical Review B*, 41(2):1090, 1990.
- [50] Philipp Steinleitner, Philipp Merkl, Philipp Nagler, Joshua Mornhinweg, Christian Schuller, Tobias Korn, Alexey Chernikov, and Rupert Huber. Direct observation of ultrafast exciton formation in a monolayer of WSe<sub>2</sub>. *Nano Letters*, 17(3):1455–1460, 2017.
- [51] Soonyoung Cha, Ji Ho Sung, Sangwan Sim, Jun Park, Hoseok Heo, Moon-Ho Jo, and Hyunyoung Choi. 1s-intraexcitonic dynamics in monolayer MoS<sub>2</sub> probed by ultrafast mid-infrared spectroscopy. *Nature communications*, 7(1):1–7, 2016.
- [52] Galan Moody, Kha Tran, Xiaobo Lu, Travis Autry, James M Fraser, Richard P Mirin, Li Yang, Xiaoqin Li, and Kevin L Silverman. Microsecond valley lifetime of defect-bound excitons in monolayer WSe<sub>2</sub>. *Physical review letters*, 121(5):057403, 2018.
- [53] Zhipeng Li, Tianmeng Wang, Chenhao Jin, Zhengguang Lu, Zhen Lian, Yuze Meng, Mark Blei, Shiyuan Gao, Takashi Taniguchi, Kenji Watanabe, et al. Emerging photoluminescence from the dark-exciton phonon replica in monolayer WSe<sub>2</sub>. *Nature communications*, 10(1):1–7, 2019.
- [54] Matteo Barbone, Alejandro R-P Montblanch, Dhiren M Kara, Carmen Palacios-Berraquero, Alisson R Cadore, Domenico De Fazio, Benjamin Pingault, Elaheh Mostaani, Han Li, Bin Chen, et al. Charge-tuneable biexciton complexes in monolayer WSe<sub>2</sub>. *Nature communications*, 9(1):1–6, 2018.
- [55] Zhipeng Li, Tianmeng Wang, Zhengguang Lu, Chenhao Jin, Yanwen Chen, Yuze Meng, Zhen Lian, Takashi Taniguchi, Kenji Watanabe, Shengbai Zhang, et al.

Revealing the biexciton and trion-exciton complexes in BN encapsulated WSe<sub>2</sub>. *Nature communications*, 9(1):1–7, 2018.

- [56] Zhipeng Li, Tianmeng Wang, Shengnan Miao, Zhen Lian, and Su-Fei Shi. Fine structures of valley-polarized excitonic states in monolayer transitional metal dichalcogenides. *Nanophotonics*, 9(7):1811–1829, 2020.
- [57] Alexander Steinhoff, Matthias Florian, Akshay Singh, Kha Tran, Mirco Kolarczik, Sophia Helmrich, Alexander W Achtstein, Ulrike Woggon, Nina Owschimikow, Frank Jahnke, et al. Biexciton fine structure in monolayer transition metal dichalcogenides. *Nature Physics*, 14(12):1199–1204, 2018.
- [58] Thomas P Lyons, Scott Dufferwiel, Matthew Brooks, Freddie Withers, T Taniguchi, Kenji Watanabe, KS Novoselov, Guido Burkard, and Alexander I Tartakovskii. The valley Zeeman effect in inter-and intra-valley trions in monolayer WSe<sub>2</sub>. *Nature communications*, 10(1):1–8, 2019.
- [59] Erfu Liu, Jeremiah van Baren, Ching-Tarng Liang, Takashi Taniguchi, Kenji Watanabe, Nathaniel M Gabor, Yia-Chung Chang, and Chun Hung Lui. Multipath optical recombination of intervalley dark excitons and trions in monolayer wse<sub>2</sub>. *Physical Review Letters*, 124(19):196802, 2020.
- [60] Patrick Back, Meinrad Sidler, Ovidiu Cotlet, Ajit Srivastava, Naotomo Takemura, Martin Kroner, and Atac Imamoglu. Giant paramagnetism-induced valley polarization of electrons in charge-tunable monolayer MoSe<sub>2</sub>. *Physical review letters*, 118(23):237404, 2017.
- [61] Zefang Wang, Jie Shan, and Kin Fai Mak. Valley-and spin-polarized Landau levels in monolayer WSe<sub>2</sub>. *Nature nanotechnology*, 12(2):144–149, 2017.
- [62] Andor Kormányos, Guido Burkard, Martin Gmitra, Jaroslav Fabian, Viktor Zólyomi, Neil D Drummond, and Vladimir Fal’ko.  $k \cdot p$  theory for two-dimensional transition metal dichalcogenide semiconductors. *2D Materials*, 2(2):022001, 2015.
- [63] Hongyi Yu, Gui-Bin Liu, Pu Gong, Xiaodong Xu, and Wang Yao. Dirac cones and Dirac saddle points of bright excitons in monolayer transition metal dichalcogenides. *Nature communications*, 5(1):1–7, 2014.
- [64] Emmanuel Courtade, M Semina, Marco Manca, MM Glazov, Cédric Robert, Fabian Cadiz, Gang Wang, T Taniguchi, K Watanabe, M Pierre, et al. Charged excitons in monolayer WSe<sub>2</sub>: Experiment and theory. *Physical Review B*, 96(8):085302, 2017.
- [65] Alexey Chernikov, Arend M Van Der Zande, Heather M Hill, Albert F Rigosi, Ajanth Velauthapillai, James Hone, and Tony F Heinz. Electrical tuning of exciton binding energies in monolayer WS<sub>2</sub>. *Physical review letters*, 115(12):126802, 2015.
- [66] Jonas G Roch, Nadine Leisgang, Guillaume Froehlicher, Peter Makk, Kenji Watanabe, Takashi Taniguchi, Christian Schonenberger, and Richard J Warburton.



Quantum-confined stark effect in a MoS<sub>2</sub> monolayer van der Waals heterostructure. *Nano letters*, 18(2):1070–1074, 2018.

- [67] Kin Fai Mak. Observation of the valley Hall effect in MoS<sub>2</sub> transistors. *Bulletin of the American Physical Society*, 59, 2014.
- [68] Dmitry K Efimkin and Allan H MacDonald. Many-body theory of trion absorption features in two-dimensional semiconductors. *Physical Review B*, 95(3):035417, 2017.
- [69] Colin M Chow, Hongyi Yu, Aaron M Jones, Jiaqiang Yan, David G Mandrus, Takashi Taniguchi, Kenji Watanabe, Wang Yao, and Xiaodong Xu. Unusual exciton–phonon interactions at van der Waals engineered interfaces. *Nano letters*, 17(2):1194–1199, 2017.
- [70] J Serrano, A Bosak, Raul Arenal, M Krisch, Kenji Watanabe, T Taniguchi, H Kanda, Angel Rubio, and Ludger Wirtz. Vibrational properties of hexagonal boron nitride: inelastic X-ray scattering and ab initio calculations. *Physical review letters*, 98(9):095503, 2007.
- [71] Chenhao Jin, Jonghwan Kim, Joonki Suh, Zhiwen Shi, Bin Chen, Xi Fan, Matthew Kam, Kenji Watanabe, Takashi Taniguchi, Sefaattin Tongay, et al. Interlayer electron–phonon coupling in WSe<sub>2</sub>/hBN heterostructures. *Nature Physics*, 13(2):127–131, 2017.
- [72] Zhenghe Jin, Xiaodong Li, Jeffrey T Mullen, and Ki Wook Kim. Intrinsic transport properties of electrons and holes in monolayer transition-metal dichalcogenides. *Physical Review B*, 90(4):045422, 2014.
- [73] Joanna Jadczak, Joanna Kutrowska-Girzycka, Janina J Schindler, Joerg Debus, Kenji Watanabe, Takashi Taniguchi, Ching-Hwa Ho, and Leszek Bryja. Investigations of Electron-Electron and Interlayer Electron-Phonon Coupling in van der Waals hBN/WSe<sub>2</sub>/hBN Heterostructures by Photoluminescence Excitation Experiments. *Materials*, 14(2):399, 2021.
- [74] Erfu Liu, Jeremiah van Baren, Takashi Taniguchi, Kenji Watanabe, Yia-Chung Chang, and Chun Hung Lui. Valley-selective chiral phonon replicas of dark excitons and trions in monolayer WS<sub>e</sub> 2. *Physical Review Research*, 1(3):032007, 2019.
- [75] Minhao He, Pasqual Rivera, Dinh Van Tuan, Nathan P Wilson, Min Yang, Takashi Taniguchi, Kenji Watanabe, Jiaqiang Yan, David G Mandrus, Hongyi Yu, et al. Valley phonons and exciton complexes in a monolayer semiconductor. *Nature communications*, 11(1):1–7, 2020.
- [76] David MacNeill, Colin Heikes, Kin Fai Mak, Zachary Anderson, Andor Kormányos, Viktor Zólyomi, Jiwoong Park, and Daniel C Ralph. Breaking of valley degeneracy by magnetic field in monolayer MoSe<sub>2</sub>. *Physical review letters*, 114(3):037401, 2015.

- [77] Yilei Li, Jonathan Ludwig, Tony Low, Alexey Chernikov, Xu Cui, Ghidewon Arefe, Young Duck Kim, Arend M Van Der Zande, Albert Rigosi, Heather M Hill, et al. Valley splitting and polarization by the Zeeman effect in monolayer MoSe 2. *Physical review letters*, 113(26):266804, 2014.
- [78] J Klein, A Hötger, M Florian, A Steinhoff, A Delhomme, T Taniguchi, K Watanabe, F Jahnke, AW Holleitner, M Potemski, et al. Controlling exciton many-body states by the electric-field effect in monolayer MoS 2. *Physical Review Research*, 3(2):L022009, 2021.
- [79] Zefang Wang, Kin Fai Mak, and Jie Shan. Strongly interaction-enhanced valley magnetic response in monolayer WSe 2. *Physical review letters*, 120(6):066402, 2018.
- [80] Wenchao Liu, Chaobo Luo, Xudong Tang, Xiangyang Peng, and Jianxin Zhong. Valleytronic properties of monolayer WSe2 in external magnetic field. *AIP Advances*, 9(4):045222, 2019.
- [81] E Cappelluti, Rafael Roldán, JA Silva-Guillén, Pablo Ordejón, and F Guinea. Tight-binding model and direct-gap/indirect-gap transition in single-layer and multilayer MoS 2. *Physical Review B*, 88(7):075409, 2013.
- [82] Ashish Arora. Magneto-optics of layered two-dimensional semiconductors and heterostructures: Progress and prospects. *Journal of Applied Physics*, 129(12):120902, 2021.
- [83] G Wang, L Bouet, MM Glazov, Thierry Amand, EL Ivchenko, Etienne Palleau, Xavier Marie, and B Urbaszek. Magneto-optics in transition metal diselenide monolayers. *2D Materials*, 2(3):034002, 2015.
- [84] Zhipeng Li, Tianmeng Wang, Zhengguang Lu, Mandeep Khatoniar, Zhen Lian, Yuze Meng, Mark Blei, Takashi Taniguchi, Kenji Watanabe, Stephen A McGill, et al. Direct observation of gate-tunable dark trions in monolayer WSe2. *Nano letters*, 19(10):6886–6893, 2019.
- [85] Jonathan Förste, Nikita V Tepliakov, Stanislav Yu Kruchinin, Jessica Lindlau, Victor Funk, Michael Förg, Kenji Watanabe, Takashi Taniguchi, Anvar S Baimuratov, and Alexander Högele. Exciton g-factors in monolayer and bilayer WSe2 from experiment and theory. *Nature Communications*, 11(1):1–8, 2020.
- [86] M Goryca, Jing Li, Andreas V Stier, Takashi Taniguchi, Kenji Watanabe, Emmanuel Courtade, Shivangi Shree, Cedric Robert, Bernhard Urbaszek, Xavier Marie, et al. Revealing exciton masses and dielectric properties of monolayer semiconductors with high magnetic fields. *Nature communications*, 10(1):1–12, 2019.
- [87] S Das Sarma, EH Hwang, and Qi Li. Valley dependent many-body effects in 2D semiconductors. *arXiv preprint arXiv:0904.2622*, 2009.

- [88] Bf-ld-series cryogen-free dilution refrigerator system user manual version 1.5.0. BF-LD-SERIES CRYOGEN-FREE DILUTION REFRIGERATOR SYSTEM User manual Version 1.5.0. January, 2016.
- [89] JI Colless and DJ Reilly. Modular cryogenic interconnects for multi-qubit devices. *Review of Scientific Instruments*, 85(11):114706, 2014.
- [90] User’s guide to the andor newton. User’s Guide to the Andor Newton Version 1.3. August, 2008.
- [91] Ozgur Burak Aslan, Minda Deng, and Tony F Heinz. Strain tuning of excitons in monolayer WSe 2. *Physical Review B*, 98(11):115308, 2018.
- [92] American magnetics model 4q06125ps-430 integrated power supply system installation, operation, and maintenance instructions. American Magnetism Model 4Q06125PS-430 Integrated Power Supply System Installation, Operation, and Maintenance Instructions. November, 2011.
- [93] Sirah matisse 2 dye. <https://www.sirah.com/lasers/cw/matisse-2/matisse-2-d/>. Accessed: 2022-02-24.
- [94] Sirah matisse user’s guide version 2.2. Sirah Matisse User’s Guide Version 2.2.
- [95] Semrock versachrome edge™ tunable long-wave and short-wave pass filters. <https://www.semrock.com/versachrome-edge-tunable-filters.aspx>. Accessed: 2022-03-01.
- [96] DG Purdie, NM Pugno, T Taniguchi, K Watanabe, AC Ferrari, and Antonio Lombardo. Cleaning interfaces in layered materials heterostructures. *Nature communications*, 9(1):1–12, 2018.
- [97] Filippo Pizzocchero, Lene Gammelgaard, Bjarke S Jessen, José M Caridad, Lei Wang, James Hone, Peter Bøggild, and Timothy J Booth. The hot pick-up technique for batch assembly of van der Waals heterostructures. *Nature communications*, 7(1):1–10, 2016.
- [98] PJ Zomer, MHD Guimarães, JC Brant, N Tombros, and BJ Van Wees. Fast pick up technique for high quality heterostructures of bilayer graphene and hexagonal boron nitride. *Applied Physics Letters*, 105(1):013101, 2014.